

# Passive Film Behavior of Novel Titanium alloys in Simulated Body conditions

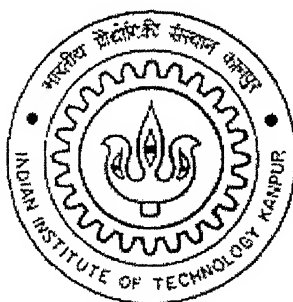
A Thesis submitted

In Partial Fulfillment of the Requirements  
For the degree of

**MASTER OF TECHNOLOGY**

by

**Anoop Kumar Shukla**



*to the*

DEPARTMENT OF MATERIALS AND METALLURGICAL ENGINEERING

**INDIAN INSTITUTE OF TECHNOLOGY, KANPUR**

**INDIA 208016**

**May 2004**

3331 / MME

148413

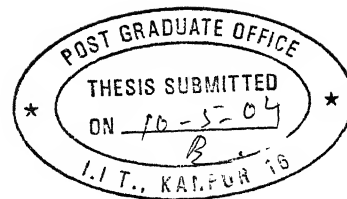
2000



A148413



**Dedicated to My Parents**



## CERTIFICATE

This is to certify that the thesis entitled **Passive Film Behavior of Novel Titanium alloys in Simulated Body Conditions** by Anoop Kumar Shukla (Y-210605) has been carried out under my supervision and has not been submitted elsewhere for the award of a degree.

**Dr. R. Balasubramaniam**

Professor

Materials and Metallurgical Engg.

Indian Institute of Technology

Kanpur, INDIA.

**Dr. S. Bhargava**

Professor

Materials and Metallurgical Engg.

Indian Institute of Technology

Kanpur, INDIA.

# ACKNOWLEDGEMENTS

I express my deep sense gratitude and sincere thanks to Dr. R. Balasubramaniam and Dr. S. Bhargava for their able guidance, remarkable patience and constant encouragement throughout the course of the thesis. I consider it my privilege that I got the opportunity to work under them.

I would like to thank Dr. M.N. Mungole, Senior Research Engineer, Department of MME, IIT Kanpur for his useful comments and valuable suggestions.

I find myself quite lucky that I got such a nice environment in corrosion lab. All my lab-mates were very supportive. I would like to thank Anand Kr. Nigam, Ashish Srivastava, Ajit Misra, T.S.R.Ch. Murthy, Ravishankar, Gopi Kishore Mandal and all other friends who have helped me in various capacities throughout my thesis at IIT Kanpur. I will never forget the nice time I spent with my colleagues in the laboratory.

I would like to thank my friends Anupam, Bijoy, Deepak, Kisun, Prasad, Prince, Soumya and Sudhish for their smiles and friendship making the life at I.I.T. Kanpur enjoyable and memorable.

I am also thankful to Harishji and Santosh for helping me in many ways during my experimental work.

I could not have reached this stage in my life without the sacrifice, constant encouragement and unfailing emotional support from my loving parents Sri. B. K. Shukla and Smt. Uma Shukla, my brother Praveen and my sister Kalpana.

Anoop Kumar Shukla  
May 2004  
IIT Kanpur, INDIA

# TABLE OF CONTENTS

CERTIFICATE	i
ACKNOWLEDGEMENTS	ii
ABSTRACT	vi
LIST OF FIGURES	viii
LIST OF TABLES	xviii
 1. INTRODUCTION	
1.1 Biomaterial	1
1.2 Historical Perspective	2
1.3 Aim of Study	4
1.4 Work Plan	5
 2. LITERATURE SURVEY	
2.1 Fundamental Aspects of Corrosion of Metallic Implants	6
2.1.1 Human Body Environment	8
2.1.2 Clinical Importance of the Process of Corrosion	11
2.1.3 Corrosion Susceptibility of Orthopaedic Implants	16
2.2 Titanium as an Implant Material	21
2.2.1 Applications of Titanium in Human Body	24
2.2.2 Corrosion behavior of Ti and its alloys under simulated physiological conditions	27
2.2.3 Repassivation of Titanium alloys	33
2.3 Passive layer on Ti based implant materials	37
2.3.1 Immersion in Hank's solution	37
2.3.2 Effect of alloying elements	39

2.3.3	Surface treatments on Titanium alloys	43
2.4	Electrochemical Corrosion Testing	49
2.4.1	Electrochemical Corrosion	49
2.4.2	Polarization	52
2.4.3	Corrosion Rates	58
	Tafel Extrapolation	61
	Potentiodynamic Polarization	65
2.5	Electrochemical Impedance Spectroscopy	68
2.5.1	Introduction	68
2.5.2	AC Circuit Theory and representation of Complex Impedance values	68
2.5.3	Data Presentation	69
2.5.4	Physical Electrochemistry and Equivalent Circuit Elements	73

### 3. EXPERIMENTAL PROCEDURE

3.1	Materials	78
3.1.1	Preparation of Pancakes	78
3.2	Sample Preparation	81
3.2.1	Sample Preparation for electrochemical Studies	81
3.2.2	Sample Preparation for material Characterization	81
3.2.3	sample Preparation for Mechanical testing	82
3.3	Electrochemical Studies	84
3.3.1	Cell Design	84
3.3.2	Solution Preparation	88
3.3.3	Tafel Extrapolation	88
3.3.4	Potentiodynamic Polarization	89
3.3.5	Electrochemical Impedance Spectroscopy	89

3.4 Material Characterization	90
3.4.1 Microstructural Characterization	90
3.4.2 Tensile Testing	91
3.4.3 Scanning Electron Microscopy	91
3.4.4 X-Ray Diffraction	92
4. RESULTS AND DISCUSSIONS	
4.1 Tafel Extrapolation	93
4.2 Effect of Immersion time in Hank's Solution	102
4.2.1 Potentiodynamic Polarization	102
4.2.2 Electrochemical Impedance Spectroscopy	117
4.3 Effect of NaOH Treatment	146
4.3.1 Surface Characterization	146
4.3.1.1 X-Ray Diffraction	146
4.3.1.2 Scanning Electron Microscopy	152
4.3.2 Potentiodynamic Polarization	166
4.3.3 Electrochemical Impedance Spectroscopy	173
4.3.3.1 Models used to fit EIS data	173
4.3.3.2 EIS data analysis	176
4.4 Mechanical Properties	189
4.5 Microstructural Characterization	200
4.5.1 Alpha and Near-Alpha Phase Titanium alloys	201
4.5.2 Alpha-Beta Titanium alloys	203
4.5.3 Beta and Near-Beta Titanium alloys	209
5. Summary	213
5.1 Conclusion	213
5.2 Suggestions for Future work	216
REFERENCES	217
APPENDIX A	
APPENDIX B	
APPENDIX C	
APPENDIX D	

# ABSTRACT

The behavior of passive films on metallic human body implant materials is of major concern because they limit the life of body implants. In this research, the electrochemical behavior, especially the passivation nature, of several Ti-based alloys was addressed. The materials used in the study were CP Titanium, Ti-6Al-4V, Ti-13Nb-13Zr, Ti-5Al-2.5Fe, Ti-6Al-4Fe, Ti-6Al-4Nb, Ti-8.4Al-15.4Nb and Ti-13.4Al-29Nb alloys (all the compositions were in wt %). The Hank's solution (pH=7.4) was used in this study for simulating body fluid conditions. All the experiments were conducted at 37°C. The electrochemical behavior of Ti alloys in Hank's solution was studied as a function of time. The corrosion rate was determined by the Tafel extrapolation method. All the Ti alloys exhibited  $i_{\text{corr}}$  (i.e. corrosion rate) in a narrow region between 0.025 and 0.090  $\mu\text{A}/\text{cm}^2$ . The corrosion rate was not drastically affected by addition of alloying elements like aluminum, niobium, iron, zirconium and vanadium to CP titanium ( $i_{\text{corr}}$  of 0.047  $\mu\text{A}/\text{cm}^2$ ). Ti-6Al-4Fe and Ti-5Al-2.5Fe alloys exhibited  $i_{\text{corr}}$  of 0.045 and 0.028  $\mu\text{A}/\text{cm}^2$ , respectively. This indicated lowering of corrosion rate with higher amount Fe as alloying element. However, this change was quite low.

Potentiodynamic polarization and electrochemical impedance spectroscopy (EIS) techniques were used to study the passivation behavior of Ti alloys as a function of immersion time in Hank's solution. Potentiodynamic polarization studies showed that corrosion current density and passive current density for all the Ti alloys decreased with immersion time in Hank's solution. It indicated that the passive film behavior improved after immersion in Hank's solution. Alloying of Fe and Nb along with Al showed greater improvement in passive film behavior. EIS studies indicated that all the Ti alloys exhibited higher passive film resistance after prolonged immersion in Hank's solution. The Ti-6Al-4Nb, Ti-8.4Al-15.4Nb and Ti-13.4Al-29Nb revealed sharp increase in passive film resistance. This was attributed to presence of Nb as the alloying element. Alloying of Fe increased passive film resistance. Moreover, Ti-6Al-4Fe alloy showed greater increase in passive film resistance as compared to Ti-5Al-2.5Fe alloy. Hence, it was concluded

that increased Fe content proved beneficial for the passive surface film on Ti alloys.

Three of the alloys, CP Titanium, Ti-6Al-4V and Ti-13Nb-13Zr, were also treated chemically in 5M NaOH solution at 60°C for 24Hrs and immersed in Hank's solution. The electrochemical and morphological behaviour of the modified surface film on these alloys was studied. Attention was focused on the corrosion current density, passive current density and polarization resistance, the ability to form protective films and also their nature. The layer formed on these alloys was characterized using SEM as well as XRD techniques. The XRD pattern obtained from the surface of NaOH-treated Ti-6Al-4V and Ti-13Nb-13Zr exhibited peaks for sodium titanate whereas such peaks were not obtained for NaOH-treated CP Titanium. SEM micrograph, of the surface of NaOH-treated alloys, obtained after NaOH treatment showed cracked layer on Ti-6Al-4V and Ti-13Nb-13Zr alloys, whereas, only a porous structure was evident on NaOH-treated CP Titanium surface. It indicated that Ti-6Al-4V and Ti-13Nb-13Zr alloys had enhanced interaction with NaOH solution compared to CP Titanium. SEM micrographs exhibited growth of apatite on the surface of all the NaOH-treated titanium alloys after immersion in Hank's solution. Potentiodynamic polarization experiments showed lower passive current density for NaOH-treated Ti-6Al-4V and Ti-13Nb-13Zr alloys compared to CP titanium, after 168 hrs of immersion in the Hank's solution. The EIS studies revealed that apatite layer resistance, which formed after immersing NaOH-treated alloys in Hank's solution, was higher for Ti-13Nb-13Zr which was indicative of higher amount of apatite on the surface of NaOH-treated Ti-13Nb-13Zr alloy.

Tensile testing experiments were performed for Ti-6Al-4Fe and Ti-6Al-4Nb alloys. The fractured surfaces of these alloys were examined using SEM. Both the alloys showed similar tensile strength (UTS) which was around 700 MPa. Ti-6Al-4Nb alloy showed higher ductility compared to Ti-6Al-4Fe, which was related to fracture characteristics. The fracture mode in Ti-6Al-4Fe was essentially brittle while, the Ti-6Al-4Nb exhibited mixed mode failure.



# List of Figures

Figure 1:	Potential-pH schematic illustrating complexity of environmental conditions that may be experienced by the implant alloy in the body [138].	10
Figure 2:	Mechanical stresses and corrosive effects to which a joint endoprosthesis is exposed in the human body; W-wear (mechanical and/or depassivation), B-bending (corrosion fatigue), T-torsion, G-general and localized attack [64].	13
Figure 3:	A schematic drawing of a hip prosthesis.	25
Figure 4:	$E_b-E_p$ values for all three Ti alloys in PBS and 1 mg/ml bovine albumin solution at different pH values, presented as the mean and the range of three measurements [98].	31
Figure 5:	$E_b-E_p$ values for all three Ti alloys in PBS, bovine albumin at different concentrations and 10% foetal calf serum, presented as the mean and the range of three measurements [98].	32
Figure 6:	Theoretical model of charged double layer showing the transfer of charge at the metal/oxide/protein interfaces before and during the corrosion process.	35
Figure 7:	Schematic view of the stoichiometric titanium(IV)oxide (exhibiting rutile structure), the non-stoichiometric titanium(IV)oxide with Ti(III) ions and the titanium(IV) oxide with Ti(III) and Nb(V) ions.	42
Figure 8:	X-ray diffraction of the alkaline titanate hydrogel obtained and Standard [193].	47
Figure 9:	Equivalent circuits used for alkaline treated Ti6Al4V immersed in the SBF solution at 36.5°C at regular intervals, and schematic representation of the apatite layer, hydrogel layer and inner layer of oxide film on	47

treated Ti6Al4V.

Figure 10:	SEM micrographs of untreated Ti6Al4V and Ti6Al4V treated with 5.0 M NaOH solution at 60°C for 24 h (a) untreated Ti6Al4V substrate (b) NaOH treated Ti6Al4V substrate.	48
Figure 11:	SEM micrographs of the surfaces of pretreated Ti6Al4V substrates immersed in the SBF solution at 36.5°C at regular intervals (a) 1 week (mixture of Ca-titanate and apatite) (b) 2 weeks (mixture of Ca-titanate and apatite) (c) 3 weeks (apatite) (d) 4 weeks (apatite)[202].	48
Figure 12:	The thermodynamic energy profile for metals and their Compounds.	50
Figure 13:	A basic wet corrosion cell [2].	51
Figure 14:	Schematic anodic polarization diagram for an active-passive metal illustrating important passivity parameters.	54
Figure 15:	Schematic illustrations outlining the theoretical aspects governing the development of experimental polarization diagrams: (a) active behavior, (b) stable and (c) unstable passive behavior.	57
Figure 16:	Polarization diagram for dissolution of Zn in acid (active corrosion case).	60
Figure 17:	Various types of polarization methods.	60
Figure 18:	Tafel plot for activation controlled corrosion rates.	63
Figure 19:	Corrosion current from activation controlled Tafel plots.	63
Figure 20:	Determining Tafel slopes from Tafel plots.	64
Figure 21:	Potentiodynamic polarization plot for active-passive metal.	67
Figure 22:	Schematic polarization diagrams illustrating the selection of alloy depending upon the nature of the environment.	67
Figure 23:	Sinusoidal Current Response in a Linear System.	70
Figure 24:	Nyquist Plot with Impedance Vector.	70
Figure 25:	Simple Equivalent Circuit with One Time Constant.	72
Figure 26:	Bode plot with one time constant.	72

Figure 27:	Basic diagram showing (a) Pancake, (b) samples taken out from the Pancake for Electrochemical study and (c) samples taken out for tensile tests.	83
Figure 28:	The basic diagram of a potentiostat connected with the working cell.	86
Figure 29:	Schematic representation of round bottom Cell.	86
Figure 30:	Electrochemical cell used for conducting long term electrochemical impedance spectroscopy (EIS) experiments.	87
Figure 31:	Schematic of constant temperature bath.	87
Figure 32:	Free corrosion potential as function of time for CP Titanium, Ti-6Al-4V and Ti-13Nb-13Zr in Hank's solution at 37°C temperature and 7.4 pH.	94
Figure 33:	Free corrosion potential as function of time for Ti-5Al-2.5Fe and Ti-6Al-4Fe alloys in Hank's solution at 37°C temperature and 7.4 pH.	94
Figure 34:	Free corrosion potential as function of time for Ti-6Al-4Nb, Ti-8.4Al-15.4Nb and Ti-13.4Al-29Nb in Hank's solution at 37°C temperature and 7.4 pH.	95
Figure 35:	Free corrosion potential as function of time for Ti-6Al-4Nb, Ti-6Al-4V and Ti-6Al-4Fe in Hank's solution at 37°C temperature and 7.4 pH.	95
Figure 36:	Tafel polarization curves for CP Titanium, Ti-6Al-4V and Ti-13Nb-13Zr in Hank's solution at 37°C temperature and 7.4 pH.	97
Figure 37:	Tafel polarization curves for Ti-5Al-2.5Fe and Ti-6Al-4Fe in Hank's solution at 37°C temperature and 7.4 pH.	97
Figure 38:	Tafel polarization curves for Ti-6Al-4Nb, Ti-8.4Al-15.4Nb and Ti-13.4Al-29Nb in Hank's solution at 37°C temperature and 7.4 pH.	98
Figure 39:	Tafel polarization curves for Ti-6Al-4Nb, Ti-6Al-4V and Ti-6Al-4Fe in Hank's solution at 37°C temperature and 7.4 pH	98

Figure 40:	Potentiodynamic polarization curves for CP Titanium, Ti-6Al-4V and Ti-13Nb-13Zr after 1 Hr of immersion in Hank's solution.	103
Figure 41:	Potentiodynamic polarization curves for Ti-5Al-2.5Fe and Ti-6Al-4Fe after 1 Hr of immersion in Hank's solution.	103
Figure 42:	Potentiodynamic polarization curves for Ti-6Al-4Nb, Ti-8.4Al-15.4Nb and Ti-13.4Al-29Nb after 1 Hr of immersion in Hank's solution.	104
Figure 43:	Potentiodynamic polarization curves for Ti-6Al-4Nb, Ti-6Al-4V and Ti-6Al-4Fe after 1 Hr of immersion in Hank's solution.	104
Figure 44:	Potentiodynamic polarization curves for CP Titanium, Ti-6Al-4V and Ti-13Nb-13Zr after 168 Hrs of immersion in Hank's solution.	105
Figure 45:	Potentiodynamic polarization curves for Ti-5Al-2.5Fe and Ti-6Al-4Fe after 168 Hrs of immersion in Hank's solution.	105
Figure 46:	Potentiodynamic polarization curves for Ti-6Al-4Nb, Ti-8.4Al-15Nb and Ti-13.4Al-29Nb after 1 Hr of immersion in Hank's solution.	106
Figure 47:	Potentiodynamic polarization curves for Ti-6Al-4Nb, Ti-6Al-4V and Ti-6Al-4Fe after 1 Hr of immersion in Hank's solution.	106
Figure 48:	Potentiodynamic polarization curves for CP Titanium at immersion time of 1 Hr and 168 Hrs in Hank's solution.	108
Figure 49:	Potentiodynamic polarization curves for Ti-6Al-4V at immersion time of 1 Hr and 168 Hrs in Hank's solution.	108
Figure 50:	Potentiodynamic polarization curves for Ti-13Nb-13Zr at immersion time of 1 Hr and 168 Hrs in Hank's solution.	109
Figure 51:	Potentiodynamic polarization curves for Ti-5Al-2.5Fe at immersion time of 1 Hr and 168 Hrs in Hank's solution.	109
Figure 52:	Potentiodynamic polarization curves for Ti-6Al-4Fe at immersion time of 1 Hr and 168 Hrs in Hank's solution.	110

Figure 53:	Potentiodynamic polarization curves for Ti-6Al-4Nb at immersion time of 1 Hr and 168 Hrs in Hank's solution.	110
Figure 54:	Potentiodynamic polarization curves for Ti-8.4Al-15.4Nb at immersion time of 1 Hr and 168 Hrs in Hank's solution.	111
Figure 55:	Potentiodynamic polarization curves for Ti-13.4Al-29Nb at immersion time of 1 Hr and 168 Hrs in Hank's solution.	111
Figure 56:	Model used to fit the EIS data obtained at different immersion times in hank's solution for all the Ti based alloys: (a) equivalent circuit, and (b) physical model	118
Figure 57:	EIS data for CP Titanium as a function of immersion time in Hank's solution: (a) Nyquist plots (b) Bode phase plots and (c) Bode magnitude plots.	119
Figure 58:	EIS data for Ti-6Al-4V as a function of immersion time in Hank's solution: (a) Nyquist plots (b) Bode phase plots and (c) Bode magnitude plots.	120
Figure 59:	EIS data for Ti-13Nb-13Zr as a function of immersion time in Hank's solution: (a) Nyquist plots (b) Bode phase plots and (c) Bode magnitude plots.	121
Figure 60:	EIS data for Ti-5Al-2.5Fe as a function of immersion time in Hank's solution: (a) Nyquist plots (b) Bode phase plots and (c) Bode magnitude plots.	122
Figure 61:	EIS data for Ti-6Al-4Fe as a function of immersion time in Hank's solution: (a) Nyquist plots (b) Bode phase plots and (c) Bode magnitude plots.	123
Figure 62:	EIS data for Ti-6Al-4Nb as a function of immersion time in Hank's solution: (a) Nyquist plots (b) Bode phase plots and (c) Bode magnitude plots.	124
Figure 63:	EIS data for Ti-8.4Al-15.4Nb as a function of immersion time in Hank's solution: (a) Nyquist plots (b) Bode phase plots and (c) Bode magnitude plots.	125
Figure 64:	EIS data for Ti-13.4Al-29Nb as a function of immersion time in Hank's solution: (a) Nyquist plots (b) Bode phase plots and (c) Bode magnitude plots.	126

Figure 65:	Polarization resistance ( $R_p$ ) as a function of immersion time in Hank's solution for CP titanium, Ti-6Al-4V and Ti-13Nb-13Zr alloys.	130
Figure 66:	Constant phase element ( $Q_p$ ) as a function of immersion time in Hank's solution for CP titanium, Ti-6Al-4V and Ti-13Nb-13Zr alloys.	130
Figure 67:	Polarization resistance ( $R_p$ ) as a function of immersion time in Hank's solution for Ti-5Al-2.5Fe and Ti-6Al-4Fe alloys.	131
Figure 68:	Constant phase element ( $Q_p$ ) as a function of immersion time in Hank's solution for Ti-5Al-2.5Fe and Ti-6Al-4Fe alloys.	131
Figure 69:	Polarization resistance ( $R_p$ ) as a function of immersion time in Hank's solution for Ti-6Al-4Nb, Ti-8.4Al-15.4Nb and Ti-13.4Al-29Nb alloys.	132
Figure 70:	Constant phase element ( $Q_p$ ) as a function of immersion time in Hank's solution for Ti-6Al-4Nb, Ti-8.4Al-15.4Nb and Ti-13.4Al-29Nb alloys.	132
Figure 71:	Polarization resistance ( $R_p$ ) as a function of immersion time in Hank's solution for Ti-6Al-4Nb, Ti-6Al-4V and Ti-6Al-4Fe alloys.	133
Figure 72:	Constant phase element ( $Q_p$ ) as a function of immersion time in Hank's solution for Ti-6Al-4Nb, Ti-6Al-4V and Ti-6Al-4Fe alloys.	133
Figure 73:	X-Ray Diffraction pattern obtained from the surface of CP Titanium: (a) untreated (b) treated with NaOH, and (c) Treated with NaOH and immersed in Hank's solution for 168 hrs.	149
Figure 74:	X-Ray Diffraction pattern obtained from the surface of Ti-6Al-4V: (a) untreated (b) treated with NaOH, and (c)	150

treated with NaOH and immersed in Hank's solution for 168 hrs.

Figure 75:	X-Ray Diffraction patterns obtained from the surface of Ti-13Nb-13Zr: (a) untreated (b) treated with NaOH, and (c) treated with NaOH and immersed in Hank's solution for 168 hrs.	151
Figure 76:	SEM micrographs of NaOH treated surface of CP Titanium.	154
Figure 77:	SEM micrographs of surface of NaOH-treated Ti-6Al-4V alloy.	156
Figure 78:	SEM micrographs of surface of NaOH-treated Ti-13Nb-13Zr alloy.	158
Figure 79:	SEM micrographs of surface of NaOH-treated CP titanium after immersion of 1week in Hank's Solution.	160
Figure 80:	SEM micrographs of the surface of NaOH-treated Ti-6Al-4V alloy after immersion of 1week in Hank's Solution.	162
Figure 81:	SEM micrographs of surface of NaOH-treated Ti-13Nb-13Zr alloy after immersion of 1week in Hank's Solution.	164
Figure 82:	Potentiodynamic curves for NaOH-treated CP Titanium, Ti-6Al-4V and Ti-13Nb-13Zr after immersion time of (a) 1 hr and (b) 168 hrs in Hank's solution.	168
Figure 83:	Potentiodynamic polarization curves of NaOH-treated CP Titanium after immersion in Hank's solution for 1 hr and 168 hrs.	169
Figure 84:	Potentiodynamic polarization curves of NaOH-treated Ti-6Al-4V alloy after immersion in Hank's solution for 1 hr and 168 hrs.	170
Figure 85:	Potentiodynamic polarization curves of NaOH-treated Ti-13Nb-13Zr alloy after immersion in Hank's solution for 1 hr and 168 hrs.	171
Figure 86:	Models used to fit the EIS data: (a) R(QR) model, (b)	175

R(QR)(CR) and (c) R(QR)(QR)(CR) model [201].

Figure 87:	EIS data for NaOH-treated CP Titanium as a function of immersion time in Hank's solution: (a) Nyquist plots (b) Bode phase plots and (c) Bode magnitude plots.	177
Figure 88:	EIS data for NaOH-treated Ti-6Al-4V as a function of immersion time in Hank's solution: (a) Nyquist plots (b) Bode phase plots and (c) Bode magnitude plots.	178
Figure 89:	EIS data for NaOH-treated Ti-13Nb-13Zr as a function of immersion time in Hank's solution: (a) Nyquist plots (b) Bode phase plots and (c) Bode magnitude plots.	179
Figure 90:	Inner passive layer resistance as a function of immersion time in Hank's solution for NaOH-treated CP Titanium, Ti-6Al-4V and Ti-13Nb-13Zr alloys.	181
Figure 91:	Constant phase element of inner passive layer as a function of immersion time in Hank's solution for NaOH-treated CP Titanium, Ti-6Al-4V and Ti-13Nb-13Zr alloys	181
Figure 92:	Hydrogel layer resistance as a function of immersion time in Hank's solution for NaOH-treated Ti-6Al-4V and Ti-13Nb-13Zr alloys.	182
Figure 93:	Constant phase element of hydrogel layer as a function of immersion time in Hank's solution for NaOH-treated Ti-6Al-4V and Ti-13Nb-13Zr alloys	182
Figure 94:	Apatite layer resistance as a function of immersion time in Hank's solution for NaOH-treated CP Titanium, Ti-6Al-4V and Ti-13Nb-13Zr alloys.	183
Figure 95:	Constant phase element of apatite layer as a function of immersion time in Hank's solution for NaOH-treated CP Titanium, Ti-6Al-4V and Ti-13Nb-13Zr alloys	183
Figure 96:	Stress vs. strain curves for Ti-6Al-4Nb alloy.	190
Figure 97:	Stress vs. strain curves for Ti-6Al-4Nb alloy.	190
Figure 98:	SEM micrographs of fracture surface of Ti-6Al-4Fe alloy.	191



Figure 99:	SEM micrographs of fracture surface of Ti-6Al-4Nb alloy.	193
Figure 100:	Optical micrograph showing microstructural variation in pancake for (a) Ti-6Al-4Fe and (b) Ti-6Al-4Nb alloys.	195
Figure 101:	Schematic showing the locations where micrographs were obtained.	196
Figure 102:	Optical micrographs of the surface of Ti-6Al-4Fe alloy.	197
Figure 103:	Optical micrographs of the surface of Ti-6Al-4Nb alloy.	198
Figure 104	Optical micrographs of the surface of CP titanium. The microstructures were obtained on the area used for electrochemical testing in simulated body fluid solution at 37°C and 7.4 pH.	202
Figure 105	Optical micrographs of the surface of Ti-6Al-4V. The microstructures were obtained on the area used for electrochemical testing in simulated body fluid solution at 37°C and 7.4 pH.	205
Figure 106:	Optical micrographs of the surface of Ti-6Al-4Nb. The microstructures were obtained on the area used for electrochemical testing in simulated body fluid solution at 37°C and 7.4 pH.	206
Figure 107:	Optical micrographs of the surface of Ti-5Al-2.5Fe. The microstructures were obtained on the area used for electrochemical testing in simulated body fluid solution at 37°C and 7.4 pH.	207
Figure 108:	Optical micrographs of the surface of Ti-6Al-4Fe. The microstructures were obtained on the area used for electrochemical testing in simulated body fluid solution at 37°C and 7.4 pH.	208
Figure 109:	Optical micrographs of the surface of Ti-8.4Al-15.4Nb. The microstructures were obtained on the area used for electrochemical testing in simulated body fluid solution at	210

37°C and 7.4 pH.

- Figure 110: Optical micrographs of the surface of Ti-13Al-28Nb. The microstructures were obtained on the area used for electrochemical testing in simulated body fluid solution at 37°C and 7.4 pH. 211
- Figure 111: Optical micrographs of the surface of Ti-13Nb-13Zr. The microstructures were obtained on the area used for electrochemical testing in simulated body fluid solution at 37°C and 7.4 pH. 212

# List of Tables

Table 1:	Breakdown potentials (mV) for 316 stainless steel, titanium and cobalt-chromium-molybdenum alloy in oxygen-free 0.17 M NaCl solution at 37 °C. using silver/silver chloride reference electrode.	14
Table 2:	Breakdown potentials (mV) for 316S12 stainless steel (cold worked), high nitrogen stainless steel (cold worked), Ti-6Al-4V and cast Co-Cr-Mo alloy in continuously aerated aqueous acidified chloride solution 0.23 M (Cl <sup>-</sup> ) pH 1.5 at 25 °C (results provided by De Puy international Ltd. Leeds).	14
Table 3:	Titanium Medical Specifications [77].	23
Table 4:	Composition of Ringer's [88-89] solution.	29
Table 5:	Composition of Hank's solution [92].	29
Table 6:	Breakdown Potentials and Corrosion rates of different materials in de-aerated Hank's solution at 37 °C. [95].	29
Table 7:	Ionic, covalent and metallic radii of titanium, niobium, vanadium and aluminum [147].	42
Table 8:	Standard reference electrode potentials [2].	52
Table 9:	Charge of different metals used to produce the pancake of desired composition.	80
Table 10:	Composition of elements used in making the pancakes.	80
Table 11:	Corrosion rates determined by Tafel extrapolation method for different biomaterials used in present study.	101
Table 12:	Values estimated from potentiodynamic polarization curves obtained at immersion time of 1 Hr and 168 Hrs in Hank's solution.	116
Table 13:	Values of fitting parameters obtained by fitting R(QR) model to the EIS data obtained as a function of immersion time in Hank's solution for CP Titanium.	137
Table 14:	Values of fitting parameters obtained by fitting R(QR) model to the EIS data obtained as a function of immersion time in Hank's	138

	solution for Ti-6Al-4V alloy.	
Table 15:	Values of fitting parameters obtained by fitting R(QR) model to the EIS data obtained as a function of immersion time in Hank's solution for Ti-13Nb-13Zr alloy.	139
Table 16:	Values of fitting parameters obtained by fitting R(QR) model to the EIS data obtained as a function of immersion time in Hank's solution for Ti-5Al-2.5Fe alloy.	140
Table 17:	Values of fitting parameters obtained by fitting R(QR) model to the EIS data obtained as a function of immersion time in Hank's solution for Ti-6Al-4Fe alloy.	141
Table 18:	Values of fitting parameters obtained by fitting R(QR) model to the EIS data obtained as a function of immersion time in Hank's solution for Ti-6Al-4Nb alloy.	142
Table 19:	Values of fitting parameters obtained by fitting R(QR) model to the EIS data obtained as a function of immersion time in Hank's solution for Ti-8.4Al-15.4Nb alloy.	143
Table 20:	Values of fitting parameters obtained by fitting R(QR) model to the EIS data obtained as a function of immersion time in Hank's solution for Ti-13.4Al-29Nb alloy.	144
Table 21:	Passive film resistance ( $R_p$ ) and constant phase element ( $Q_p$ ) values obtained by fitting R(QR) model to the EIS data for the Ti alloys used in the study as a function of immersion time in Hank's solution.	145
Table 22:	Values estimated from Potentiodynamic polarization curves obtained for NaOH-treated samples at immersion time of 1 Hr and 168 Hrs in Hank's solution.	172
Table 23:	Parameters obtained by fitting R(QR) model for immersion time of 1 hr and R(CR)(QR) model for immersion time of 24 hrs, 72 hrs and 168 hrs in Hank's solution for NaOH-treated CP Titanium.	186
Table 24:	Parameters obtained by fitting R(QR)(CR) model for immersion time of 1 hr and R(QR)(QR)(CR) model for immersion time of	187

24 hrs, 72 hrs and 168 hrs in Hank's solution for NaOH-treated Ti-6Al-4V .

Table 25:	Parameters obtained by fitting R(QR)(CR) model for immersion time of 1 hr and R(QR)(QR)(CR) model for immersion time of 24 hrs, 72 hrs and 168 hrs in Hank's solution for NaOH-treated Ti-13Nb-13Zr.	188
Table 26:	Dimensions of tensile test samples before and after fracture for Ti-6Al-4Nb and Ti-6Al-4Fe alloys.	199
Table 27:	Values of different material properties obtained from tensile test experiments for Ti-6Al-4Nb and Ti-6Al-4Fe alloys.	199

# Chapter 1

## INTRODUCTION

### 1.1 Biomaterial

The definition of biomaterials covers a broad area. In fact, any natural or synthetic material that interfaces with living tissues and/or biological fluids may be defined as a biomaterial [1]. Several common materials have shown some usefulness in some biomedical applications. However, certain physical and mechanical characteristics render some materials more desirable than the others for biomedical applications. To complicate things further, the determination of these desirable traits depends on the materials intended for use in the human body. For example, the material for a bone implant must exhibit greater compressive strength, while the material for a ligament replacement must exhibit far more flexibility and tensile strength [2]. In all cases, however, the biomaterial must be compatible with the body. In other words, the biocompatibility and in some cases, bioactivity, of the material are the key factors in determining the performance of a biomaterial.

Typically, a biocompatible material disrupts normal body function as little as possible. For a material to be deemed biocompatible, any adverse reactions, which may ensue at the blood/material interface, must be minimal, while resistance to biodegeneration must be high. This requires a biomaterial to interact as a natural material in the presence of blood and tissues [3]. A biocompatible material, should **not** exhibit following characteristics:

- Cause thrombus formation (the possible effect of biomaterials on the living environment due to a lack of blood compatibility is known as thrombogenicity).
- Destroy or sensitize the cellular blood elements.

- Alter plasma proteins (including enzymes) so as to trigger undesirable reactions.
- Cause adverse immune responses (Immunogenic).
- Cause cancer (Carcenogenic).
- Cause teratological effects.
- Deplete electrolytes.
- Be affected by sterilization.

Bioactive materials play a more aggressive role in the body. While a biocompatible material typically affects the equilibrium function of the body as little as possible, a bioactive material introduces specific interactions between the material and surrounding tissue. For example, a bioactive material can encourage, tissue integration to aid in the fixation of the implant in the body. Many total hip implant operations today rely partially on a porous coating of hydroxyapatite (HA), a normal component of bone, to help permanently stabilize the stem of the implant in the bone. The coating encourages growth from the surrounding tissue that interlocks within the pores [4].

## 1.2 Historical Perspective

Metallic devices have been used to repair and replace parts of the human body for centuries. Archaeological evidence clearly indicates that surgical procedures were performed in several ancient civilizations. The use of surgical metal implants in humans was first recorded in 1562 when a gold prosthesis was used to close a defect in a cleft plate [5].

Progress in surgery, however, was slow and mixed liberally with superstition until the latter part of the nineteenth century. Pasteur's and Lister's aseptic surgical techniques, developed around 1883, and shortly thereafter Roentgen's discovery of X-rays in 1895, added a new dimension to orthopedic surgery [6]. As the occurrence of the infection was brought under control, the relationship between material properties and success of implant

surgery became more clearly apparent. Tissue compatibility, corrosion resistance and strength were critical characteristics found to be necessary. The noble materials like gold and silver met the first two criteria but lacked strength for applications with high stress. Metals such as brass, copper and steel possessed adequate strength for many applications but exhibited poor corrosion behavior and tissue compatibility.

In the beginning of the twentieth century, surgical techniques were developed for the fixation of bone fractures with a plate and screw combination. Sherman-type bone plates were fabricated from the best available alloy at that time, vanadium steel. By 1920s the use of vanadium steel became questionable due to poor tissue compatibility. At that time however, no other alloy was available with high strength and good corrosion resistant properties. During 1930s, stainless steel containing 18% chromium and 8% nickel were first used for surgical implants. This material had far superior corrosion resistant properties than anything that had been available up to that time and immediately attracted the interest of orthopedic surgeons. Bone plates, screws and other fixation devices were fabricated and used as surgical implants. Although the material performed better than anything else available, it still showed some susceptibility to attack in the saline environment of the human body. In 1926 when Strauss patented the 18-8 molybdenum stainless steel, containing 2 to 4% molybdenum and a reduced carbon content of 0.08%, a material was created which promised improved resistance to acid and chloride containing environments. This material formed the basis for the type 316L alloy in common use today. Also, in the 1930s, a cobalt-chromium-molybdenum casting alloy previously used for dental appliances began to be used for surgical implants.

When titanium became commercially developed in the late 1940s it was very soon evaluated as a suitable surgical implant material. The metal possessed a good combination of mechanical and corrosion resistance properties and also demonstrated outstanding tissue compatibility characteristics. Although a few internal fixation devices were also used in United States in 1950s and 1960s, the most extensive clinical use of titanium



alloys was in England. Interest in the Ti-6Al-4V alloy and Extra Low Interstitial (ELI) versions of this alloy for total joint prostheses spurred in United States in late 1970s. This alloy now finds wide scale application in orthopedic surgery [7].

### 1.3 Aim of Study

The aim of present study was to understand the electrochemical behavior (especially the passivation) of different Ti-based alloys in simulated human body conditions (i.e. Hank's solution having pH 7.4 and temperature 37°C). Specific attention was focused on understanding the ability to form protective passive films and their stability with time. The thesis was planned to consist of:

- Selection of novel Ti alloys. The CP Titanium, Ti-6Al-4V, Ti-13Nb-13Zr and Ti-5Al-2.5Fe are common Ti alloys used for biomedical applications. Apart from these, Ti-6Al-4Nb and Ti-6Al-4Fe were to be study to observe the effect of replacement of alloying element V in Ti-6Al-4V by Nb and Fe. Ti-8.4Al-15.4Nb and Ti-13Al-28Nb alloys were to be studied to examine the effect of alloying element Nb.
- Study of the passivation behavior of the Ti-based alloys in Hank's solution (pH 7.4 and temperature 37°C) and understanding the influence of the alloying element on the corrosion behavior of these alloys.
- Effect of immersion time in Hank's solution on surface film behavior of Ti alloys.
- Analysis of surface film properties by EIS studies and modeling of EIS data using relevant equivalent circuits.

- Effect of surface treatment in NaOH solution on CP Titanium (alpha alloy), Ti-6Al-4V (alpha-beta alloy) and Ti-13Nb-13Zr (beta alloy).
- Understanding the development of surface film on NaOH-treated Ti alloys.
- Study the mechanical behavior of Ti-6Al-4Fe and Ti-6Al-4Nb alloys.
- Study the microstructural characteristics of different Ti alloys.

## 1.4 Work Plan

The strategy for experimental work was as per the following sequence:

1. Procurement of Ti alloys from DMRL, Hyderabad.
2. Preparation of as-received samples for electrochemical, microstructural and for X-Ray diffraction analysis.
3. Design and installation of electrochemical experimental arrangement.
4. Experimental program consisting of Tafel extrapolation, potentiodynamic polarization and electrochemical impedance spectroscopy techniques.
5. Analysis and interpretation of electrochemical and EIS data.
6. Material microstructure characterization.
7. Mechanical properties assessment of select alloys.

The current research aims at understanding the passive film behavior of some potential Ti-based alloys in simulated human body environment. Chapter 2 deals with literature survey and experimental procedures are discussed in Chapter 3. The results are presented and discussed in Chapter 4. Conclusions and suggestions for future work are listed in Chapter 5. The references and appendix are provided in the end.

## Chapter 2

### LITERATURE SURVEY

Over the recent decades, quantitative analysis of basic biomaterial properties has been utilized to better optimize biocompatibility profile for surgical implant devices [8]. In this regard, relevant correlations between results from pre-clinical and clinical investigations have provided intercomparisons of cause-effect relationships between the synthetic material properties and longer-term device function. Significant relationship exists between biomaterial/biomechanical properties and the complex aspects of force transfer/motion (fretting and wear) and that is now recognized as critical to many types of biodegradation or corrosion. While ASTM G5 is still the governing standard for corrosion testing of materials [9], it is imperative that the environment in which the tests are conducted and examples of data used to explain the analytical process be representative of the end application [10]. The focus of this chapter is to summarize the corrosion and wear behavior of Ti-based alloys.

#### 2.1 Fundamental Aspects of Corrosion of Metallic Implants

The corrosion of metals in aqueous environment of the body fluids involves the setting up of electrochemical corrosion cells. The corrosion produced by these cells is controlled by thermodynamic and kinetic factors. The thermodynamic factors determine the corrosion tendencies; the kinetic factors determine the rate. Galvanic corrosion is affected by both thermodynamic and kinetic factors and occurs when two metals with widely differing potentials are placed in contact with each other. Other forms of corrosion depend more directly on factors controlling the rate of corrosion. For most alloys used in implants the corrosion rate is mainly dependent on the protective properties of the thin passive films that exists on the surface of these alloys. The quality of protection afforded by passive films is related

to their ability to resist chemical breakdown by damaging species and, once broken down, their ability to reform rapidly (repassivate). The interplay between breakdown and repassivation is important in determining the susceptibility of metallic implants to pitting, crevice corrosion, stress corrosion, corrosion fatigue, intergranular corrosion and fretting corrosion. [11].

Corrosion, the gradual degradation of materials by electrochemical attack, is a concern particularly when a metallic implant is placed in the hostile electrolytic environment provided by the human body [12]. Even though the freely corroding implant materials used in the past have been replaced with modern corrosion resistant superalloys, deleterious corrosion processes have been observed in certain clinical settings [13].

Two characteristics determine implant corrosion. First, thermodynamic forces, which cause corrosion (oxidation and reduction) reactions. These forces correspond to the energy required or released during a reaction [13]. The electrochemical series links the normal electrode potentials of metals, usually in relation to hydrogen. Unfortunately, this series does not take into account the oxide film forming capability of these metals in any given electrolyte and it is more useful from the engineer's point of view to refer to the galvanic series in which metals are ranked in order of their relative reactivity in saline solutions [14]. Secondly, kinetic barriers to corrosion, that are related to factors that physically impede or prevent corrosion reactions from taking place [13]. Only those metals, which have the capacity to form a protective oxide layer against corrosion, can be used in orthopedic implants. In order to limit oxidation, passive films must have certain characteristics. They must be non-porous and must fully cover the metal surface; they must have an atomic structure that limits the migration of ions and electrons across the metal oxide-solution interface; and they must be able to remain on the surface of the material even with mechanical stressing or abrasion, which can be expected in association with orthopedic devices [13].

### 2.1.1 Human Body Environment

It is widely appreciated that the deterioration of metal and plastic implant materials within the body is one of the most important aspects of implant surgery. This particular application of materials places an almost unique demand on the resistance to deterioration. The reasons are basically two fold, for not only may the environmental effects alter the structure and properties of the material, which may itself affect the function of implant and hence the well being of the patient, but also the by-products of any structural change may have harmful effects on the patient [15].

Ideally a metallic implant should be completely inert in the body. However, that is rarely the case. The body environment is extremely hostile to all foreign materials and therefore, the effect of the environment on the implant and the effect of implant on its host tissue are of primary concern. The adapted potential-pH chart in Figure 1 illustrates the range and complexity of conditions that could be experienced by an implant alloy used for different applications. A surgical implant is constantly bathed in extra cellular tissue fluid. Basically water, this fluid contains electrolytes, complex compounds, oxygen and carbon dioxide. Electrolytes present in largest amounts are sodium ( $\text{Na}^+$ ) and chloride ( $\text{Cl}^-$ ) ion. Most of the fluids existing in the body (such as blood, plasma and lymph) have chloride content (and pH) somewhat similar to sea water (about 5 to 20 g/l and pH about 8) [16].

A 0.9% salt solution is considered to be isotonic with blood. Other electrolytes present include bicarbonate ions ( $\text{HCO}_3^-$ ) and small amounts of potassium, calcium, magnesium, phosphate, sulphate and organic acid ions. Included among the complex compounds and present in smaller amounts are phospholipids, cholesterol, natural fats, proteins, glucose and amino acids. Under normal conditions the extra cellular body fluid is slightly alkaline with a pH of 7.4 [17].

In 1965, Zapffe [18] found that after fracture trauma, local pH values decreased to 5.3-5.6. As healing took place, the pH increased gradually to normal (pH-7.4). Another source of low pH *in vivo* is the presence of crevices between components of fixation device. A restriction of the oxygen supply to

these locations can lead to pH values of about unity [19]. When an implant is surgically inserted into the human body, the internal environment is greatly disturbed. Haematomas are likely to collect around the implant, resulting in a lowered pH. Laing [24] observed pH values as low as 4.0 in healing wounds. The low pH usually persists until the haematomas are reabsorbed after several weeks [17]. From what has been said it is quite obvious that the environmental conditions within the human body are quite hostile and vary according to the degree of interaction with the body and the implant and the degree of trauma and infection associated with implantation procedure.

With internal fixation, the disturbance of the blood supply to the bones is often accompanied by severe pathological changes that may effect healing and variation in the equilibrium state electrochemically [20,21]. The ionic species also perform numerous functions, which include maintenance of the body pH and participation in oxidation-reduction reactions [22]. Normal imbalance occurs in the fluid compartment and different transport of ions and non-uniform changes normally accompany disease state. For example, during intensive care, after accidents or surgical operation, the fluid compartments are often disturbed. From an electrochemical viewpoint, the acceleration of corrosion can be due to differential conditions existing along the implant interface. These conditions may be responsible for the formation of electrochemical cells accompanied by active metal dissolution at favored localized spots at the implant-body fluid interface [23].

Reaction of the host tissue to the metallic implants affected by many factors including shape and size of the implant, movement between the implant and the tissue, extent of corrosion attack, general degradation of the implant, and the biological activity of the resulting by-products of corrosion or degradation.

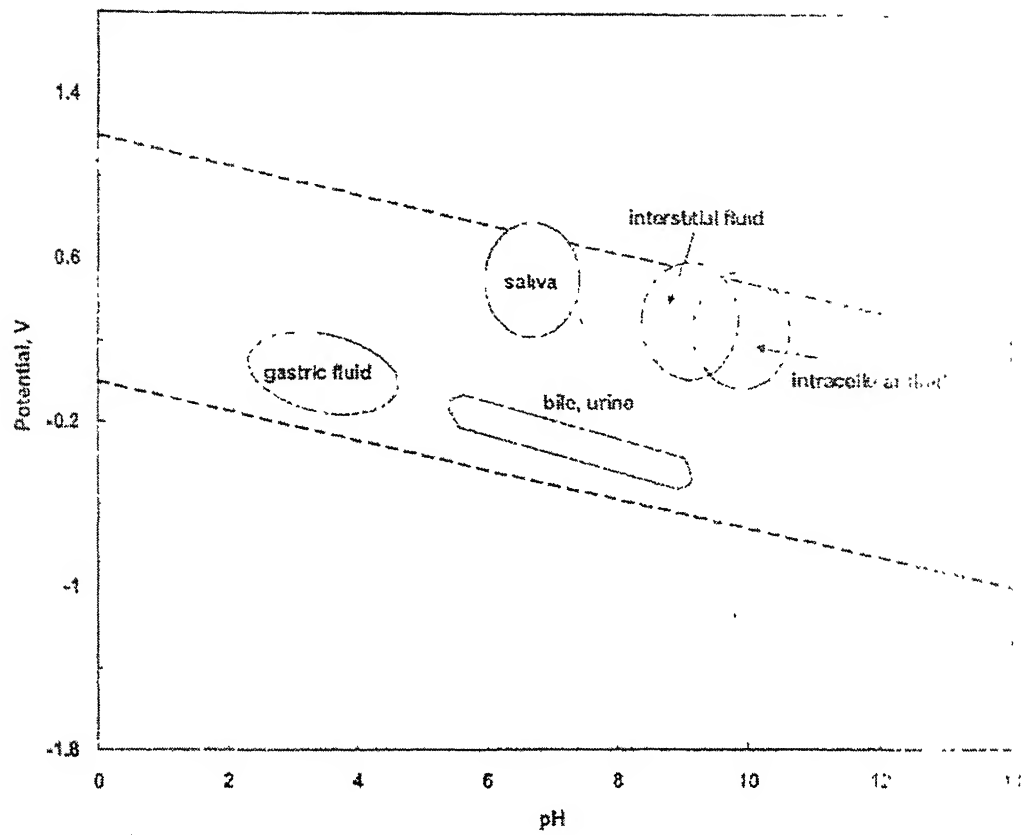


Figure 1: Potential-pH schematic illustrating complexity of environmental conditions that may be experienced by the implant alloy in the body [230].

## 2.1.2 Clinical Importance of the Process of Corrosion

Corrosion can severely limit the fatigue life and ultimate strength of the material, leading to the mechanical failure of implant. There is a low but finite prevalence of corrosion-related fracture of the implant [13]. The release of corrosion products may elicit an adverse biological reaction in the host, and several authors have reported increased concentrations of local and systemic trace metals in association with metal implants [25,26]. Although there is no specific histological evidence of the slow release of metal species that is thought to occur in association with all metal implants, accelerated corrosion and a tissue response (e.g., discoloration, foreign body response) that can be related directly to identifiable corrosion products have been demonstrated in the tissues surrounding multiple-part devices [27].

Corrosion products have been implicated in causing local pain and swelling in the region of the implant, in the absence of infection [28]. The presence of particulate corrosion and wear products in the tissue surrounding the implant may ultimately result in a cascade of events leading to periprosthetic bone loss [27], excretion of excess metal ions (especially chromium, cobalt and nickel) and their suspected role in induction of tumors e.g. malignant fibrous histiocytoma [29]. It remains to be proven whether the reports of tumors developing in the vicinity of metal implants are coincidental or otherwise. When the litany of documented toxicities (metabolic, bacteriological, immunological or carcinogenic) of these elements is considered, it should be emphasized that they generally apply to soluble forms of the elements and may not apply to the degradation products of prosthetic implants [13].

A number of studies have been carried out on the difficult task of measuring corrosion parameters *in-vivo*. These have involved measurement of corrosion potential [30-32] or corrosion rate using the polarization methods [33-36]. Only one of these studies has involved a functional loading situation. Brown and Simpson [37] measured corrosion potential versus time for a 316L stainless steel bone screw/plate combination in a sheep tibia *in-vivo*. Potential shift towards more active potentials was observed as the sheep increased the loading of the device by walking on the treadmill. Thull



*et al.* [38] have performed corrosion experiments in dogs using telemetric methods. Corrosion potential versus time measurements were made from various implant alloys. The results were interpreted in terms of a situation where implant/tissue relative movement established a fretting corrosion situation. No information on stress levels or corrosion rates were obtained in either of these studies.

*In-vitro* fretting corrosion potential experiments have been performed using weight loss [37], polarization [35] and corrosion potential measurements. Thull and Schaldach [38] have performed corrosion potential versus time measurements *in-vitro* in a joint simulator with different values of applied load. Brown and Simpson [37] have performed similar studies with screw/plate fretting. Both studies found larger shifts towards active potentials with larger loads [39]. One of the main problems of corrosion testing *in-vivo* and the interpretation of the mechanism of corrosion, which have taken place *in-vivo* after the implant has been removed from the patient, is well illustrated in Figure 2 used by Semlitsch and Willet [40] to illustrate the types of corrosion, which are associated with a total hip joint replacement. This figure shows that many corrosion mechanisms could be taking place simultaneously in a system of this nature. To understand each of the corrosion mechanisms that could take place *in-vivo* and because of the difficulties of conducting *in-vivo* experiments most of the experimental work has been carried out *in-vitro* under somewhat simplified experimental conditions.

Anodic polarization curves for the basic materials used for implants (e.g. stainless steel type 316 S12, Ti-6Al-4V and Co-28Cr-6Mo casting alloy) have been obtained under varying conditions of surface finish, environment, chloride ion concentration, pH, aerated and deaerated in the literature [41-43]. Typical results are shown in Tables 1 and 2.

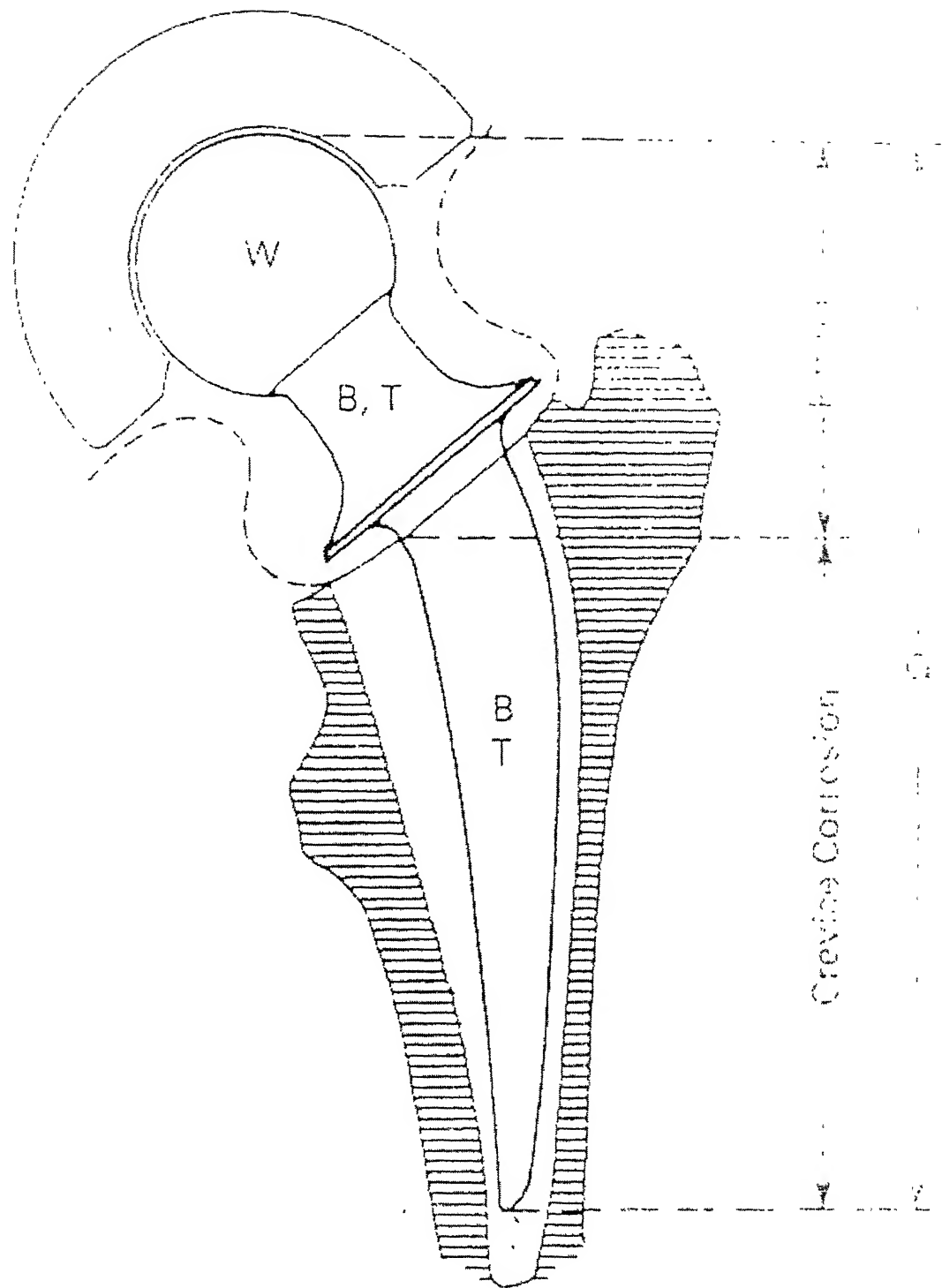


Figure 2: Mechanical stresses and corrosive effects to which a joint endoprosthesis is exposed in the human body; W-wear (mechanical and/or depassivation), B-bending (corrosion fatigue), T-torsion, G-general and localized attack [64].

Table 1: Breakdown potentials (mV) for 316 stainless steel, titanium and cobalt-chromium-molybdenum alloy in oxygen-free 0.17 M NaCl solution at 37 °C. using silver/silver chloride reference electrode.

Material	E <sub>b</sub> (mV vs. Ag-AgCl)	
	Hank's solution [92]	Ringer's Solution [43]
316 Stainless steel	400-800	160-650
Titanium	9000	800
Co-Cr-Mo	870	790

Table 2: Breakdown potentials (mV) for 316S12 stainless steel (cold worked), high nitrogen stainless steel (cold worked), Ti-6Al-4V and cast Co-Cr-Mo alloy in continuously aerated aqueous acidified chloride solution 0.23 M (Cl<sup>-</sup>) pH 1.5 at 25 °C (results provided by De Puy international Ltd. Leeds).

Material	British standard	Condition	Breakdown potential (mV vs SCE)	Free Corrosion potential (mV vs SCE)
316 S12 Stainless steel	BS7252/1 Comp. D	Cold worked	180	-100
High nitrogen stainless steel	BS7252/9	Cold worked	850	300
Ti-6Al-4V	BS7252/3	Annealed	1700	150
Co-Cr-Mo	BS7252/4	Cast	850	155

These results show that the basic material used for implantation exhibit good corrosion resistant properties in simulated body fluid environments (Hank's physiological solution) and in much more aggressive solutions such as 0.23 M ( $\text{Cl}^-$ ) acidified to pH 1.5, which simulate deep crevice and infection conditions. The material's free corrosion potential is well below their respective breakdown potentials and are therefore stable under these conditions. These results only provide an indication of how materials behave under non-stressed, non-crevice and non-fretting conditions [44].

Ogundele and White [44] carried out a series of polarization studies on surgical grade stainless steel in Hank's physiological solution. Under varying conditions of temperature, ( $\text{Cl}^-$ ), ( $\text{HCO}_3^-$ ) and pH. Their results are summarized as follows:

1. Increasing concentrations of chloride ions adversely affected corrosion resistance in lowering passivation breakdown potentials, marginally lowering corrosion potentials, lowering passivation potentials and generally increasing the propensity to pitting attack as evidenced by the increase in size of hysteresis loops from potentiodynamic cycling tests.
2. Increasing concentration of bicarbonate tended to raise the break down potentials but also increased the corrosion potentials. This, in combination with high chloride concentration, high bicarbonate concentrations may raise the corrosion potentials such that they border on passivation breakdown. The increase in hysteresis loop size on potentiodynamic cycles with increasing bicarbonate concentration shows a lowered resistance to pitting attack and crevice corrosion.
3. Variations in pH promoted increases in corrosion potentials from acid pH levels to neutral pH; thereafter, however, corrosion potentials were lowered in alkaline solutions to more active values. Decreasing pH caused a lowering of

breakdown potentials in the presence of  $\text{Cl}^-$  and an increase in the current densities for passivation.

4. Increasing temperature tended to raise corrosion potentials, lower breakdown potentials, thereby generally lowering corrosion resistance. Ogundele and White [44] re-emphasized that 316L type stainless steels are generally corrosion resistant in biological fluids and are suited to application in orthopedic implants. They support their argument by the fact that there is a low incidence of implant failures (<5% from corrosion and corrosion related mechanisms or both) [45].

### 2.1.3 Corrosion Susceptibility of Orthopaedic Implants

Typical implant materials commercially in use are 316L stainless steel (for femoral stem and as a temporary implant device), Ti-6Al-4V (for femoral stem) and Co-28Cr-6Mo (for femoral head). Different types of corrosion attack to which these implant materials are susceptible is (seen in Figure 2) is elaborated below:

#### a) Uniform Attack

This refers to the inevitable corrosion to which all metals immersed in electrolytic solutions are condemned [46]. Titanium-base alloys have lower overall corrosion rates compared to stainless steel and cobalt chromium alloys. However, serum proteins can complex with chromium and nickel, increasing uniform attack by 2-to 10-fold [46].

#### b) Galvanic Corrosion

It is defined as dissolution of metals driven by macroscopic differences in electrochemical potentials, usually as a result of dissimilar metals in proximity [13]. It is caused by inappropriate use of metals, e.g., a stainless steel cerclage wire in contact with a cobalt or titanium-alloy femoral stem, a

cobalt-alloy femoral head in contact with a titanium-alloy femoral stem, and a titanium– alloy screw in contact with a stainless-steel plate [47].

Due to cold-welding between instrument and implants using radioactive tracer techniques, Bowden and coworkers (1955) have shown that significant amounts of metal were transferred from screwdrivers to screw heads and from drill bits to plates. Work hardening and surface-finishing processes that produce plastic deformation generally make the deformed metal basic with respect to undeformed material of the same composition [46]. Compositional differences, either between parts because of manufacture from different master ingots within the same specification limits or because of deliberate mixing of metals, is the most likely cause of such effects [46].

### c) Pitting and Crevice Corrosion

Pitting is a form of localized, symmetric corrosion in which pits form on the metal surface [46]. Stainless steel is particularly predisposed to pitting corrosion due to inclusions of a dissimilar material trapped in the metal during a manufacturing process. These impurities may initiate pitting corrosion in relation to a grain boundary and thus can lead to component failure [28]. It can also be initiated by scratches or handling damage [46]. Pitting was frequently observed in older stainless steel fracture fixation hardware, e.g., on the underside of screw heads [46]. It also occurs infrequently on the neck or the underside of the flange of proximal femoral endoprostheses [46].

The literature contains a number of studies on the susceptibility of the cobalt-based alloys to pitting corrosion. In-vitro studies conducted by Muller and Greener [43], involving static conditions, revealed no evidence of pitting having occurred. Syrett and Wing [48], utilizing cyclic polarization analyses, observed that neither as-cast nor annealed Co-Cr-Mo alloy demonstrated hysteresis loops in their cyclic polarization curves. They concluded that this substantiated the fact that neither should be susceptible to pitting or crevice corrosion. Other investigators [49-55], studying the susceptibility of the cobalt alloy to pitting corrosion under in-vitro static conditions has shown the

alloy not to be susceptible. However, when the alloy is either severely cold worked or subjected to fretting or cyclic loading [56-57] conditions, pitting corrosion has been observed *in-vitro* [58].

The addition of a minimum of 2% of molybdenum content in type 316 stainless steel has been shown to reduce the tendency for pitting-type corrosion in chloride environments. Hoar and Mears [30] postulated that chloride ions accelerate the corrosion of stainless steel by penetrating the oxide film. The chloride-contaminated film then loses its passivating quality and a local attack on the metal follows, creating a pit. The exact mechanism by which molybdenum strengthens the oxide film is not clearly understood [17].

Crevice is a form of local corrosion due to differences in oxygen tension or concentration of electrolytes or changes in pH in a confined space, such as in the crevices between a screw and a plate [59]. The narrower and deeper the crack is, the more likely crevice corrosion is to start [46]. Recent retrieval studies have shown that 16 to 35% of modular total hip implants demonstrated moderate to severe corrosion in the conical head-neck taper connections [60]. Studies of retrieved stainless steel multipart internal fixation devices show visible corrosion at the junction between screw head and the plate in 50-75% of all devices [46]. Other typical crevices are scratches on the surface of an implant, the interface between bone and an implant, the cement-metal interface, and any other sharp interface likely to be depleted of oxygen relative to another oxygenated area [61].

#### d) Stress Corrosion Cracking

It is a phenomenon in which a metal in a certain environment, especially those rich in chlorides, is subjected to stress and fails at a much lower level than usual as a result of corrosion [62]. Pitting and stress corrosion cracking, although usually associated with stainless steel in chloride media, have not been observed on recovered surgical implants. Implants often exhibit cracks and surface pitting, but these are most likely the result of improper manufacture rather than corrosion [63-64].

Sheehan *et al.* [65] studied stress corrosion cracking (SCC) of type 316L stainless steel *in-vitro*. Tests were conducted using specimens with electropolished surface in slow strain rate tension tests and Schneider intramedullary nails in static bend tests. They concluded, as previous investigators had done, that SCC is not a mode of failure of 316L stainless steel implants *in-vitro* and found no indication that SCC of this material would occur *in-vivo*. Bundy and Desai [66] studied SCC of type 316L stainless steel and ELI (extra low interstitial) Ti-6Al-4V using fracture mechanics and measuring crack propagation velocity versus stress intensity in environments of  $MgCl_2$ , HCl and Ringer's solution. Crack propagation occurred in precracked type 316L stainless steel in Ringer's solution held at a potential that disrupted the passive film. The conclusion from this investigation was that SCC of type 316L could occur *in-vivo* if these conditions existed. A straight fracture plate, when flexed, will experience a tensile stress on its convex surface and a compressive stress on its concave surface. This produces a difference in electrochemical potential, which renders, the convex surface anodic with respect to the rest of the plate. Corrosion, as an acceleration of uniform attack, or perhaps secondary tensile rupture of the passive film, will then attack the convex surface preferentially [46]. The same process will occur at stress risers in loaded devices, such as screw holes in fracture fixation plates or kinks in cerclage wire. In this case, the regions of higher stress, in the immediate vicinity of the stress risers, will corrode at the expense of the surrounding less stressed material [46].

#### e) Corrosion Fatigue

The corrosion fatigue failure of total joint prostheses has been widely studied. It can be concluded from an extensive literature survey carried out by Leclerc [67] that provided the alloy used in the manufacture of the joint prosthesis conforms to the current national and international standards and that it is in the correct metallurgical condition the contribution of corrosion in the corrosion fatigue failures of joint prostheses is marginal. The corrosion contribution increases with the time that the prosthesis is present in the patient. It has also been shown by various testing laboratories that the



*in-vivo* failures can be simulated using *in-vitro* simulators without the presence of a corrosive medium and provided that a torsional component of load is applied to the prosthesis. Bechtol [68] in reviewing his clinical experience with 1087 cemented Charnley and Bechtol total hip replacements conclude that prosthetic stem failure is actually the final sequence of previous failures of bony and cement support. His suggested sequence of prosthetic stem failure has been substantiated in the literature and are as follows:

1. Poor blood supply in the area of the medial femoral neck (as the consequence of a pre-existing pathological condition or excessive early weight bearing) leads to initial loosening of the cement bond;
2. Resorption of the bone in the medial neck places the forces of continued weight bearing on the bone cement in that area and may lead to medial and/ or distal migration of the femoral cement and prosthetic component;
3. Fracture of cement transversely near the distal end of the prosthetic stem or in the area of the medial neck results in slight downward or medial shift of stem position and further increase the forces upon the stem;
4. Repeated fixing of the proximal stem in a fatigue mode over a period of months or years results in a widening of the separation between the metal and cement laterally and ultimately in an actual deformity or fracture of the metal stem.

Hughes et al. [19] reported some corrosion fatigue tests that carried out on an Amsler Vibrophone with specimens immersed in saline environments with a pH range 2 to 7.4. They found that titanium showed slight decrease in fatigue properties over the pH range whereas stainless steel showed a drastic decline in fatigue strength at pH 4 and below this level

became inferior to the titanium. Rollins et al. [70] tested steels in chloride solutions of varying pH and found that corrosion in the range pH 4-10 was independent of pH since the process was controlled by oxygen diffusion to cathodic areas, i.e. it depended on the solubility of oxygen in the solution. Below pH 4 there was an increase in corrosion rate associated with cathodic hydrogen evolution. Although there was insufficient data to analyze fully the effects of changes of pH, it is clear that the increased corrosion rate reported below pH 4 was making a contribution to the reduction of the fatigue strength of the stainless steel. Piehler et al. [71] reported on corrosion fatigue of hip nails and emphasized the importance of materials selection and design. Large plate designs had superior corrosion-fatigue performance over small plates.

## 2.2 Titanium as an Implant Material

The high strength, low weight, outstanding corrosion resistance possessed by titanium and titanium alloys have led to a wide and diversified range of successful applications which demand high levels of reliable performance in surgery and medicine as well as in aerospace, automotive, chemical plant, power generation, oil and gas extraction, sports, and other major industries [72]. More than 1000 tonnes (2.2 million pounds) of titanium devices of every description and function are implanted in patients worldwide every year. Requirements for joint replacement continue to grow as people live longer or damage themselves more in by hard sports play or jogging, or are seriously injured in road traffic and other accidents. Light, strong and totally biocompatible, titanium is one of few materials that naturally match the requirements for implantation in the human body [24].

Medical grade titanium alloys have a significantly higher strength to weight ratio than competing stainless steels. The range of available titanium alloys enables medical specialist's designers to select materials and forms closely tailored to the needs of the application. The full range of alloys reaches from high ductility commercially pure titanium used where extreme formability is essential, to fully heat treatable alloys with strength above 1300 MPa, (190ksi) [73]. Shape-memory alloys based on titanium further

extend the range of useful properties and applications. A combination of forging or casting, machining and fabrication are the process routes used for medical products. Surface engineering frequently plays a significant role, extending the performance of titanium several times beyond its natural capability.

'Fit and forget', is an essential requirement where equipment in critical applications, once installed, cannot readily be maintained or replaced. There is no more challenging use in this respect than implants in the human body. The effectiveness and reliability of implants, and medical and surgical instruments and devices is an essential factor in saving lives and in the long-term relief of suffering and pain. Implantation represents a potential assault on the chemical, physiological and mechanical structure of the human body. There is nothing comparable to a metallic implant in living tissue. Most metals in body fluids and tissue are found in stable organic complexes. Corrosion of implanted metal by body fluids, results in the release of unwanted metallic ions, with likely interference in the processes of life. Corrosion resistance is not sufficient of itself to suppress the body's reaction to cell toxic metals or allergenic elements such as nickel, and even in very small concentrations from a minimum level of corrosion, these may initiate rejection reactions. Titanium is judged to be completely inert and immune to corrosion by all body fluids and tissue, and is thus wholly biocompatible [36].

The natural selection of titanium for implantation is determined by a combination of most favorable characteristics including immunity to corrosion, biocompatibility, strength, low modulus and density and the capacity for joining with bone and other tissue (osseointegration) [74]. The mechanical and physical properties of titanium alloys combine to provide implants, which are highly damage tolerant. The human anatomy naturally limits the shape and allowable volume of implants. The lower modulus of titanium alloys compared to steel is a positive factor in reducing bone resorption [75]. Two further parameters define the usefulness of the implantable alloy, the notch sensitivity, the ratio of tensile strength in the notched vs. un-notched condition, and the resistance to crack propagation, or fracture toughness. Titanium scores well in both cases. Typical NS/TS

ratios for titanium and its alloys are 1.4 - 1.7 (1.1 is a minimum for an acceptable implant material). Fracture toughness of all high strength implantable alloys is above 50 MPa m<sup>-1/2</sup> with critical crack lengths well above the minimum for detection by standard methods of non-destructive testing [76].

Forms and material specifications are detailed in a number of international and domestic specifications, including ASTM and BS7252/ ISO 5832 examples, which are listed below:

Table 3: Titanium Medical Specifications [77].

ASTM	BS/ISO	Alloy designation	
F67	Part 2	Unalloyed titanium - CP Grades 1- 4	(ASTM F1341 specifies wire)
F136	Part 3	Ti-6Al-4V ELI wrought	(ASTM F620 specifies ELI forgings)
F1472	Part 3	Ti-6Al-4V standard grade (SG) wrought	(F1108 specifies SG castings)
F1295	Part 11	Ti-6Al-7Nb wrought	
-	Part 10	Ti-5Al-2.5Fe wrought	
F1580	-	CP and Ti6Al-4V SG powders for coating implants	
F1713	-	Ti-13Nb-13Zr Wrought	
F1813	-	Ti-12Mo-6Zr-2Fe Wrought	

### 2.2.1 Applications of Titanium in Human Body [78]

Some specific bio-medical applications of Titanium and its alloys are listed below.

- **Bone and Joint Replacement:** About one million patients worldwide are treated annually for total replacement of arthritic hips and knee joints. The prostheses come in many shapes and sizes. Hip joints normally have a metallic femoral stem and head which locates into an ultrahigh molecular weight low friction polyethylene socket, both secured in position with polymethyl methacrylate bone cement (Figure 3) Some designs, including cementless joints, use roughened bioactive surfaces (including hydroxyapatite) to stimulate osseointegration, limit resorption and thus increase the implant lifetime for younger recipients. Internal and external bone-fracture fixation provides a further major application for titanium as spinal fusion devices, pins, bone-plates, screws, intramedullary nails, and external fixators.
- **Dental Implants:** A major change in restorative dental practice worldwide has been possible through the use of titanium implants. Titanium 'root' is introduced into the jawbone with time subsequently allowed for osseointegration. The superstructure of the tooth is then built onto the implant to give an effective replacement.
- **Maxillo and Cranio/facial treatments:** Surgery to repair facial damage using the patients own tissue cannot always obtain the desired results. Artificial parts may be required to restore the ability to speak or eat as well as for cosmetic appearance, to replace facial features lost through damage or disease. Osseointegrated titanium implants meeting all the requirements of biocompatibility and strength have made possible unprecedented advances in surgery, for the successful treatment of patients with large defects and hitherto highly problematic conditions.

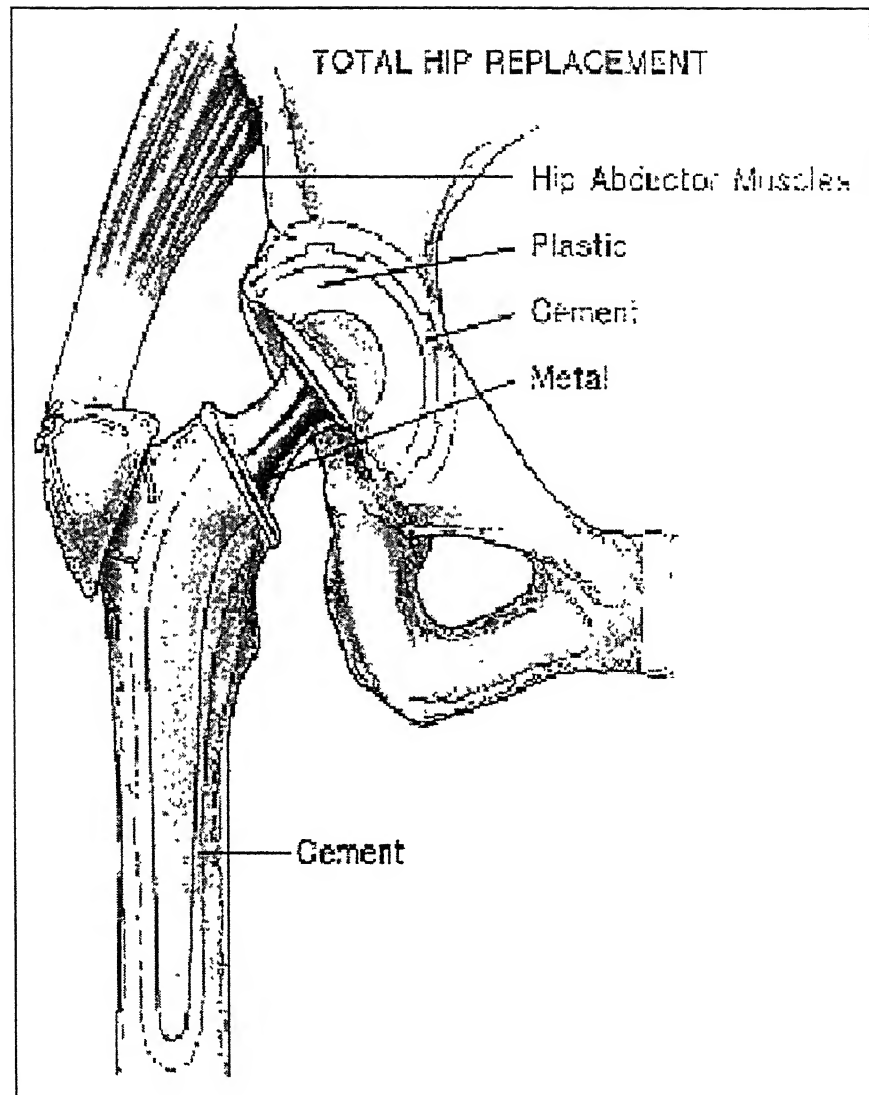


Figure 3: A schematic drawing of a hip prosthesis.

- **Cardiovascular devices:** Titanium is regularly used for pacemaker cases and defibrillators, as the carrier structure for replacement heart valves, and for intra-vascular stents.

- **External Prostheses:** Titanium is suitable for both temporary and long term external fixations and devices as well as for orthotic calipers and artificial limbs, both of which use titanium extensively for its light weight, toughness and corrosion resistance.
- **Surgical Instruments:** Wide ranges of surgical instruments are made in titanium. The metal's lightness is a positive aid to reducing any fatigue of the surgeon. Instruments are frequently anodized to provide a non-reflecting surface, essential in microsurgical operations, for example in eye surgery. Titanium instruments withstand repeat sterilization without compromise to edge or surface quality, corrosion resistance or strength. Titanium is non magnetic, and there is therefore no threat of damage to small and sensitive implanted electronic devices.

Titanium also tends to seize when in sliding contact with itself or other metal. Titanium-based alloys having high co-efficient of friction can cause problems. Wear particles are formed in a piece of bone if a piece of bone rubs against the implant, or if two parts of an implant rub against one another. Therefore, implants of self-mated titanium generally are not used as joint surfaces. Titanium derives its corrosion resistance due to the formation of a surface oxide film. Under *in vivo* conditions, the oxide is the only stable reaction product [79].

Most common alloy used for implants is Ti-6Al-4V. It contains titanium, aluminum, and vanadium. Aluminum increases transformation temperature between alpha and beta phases. Vanadium decreases the transformation temperature between the alpha and beta phases. Alpha alloys have, good weldability, high strength, oxidation resistance at high temperatures [80]. Beta alloys are stronger than alpha phased alloy. Alpha-beta alloys formed by heat-treating beta solutions are stronger than annealed alpha-beta alloys. Although this alloy has an excellent corrosion resistance and biocompatibility, considerable controversy has developed over the biocompatibility of the alloy [81].

There are two main points to consider in this controversy.

- a. Firstly although titanium has an excellent corrosion resistance, if titanium is released into the tissue even by the way of passive dissolution or perhaps another process involving wear, the tissue reaction may vary. This reaction could be anything ranging from a mild response (e.g. a discoloration of the surrounding tissue) to a more severe one (e.g. inflammatory reaction causing pain and even leading to loosening owing to osteolysis) [82].
- b. Secondly, if deposits of titanium alloy particles are present in the tissue, then concentrations of aluminium and vanadium (which themselves have different biological properties than titanium) will also be present. It has thus been proposed that better performance in terms of corrosion resistance and biocompatibility would be achieved through the use of alloys of different composition. However, even though several such alloys have been investigated there is still very little data to support this view [83].

### 2.2.2 Corrosion behavior of Ti and its alloys under simulated Physiological conditions

Corrosion of metal implants is critical because it can adversely affect biocompatibility and mechanical integrity. The material used must not cause any adverse biological reaction in the body, and it must be stable and retain its functional properties. Corrosion and surface film dissolution are two mechanisms for introducing additional ions in the body. Extensive release of metal ions from prosthesis can result in adverse biological reactions and can lead to mechanical failure of the device. The passive films formed on titanium and its alloys consist mainly of amorphous titanium dioxide [84-86]. The physico-chemical and electrochemical properties of the oxide film and its long-term stability in biological environments play a decisive role for the biocompatibility of titanium implants [87]. Electrochemical impedance spectroscopy study regarding the influence of alloying elements and the potential on the corrosion resistance of Ti and other Ti-based biomedical implant alloys under simulated physiological conditions (Ringer's solution



Table 4) has proved to be very successful [89]. Deaerated Hank's Solution also simulates human body environment at pH of 7.4 (Table 5). Table 6 illustrates the corrosion rate and break down potentials of different materials as compared to Ti-6Al-4V in de-aerated Hank's Solution at 37 °C. and 7.4 pH. The other material being considered is Ti-13Nb-13Zr, which once again relies on niobium as a beta phase stabilizer. The other alloying element, zirconium, is one that is unique in that it is isomorphous with both the alpha and beta phases of titanium [90]. A combination of these two alloying elements has made it possible to develop a structure that is a 'near' beta phase supposedly possessing a superior corrosion resistance over the alpha-beta phase alloys mentioned earlier, but one that still has enough alpha phase present in the final structure to provide the necessary mechanical strength. It has been proposed that Ti-13Nb-13Zr alloy is more favorable for orthopaedic implants than Ti-6Al-4V alloy because of its superior corrosion resistance and biocompatibility [91]. Reasons for this superiority have included the fact that less metal ion release is likely to occur during spontaneous passivation of Ti-13Nb-13Zr alloy because the corrosion products of the minor alloying elements, niobium and zirconium, are less soluble than those of aluminium and vanadium. Also, that the passive oxide layer on the surface of the alloy is more inert consisting of a dense rutile structure providing greater protection to the underlying alloy [93].

It is well known that proteins affect the corrosion behavior of some metals, and that their presence can either inhibit or accelerate the corrosion phenomena. They are known to behave differently with different metals, since their role in a corrosive environment is governed by many factors such as the surface chemistry of the metal, protein adsorption characteristics, interaction of protein molecules with other ions present in the electrolyte solution to produce organic complexes, and the transport of anionic and cationic charges around and away from the local environment [94].

Table 4: Composition of Ringer's [88-89] solution.

Compound	Composition g/lit.
NaCl	6.80
KCl	0.40
CaCl <sub>2</sub>	0.20
MgSO <sub>4</sub> .7H <sub>2</sub> O	0.20
NaH <sub>2</sub> PO <sub>4</sub> .H <sub>2</sub> O	0.14
NaHCO <sub>3</sub>	2.20
Glucose	1.00

Table 5: Composition of Hank's solution [92].

Compound	Composition g/lit.
NaCl	8.0
KCl	0.40
CaCl <sub>2</sub>	0.14
MgSO <sub>4</sub> .7H <sub>2</sub> O	0.06
NaH <sub>2</sub> PO <sub>4</sub> .2H <sub>2</sub> O	0.06
NaHCO <sub>3</sub>	0.35
Glucose	1.00
KH <sub>2</sub> PO <sub>4</sub>	0.60
MgCl <sub>2</sub> .6H <sub>2</sub> O	0.10

Table 6: Breakdown Potentials and Corrosion rates of different materials in de-aerated Hank's solution at 37 °C. [95].

Material	Breakdown Potential (mV vs SCE)	Corrosion rate (mils/year)
316L stainless steel	280	0.17
Cobalt alloy	600	0.056
Ti-6Al-4V	1900	0.007

The corrosion resistance of the alloys was studied using cyclic anodic polarization techniques to break down the passive layer and then allow repassivation to occur. The value of the breakdown potential for Ti alloys is difficult to assess owing to the instability of the aqueous electrolytes at the high potentials required. The ability of the surfaces to repassivate in the environment, as measured by the hysteresis in the cyclic polarization curve, is a better measure of the corrosion behavior of these materials. For these reasons the corrosion resistance of these alloys was estimated by recording the difference between the breakdown potential ( $E_b$ ) and the repassivation potential ( $E_p$ ) [96]. This study showed that in different environments (i.e. at different pHs or in the presence of proteins) the ability of the alloys to repassivate is affected. Hardness measurements were done to evaluate the surface oxide formed during repassivation and to determine that it is different from the original surface oxide [97]. Figures 4 and 5 present the corrosion resistance data for the three alloys in different environments. From Figure 4 the corrosion resistance of the alloys (i.e.  $E_b - E_p$  values) at three different pH levels (i.e. 5, 7.4 and 9) can be evaluated. Generally, it was noticed that as the pH level increased in Phosphate buffered saline solution, the corrosion resistance of Ti-6Al-4V and Ti-6Al-7Nb decreased, whereas that of Ti-13Nb-13Zr was seen to increase but only slightly [98].

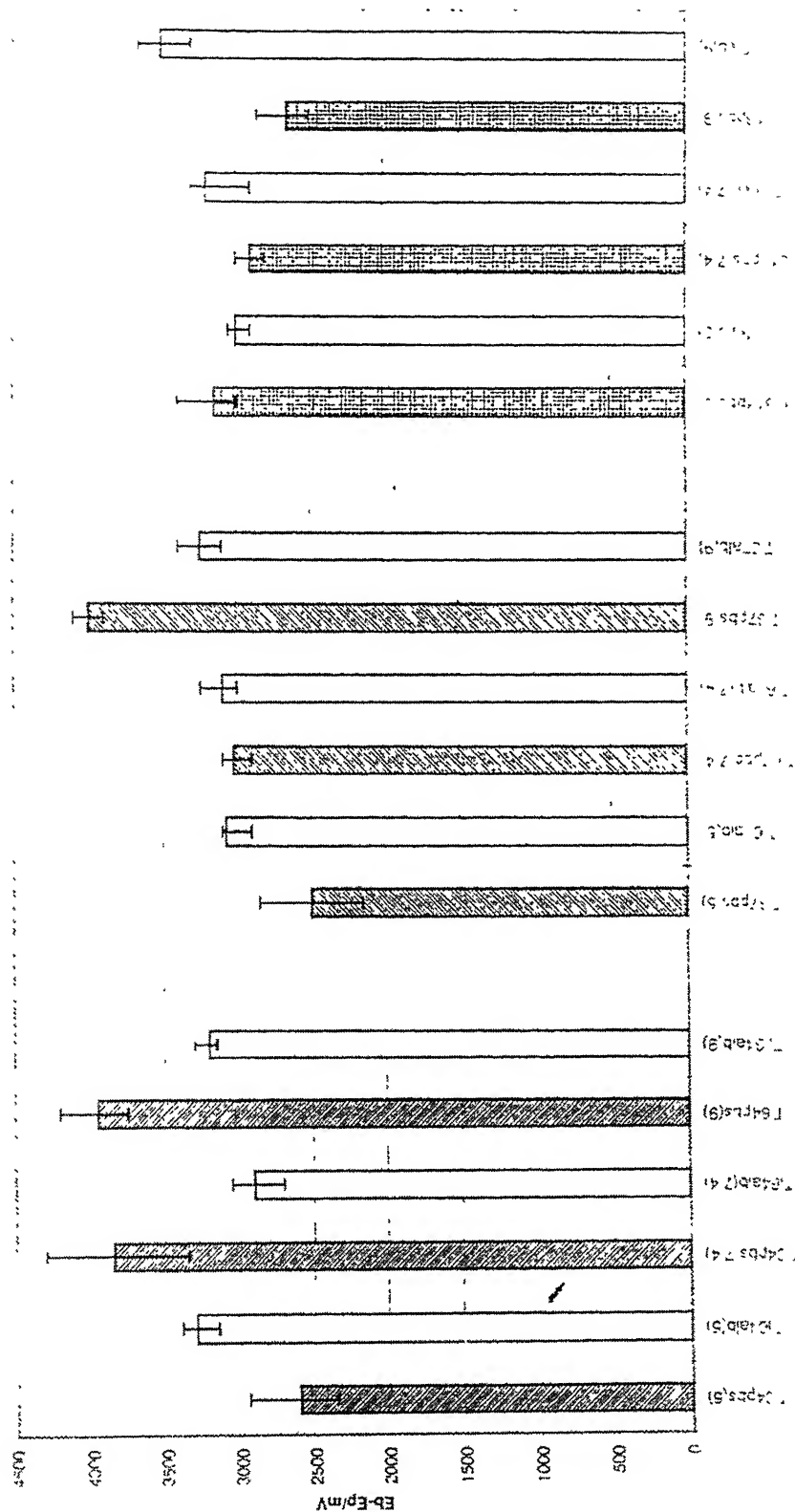


Figure 4:  $E_b-E_p$  values for all three Ti alloys in PBS and 1 mg/ml bovine albumin solution at different pH values, presented as the mean and the range of three measurements. Ti64=Ti-6Al-4V, Ti67=Ti-6Al-7Nb, Ti1313=Ti-13Nb-13Zr, PBS=phosphate-buffered saline, Alb=bovine albumin, the value in parenthesis is the pH of the electrolyte [98].



When albumin, at a concentration of 1 mg/ml, was added, the effect of pH on the corrosion resistance of Ti-6Al-4V and Ti-6Al-7Nb was reduced whereas for Ti-13Nb-13Zr the addition of albumin caused a decrease in corrosion resistance as the pH increased, although again the changes were small. From Figure 5 the corrosion resistance of the alloys, in environments containing progressively increasing concentrations of albumin, can be evaluated. It was observed that by adding albumin (0.1 mg/ml) to PBS, the corrosion resistance increased for Ti-6Al-4V. For Ti-6Al-7Nb and Ti-13Nb-13Zr the changes in corrosion resistance were smaller showing a slight increase for Ti-6Al-7Nb and a slight decrease for Ti-13Nb-13Zr.

As the concentration of albumin increased the corrosion resistance of Ti-13Nb-13Zr appeared to remain at the same level, whereas, that for the other two alloys tended to decrease. The Ti-6Al-4V alloy was more corrosion resistant in all the albumin solutions than in PBS, whereas the Ti-6Al-7Nb and Ti-13Nb-13Zr alloys were generally less corrosion resistant in protein solutions than in PBS. The addition of foetal calf serum produced a similar effect with each alloy, as had the presence of higher concentrations of albumin.

### 2.2.3 Repassivation of Titanium alloys

Titanium alloys are used in orthopaedic applications and there is concern about the release and subsequent build up of material in the tissues. It is unlikely that the passive layers on these alloys will be broken down electrochemically in the physiological environment. It is known, however, that the integrity of the passive layer can be influenced by wear [99]. It is important therefore to investigate the repassivation processes of these alloys in a biological environment. In this study electrochemical techniques were used to break down the passive layer so that one could investigate the repassivation and the interaction of proteins with this process. To understand comprehensively how corrosion takes place in terms of charge transfer at the metal/electrolyte interface, it is necessary to consider an accepted model for the charge distribution in terms of a charge double layer structure (Figure 6). In this case, a double-layer is present due to hydroxylated ions at the metal

surface and charge transfer can occur within the layer depending on whether the metal oxide is stable (i.e. acting as a cathode) or whether it is passivating up to and beyond removal of its protective oxide layer (i.e. as an anode).

When the passive layer is broken the titanium alloy is able to release ions into solution until the passive layer is rebuilt. The action of rebuilding this layer results from the chemical interaction of anions in the environment reacting with the surface [100]. It is hypothesized that any anions in the environment may have a bearing on the final composition of the repassivated layer and its ability to form. Cyclic polarization studies were used to assess the ability of the surface to repassivate and hardness measurements to investigate the properties of the repassivated surface [101].

Examination of the surface under a microscope following cyclic polarization indicated an evidence of pit formation. This evidence and the presence of hysteresis during cyclic polarization suggests that the passive layer is being broken down and repassivated under these experimental conditions. The difference between the breakdown potential and the repassivation potential is related to the reactions that are taking place at the surface of the material as repassivation occurs. This study [98] revealed that proteins in the environment might be interacting with the repassivating process and thus influencing the properties of the passive layer. When the pH of the environment changes the proteins will have a different charge owing to their zwitterion character and therefore it is reasonable to suspect that they may interact with the repassivation process in a different way [98].

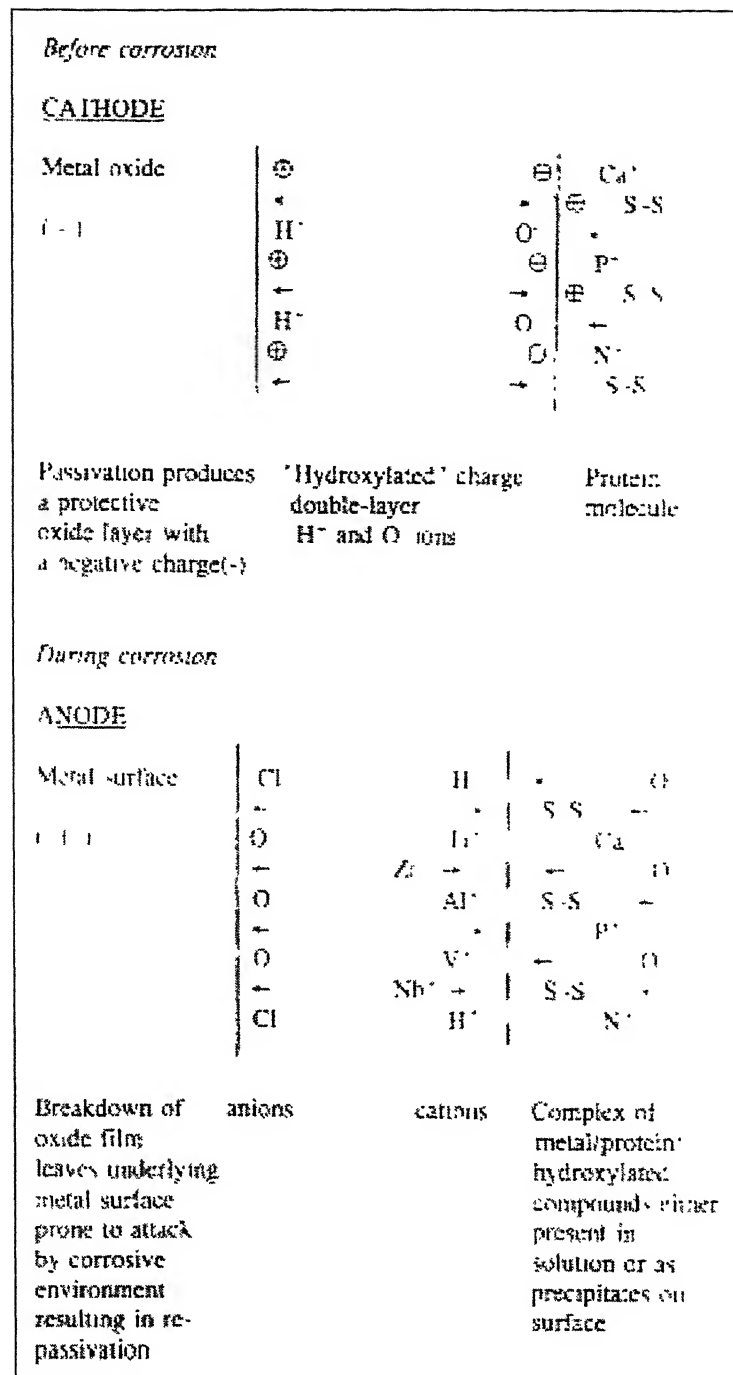


Figure 6: Theoretical model of charged double layer showing the transfer of charge at the metal/oxide/protein interfaces before and during the corrosion process.



In an environment without the presence of proteins it was observed that as the pH increased the corrosion resistance of Ti-6Al-4V and Ti-6Al-7Nb was reduced. In other words, the repassivation process became more difficult and therefore there was the possibility of greater release of metal ions into solution. This occurred with these two alloys owing to the solubility of Al and V ions and their increased solubility in the presence of increased hydroxyl concentration. The investigation showed that, under the same conditions the corrosion resistance of Ti-13Nb-13Zr increased slightly although the changes were very small. This could be explained by the lower solubility of Zr and Nb ions, in comparison with Al and V, thus repassivation occurs in preference to dissolution [102]

From the experimental work performed by Khan et al. [98], it was clear that when albumin is added to the phosphate buffer saline (PBS) solution at the three pH levels it appears to reduce the effect of pH on the corrosion resistance of Ti-6Al-4V and Ti-6Al-7Nb. Proteins can interact with the corrosion reactions in several ways and thus shift the position of equilibrium. For example, proteins can bind to metal ions and transport them away from the interface thus encouraging further dissolution or proteins may adsorb onto the metal surface thus restricting the diffusion of oxygen to the surface thus make it harder for the surface to repassivate. Both these mechanisms might be expected to decrease the corrosion resistance of the alloy. Data [103] suggests that the proteins are increasing the corrosion resistance of the alloy, in particular, at the higher pH level. At these pH levels albumin has a negative charge since its isoelectric point is 4.9. It may be possible that under these conditions metal/ protein/ hydroxide complex forms and becomes adsorbed to the surface restricting metal dissolution. Following corrosion in PBS at pH 7.4 the hardness of all the surfaces was reduced but this reduction was small for Ti-6Al-4V and greatest for Ti-13Nb-13Zr. As the pH of the PBS was increased or decreased the hardness of the repassivated surface was significantly reduced for all the alloys suggesting that the repassivated surface had a different character to the original Ti oxide surface [98].

## 2.3 Passive layer on Ti based implant materials

### 2.3.1 Immersion in Hank's solution

Titanium and its alloys have been used for many years as implant materials. The Ti alloys promoted the fabrication of orthopaedic prostheses thanks to the improved mechanical strength compared to the unalloyed form [104-110]. The superior corrosion resistance of titanium and its alloys in comparison to stainless steel and CoCr alloys has been widely reported [111-113]. Their oxide films, in fact, have been shown to be highly stable and fairly unreactive, although the alloys are generally considered to be less corrosion resistant than the metal itself. Nonetheless, observations from revision surgery and results from in vivo experiments have indicated that a higher metal release and oxide layer growth than first envisaged from in vitro experiments actually occurs [111-118]. Accumulation of Ti as well as of its alloying elements in tissues adjacent to the implant has been reported, and the causes could not only be attributable to wear [119-120]. This triggered a series of investigations into the properties of the passive film on Ti and the specific changes resulting upon exposure to the aggressive conditions present in a biological environment.

Calcium and phosphate ions are present in physiological media and have been known to selectively interact with titanium oxide surfaces, causing a remodelling of the latter, which in turn have been shown to induce nucleation of calcium phosphates of various stoichiometry on the surface [121-127]. In this direction, the effects of mineral ions on the corrosion resistance of CP Ti have been investigated via a number of surface techniques and, to a lesser extent, via electrochemical techniques. Healy et al. [128] investigated the changes in surface chemistry, stoichiometry and adsorbed surface species on titanium oxide during exposure to model physiological environments and revealed that the oxide incorporates both Ca and P elements from the extra-cellular fluid and that it increases in thickness as a function of implantation time. The  $\text{H}_2\text{PO}_4^-$  adsorption was thought to be an exchange reaction with the basic hydroxyl groups, since the titanium

surface, although amphoteric in character, at physiological pH is negatively charged [128]. XPS studies conducted by Ellingsen et al. on the other hand, indicated that calcium is adsorbed by the negatively charged TiO<sub>2</sub> surface, which then further promotes the adsorption of calcium binding proteins [129]. Sousa et al. reported that in the presence of these ions a decrease in the corrosion resistance of Ti takes place both in the presence and absence of film breakdown [121]. The authors reported that when film breakdown occurs calcium phosphate decreases the film resistance to chloride attack. EDS (energy dispersive spectroscopy) analysis of corrosion products obtained from galvanostatic experiments showed the formation of different types of calcium phosphate on the titanium surface.

Sundgren et al. [130-131] used Auger electron spectroscopy to reveal that the titanium oxide layer grows and takes up ions during implantation time. This growth and uptake was demonstrated to occur even in the presence of an adsorbed layer of protein. Hanawa et al. [123] also reported that the titanium oxide layer on both Ti and Ti6Al4V reacts with phosphate and calcium ions upon immersion in artificial saliva. The authors investigated the incorporation of inorganic ions into the surface of titanium by XPS and FTIR-RAS and found that upon immersion of titanium in biofluids of different pH, the surface adsorbed only oxygen, hydroxyl groups, water, calcium ions and phosphate ions even though the solution contained other ions.

The calcium phosphate formed on Ti at pH 7.4 was similar to apatite. The same authors investigated the re-passivation of Ti after abrasion in bioliquids, and found that the kinetics were slower compared with that in saline or water solutions, leading to more Ti dissolution. The re-passivation step was also found to selectively incorporate phosphate ions and, in the outer layer, both calcium and phosphate ions [132]. Frauchinger et al. [126] also observed a spontaneously formed adsorbed layer of calcium phosphate on a titanium dioxide surface and its thickness as well as the Ca/P ratio was found to increase with immersion time. After 71 days of immersion, the Ca/P ratio was reported to correspond to that of brushite or monetite whilst after 6 months close to that of hydroxyapatite. The presence of phosphate was seen

to be a prerequisite to the adsorption of calcium ions [126] whilst according to Panjian et al. [133] the formation of TiOH groups in simulated body fluid appeared to be the prerequisite for the formation of a hydroxyapatite layer.

Hodgson et al. [134] employed electrochemical impedance spectroscopy (EIS) and photoelectrochemistry to investigate changes in the electronic and semi-conductive properties of Ti6Al4V and Ti6Al7Nb passive film/electrolyte interface under simulated body fluid conditions. In this work it has been shown that  $\text{Ca}^{2+}$  and  $\text{PO}_4^{3-}$  ions selectively interact with the surface of  $\text{TiO}_2$  both when present separately or together in a saline solution at physiological acidities. The constancy of the band-gap energy for the investigated metals under different physiological conditions lead to the conclusion that the semi-conductive properties of the films were unaltered by the presence of ions and therefore that the nature of the interaction was adsorption onto the passive oxide film.

The ability to adsorb species with positive and negative charge alike is due to the fact that the  $\text{TiO}_2$  surface at pH 7.4 is predominantly negative in character thus electrostatically capable of attracting oppositely charged ions such as calcium, but also that the hydrated surface may undergo exchange reactions with phosphate groups to form Ti-phosphates, which in turn may also react with calcium ions to form calcium phosphates [135-137]. The evolution of the adsorption of the ions has been shown to take place already within the first hours of exposure to simulated biological environments at 37 °C, and the techniques employed showed that immediate to short-term changes at the metal oxide/electrolyte solution interface in situ may be easily monitored.

### 2.3.2 Effect of alloying elements

The properties of the surface film can be described in terms of the presence of various types of point defects, dislocations and grain boundaries, i.e. in terms of oxide film formation morphology [138]. When alloying elements are present in the metal oxide film, beneficial or deleterious effects may occur, depending on the following factors: (i) the affinity of the

component metals for each other and for non-metal species, particularly oxygen; (ii) the diffusion rate of atoms in the alloy and ions in the oxide; (iii) the mutual solubility in the oxidation layers, and finally (iv) the relative volumes of the various phases.

Several studies have been performed to examine the effect of various alloying elements on passive film properties of Ti alloys in Hank's solution. It has been reported that the Ti6Al6Nb alloy exhibits better corrosion resistance properties than the Ti6Al4V alloy [139,140]. In vitro cellular response study confirmed that human monocytes released significantly more bone-resorbing mediators after exposure to Ti6Al4V particles compared with Ti6Al6Nb particles, because the Ti6Al6Nb alloy is less susceptible to corrosion [141].

Kolman and Scully [142] found that the inferior pitting resistance of Ti-15V-3Cr-3Al-3Sn is apparently attributable to the alloying additions of Al and V.

In investigations of the Ti-Nb alloy Yu and Scully [143-145] concluded that alloying addition of Nb results in improved resistance to active dissolution in acidic solution and enhanced passivation relative to pure titanium. This was attributed to the enrichment of Ti surface with elemental Nb and oxidized Nb<sub>2</sub>O<sub>5</sub>, due to preferential dissolution of Ti. Scully explained the beneficial effect of Nb or Zr alloying addition through the formation of strong covalent bonds between near neighbors Ti, Nb and Zr by the sharing of unpaired d-level electron [143].

The influence of niobium and vanadium as alloying elements on titanium alloy passivity has been investigated by Metikoš-Huković et al. [146] in Hank's solution. A consideration of the size of alloying elements pointed to the advantages of alloying titanium with niobium rather than vanadium. The ionic and covalent radii of titanium, niobium, aluminum and vanadium are given in Table 7 [147]. The similarity of Ti and Nb radii is evident from the data, while vanadium and titanium radii are different. Since point defect occurs when the size of foreign cation being incorporated in the crystal lattice does not match the "host" ion, it is obvious that mere presence of vanadium

in the oxide of titanium will cause an increase in the concentration of defects and a decrease in corrosion resistance, while niobium ions could successfully replace the titanium cations (Figure 7). The optimal niobium content in the alloy may exert a manifold contribution to an increase in homogeneity of the titanium alloy oxide, as well as an increase in its corrosion resistance. Therefore, it is very important to determine the amount of niobium in the alloy with respect to the concentration of point defects.

	Coordination	Ionic radius (Å)	Covalent radius (Å)	$\frac{r_c}{r_i}$	$\frac{r_m}{r_i}$
Ti (4+)	6	0.61	1.33	2.18	1.78
Nb (5+)	6	0.64	1.31	2.05	1.74
Nb (5+)	6	0.72	1.31	1.82	1.74
V (2+)	6	0.79	1.72	2.18	1.78
V (5+)	6	0.54	1.33	2.46	1.78
Al (3+)	4	0.39	1.25	3.21	1.41
Al (3+)	6	0.51	1.25	2.45	1.41

Table 7. Ionic, covalent and metallic radii of titanium, niobium, vanadium and aluminum [147].

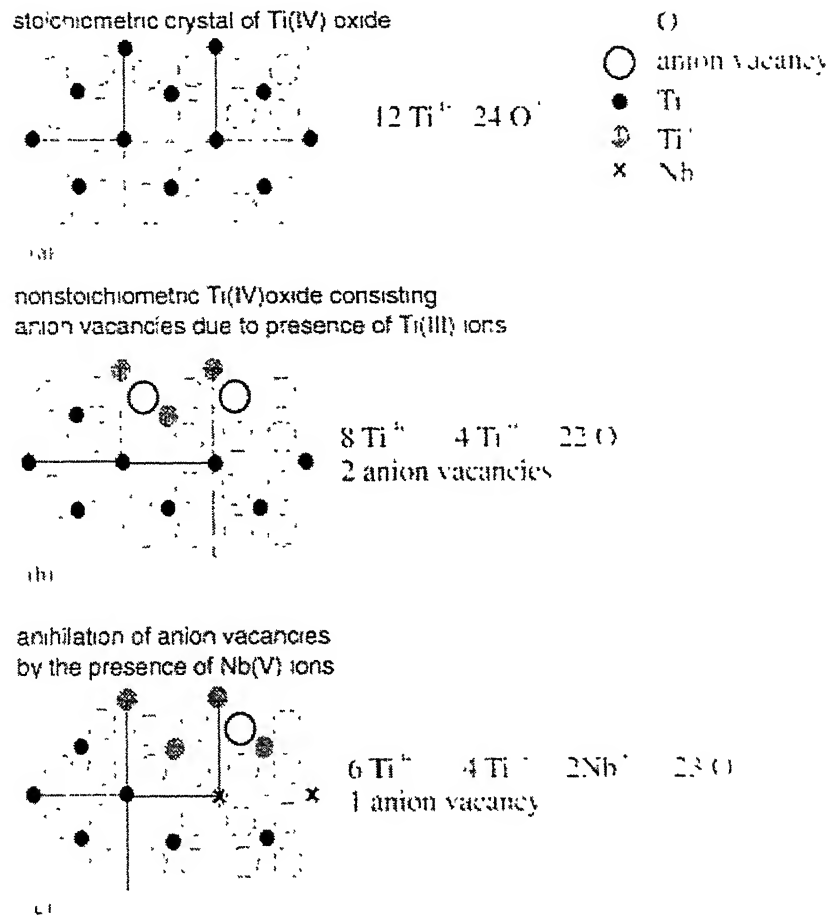


Figure 7: Schematic view of the stoichiometric titanium(IV)oxide (exhibiting rutile structure), the non-stoichiometric titanium(IV)oxide with Ti(III) ions and the titanium(IV) oxide with Ti(III) and Nb(V) ions.

### 2.3.3 Surface treatment on titanium alloys

Titanium (Ti) and its alloys have long been used as implant materials in dental and orthopedic applications [148]. To improve the implant-tissue osseointegration, effort has been directed to the modification of Ti surfaces [149-151]. In practice, the very thin (at most several tens of nanometers) oxide film on the Ti surface, which is formed in an aqueous environment, plays a decisive role in determining the biocompatibility and corrosion behavior of the Ti implant [156].

Since the corrosion resistance is known to increase with the thickness of the oxide layer [157,158], many attempts have been made to form a thick TiO<sub>2</sub> layer on the Ti substrate using various methods, such as anodization, thermal oxidation, and the sol-gel process [159-163].

In practice, an increase in the TiO<sub>2</sub> layer thickness was observed to result in a decrease in the bonding strength of the double layer coating, due to the thermal mismatch between the Ti and TiO<sub>2</sub> layers being increased. For this reason, the application of a thinner layer of TiO<sub>2</sub> might be favored. However, reducing the thickness of the TiO<sub>2</sub> layer decreases its ability to act as a barrier against the corrosion of the Ti substrate, since the corrosion resistance is proportional to the thickness of the layer [157,158]. Therefore, the TiO<sub>2</sub> thickness should be controlled in such a way as to produce a compromise between the bonding strength and the corrosion properties.

Kim et al. [164] coated CP titanium substrate with hydroxyapatite (HA) with the insertion of a titania (TiO<sub>2</sub>) buffer layer by the sol-gel method. In the study, the TiO<sub>2</sub> layer was first coated by spin coating at a speed of 3000 rpm for 20 s, and this was followed by heat treatment at 500°C for 1 hr. The HA layer was subsequently spin coated and heat treated at temperatures of 400–500°C. In order to make the TiO<sub>2</sub> sol, 0.5 m titanium propoxide (Ti(OCH<sub>2</sub>CH<sub>2</sub>CH<sub>3</sub>)<sub>4</sub>) was hydrolyzed in ethanol mixed with diethanolamine (HOCH<sub>2</sub>CH<sub>2</sub>)<sub>2</sub>NH (diethanolamine/ethanol=20% v/v), and then a small amount of distilled water was added to the solution, followed by stirring for 24 hrs to obtain a clear TiO<sub>2</sub> sol. The HA sol was fabricated from



its precursors, calcium nitrate tetrahydrate ( $\text{Ca}(\text{NO}_3)_2 \cdot 4\text{H}_2\text{O}$ ) and triethyl phosphite ( $\text{P}(\text{C}_2\text{H}_5\text{O})_3$ ) within an ethanol–water mixed solvent, as described previously [165]. The  $\text{TiO}_2$  thickness of around 200 nm obtained in this study was observed to be highly effective at improving both the bonding strength and the corrosion resistance.

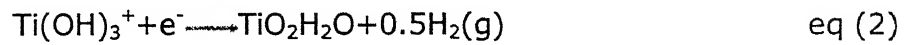
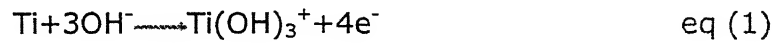
The main disadvantage of the conventional methods (plasma spray) is related to the high temperature used. Due to the low thermal properties of titanium alloys, local heating of the surface is produced, thus changing the structure and the mechanical properties of the surface material. Another main problem concerns the control of the chemical composition and crystallinity of the apatite coating as well as its physical and mechanical properties during and after deposition [166-168]. Hydroxyapatite is thermally unstable during cooling, thus producing amorphous calcium phosphate phases. The presence of amorphous phases in the coating goes against the stability of the coating at long term after implantation. As it is known, amorphous calcium phosphates and even phases as tetracalcium and tricalcium phosphates, which are also formed during cooling, dissolve faster than hydroxyapatite, thus leading to complete mechanical disintegration of the coating and loosening of the implant fixation [168-170]. It has also been reported that adhesion of the coating to the implant is very limited, leading to early decohesion of the coating even after short implantation. This is related to the absence of any chemical link between the titanium surface and the hydroxyapatite coating.

In order to create an implant with both superior mechanical properties and excellent bioactivity, attempts were made to produce bioactive titanium and its alloys. Recently, it has been reported that chemically treated titanium and its alloys can induce bone-like apatite formation in vitro and in vivo [171-191], which means that titanium and its alloys have potential bioactivity. This apatite layer does not have the problems associated with conventional coating techniques such as the plasma-spray technique and is an essential requirement for artificial materials bond to living bone. The reagents most frequently employed in the treatments were NaOH [171-186] and hydrogen peroxide ( $\text{H}_2\text{O}_2$ ) solution [187-189], and HCl and  $\text{H}_2\text{SO}_4$  were also used to etch titanium before alkaline treatment [190,191]. Treatment

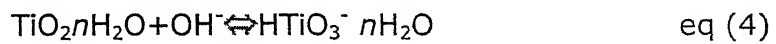
with an NaOH solution produced a sodium titanate gel layer on titanium surface while H<sub>2</sub>O<sub>2</sub> treatment produced a titania gel layer. Both gel layers have the ability to induce formation of bone-like apatite during immersing in simulated body fluid (SBF) and thus are considered bioactive. The gel layers can initiate apatite nucleation on itself. Once apatite nucleation occurs, it spontaneously grows by taking calcium and phosphate ions from the surrounding environment.

Gil et al. [192] in their study on growth of bioactive surfaces on titanium and its alloys for orthopaedic and dental implants, treated titanium and its alloys with NaOH solution and characterized the surface film behavior of NaOH-treated titanium sample with immersion time in simulated body fluid (Hank's solution). The study showed that a microporous layer made up of an alkaline titanate hydrogel formed during the alkaline/heat treatment. This layer was characterised by a thin-film X-ray diffractometer as shown by the spectrum in Figure 8. This spectrum showed that this surface layer is an amorphous sodium titanate layer containing of small amounts of a mixture of crystalline sodium titanates (Na<sub>2</sub>Ti<sub>5</sub>O<sub>11</sub>) and rutile (TiO<sub>2</sub>). During the alkali treatment, the surface-passive TiO<sub>2</sub> layer partially dissolves into alkaline solution because of the corrosive attack of hydroxyl groups [193,194-196].

The reaction mechanism was assumed to be [197,198].

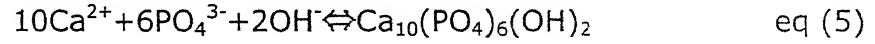


A further hydroxyl attack to hydrated TiO<sub>2</sub> will produce negatively charged hydrates on the surfaces of the substrates as follows.



These negatively charged species are combined with alkali ions in the aqueous solution, resulting in the formation of an alkali titanate layer. During heat treatment, the hydrogel layer is dehydrated and has densified the titanate layer.

When exposed to simulated body fluid, the alkali titanate layer is again hydrated to transform into TiO<sub>2</sub> hydrogel via release of alkali ions from the alkali titanate layer into SBF. The alkali release and the ion exchange with H<sub>3</sub>O<sup>+</sup> ions in simulated body fluid results in a pH increase in the surrounding fluid. The pH increase gives rise to an increase in the ionic activity product of apatite according to the following equilibrium in simulated body fluid [199-200].



Wang et al. also showed similar observations in their study on NaOH treated CP titanium and Ti-6Al-4V [201,202]. EIS studies on these alloys, reported by them, showed that three layer existed on metal surface when immersed for long intervals in Hank's solution. These layers were of inner passive layer, intermediate hydrogel layer and apatite layer (Figure 9). Figure 10 shows the porous network structure of sodium titanate which formed on reaction of NaOH solution with Ti-6Al-4V.

The possible mechanism of nucleation and growth of apatite on alkaline treated titanium immersed in SBF solution has also been proposed to occur as follows [171]. The sodium titanate layer releases its Na<sup>+</sup> ions into the surrounding fluid via an ion exchange with H<sub>3</sub>O<sup>+</sup> in the fluid to form Ti-OH groups as early as 0.5 hr after immersion. The Ti-OH groups then immediately interact with the calcium ions in the fluid to form a calcium titanate. The calcium titanate incorporates the phosphate ions, as well as the calcium ions, in the fluid to form apatite nuclei in the SBF solution. At this stage, the crystalline bone-like apatite is first detected by XRD analysis. Once formed, the apatite nuclei grow by consuming the calcium and phosphate ions in the SBF solution (Figure 11). The island type of structures visible in Figure 11(a) were proposed to be apatite nuclei and the background porous network was attributed as calcium titanate. The apatite nuclei grew with immersion time in Hank's solution and covered the whole surface as can be observed in Figures 11(b,c,d).

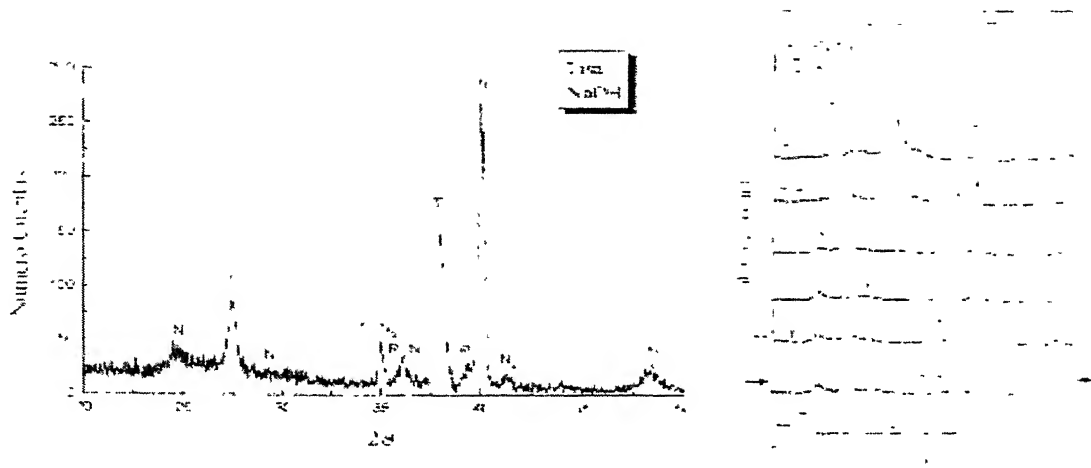


Figure 8. X-ray diffraction of the alkaline titanate hydrogel obtained and Standard [193].

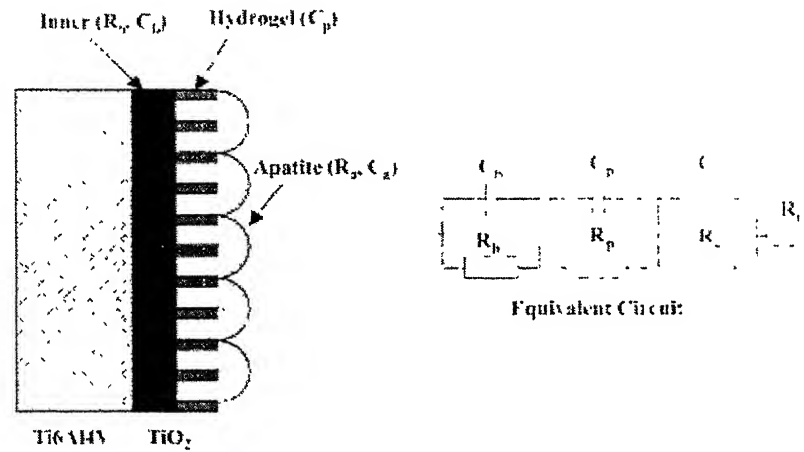


Figure 9. Equivalent circuits used for alkaline treated Ti6Al4V immersed in the SBF solution at 36.5°C at regular intervals, and schematic representation of the apatite layer, hydrogel layer and inner layer of oxide film on treated Ti6Al4V. Notations:  $R_e$  is the solution resistance;  $C_b$ ,  $R_b$  are the inner layer capacitance and resistance;  $C_p$ ,  $R_p$  are the hydrogel layer capacitance and resistance;  $C_a$ ,  $R_a$  are the apatite layer capacitance and resistance[202].

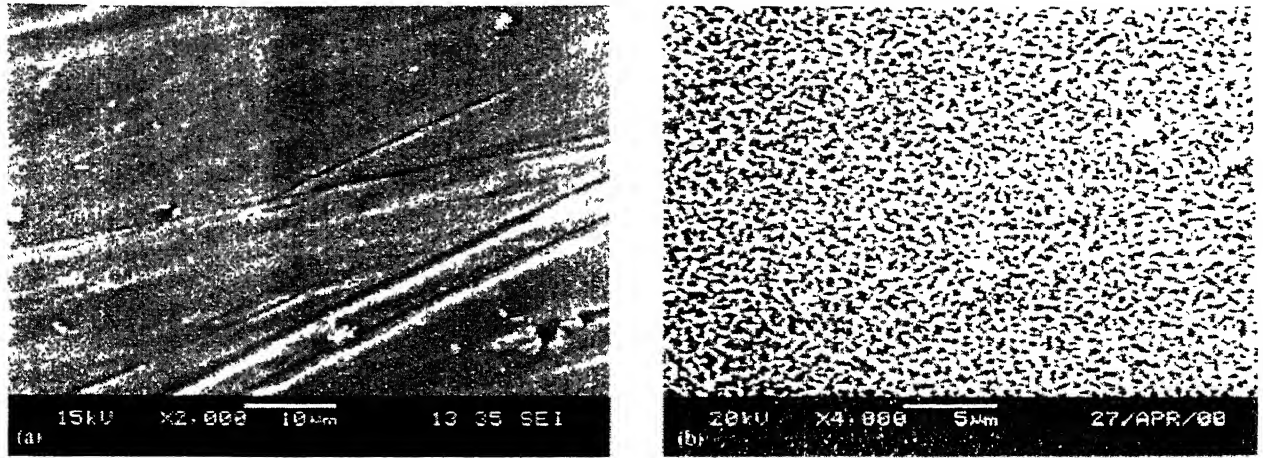


Figure 10. SEM micrographs of untreated Ti6Al4V and Ti6Al4V treated with 5.0 % NaOH solution at 60°C for 24 h (a) untreated Ti6Al4V substrate (b) NaOH treated Ti6Al4V substrate[202].

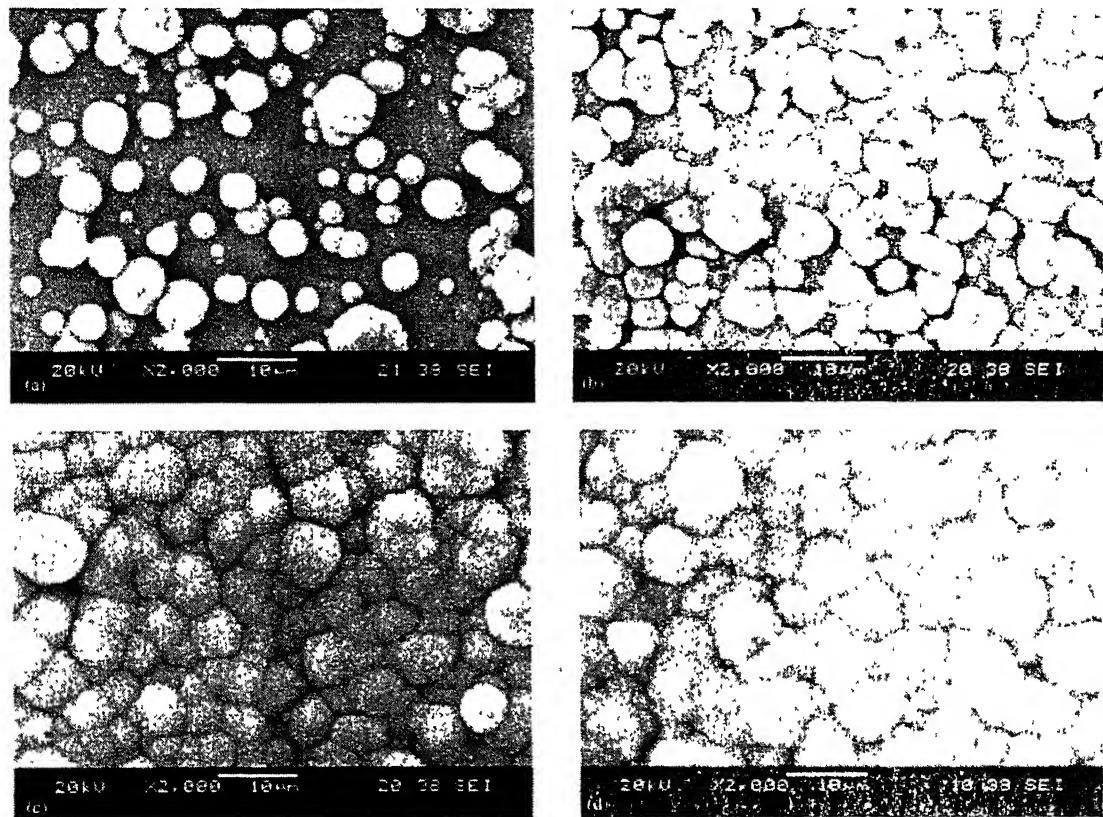


Figure 11. SEM micrographs of the surfaces of pretreated Ti6Al4V substrates immersed in the SBF solution at 36.5°C at regular intervals (a) 1 week (mixture of Ca-titanate and apatite) (b) 2 weeks (mixture of Ca-titanate and apatite) (c) 3 weeks (apatite) (d) 4 weeks (apatite)[202].

## 2.4 Electrochemical Corrosion Testing

### 2.4.1 Electrochemical Corrosion

Corrosion can be defined as the degradation of a metal by an electrochemical reaction with its environment [203]. Corrosion is an electrochemical process. Electrochemical processes require anodes and cathodes in electrical contact and ionic conduction path through an electrolyte. The electrochemical process includes electron flow between the anodic and cathodic areas; the rate of this flow corresponds to the rates of oxidation and reduction reactions that occur at the surfaces. Monitoring this electron flow provides the capability of assessing the kinetics of the corrosion process, not simply the thermodynamic tendencies for the process to occur spontaneously but also the accumulated metal loss registered after the test. Measurements of this type are known as electrochemical measurements of corrosion [204,205].

Electrochemical techniques are finding increased use in corrosion research and in engineering applications. Such methods are practical because the corrosion behavior of material-electrolyte combinations is a direct function of the mechanisms as well as the kinetics of the electrochemical reactions responsible. The availability of better electrochemical techniques and the demonstrated accuracy of such methods for investigating corrosion phenomena have been the subject of several recent technical symposia [206,207].

All metals are found in their low energy state ores, in the form of their oxides, sulfides, carbonates or more complex compounds. Large amount of energy is supplied in order to extract a pure metal from its ore. This pure metal is in a high-energy state and hence they try to come back to the low energy state by recombining with the environment. This process is called corrosion. Figure 12 shows the thermodynamic energy profile for metals and their compounds. The thermodynamic aspects of corrosion will be briefly discussed. All the interactions between elements and compounds are governed by the free energy changes ( $\Delta G$ ). Any reaction is said to be spontaneous when  $\Delta G$  for the reaction is negative. At room temperature most

of the chemical compounds of metals have lower free energy than the pure metals and hence most of the metals have an inherent tendency to corrode.

In all kinds of aqueous corrosion, there are two reactions occurring at the metal/liquid interface; an electron producing reaction (anodic or oxidation reaction) and an electron consuming reaction (cathodic or reduction reaction). The corrosion reaction for the creation of a wet electrochemical cell requires four basic requirements, the cathode on which the reduction reaction occurs, an anode on which oxidation occurs, an electrolyte to act as the conducting medium for ions and a electrical connection for electron to flow between the anode and cathode.

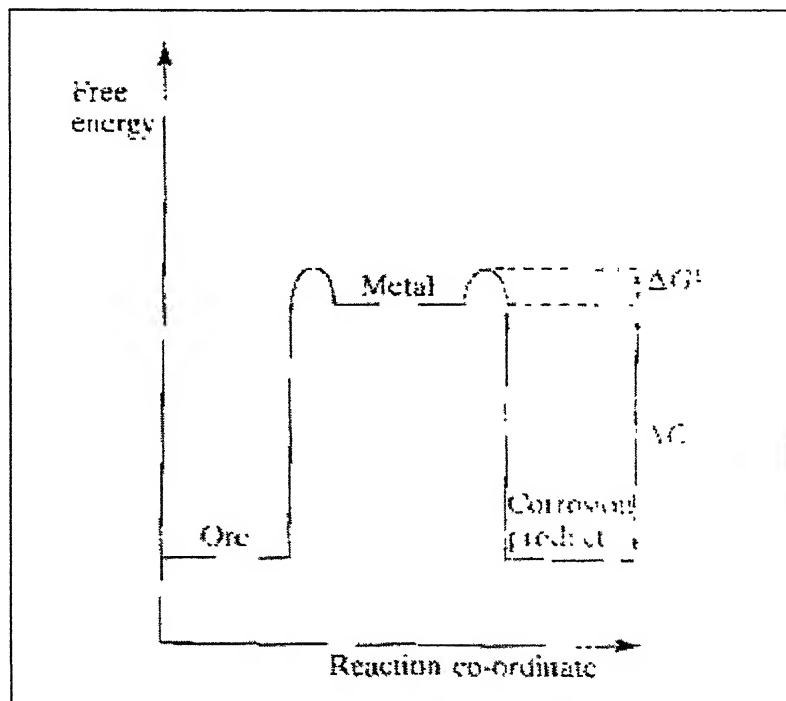
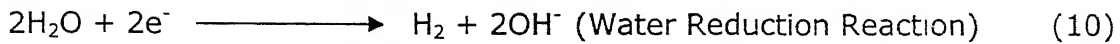
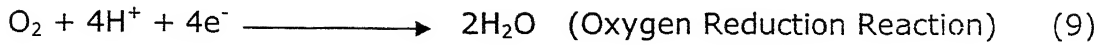


Figure 12: The thermodynamic energy profile for metals and their Compounds.

The anodic reaction is invariably corrosion of the metal as shown in equation 6. Several cathodic reactions can occur during corrosion [203][116]. The simplest of them is reduction of hydrogen ions (equation 7). Another is reduction of an oxidized ion in solution (redox reaction) as in equation 8. Another reaction is reduction of dissolved oxygen as in equation

9. In the absence of any of these reactions water reduction will occur as in equation 10.



A basic wet corrosion cell is shown in the Figure 13. The potential difference between the anode and the cathode could be measured by using a voltmeter in the circuit.

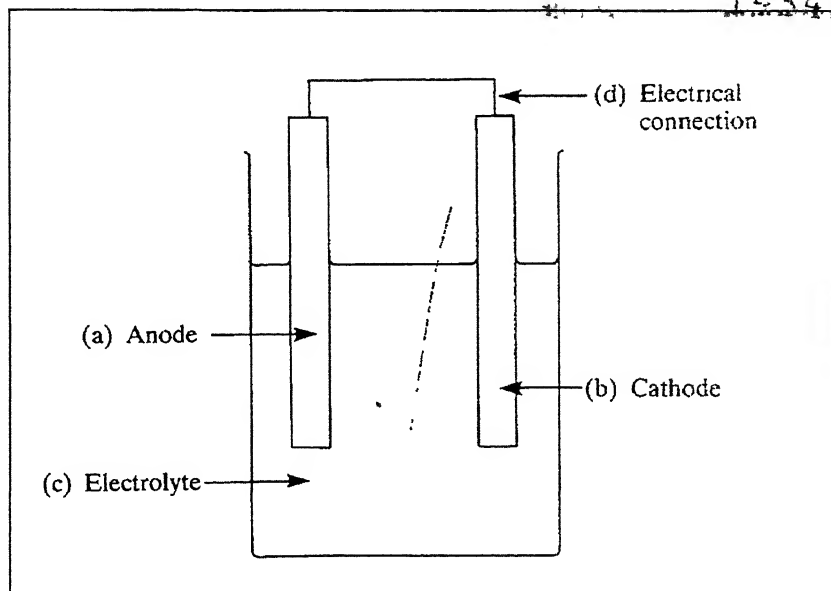


Figure 13: A basic wet corrosion cell [2].

But this gives only the potential difference between the electrodes and in order to measure the absolute potential we need a third electrode. This third electrode is called as the standard electrode against which all the measurements can be made. The standard hydrogen electrode, saturated



calomel electrode (SCE) etc. are usually used as the standard electrodes. Table 8 gives some commonly used standard electrodes and their potentials.

Table 8: Standard reference electrode potentials [2].

Electrode	Electrolyte	Potential (V)
Calomel (SCE)	Saturated KCl	+0.2420
Calomel (NCE)	1.0 M KCl	+0.2810
Calomel	0.1 M KCl	+0.3335
Silver/Silver Chloride (SSC)	1.0 M KCl	+0.2224
SSC	Sea Water	+0.25
Copper/Copper Sulphate (CSE)	Sea Water	+0.30
Zinc	Sea Water	-0.79

## 2.4.2 Polarization

When a metal is not in equilibrium with the solution of ions, the electrode potential differs from the free corrosion potential by an amount known as the polarization [203]. It can also be said as overpotential or overvoltage. Polarization is a very important corrosion parameter as it is useful in calculating the rates of the corrosion process. The deviation of the equilibrium potential is a combination of an anodic polarization of metal and a cathodic polarization of the environment. If the electrons are made available to the metal, the potentials at the surface becomes more negative, suggesting that excess electrons with their negative charges accumulate at the metal/solution interface. This negative potential charge with respect to the reversible condition is called as cathodic polarization. Similarly, when electrons are removed from the metal, there will be a deficiency of electrons on the metal surface interface, which produces a positive potential change, called anodic polarization [208]. In an aqueous electrolyte solution the surface will reach a steady potential called free corrosion potential,  $E_{\text{corr}}$ , which depends on the ability and rate at which electrons can be exchanged by the anodic and cathodic reactions.

When an adherent surface film forms on anodic polarization under oxidizing conditions, this is termed as passivation [203]. Passivity of metals has been a subject of significant research. The nature of the passive films that form on a wide variety of materials has been explored utilizing special electrochemical characterization techniques like impedance spectroscopy, ellipsometry, etc. [203].

The mechanism of passive film formation can be understood by modern electrochemical theory, with the aid of polarization diagrams. The polarization diagram is a plot between the potential (i.e. the thermodynamic axis) and current density (i.e. the kinetic axis). The changes in the current density as a function of polarization (i.e. deviation of potentials away from equilibrium) is represented in these polarization diagrams and several processes related to corrosion (and electrochemistry) can be easily understood utilizing these diagrams. The anodic polarization diagram for a metal exhibiting passivity (i.e. condition of corrosion resistance due to formation of an adherent non-dissolving passive film on anodic polarization under oxidizing conditions) is schematically depicted in Figure 14 [209]. It must be remembered that experiments have to be performed by controlling the potential and measuring the current (i.e. either potentiostatically or potentiodynamically) rather than vice versa, in order to understand passivation phenomenon [203]. At the equilibrium reversible potential of the metal ( $E_{rev}$ ), the exchange current density ( $i_o$ ) depicts the rate of the forward reaction (i.e. corrosion) being equal to the rate of the reverse reaction (i.e. reduction).

On anodically polarizing the material, thermodynamic conditions for the formation of a stable surface film are established at point A. On further anodically polarizing the material, the passive film nucleates on the surface from point B onwards and this indicates the potential for initiation of passivity ( $E_p$ ). On further increasing the potential, the film starts covering the surface laterally and at optimum coverage, the critical current density ( $i_{crit}$ ) is achieved (point C), corresponding to which the primary passivation potential

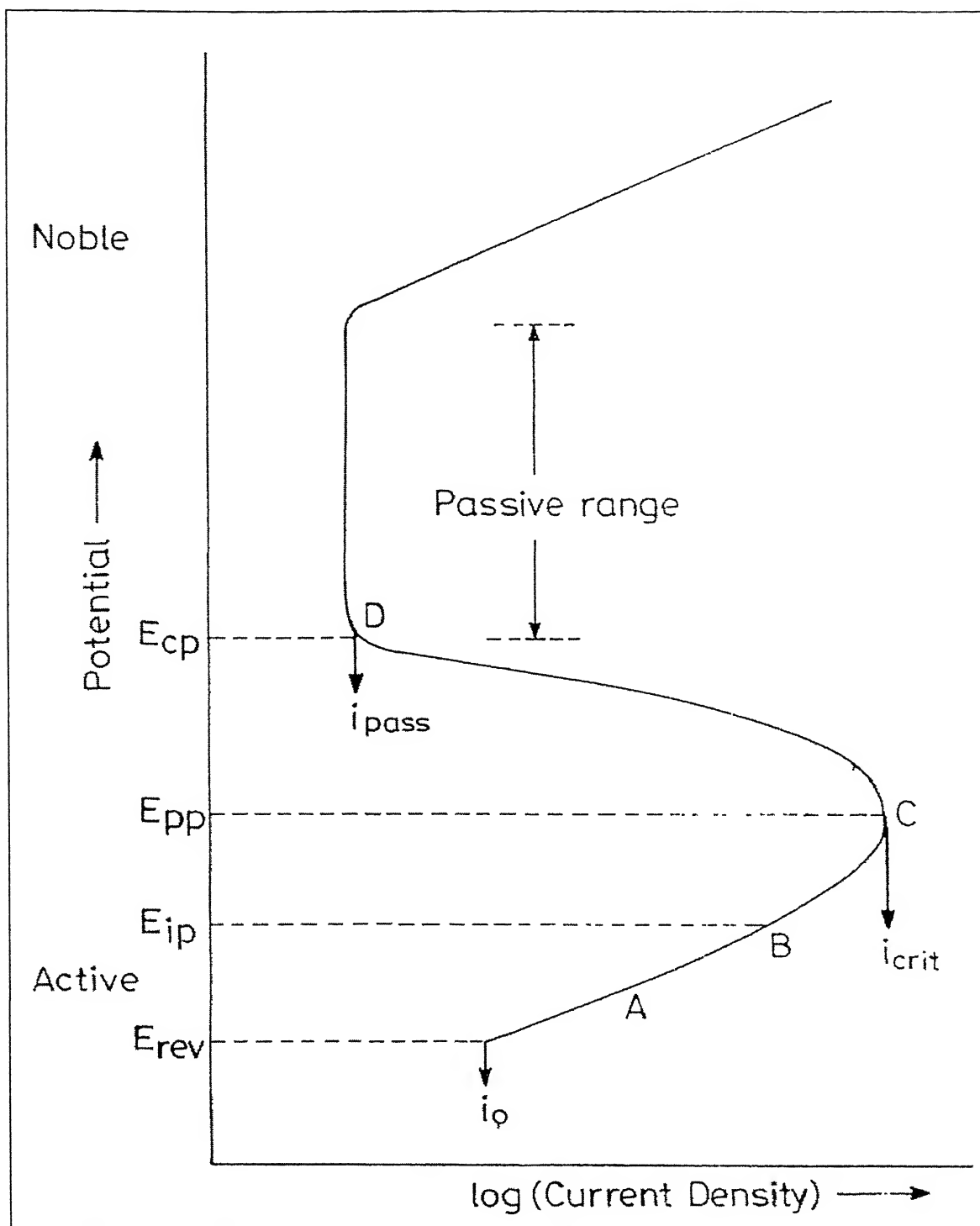


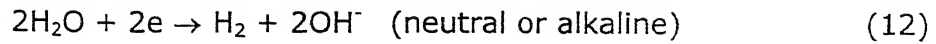
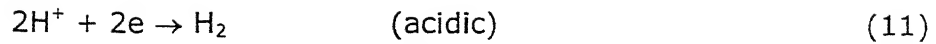
Figure 14: Schematic anodic polarization diagram for an active-passive metal illustrating important passivity parameters.

( $E_{pp}$ ) is defined. On further anodic polarization beyond  $E_{pp}$ , the surface passive film completely covers the surface and the current density decreases with increasing anodic polarization until the point D, when the passive film completely covers the surface. The potential corresponding to point D is referred to as the potential for complete passivation ( $E_{cp}$ ). On polarizing past this potential, the current density remains constant with increasing potential in the passive range (Figure 14). On further anodically polarizing the material, several reactions can lead to the destruction of passivity (i.e. indicated by increasing current density with increasing potential), which is understood by the breakdown potential,  $E_b$ . Some of the processes leading to increasing current density with polarization beyond the breakdown potential are oxygen evolution, transpassive dissolution due to conversion of the passive film forming ion to a higher oxidation state, pitting caused by destabilization of the passive film due to the presence of halide ions or changes in the nature of the passive film (for example anodizing wherein there is a change in porosity of the passive film).

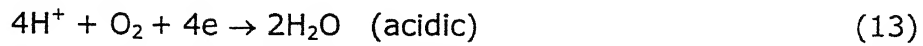
In the passive region, the current density remains constant with increasing anodic polarization, which is due to thickening of the passive film [209]. It is important to note the fine dimensions of the passive films. The current density remains constant over a significant range of potential in the passive range, and this is called the passive current density ( $i_{pass}$ ). The passive current density is dictated by the constant rate of dissolution of the metal ions into the electrolyte from the passive film surface. The increasing anodic positive potentials in the passive range are accommodated by thickening of the film.

After the above discussion on the anodic polarization characteristic, the development of free corrosion potentials needs to be addressed. Modern electrochemical theory states that equilibrium corrosion condition obtains when the net cathodic rate is equal to the net anodic rate. Practically, this implies that the free corrosion potential will be established at the potential where the cathodic polarization curve (i.e. of the cathodic reaction) intersects the anodic polarization curve. The rate of the anodic reaction is therefore directly related to the rate of chemical reduction reaction(s) at cathodic areas. The cathodic reaction in de-aerated solutions is hydrogen evolution,

given by



The hydrogen evolution reaction proceeds rapidly in acids, but slowly in alkaline or neutral media. Dissolved oxygen in the electrolyte takes part in the cathodic reaction in accordance with one of the following reactions.



Dissolved oxygen reacts with hydrogen/water adsorbed at random on the metal surface, independent of the presence or absence of impurities. Therefore, the oxidation reaction proceeds as rapidly as oxygen reaches the metal surface.

The oxygen reduction reaction will be considered to illustrate the development of free corrosion potentials (FCP) or mixed potential under atmospheric corrosion conditions. The cathodic polarization curve corresponding to oxygen reduction reaction can intersect the anodic polarization curve at different locations and based on this; different conditions of passivity (stable or unstable) or active behavior can be realized. Three possible situations are depicted in Figure 15. In Figure 15a, the cathodic polarization curve intersects the anodic curve in the active region and the FCP is established at the potential corresponding to the intersection of both these curves. The metal corrodes in the active state. In practical cases, this situation generally depicts corrosion of fresh surface of metal, free of any surface film. In case the anodic polarization curve intersects the cathodic polarization curve *only* in the passive region, then the FCP would be established in the passive region. This is the condition of stable passivity (Figure 15b). When the cathodic polarization curve intersects the anodic

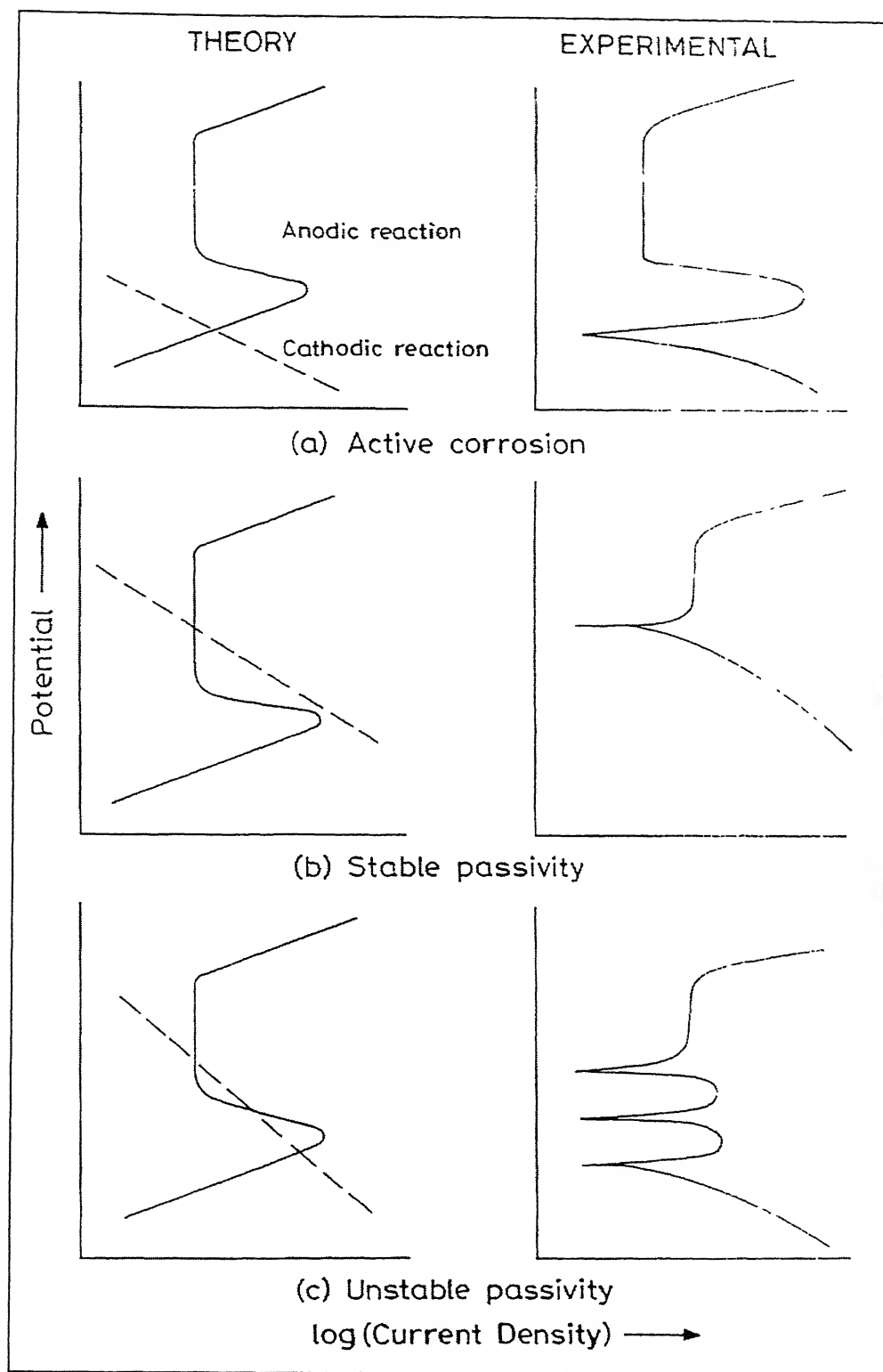


Figure 15: Schematic illustrations outlining the theoretical aspects governing the development of experimental polarization diagrams: (a) active behavior, (b) stable and (c) unstable passive behavior.

polarization curve as shown in Figure 15c, there are three potentials where the anodic and cathodic current densities are equal. The FCP that the material will achieve depends on its prior surface condition. In case a fresh surface is exposed without any film present, then the FCP would establish in the active region, whereas if there is a pre-existing passive film, the FCP would establish in the passive region. The schematic depicted in Figure 10c is indicative of unstable passivity and the experimental polarization diagram for this situation would show the existence of a cathodic loop [203]. The above discussion establishes that surface electrochemical potential depends upon the nature of the surfaces as well as the cathodic reaction kinetics.

### 2.4.3 Corrosion Rates

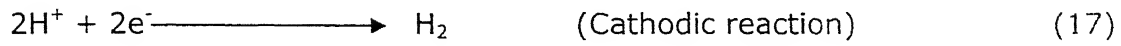
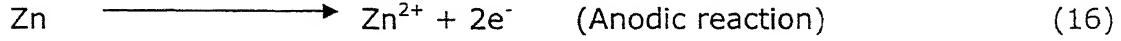
There are two methods available for measurement of corrosion rate using polarization methods, namely Tafel extrapolation and polarization resistance. The polarization methods to measure corrosion rates have their inherent advantages [210]. The main advantage of these methods is that the time taken for conducting experiments is relatively short, whereas the conventional weight loss methods require several days. The polarization methods are highly sensitive, and accelerating factors such as elevated temperature, to increase rates is generally not necessary. Moreover these methods are non-destructive and several repetition experiments can be carried out using the same sample.

The mixed potential theory forms a basis for explaining the polarization techniques. The mixed potential theory consists of two simple hypothesis:

1. Any electrochemical reaction can be divided into two or more partial oxidation and reduction reactions.
2. There cannot be net accumulation of electrical charge during a chemical reaction i.e., corrosion reaction the sum of the anodic oxidation currents should be equal to the sum of the cathodic

reduction currents. In other words the total rate of oxidation should be equal to total rate of reduction [211].

Consider the reactions for zinc getting corroded in an acid solution. Then the anodic and cathodic reactions are given by,



These reactions are called as the half-cell reactions and the potential corresponding to them are called cell potential. The potentials cannot coexist separately on an electrically conducting surface. The potentials will polarize to an intermediate value called as the corrosion potential or mixed potential ( $E_{\text{corr}}$ ). When there is no external current flowing into the system, then the equilibrium potential attained is called free corrosion potential ( $E_{\text{corr}}$ ) [208][121]. As the reactions polarize on the same surface the change in potentials is given by,

$$\eta_a = \beta_a \log (i_a/i_o) \quad (18)$$

$$\eta_c = \beta_c \log (i_c/i_o) \quad (19)$$

where  $\eta_a$  and  $\eta_c$  are anodic and cathodic polarization,  $\beta_a$  and  $\beta_c$  are the Tafel constants,  $i_a$  and  $i_c$  are the anodic and cathodic currents, respectively. At  $E_{\text{corr}}$  the rate of anodic and cathodic reactions are equal and is equal to the current density,  $i_{\text{corr}}$ . The half-cell reactions for dissolution of Zn in acid are shown in the Figure 16. This figure is also called as Evans diagram and represents active corrosion of the metal.



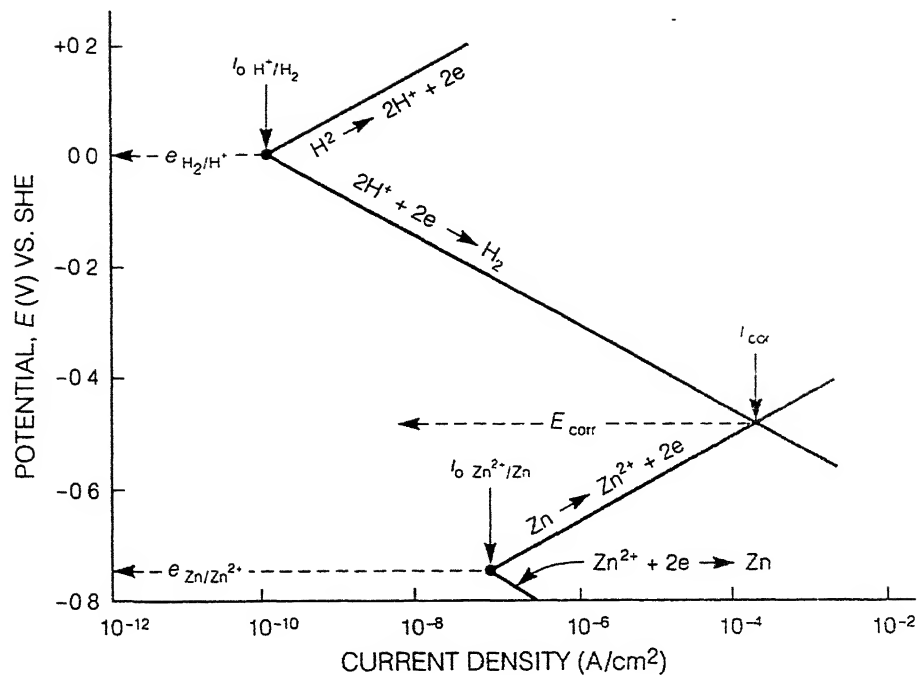


Figure 16: Polarization diagram for dissolution of Zn in acid (active corrosion case).

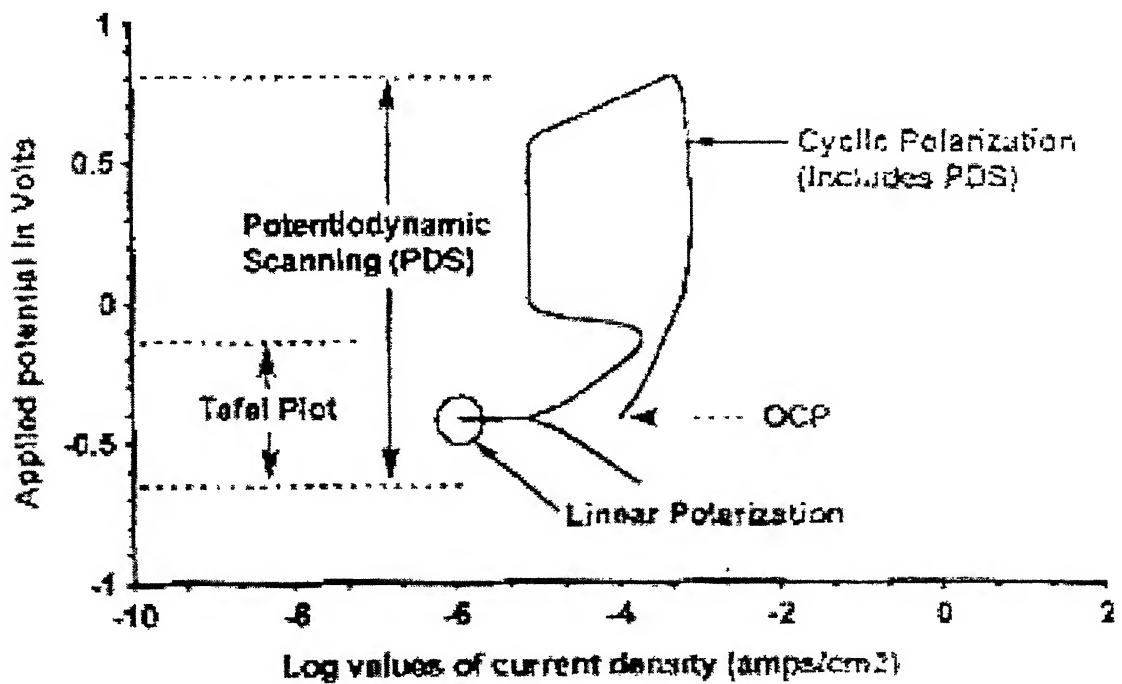


Figure 17: Various types of polarization methods.

The various polarization techniques that are commonly used are linear polarization, Tafel extrapolation, potentiostatic polarization and cyclic polarization. These four polarization techniques are summarized in the Figure 17.

The corrosion rate is directly proportional to the corrosion current and can be converted into corrosion rate using the formula [116],

$$\text{Corrosion rate in mil/year (MPY)} = 0.129 (i_{\text{corr}})(A/n)(1/\rho) \quad (20)$$

where,  $i_{\text{corr}}$  is corrosion current ( $\mu\text{A}/\text{cm}^2$ ),  $A$  the atomic weight,  $n$  the number of equivalents exchanged and  $\rho$  is the metal density in  $\text{gm}/\text{cm}^3$ . There are various assumptions made in the equation (12) which are listed below,

1. The reactions of the systems are reversible.
2. The corrosion reaction is controlled by the activation energy.
3. There is no change on the electrode surface during polarization.
4. Polarization is due to corrosion.

The energy barriers for the forward and reverse reactions are symmetrical.

## Tafel Extrapolation

The Tafel extrapolation method was introduced to illustrate the application of mixed potential theory. The Tafel extrapolation method uses a wider potential spectrum than linear polarization and hence provides more information. The linear polarization plot provides information about the corrosion rate, whereas the Tafel plot provides information about the corrosion rate as well as the kinetic data. The Tafel plot is carried out normally in a potential range of  $\pm 250\text{mV}$  from FCP. An idealized Tafel plot is shown in the Figure 18. The figure shows distinct anodic and cathodic polarization regions and the inflection point of the two curves gives the FCP. The linear region in the graph is extrapolated and the slopes of the linear regions are calculated. These are called as Tafel slopes. The linearity over which the Tafel slopes are calculated should have one decade of magnitude. A vertical line is drawn from the inflection point to the X-axis to give the

corrosion current (Figure 19). From the value of corrosion current the rate of corrosion can be calculated using equation 12. In certain cases, where dilute solutions are used, concentration polarization and ohmic resistance effects are likely at higher current densities. In such cases, Tafel extrapolation is carried out only in the cathodic region. The cathodic polarization slope is extrapolated and is allowed to intersect the corrosion potential  $E_{\text{corr}}$ . From this inflection point the corrosion current is calculated [203].

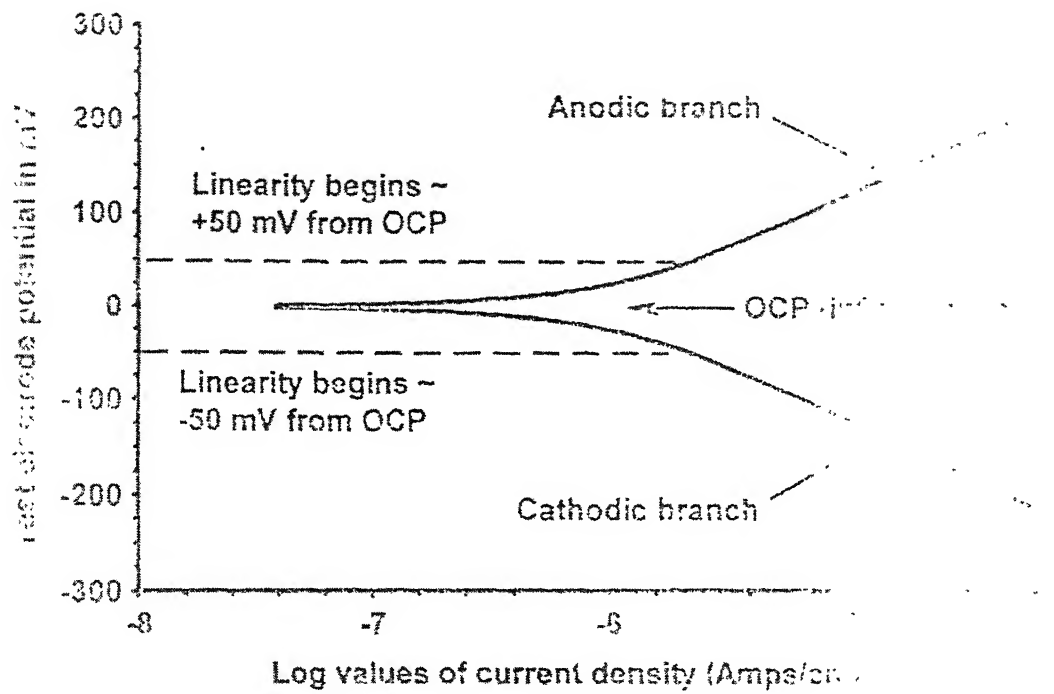


Figure 18: Tafel plot for activation controlled corrosion rates.

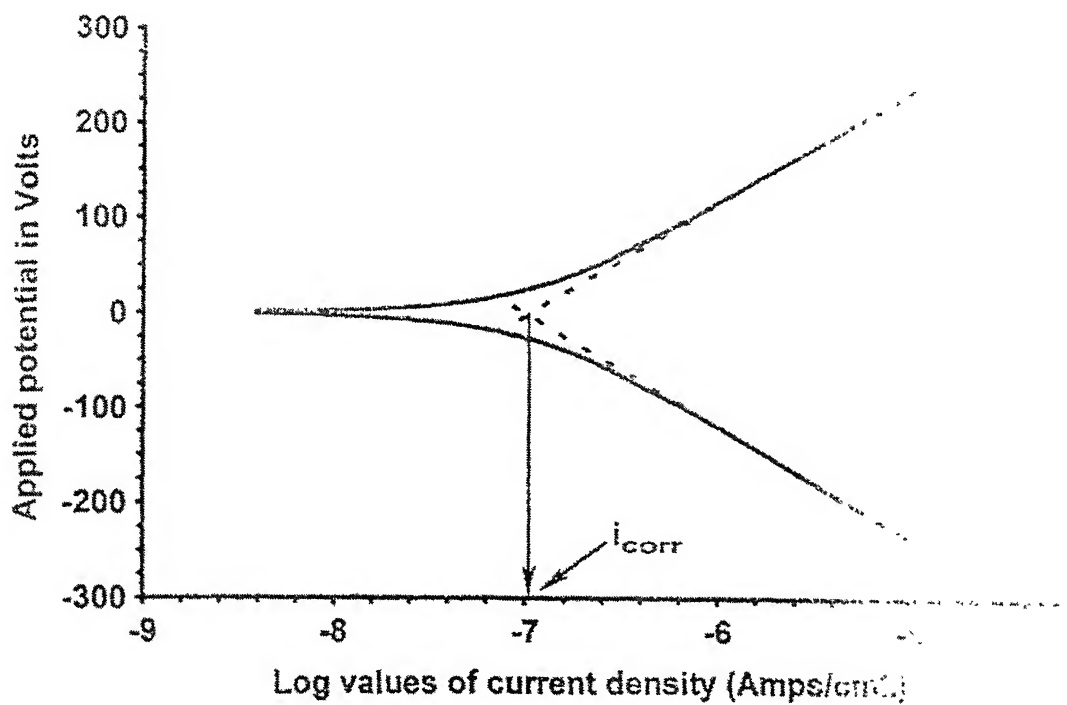


Figure 19: Corrosion current from activation controlled Tafel plots.

The main limitation of Tafel extrapolation when compared with the linear polarization is that the test electrode can be polarized only for a limited number of times. This is due to the surface roughening that takes place with each polarization. Moreover the Tafel plot cannot predict about the passive behavior of the system studied. It cannot be used for studying the localized corrosion behavior of the system [214].

Tafel slopes have units of Volts per current-density-decade, where a decade is one order of magnitude current density, such as from 0.10 amp/cm<sup>2</sup> to 1.0 amp/cm<sup>2</sup> in Figure 20.

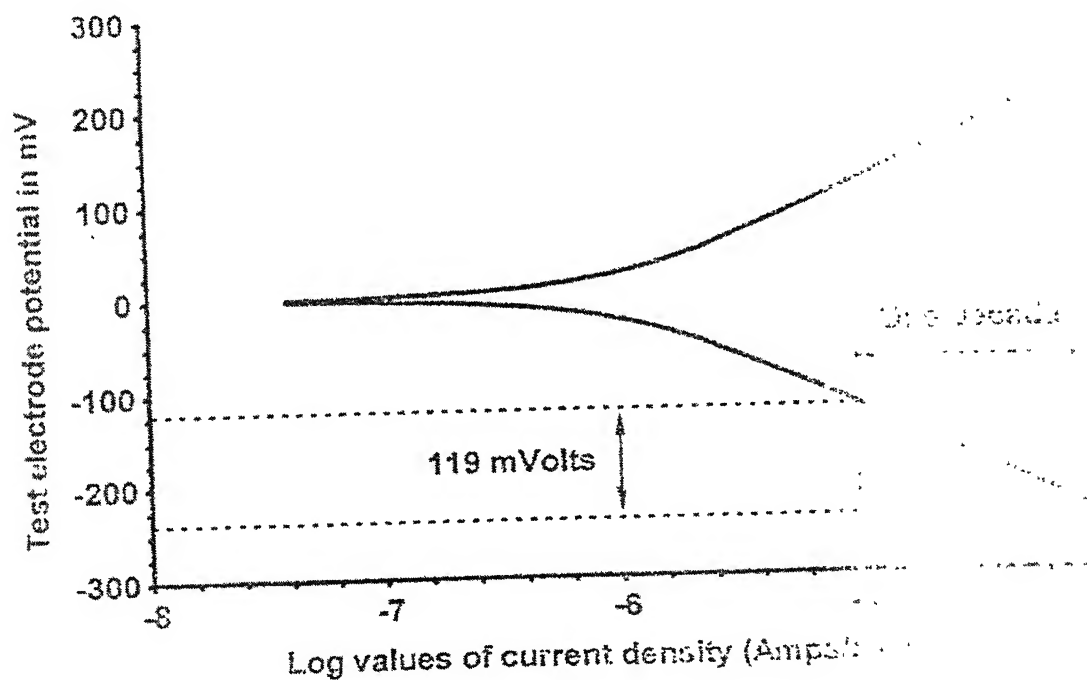


Figure 20: Determining Tafel slopes from Tafel plots.

## Potentiodynamic Polarization

The electrochemical behavior can also be understood from the potentiodynamic polarization curves [215]. The potentiodynamic polarization is carried out in a wider range of potential spectrum of  $-250$  mV to  $+1600$  mV from FCP and gives much more details about the sample's response to the environment. The potentiodynamic polarization provides data about the metal behavior i.e., whether the metal is active or passive or active passive in the given environment. The plot elucidates the properties of the passive film and the effect of inhibitors on the corrosion behavior of the metal. Depending upon the nature of potentiodynamic polarization curve, alloys can be divided into active alloys and active-passive alloys. For an active metal the corrosion rate increases linearly with increase in the anodic polarization potential. This is due to the non-protective oxide layer, which forms on the metal surface. For an active passive metal the corrosion rate increases with polarization potential up to a critical current density after which it falls down rapidly due to the formation of a protective passive film (Figure 21) [212]. The potentiodynamic polarization curve can be used for a quick evaluation of the material for application in a certain environment. The schematic diagram in Figure 22 shows the selection criterion of an alloy depending upon the nature of the environment. The figure shows four types of alloys and cathodic reactions corresponding to three environments. For a reducing atmosphere, as in 1, either the non-passivating alloy or the partially passivating alloy B is superior because they have better corrosion resistance in the active conditions. The alloys C and D produce strong passivity and hence alloying elements like chromium should be added. This makes the alloys more expensive and thus unjustifiable for the service condition [203]. For a moderately oxidizing atmosphere, number 2, the alloy C would be recommended because the reduction curve exceeds the critical current density and it is the only alloy showing stable passivity. In alloy B, the reduction curve exceeds critical current density, but the passive region is not broad enough to ensure good passive resistance. Alloy D is in a state of borderline passivity, with both active and passive states possible. For strong oxidizing condition in 3, alloy D is recommended as the reduction curve

exceeds critical current density and the corrosion rate is low. In alloy C, the passivity breaks in this condition and it is in the transpassive region. Alloys A and B are not resistant to high oxidizing conditions.

The main limitation of potentiodynamic polarization is that the sample surface gets disturbed after the experiment is completed. Hence the test can be conducted only once at a time. Moreover the exact corrosion rate cannot be predicted accurately by this method.

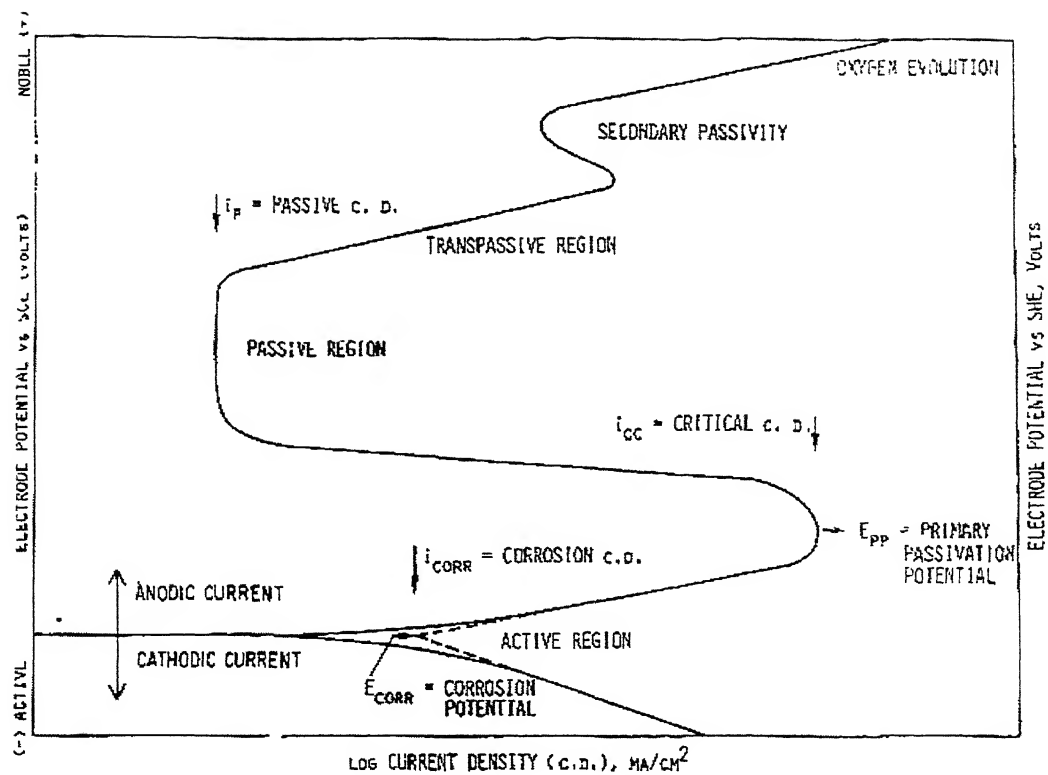


Figure 21: Potentiodynamic polarization plot for active-passive metal.

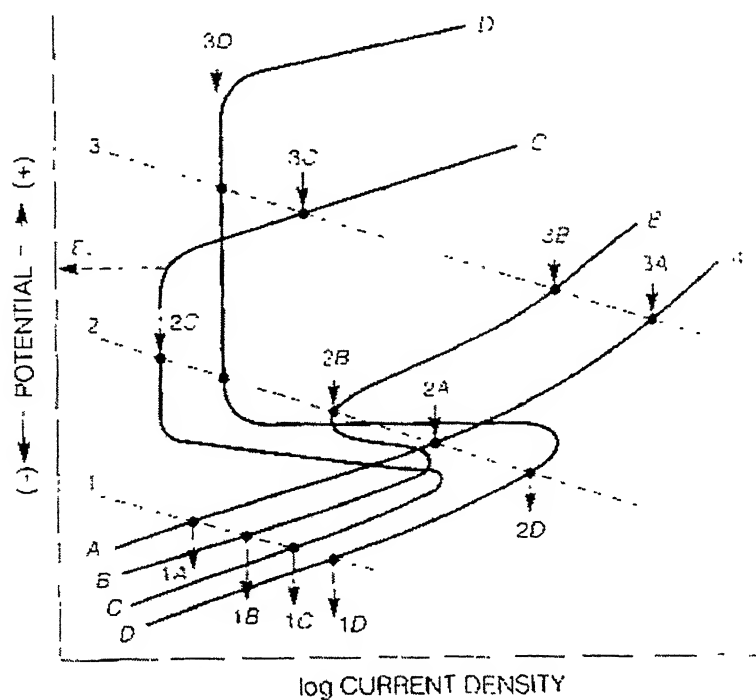


Figure 22: Schematic polarization diagrams illustrating the selection of alloy depending upon the nature of the environment.



## 2.5 Electrochemical Impedance Spectroscopy

### 2.5.1 Introduction

Electrochemical systems can be studied with the methods based on impedance measurements. These methods involve the application of a small voltage perturbation, whereas in the methods based on linear sweep or potential step the system is perturbed far from equilibrium. EIS voltages cycle from peak anodic to cathodic magnitudes (and vice versa) using a spectrum of alternating current (AC) voltage frequencies, instead of a range of single magnitude and polarity direct current (DC) voltages. Resistance and capacitance values are obtained from each frequency, and these quantities can provide information on corrosion behavior and rates, diffusion and coating properties. The passive films formed and the electrical double layer is supposed to offer resistance and capacitance to the circuit, whose values are determined from the EIS data. The comparison of these values for similar systems gives us some idea about the systems [216]. The corrosion rate of a metal in an electrolyte can be determined by AC techniques. These techniques are more or less explicitly based on the hypothesis that the impedance of the metal-electrolyte interface is equivalent to the polarization resistance,  $R_p$ , i.e. the slope of the steady-state current potential curve ( $R_p = dV/di$ )  $E = E_{\text{corr}}$ .  $R_p$  is inversely proportional to corrosion current density,  $i_{\text{corr}}$ , i.e. the current density which is proportional to the corrosion rate. For determination of  $R_p$ , a sinusoidal current or potential perturbation of very small amplitude (to ensure that the measurement is performed in the linear region of the system) is applied as a function of frequency.

### 2.5.2 AC Circuit Theory and Representation of Complex Impedance Values

Like resistance, impedance is a measure of the ability of a circuit to resist the flow of electrical current. Electrochemical impedance is usually measured by applying an AC potential to an electrochemical cell and measuring the current through the cell. The response to a sinusoidal potential excitation potential is an AC current signal, containing the excitation

frequency and its harmonics. Electrochemical impedance is normally measured using a small excitation signal [220]. This is done so that the cell's response is pseudo-linear. In a linear (or pseudo-linear) system, the current response to a sinusoidal potential is a sinusoid at the same frequency but shifted in phase (see Figure 23). The excitation signal, expressed as a function of time, has the form:

$$E(t) = E_0 \cos(\omega t) \quad \text{Eqn. 21}$$

$E(t)$  is the potential at time  $t$ ,  $E_0$  is the amplitude of the signal, and  $\omega$  is the radial frequency [217]. The relationship between radial frequency  $\omega$  (expressed in radians/second) and frequency  $f$  (expressed in hertz) is:

$$\omega = 2 \pi f \quad \text{Eqn. 22}$$

In a linear system, the response signal,  $I_t$ , is shifted in phase and has a different amplitude,  $I_0$ :

$$I(t) = I_0 \cos(\omega t - \phi) \quad \text{Eqn. 23}$$

An expression analogous to Ohm's Law allows us to calculate the impedance of the system as:

$$Z = \frac{E(t)}{I(t)} = \frac{E_0 \cos(\omega t)}{I_0 \cos(\omega t - \phi)} = Z_0 \frac{\cos(\omega t)}{\cos(\omega t - \phi)} \quad \text{Eqn. 24}$$

The impedance is therefore expressed in terms of a magnitude,  $Z_0$ , and a phase shift,  $\phi$ .

### 2.5.3 Data Presentation

The expression for impedance ( $Z$ ) is composed of a real and an imaginary part. If the real part is plotted on the Y-axis and the imaginary part on the X-axis of a chart, we get a "Nyquist plot" (see Figure 24). It can be noted, that in this plot the y-axis is negative and that each point on the Nyquist plot is the impedance at one frequency. Figure 24 is annotated to show that low frequency data are on the right side of the plot and higher frequencies are on the left [218]. This is true for EIS data where impedance usually falls as frequency rises (this is not true of all circuits). On the Nyquist plot, the impedance can be represented as a vector of length  $|Z|$ .

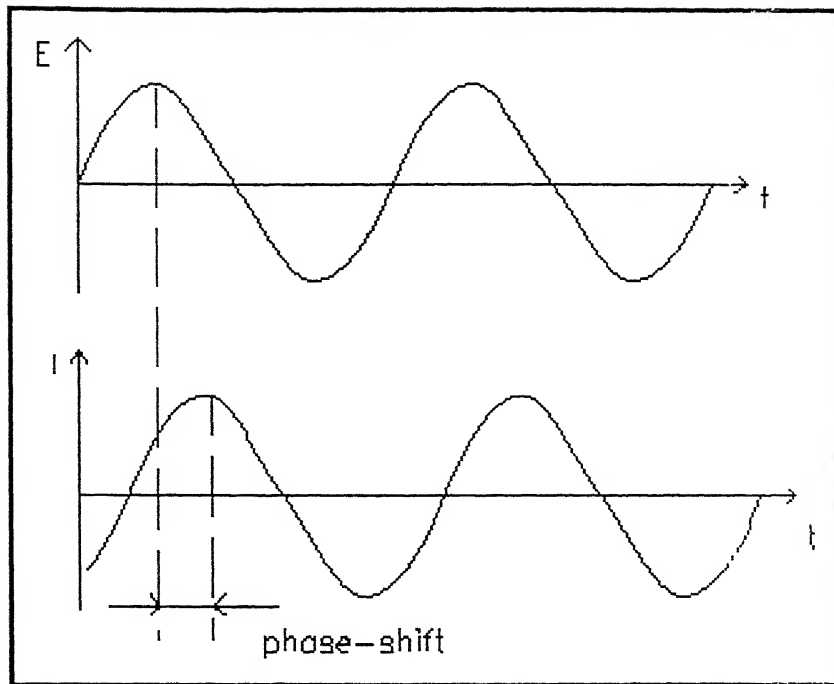


Figure 23: Sinusoidal Current Response in a Linear System.

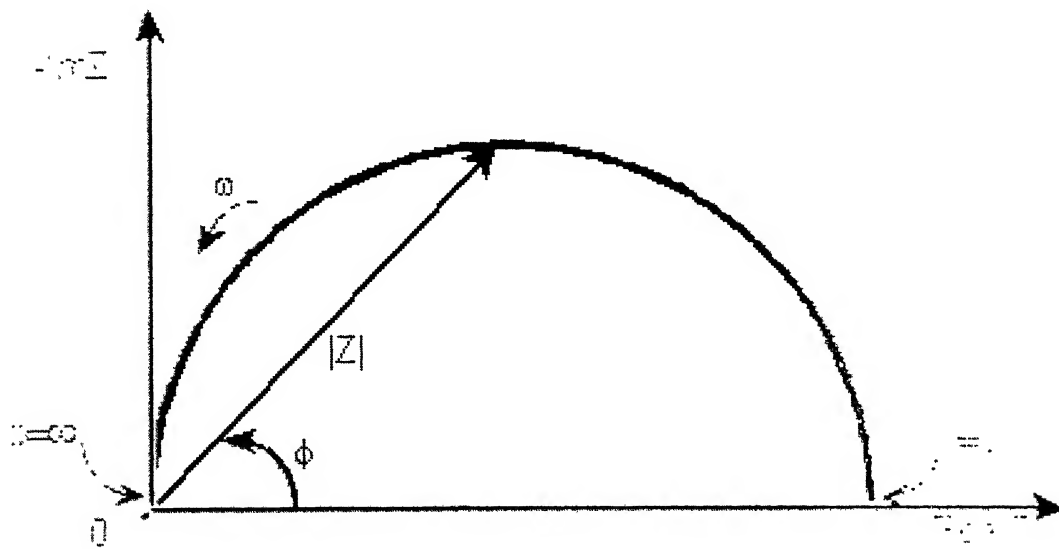


Figure 24: Nyquist Plot with Impedance Vector.

The angle between this vector and the x-axis is phase shift. However, Nyquist plots have one major shortcoming. It does not give the information about the frequency at which a data point is obtained. The Nyquist plot in Figure 24, results from the electrical circuit of Figure 25. The semicircle is characteristic of a single "time constant". Electrochemical Impedance plots often contain several time constants. Often only a portion of one or more of their semicircles is seen. Another popular presentation method is the Bode plot. The X-axis of a Bode magnitude plot contains log values of frequencies (base 10) and the Y-axis contains log values of the total impedance for each frequency. Locations for  $R_1$ ,  $R_2$  and capacitance reactance are also noted on the magnitude plot. Plot slope is zero when polarization is through resistances, and slope is less than zero when capacitive reactance becomes part of the circuit response to a polarization. Slope magnitude is determined by the ratio of  $R_2$  to  $R_1$ , and approaches -1 as the ratio increases. Bode phase plot contains log of frequency on the X-axis and the absolute value of the impedance ( $|Z| = Z_0$ ) on the Y-axis [218,219]. The Bode plot (both magnitude and phase) for the electric circuit of Figure 25 is shown in Figure 26. Unlike the Nyquist plot, the Bode plot explicitly shows frequency information.

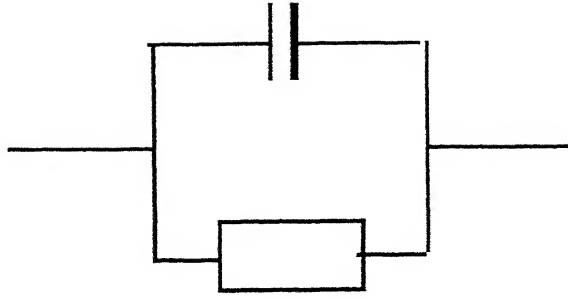


Figure 25: Simple Equivalent Circuit with One Time Constant

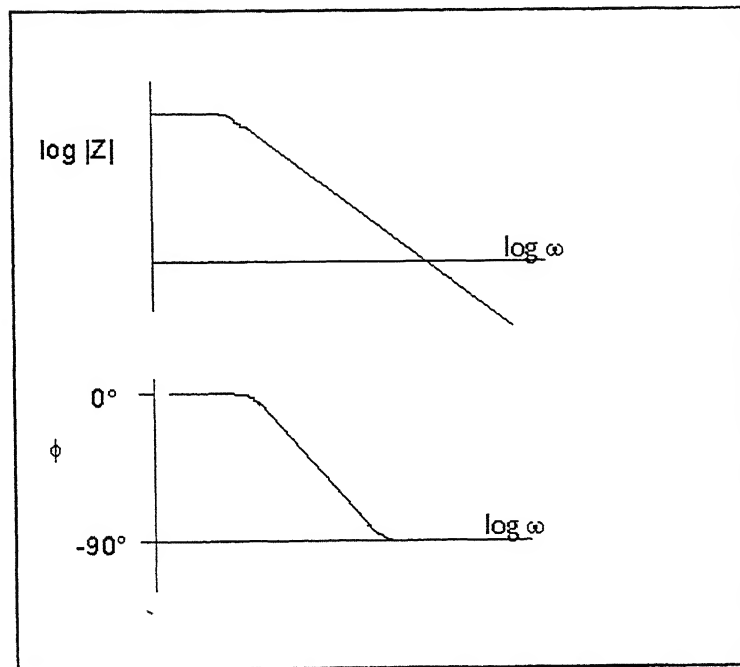


Figure 26: Bode plot with one time constant.

## 2.5.4 Physical Electrochemistry and Equivalent Circuit Elements

### Electrolyte Resistance

Solution resistance is often a significant factor in the impedance of an electrochemical cell. A modern 3 electrode potentiostat compensates for the solution resistance between the counter and reference electrodes. However, any solution resistance between the reference electrode and the working electrode must be considered when you the cell is modelled. The resistance of an ionic solution depends on the ionic concentration, type of ions, temperature and the geometry of the area in which current is carried. In a bounded area with area  $A$  and length  $l$  carrying a uniform current the resistance is defined as:

$$R = \rho \frac{l}{A} \quad \text{Eqn. 25}$$

where,  $\rho$  is the solution resistivity [221]. The conductivity of the solution ( $\kappa$ ) is more commonly used in solution resistance calculations. Its relationship with solution resistance is:

$$R = \frac{1}{\kappa} \frac{l}{A} \Rightarrow \kappa = \frac{l}{RA} \quad \text{Eqn. 26}$$

Unfortunately, most electrochemical cells do not have uniform current distribution through a definite electrolyte area. The major problem in calculating solution resistance therefore concerns determination of the current flow path and the geometry of the electrolyte that carries the current fortunately; solution resistance is not usually calculated from ionic conductance [221]. Instead, it is found when you fit a model is fit to experimental EIS data.

### Double Layer Capacitance

An electrical double layer exists at the interface between an electrode and its surrounding electrolyte. This double layer is formed as ions from the solution "stick on" the electrode surface. Charges in the electrode are separated from

the charges of these ions. The separation is very small, on the order of angstroms [222]. Charges separated by an insulator form a capacitor. The value of the double layer capacitance depends on many variables including electrode potential, temperature, ionic concentrations, types of ions, oxide layers, electrode roughness, impurity adsorption, etc.

## Polarization Resistance

Whenever the potential of an electrode is forced away from its value at open circuit, that is referred to as polarizing the electrode. When an electrode is polarized, it can cause current to flow via electrochemical reactions that occur at the electrode surface. The amount of current is controlled by the kinetics of the reactions and the diffusion of reactants both towards and away from the electrode. In cells where an electrode undergoes uniform corrosion at open circuit, the open circuit potential is controlled by the equilibrium between two different electrochemical reactions. One of the reactions generates cathodic current and the other anodic current. The open circuit potential ends up at the potential where the cathodic and anodic currents are equal. It is referred to as a mixed potential. The value of the current for either of the reactions is known as the corrosion current.

When there are two simple, kinetically controlled reactions occurring, the potential of the cell is related to the current by the following (known as the Butler-Volmer equation).

$$I = I_{corr} \left( 10^{\frac{2303(E-E_{oc})}{\beta_a}} - 10^{\frac{-2303(E-E_{oc})}{\beta_c}} \right) \quad \text{Eqn. 27}$$

where,

$I$  is the measured cell current in amps,

$I_{corr}$  is the corrosion current in amps,

$E_{oc}$  is the open circuit potential in volts,

$\beta_a$  is the anodic Beta coefficient in volts/decade,

$\beta_c$  is the cathodic Beta coefficient in volts/decade.

If a small signal approximation ( $E - E_{oc}$  is small) is applied to then following expression for  $I_{corr}$ , which is indicative of corrosion rate, is obtained:

$$I_{corr} = \frac{R_a^0 R_c^0}{2303 (R_a^0 + R_c^0)} \left( \frac{1}{R_p} \right) \quad \text{Eqn. 28}$$

This introduces a new parameter,  $R_p$ , the polarization resistance. The polarization resistance behaves like a resistor. From the above equation it is visible that  $I_{corr}$  is inversely proportional to  $R_p$ .

### Charge Transfer Resistance

A similar resistance is formed by a single kinetically controlled electrochemical reaction. In this case we do not have a mixed potential, but rather a single reaction at equilibrium. Consider a metal substrate in contact with an electrolyte. The metal molecules can electrolytically dissolve into the electrolyte, according to:



or more generally:



In the forward reaction in the first equation, electrons enter the metal and metal ions diffuse into the electrolyte. Charge is being transferred. This charge transfer reaction has a certain speed. The speed depends on the kind of reaction, the temperature, the concentration of the reaction products and the potential. The general relation between the potential and the current is:

$$i = i_0 \left[ \frac{C_o}{C_o^*} e^{\left( \frac{\alpha n F \eta}{RT} \right)} - \frac{C_R}{C_R^*} e^{\frac{-(1-\alpha)n F \eta}{RT}} \right] \quad \text{Eqn. 31}$$

with,

$i_0$  = exchange current density

$C_o$  = concentration of oxidant at the electrode surface

$C_o^*$  = concentration of oxidant in the bulk (*delete the spaces*)

$C_R$  = concentration of reductant at the electrode surface

$F$  = Faradays constant



T = temperature

R = gas constant

$\alpha$  = reaction order

n = number of electrons involved

$\eta$  = over potential (  $E - E_0$  )

The over potential,  $\eta$ , measures the degree of polarization. It is the electrode potential minus the equilibrium potential for the reaction. When the concentration in the bulk is the same as at the electrode surface,  $C_o=C_o^*$  and  $C_R=C_R^*$ . This simplifies the above equation into:

$$i = i_0 \left[ e^{\alpha \frac{nF}{RT} \eta} - e^{-(1-\alpha) \frac{nF}{RT} \eta} \right] \quad \text{Eqn. 32}$$

This equation is called the Butler-Volmer equation. It is applicable when the polarization depends only on the charge transfer kinetics. Stirring will minimize diffusion effects and keep the assumptions of  $C_o=C_o^*$  and  $C_R=C_R^*$  valid. When the over potential,  $\eta$ , is very small and the electrochemical system is at equilibrium, the expression for the charge transfer resistance changes into:

$$R_{ct} = \frac{RT}{n F i_0} \quad \text{Eqn. 33}$$

From this equation the exchange current density can be calculated when  $R_{ct}$  is known.

## Diffusion

Diffusion can create impedance known as the Warburg impedance. This impedance depends on the frequency of the potential perturbation. At high frequencies the Warburg impedance is small since diffusing reactants don't have to move very far. At low frequencies the reactants have to diffuse farther, thereby increasing the Warburg impedance. This form of the Warburg impedance is only valid if the diffusion layer has an infinite thickness. Quite often this is not the case. If the diffusion layer is bounded, the impedance at lower frequencies no longer obeys the equation above

## Coating Capacitance

A capacitor is formed when two conducting plates are separated by a non-conducting media, called the dielectric [223]. The value of the capacitance depends on the size of the plates, the distance between the plates and the properties of the dielectric. The relationship is:

$$C = \frac{\epsilon_0 \epsilon_r A}{d}$$
Eqn. 34

With,

$\epsilon_0$  = electrical permittivity

$\epsilon_r$  = relative electrical permittivity

A = surface of one plate

d = distances between two plates

## Virtual Inductor

The impedance of an electrochemical cell can also appear to be inductive. Some authors have ascribed inductive behavior to adsorbed reactants [217]. Both the adsorption process and the electrochemical reaction are potential dependent. The net result of these dependencies can be an inductive phase shift in the cell current. Inductive behavior can also result from nonhomogeneous current distribution, cell lead inductance and potentiostat non-idealities. In these cases, it represents an error in the EIS measurement.

## Chapter 3

### EXPERIMENTAL PROCEDURE

#### 3.1 Materials

The materials used in the present research were the following. All the compositions are provided in weight %.

- **Commercial Pure Titanium**
- **Ti-6Al-4V**
- **Ti-13Nb-13Zr**
- **Ti-5Al-2.5Fe**
- **Ti-6Al-4Fe**
- **Ti-6Al-4Nb**
- **Ti-8.4Al-15.4Nb**
- **Ti-13.4Al-29Nb**

The titanium alloys (CP Titanium, Ti-6Al-4V, Ti-13Nb-13Zr, Ti-5Al-2.5Fe, Ti-6Al-4Fe, Ti-6Al-4Nb, Ti-8.4Al-15.4Nb, and Ti-13.4Al-29Nb) used in present study were obtained from Defense Metallurgical Research Laboratory (DMRL), Hyderabad, India. The compositions of the alloys (as received) mentioned above are in weight % and they are nominal compositions provided by the supplier. Ti-6Al-4Fe, Ti-6Al-4Nb, Ti-5Al-2.5Fe and Ti-13Nb-13Zr were received in pancake form whereas CP titanium, Ti-6Al-4V, Ti-8.4Al-15.4Nb and Ti-13.4Al-29Nb were in rolled sheet form. Thickness of CP titanium, Ti-8.4Al-15.4Nb and Ti-13.4Al-29Nb sheets was 2 cm and thickness of Ti-6Al-4V sheet was 1cm.

##### 3.1.1 Preparation of Pancakes

The pancake melts were taken in a water-cooled Cu crucible under partial pressure of high purity Argon gas. The necessary charge was weighed

and placed in the copper crucible and evacuated to a vacuum level of  $10^{-3}$  milibar. It was then purged with Argon and then filled with argon and melted in a Lebold Hereaus furnace in the non-consumable mode of melting. The arc was struck between a tungsten electrode and the charge material. The voltage was around 30 volts and the current varied from 800 to 1000 Amps. There was a stirring coil around the crucible which stirred the molten pool for mixing. Each pancake was melted four times. It was taken out and placed upside down after each melt. The details of charge for the alloys Ti-6Al-4Fe, Ti-6Al-4Nb, Ti-5Al-2.5Fe and Ti-13Nb-13Zr alloys are provided in Table 9. The composition and source of metal used for making the pancakes are provided in Table 10.

S.No	Composition	Elements
1	Ti-6Al-4Fe – for 600g pancake	Ti = 540g Al = 36g Fe = 24g (Armco iron)
2	Ti-6Al-4Nb – for 600 g pancake	Ti = 540g Al = 36g Nb = 24g
3	Ti-5Al-2.5Fe – for 600g pancake	Ti = 555g Al shots = 30g Fe = 15g
4	Ti-13Zr-13Nb-for 600g pancake	Ti = 444g Nb Powder = 78g Zr sponge = 78g

Table 9: Charge of different metals used to produce the pancake of desired composition.

Elements	Composition	Company
Ti	Cl 0.068, Fe 0.012, O 0.029, Si 0.003, Ni 0.010, C 0.005, N 0.008	Avisma Titanium Magnesium Works, Berezniki, Russia
Al	Si 0.15, O 0.01, N 0.02, C 0.01, Zn 0.07, Cu 0.02, Fe 0.15	Madanlal & Sons Calcutta, India
Fe	C 0.004, Mn, Si, Ti & Cu <0.02, P<0.01, S0.03, N0.02, O 0.013	Armco iron
Nb	<b>All in ppm</b> H < 10, N <50, O 2000, C 45, Al < 10, Fe 35, Si < 10, Ta 200,	New Metals & Chemicals Ltd. Abbey Chambers, Highbridge Street, Waltham Abbey, ESSEX EN9 1DF
Zr	<b>All in ppm</b> Al 200, B 1.0, C 500, Cd 1.0, Cl 1500, Co 20, Cr 500, Cu 100, Fe 5000, Hf 100, Mg 600, Mn 200, Mo 50, N 250, Ni 100, O 1000, Pb 100, Si 150, Sn 100, U 3.5, V 50, W 50	NFC Hyderabad, India

Table 10: Composition of elements used in making the pancakes.

## 3.2 Sample Preparation

### 3.2.1 Sample preparation for electrochemical studies

Specimens for electrochemical studies were cut from the received material samples using a diamond cutter (Buehler-ISOMET). The areas to be exposed for electrochemical studies were in the form a square shape of 1 cm x 1 cm. Thickness of most of the samples was around 0.5 cm. The schematic of the Figure 27 shows how the samples were obtained for the electrochemical study. The samples from the pancake were cut from the portion towards the center and top surface was mounted for the experimental study as shown in the Figure 27.

A covered wire lead was attached to the back of the specimen by soldering with the help of a small amount of conducting paste. Following this, each specimen was cold mounted into a thermosetting liquid and powder in the shape of a 3 cm. diameter rod and height of about 3 cm. The time duration taken by the mixture of thermosetting liquid and powder to dry and harden was two hours. The cold mounted specimen was then polished up to 4/0 finish on emery paper and then polished using 0.5 $\mu$  alumina powder. The specimens were than washed with distilled water followed by ultrasonic cleaning with acetone. All this procedure was followed prior to each electrochemical experiment.

### 3.3.2 Samples for Material Characterization

The samples used for material characterization were cut in the same manner as was used in preparing samples for electrochemical testing. However, cold mounting procedure was not applied here. The samples, on which electrochemical tests were performed, were polished and used for taking the optical micrographs.

### 3.3.3 Samples for Mechanical Testing

Two tensile test samples were obtained from the pancakes of Ti-6Al-4Nb and Ti-6Al-4Fe alloys. Figure 27 shows the manner in which samples were cut from the pancake. Tensile test samples were polished carefully so that no scratch whatsoever was there on the gauge length of the samples. These scratches could initiate crack growth leading to early failure of the samples.

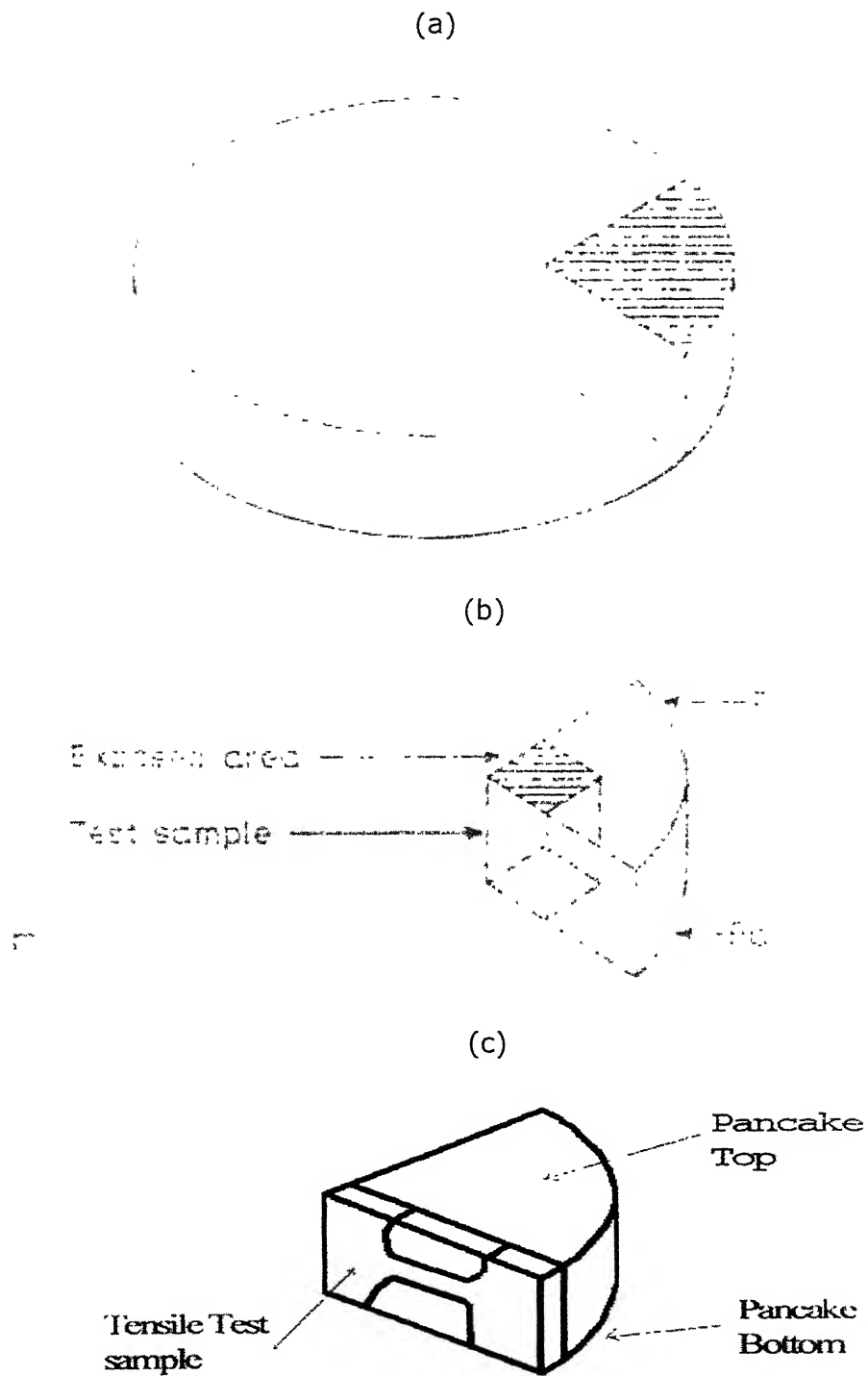


Figure 27: Basic diagram showing (a) Pancake, (b) samples taken out from the Pancake for Electrochemical study and (c) samples taken out for tensile tests.



### 3.3 Electrochemical Studies

The apparatus used for electrochemical experiments were a polarization cell and a potentiostat interfaced to a personal computer. The potentiostats used in the study were capable of performing electrochemical impedance spectroscopy and a wide variety of potentiostatic and galvanostatic functions required for basic and applied studies in the field of corrosion. The schematic of a potentiostat connected with the electrochemical cell is shown in Figure 28. The potentiostat consists of an ammeter, an electrometer and a power supply. Three probes from the potentiostat were connected to the working electrode, reference electrode and counter electrode. The fourth probe was grounded.

The electrochemical studies were carried out in the potentiostat Model 263A supplied by EG&G Instruments Inc., Princeton Applied Research, USA. Electrochemical Impedance Spectroscopy experiments were carried out in the potentiostat Model Parstat 2263, supplied by the same supplier. Potentiostat Model Parstat 2263 was very sensitive for EIS measurements. It can provide a frequency range of 1  $\mu$ Hz-1MHz. The electrolyte used for testing was Hank's solution, prepared in the laboratory from laboratory grade chemicals.

#### 3.3.1 Cell Design

The working cells for the potentiostat can be of two types, the flat cell and the round cell. The flat cell can be used for testing flat samples and can only be used when the surface of the sample is flat. The round cell can be used for any sample and usually the samples are mounted before using in the round cell. The round bottom cell was used in the current investigation.

The schematic representation of the round bottom cell is shown in Figure 29. Graphite was used as the counter electrode. The potential of the working electrode was measured against saturated calomel electrode (SCE), inserted into the Luggin capillary. The potential of the reference SCE was +242 mV with respect to standard hydrogen electrode (SHE). The Luggin

probe was adjusted so that its tip was consistently as close to the working electrode as possible. It is well known that the portion of the electrolyte between the working electrode and the capillary tip of the reference electrode also contributes towards the electrical resistance. Since resistance is a function of the distance between the electrodes, better accountability was achieved by keeping the gap as small as possible to minimize the resistance.

All the long term experiments were carried out in a specially designed electrochemical cell. The schematic representations of the cell are shown in Figure 30. This cell consists of a cylindrical flask (diameter of 8.5 cm and height of 11.5 cm) with a cover on top, which had provisions in the form of circular openings of different sizes to permit the introduction of various electrodes.

The polarization experiments in this investigation were conducted using mounted samples in the round cell and this cell was placed in a bath prepared specially to maintain a constant temperature of 37°C (human body temperature) during the experiments. The constant temperature bath was fabricated as follows. Two stainless steel pots were brazed together in a manner so as to have a minimum spacing of 1.5 cm between the walls of the pots. Inner pot had the diameter of 16.5 cm and height of 9.5 cm. the diameter of outer pot was 20.5 cm and height was 11 cm. inlet and outlet was also made in the outer pot by cutting a small hole and welding small brass tubes at these holes. This double walled stainless steel pot was insulated from outside using glass wool and thermocol. The schematic of the bath is given in the Figure 31. The inlet and outlet of the bath were connected to a JULABO, temperature control bath (Model MW, Germany), which controls the temperature of liquid flowing between the walls. Variation in the temperature of fluid circulated by it was less than 0.1°C. Distilled water was poured in the bath and the round bottom cell was placed in this. This multilayered system of heat flow kept the temperature of electrolyte constant and undisturbed from undesired external disturbances. This apparatus worked efficiently to keep the desired electrolyte temperature.

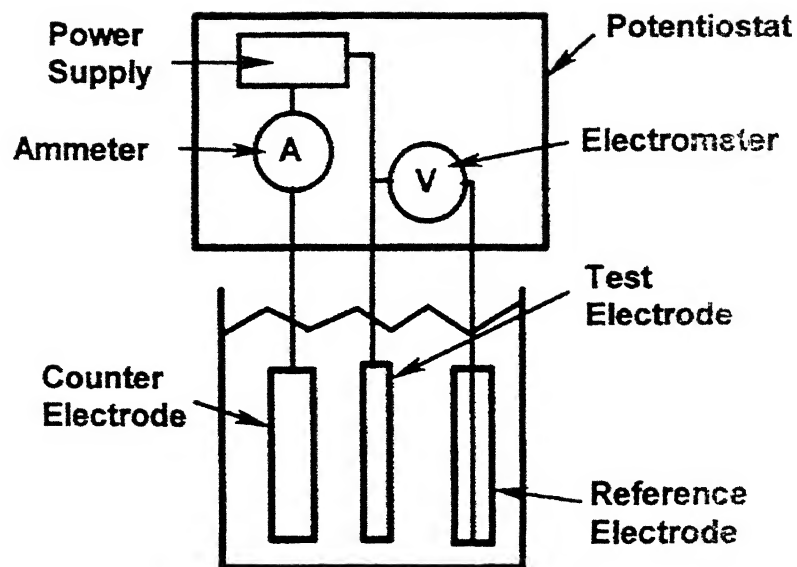


Figure 28: The basic diagram of a potentiostat connected with the working cell.

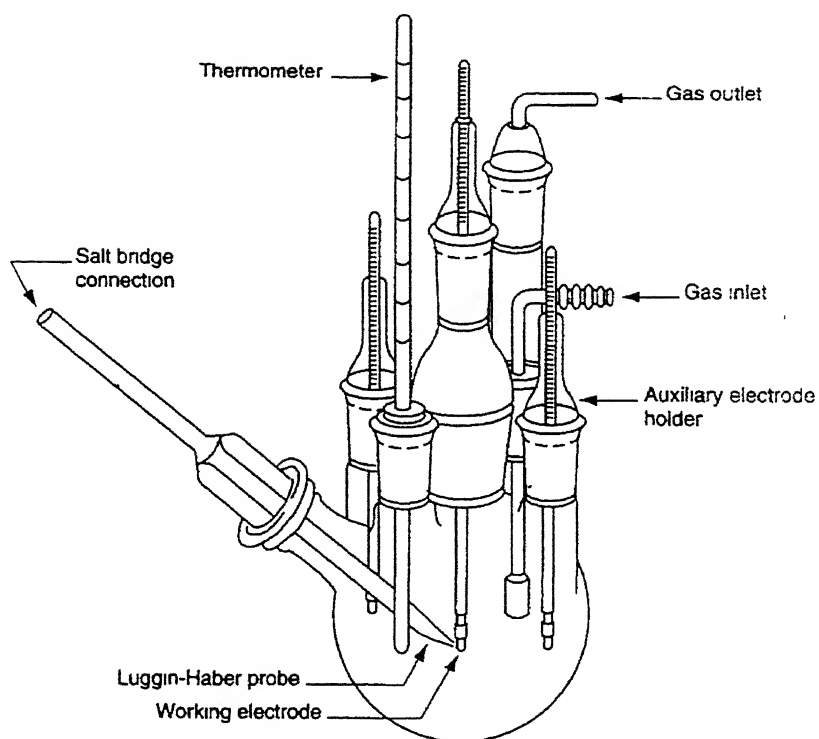


Figure 29: Schematic representation of round bottom Cell.

### 3.3.2 Solution Preparation

The composition of Hank's solution used in the electrochemical study is provided in Table 5. The medium used for preparation of the body fluid solution (Hank's solution) was double distilled water. In order to achieve full dissolution of the chemicals in the medium, addition of NaCl, KCl, CaCl<sub>2</sub>, NaH<sub>2</sub>PO<sub>4</sub>·2H<sub>2</sub>O and NaHCO<sub>3</sub> were performed after the other chemicals (MgSO<sub>4</sub>·7H<sub>2</sub>O, Glucose, KH<sub>2</sub>PO<sub>4</sub> and MgCl<sub>2</sub>·6H<sub>2</sub>O) were completely dissolved. Continuous stirring with the help of magnetic stirrer (model Remi 2 LH) aided dissolution. A slight temperature of about 30°C was also applied to achieve full dissolution of chemicals. The pH of the solution was precisely maintained at 7.4 and strictly checked every time after the solution preparation using a calibrated pH meter (Ecoscan, Eutech Instruments, Singapore). Freshly prepared Hank's solution was used for each experiment.

Three alloys, CP Titanium, Ti-6Al-4V and Ti-13Nb-13Zr, were treated with 5M NaOH at 60°C temperature for 24 Hrs. The 5M NaOH solution was prepared by dissolving laboratory-grade 200gms NaOH crystals in 1 litre distilled water. The temperature of 60°C of the NaOH solution was also kept constant using the constant temperature bath prepared in this research.

### 3.3.3 Tafel Extrapolation Experiments

Tafel extrapolation experiments were conducted from  $\pm 250$  mV from free corrosion potential (FCP), which is also called as  $E_{\text{corr}}$ . The FCP was stabilized before conducting each Tafel experiment. The scan rate used for Tafel experiments was 0.166 mV/s, as per ASTM standard [224]. The linear portion of the cathodic polarization line was extrapolated to meet the horizontal line drawn from zero current potential value, and from the point of intersection of the two lines the anodic slope was extrapolated. The corrosion rate was also obtained by this method. This methodology was adopted as the alloy exhibited stable passive behavior, and therefore well-defined Tafel slopes were not observed in anodic Tafel plot. The anodic slopes obtained for

the alloys were very high due to the stable passive nature. The slopes  $\beta_a$ ,  $\beta_c$ , and  $i_{corr}$  were calculated using the Tafel curves obtained. Duplicate tests were performed and in some cases, triplicate experiments were performed, especially if the duplicate result was markedly different from the original result.

### 3.3.4 Potentiodynamic Polarization Experiments

The potentiodynamic polarization experiments were carried out in the potential range of -250 mV to +1600 mV w.r.t free corrosion potential for all the samples after stabilizing  $E_{corr}$ .  $E_{corr}$  was stabilized prior to all experiments. The potentiodynamic polarization experiments were carried out at a scan rate of 1 mV/s. The passivation parameters like breakdown potential ( $E_b$ ), corrosion current density ( $i_{corr}$ ), passive current density ( $i_{pass}$ ) and passivation range ( $E_b$ -ZCP) were estimated from the potentiodynamic polarization curves. Duplicate tests were performed in all cases. Potentiodynamic polarization studies were conducted on all samples after 1 hr of immersion in Hank's solution and also after 168 hrs of immersion in Hank's solution. NaOH treated samples were also tested after 1 hr of immersion in Hank's solution and also after 168 hrs of immersion in Hank's solution.

### 3.3.5 Electrochemical Impedance spectroscopy

The EIS experiments were conducted using a potentiostat Model Parstat 2263 supplied by EG&G Instruments Inc., Princeton Applied Research, USA. The EIS experiments were controlled using a computer and the data were collected using PowerSuite- 2.35.2 Software and analysed by ZsimpWin Version 3.00 Software. EIS measurements were performed by applying a sinusoidal potential perturbation of 10 mV at the open circuit potentials. The impedance spectra were measured with frequency sweep from 100 kHz to 10 mHz in logarithmic increment. Total number of 36 points

was recorded for each experiment. Corrosion processes often involve slow aqueous diffusion process, which generally have relatively large time constants (on the order of 0.1 to 10 seconds). Therefore, most impedance studies of corroding systems use frequencies between a few mHz and 10 kHz (imp\_book). All the data were copied and plotted again using software Origin6.0. The impedance data was analyzed using software ZSimpWin. Different parameters obtained from the best fit equivalent circuit were tabulated and analyzed.

EIS study was performed on all the materials used in the present study after 1 hr, 24 hrs, 72 hrs and 168 hrs of immersion in Hank's solution. To take the impedance spectra counter electrode and reference electrode were inserted in the cell used for long term immersion tests. After taking the impedance spectra all the connections, reference and counter electrode were taken out and the metal was allowed to remain in the solution. Same procedure was also employed for NaOH-treated samples (CP Titanium, Ti-6Al-4V and Ti-13Nb-13Zr alloy).

### 3.4 Material Characterization

#### 3.4.1 Microstructural Characterization

The specimen surfaces used in the polarization study was microstructurally characterized after electrochemical testing. The surface of the mounted specimens was polished with 2/0, 3/0 and 4/0 emery papers and then mechanically wheel polished in fine cloth using 0.5 $\mu$  alumina powder. They were then degreased using acetone before etching. The etching was done by immersing the samples in 10% HF and 5% HNO<sub>3</sub> (rest distilled water) etching reagent for 5 to 10 seconds at room temperature. The etching time and amount of etchant needed was different for all the samples. Etching of the samples could not be done in a single step. A slight variation in etchings time of about 2-3 seconds caused over etching of samples and

samples had to be prepared again for etching. In the special cases for Ti-6Al-4V, Ti-8.4Al-15.4Nb and Ti-13.4Al-29Nb, the etchant had to be diluted with the addition of few drops of doubled distilled water, and this solution provided better etching of these samples.

The microstructures were recorded using an optical microscope (Axiolab A, Zeiss, Germany), attached with a digital camera (CE, Japan). They were later analyzed in an image-analysis program (Image-Pro Plus, version 4.1, Media Cybernetics, USA).

### 3.4.2 Tensile Test

In order to understand the effect of replacement of V by Fe and Nb on mechanical properties, tensile tests were performed on Ti-6Al-4Nb and Ti-6Al-4Fe alloys. Two tensile test samples were fabricated for each of the alloys. Schematic given in Figure 27(c) shows the location of these samples within the pancake received for these alloys. Tensile tests were conducted using Universal Testing Machine (Instron, Model 1195, U.K). The full scale load was 20 KN and crosshead speed was 0.5 mm/min. Fractured surfaces were observed using Scanning electron microscope.

### 3.4.3 Scanning Electron Microscopy

Scanning electron micrographs were obtained in a scanning electron microscope (SEM) (JEOL JSM 840A). The fracture surfaces were studied in the native condition. The non-conducting coatings cause charging problem in SEM. This not only gives bad resolution but also is harmful for the equipment. The NaOH treatment and also subsequent immersion in Hank's solution produced some type of non conducting layer on the metal surface. Hence, these samples were coated with a conductive material. The samples were placed in an evacuated chamber, where Au-Pd vapors deposited on the samples to give a very thin uniform coating of Au-Pd. This coating was used

because it has no structure of its own and also provide good electrical conductance.

#### 3.4.4 X-Ray Diffraction

X-ray diffraction (XRD) patterns from the surface of CP Titanium, Ti-6Al-4V and Ti-13Nb-13Zr, without any treatment, after NaOH treatment, after NaOH treatment and dipped in Hank's solution for 1 week. They were recorded in a Rich-Siefert 2002 X-Ray diffractometer using  $\text{CuK}\alpha$  radiation. In all the experiments, the scan rate was fixed at  $3^\circ/\text{min}$  and the chart speed was fixed at  $3\text{cm}/\text{sec}$ . The patterns were obtained between an angle of  $20^\circ$  to  $90^\circ$ . A magnification of 5K was also used in all the readings. The data was analyzed using the software Diffrac Plus.



## Chapter 4

---

### RESULTS AND DISCUSSIONS

The results obtained in the present study are first outlined and this is followed by a discussion of the results.

#### 4.1 Tafel Extrapolation

All the experiments were conducted after stabilization of free corrosion potential. The variation of free corrosion potential ( $E_{\text{corr}}$ ) versus time for CP Titanium, Ti-6Al-4V and Ti-13Nb-13Zr alloys are presented in Figure 32. Figure 33 contains the same data for Ti-5Al-2.5Fe and Ti-6Al-4Fe alloys. The variation of free corrosion potential ( $E_{\text{corr}}$ ) versus time for Ti-6Al-4Nb, Ti-8.4Al-15.4Nb and Ti-13.4Al-29Nb alloys are provided in Figure 34. A comparative data of free corrosion potential ( $E_{\text{corr}}$ ) versus time for Ti-6Al-4Nb, Ti-6Al-4V and Ti-6Al-4Fe alloys are also shown in Figure 35. All the experiments were duplicated so as to ensure reproducibility of test results. The original as well as duplicated curves of  $E_{\text{corr}}$  vs. time are presented in Appendix A.

$E_{\text{corr}}$  versus time data for all the alloys used in the study revealed similar nature of the curve (Figure 32-35). The free corrosion potential for all the alloys increased uniformly with time. Pankuch et al. studied characteristics of passive film on titanium alloys and reported that a thin film of  $\text{TiO}_2$  forms on titanium surfaces on immersion in aqueous solutions [225]. Thus, increase in free corrosion potential with immersion time in Hank's solution can be attributed to formation of a passive  $\text{TiO}_2$  film on Ti alloys. The rise of potential in the positive direction (i.e. towards the noble direction) also indicated the formation of passive film. It has been argued that a steady

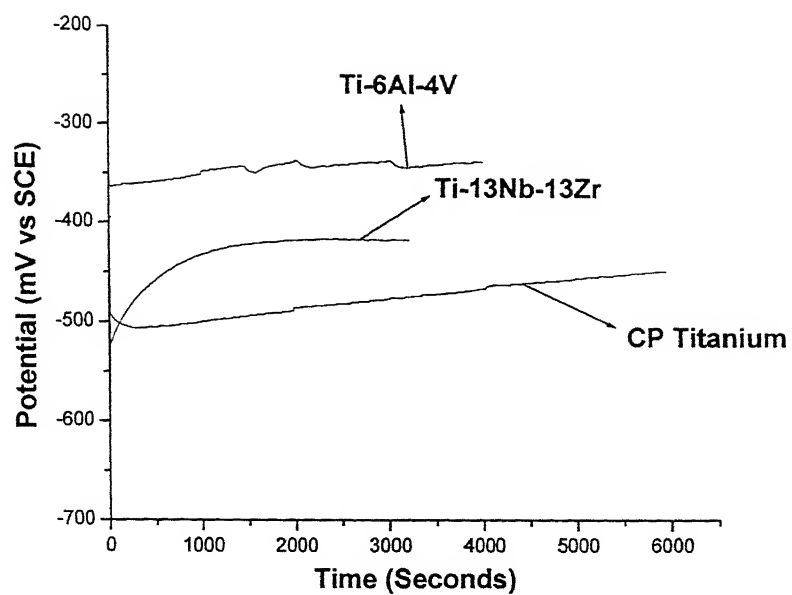


Figure 32: Free corrosion potential as function of time for CP Titanium, Ti-6Al-4V and Ti-13Nb-13Zr in Hank's solution at 37°C temperature and 7.4 pH.

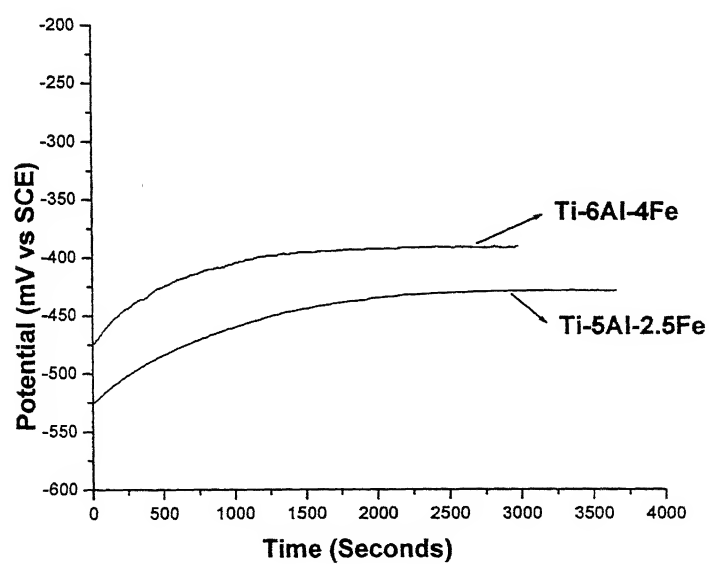


Figure 33: Free corrosion potential as function of time for Ti-5Al-2.5Fe and Ti-6Al-4Fe alloys in Hank's solution at 37°C temperature and 7.4 pH.

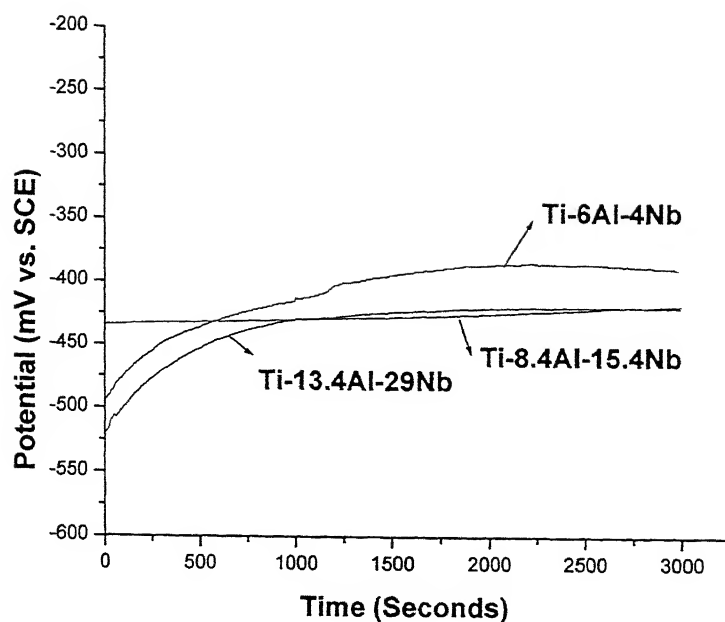


Figure 34: Free corrosion potential as function of time for Ti-6Al-4Nb, Ti-8.4Al-15.4Nb and Ti-13.4Al-29Nb in Hank's solution at 37°C temperature and 7.4 pH.

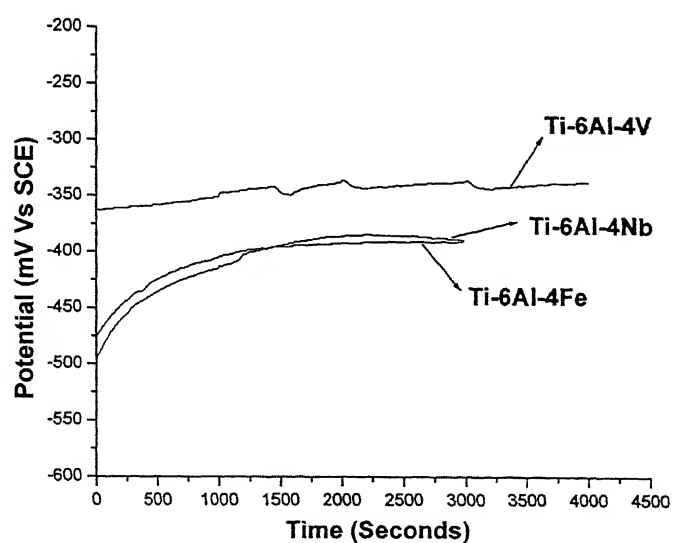


Figure 35: Free corrosion potential as function of time for Ti-6Al-4Nb, Ti-6Al-4V and Ti-6Al-4Fe in Hank's solution at 37°C temperature and 7.4 pH.

noble potential indicated that the film remained intact and protective [95]. It can be observed that free corrosion potential for all the alloys used in the study was stabilized in about 1 hr. Thus, all the subsequent experiments were conducted after 1hr of immersion in Hank's solution.

The Tafel polarization curves for all the Ti-based alloys are presented in Figures 36, 37, 38 and 39 in the same pattern as was used to present free corrosion potential ( $E_{\text{corr}}$ ) versus time data. For example, Figure 36 shows the Tafel polarization curves for CP Titanium, Ti-6Al-4V and Ti-13Nb-13Zr. All the experiments were duplicated so as to ensure reproducibility of test results. The original as well as duplicated curves of Tafel extrapolation data for all the alloys used in the study are presented in appendix A and estimated corrosion data and electrochemical parameters ( $\beta_a$  and  $\beta_c$ ) from these curves are tabulated in Appendix B.

Tafel slopes  $\beta_c$  (cathodic Tafel slope) and  $\beta_a$  (anodic Tafel slope) possess units of mV per current density decade, where a decade is one order of magnitude current density such as from 0.10 amp/cm<sup>2</sup> to 1.0 amp/cm<sup>2</sup>. Corrosion current density for activation controlled Tafel plot was obtained from the intersection of the anodic and cathodic linear extrapolations at zero current potential. It can be noted from the Tafel plots that, generally, the cathodic portion of the Tafel slopes exhibited linearity in the curve, whereas such well-defined linear portion could not be ascertained in the anodic portion due to stable passivity behavior exhibited by the samples in the solution. The cathodic Tafel slopes ranged between 150 and 301 mV/decade while the anodic Tafel slopes were also of the same order. The extrapolated corrosion current densities are provided in Table 11. The corrosion current densities were converted to corrosion rates in mpy (mils per year) using Equation (). Corrosion rates for all the materials were calculated using the same procedure and are listed in the last column of Table 11.

The corrosion data indicates that alloying of different elements to CP titanium did not significantly affect the corrosion resistance. From the corrosion current ( $i_{\text{corr}}$ ) values and corrosion rates calculated for CP Titanium, Ti-6Al-4V and Ti-13Nb-13Zr it can be seen that their corrosion rates were

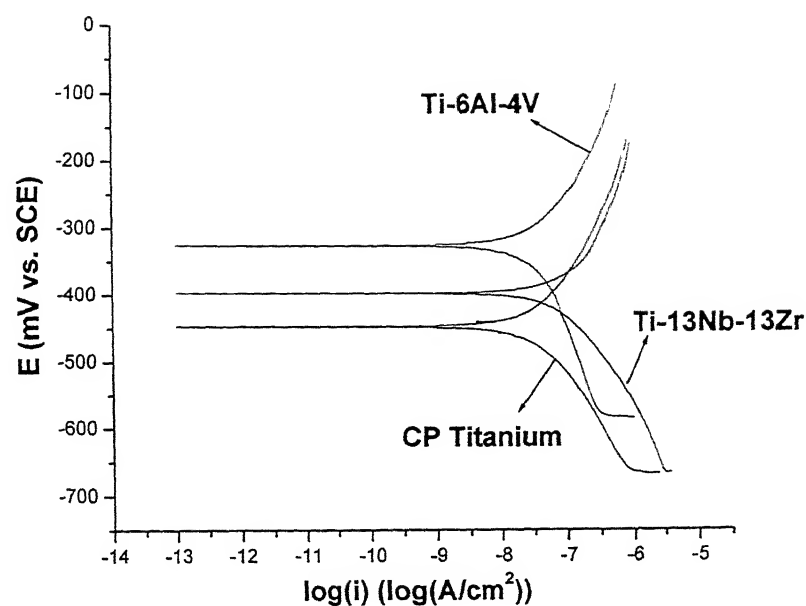


Figure 36: Tafel polarization curves for CP Titanium, Ti-6Al-4V and Ti-13Nb-13Zr in Hank's solution at 37°C temperature and 7.4 pH.

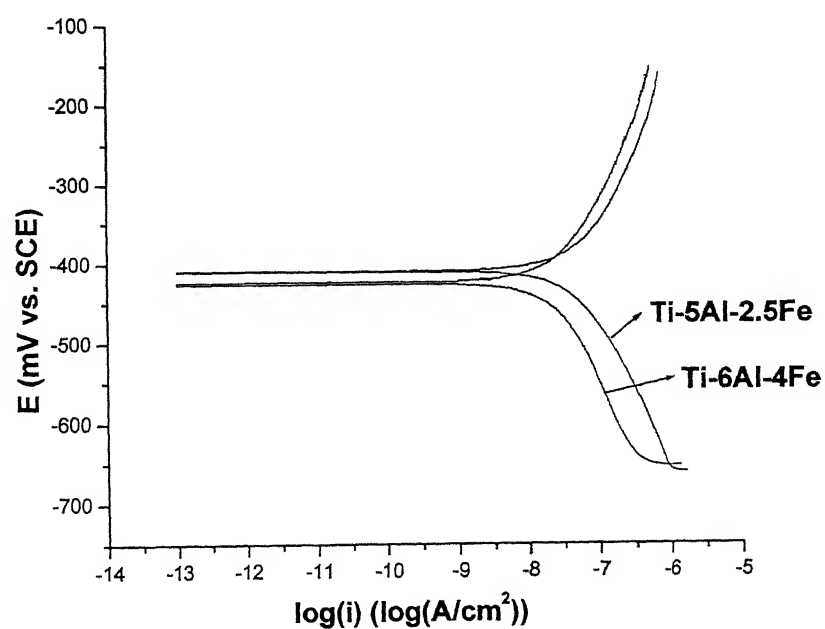


Figure 37: Tafel polarization curves for Ti-5Al-2.5Fe and Ti-6Al-4Fe in Hank's solution at 37°C temperature and 7.4 pH.

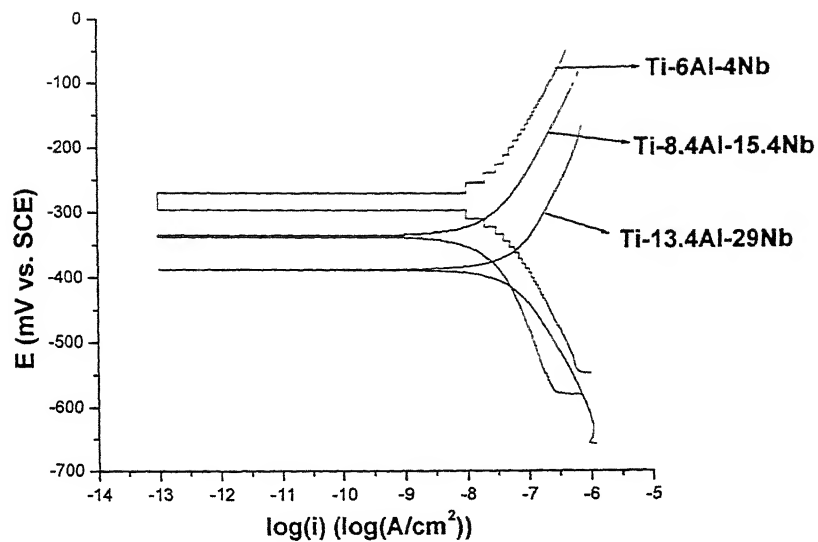


Figure 38: Tafel polarization curves for Ti-6Al-4Nb, Ti-8.4Al-15.4Nb and Ti-13.4Al-29Nb in Hank's solution at 37°C temperature and 7.4 pH.

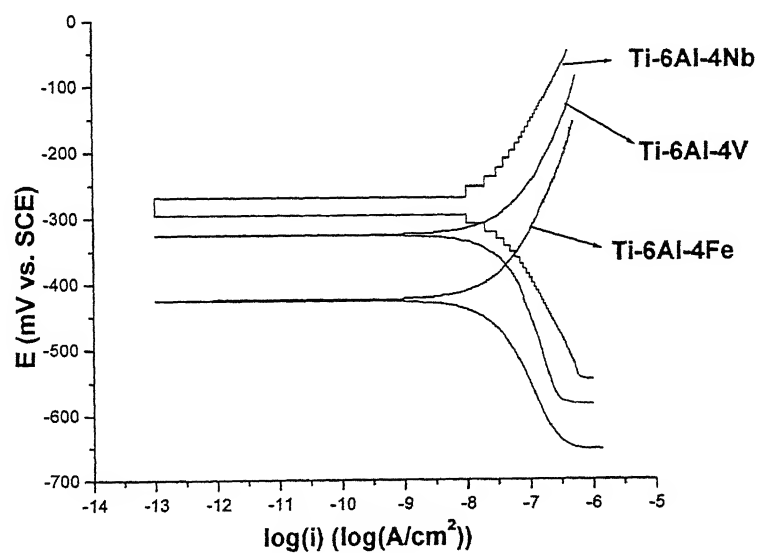


Figure 39: Tafel polarization curves for Ti-6Al-4Nb, Ti-6Al-4V and Ti-6Al-4Fe in Hank's solution at 37°C temperature and 7.4 pH.

comparable (Figure 36, Table 11). The two alloys with iron as the additional alloying element to Al i.e. Ti-5Al-2.5Fe and Ti-6Al-4Fe provided  $i_{\text{corr}}$  values  $0.0447 \mu\text{A}/\text{cm}^2$  and  $0.0275 \mu\text{A}/\text{cm}^2$  (Figure 37, Table 11). This can not be interpreted as lowering of corrosion rate with increased percentage of iron because the change is relatively small. It may be proposed that alloys with higher iron content can be examined. On comparing the data for Ti-6Al-4Nb, Ti-8.4Al-15.4Nb and Ti-13.4Al-29Nb it is clear that the increased percentage of niobium addition has not drastically affected  $i_{\text{corr}}$  values (Figure 38, Table 11). Comparing Ti-6Al-4Nb, Ti-6Al-4V and Ti-6Al-4Fe alloys, their  $i_{\text{corr}}$  values were almost similar (Figure 39, Table 11). However a very small decrease in the  $i_{\text{corr}}$  for Ti-6Al-4Nb ( $0.0331 \mu\text{A}/\text{cm}^2$ ) and Ti-6Al-4Fe ( $0.0275 \mu\text{A}/\text{cm}^2$ ) alloys was observed compared to Ti-6Al-4V ( $0.0380 \mu\text{A}/\text{cm}^2$ ). This indicates that the replacement of alloying element V by Nb and Fe did not considerably affect the corrosion rate. Animesh et al. have also reported the same observations in their study of electrochemical and tribological behavior of novel Ti based alloys for human body implants [226].

All the Ti alloys exhibited corrosion current density ( $i_{\text{corr}}$ ) in a relatively narrow region between  $0.02 \mu\text{A}/\text{cm}^2$  and  $0.09 \mu\text{A}/\text{cm}^2$ . This behavior was also corroborated in the potentiodynamic polarization and electrochemical impedance spectroscopic (EIS) studies (which will be discussed later). These observations suggest the presence of a passive layer on the surface of the Ti alloys which is similar in nature for all the alloys. Pankuch et al. studied characteristics of passive film on titanium alloys and reported that a thin film forms on titanium surfaces immediately on immersion in to aqueous solutions [225]. This surface film was identified to be highly disordered  $\text{TiO}_2$  with some  $\text{Ti}_2\text{O}_3$  also present. The present study revealed that this passive layer, which formed on the Ti alloys used in the study after immersion in Hank's solution, was not significantly affected by the alloying additions to Ti. The electrolyte used in the study, Hank's solution, is also not severely corrosive in nature so as to affect the passive layer that forms on all of the alloys used in this study. One of the major constituent of Hank's solution is  $\text{Cl}^-$  ions ( $0.2$  moles/liter). It is known that  $\text{Cl}^-$  ions cause damage to passive film forming

on almost all alloys with the notable exception of Ti.

The results in the Tafel extrapolation studies indicated that the alloying elements do not significantly affect the passive film on Ti alloys. However, they may affect the passive film on immersing these alloys for longer intervals in Hank's solution. Alloying elements can also have effect on microstructure, mechanical and wear behavior of the Ti alloys [75].



Table 11: Corrosion rates determined by Tafel extrapolation method for different biomaterials used in present study.

Material	FCP (mV vs. SCE)	$\beta_c$ (mV/dec)	$\beta_a$ (mV/dec)	Log(i)	$i_{corr}$ ( $\mu A/cm^2$ )	Corrosion rate mils per year (mm per year)
CP Ti	-448	-176	207	-7.33	0.0468	0.016 (0.0004)
Ti-6Al-4V	-325	-284	193	-7.42	0.038	0.013 (0.000325)
Ti-13Nb-13Zr	-403	-173	207	-7.06	0.0871	0.0298 (0.000745)
Ti-5Al-2.5Fe	-410	-181	190	-7.35	0.0447	0.0153 (0.000383)
Ti-6Al-4Fe	-425	-214	200	-7.56	0.0275	0.00939 (0.000235)
Ti-6Al-4Nb	-386	-301	255	-7.48	0.0331	0.0113 (0.000283)
Ti-8.4Al-15.4Nb	-334	-251	177	-7.59	0.0257	0.00878 (0.00022)
Ti-13.4Al-29Nb	-388	-186	192	-7.19	0.0646	0.0221 (0.000553)

## 4.2 Effect of immersion time in Hank's Solution

### 4.2.1 Potentiodynamic Polarization

Potentiodynamic polarization experiments were performed on all the alloys after 1 hr of immersion in Hank's solution and also after 168 hrs (1 week) of immersion. Potentiodynamic polarization curves of all the samples used in the study were analyzed and results obtained are presented below, followed by discussion of the results.

The potentiodynamic polarization data for CP Titanium, Ti-6Al-4V and Ti-13Nb-13Zr alloys, collected after 1hr of immersion in Hank's solution, are presented in Figure 40. The same data for Ti-5Al-2.5Fe and Ti-6Al-4Fe alloys are provided in Figure 41 whereas Figure 42 shows the same data for Ti-6Al-4Nb, Ti-8.4Al-15.4Nb and Ti-13.4Al-29Nb. To observe the effect of replacing the alloying element V by Nb and Fe, the potentiodynamic polarization curves for Ti-6Al-4V, Ti-6Al-4Nb and Ti-6Al-4Fe alloys have been provided in Figure 43.

Potentiodynamic polarization data were collected after 168 hrs of immersion in Hank's solution. These have also been presented in the same way as has been presented after immersion of 1 hr in Hank's solution. The potentiodynamic polarization data for CP Titanium, Ti-6Al-4V and Ti-13Nb-13Zr alloys, collected after 168 hrs of immersion in Hank's solution, are presented in Figure 44. The same data for Ti-5Al-2.5Fe and Ti-6Al-4Fe alloys are provided in Figure 45 whereas Figure 46 shows the same data for Ti-6Al-4Nb, Ti-8.4Al-15.4Nb and Ti-13.4Al-29Nb. To observe the effect of replacing the alloying element V by Nb and Fe, the comparative potentiodynamic polarization curves has been provided in Figure 47.

Different parameters like zero current potential (ZCP), corrosion current density ( $i_{\text{corr}}$ ) (estimated by the technique used in Tafel extrapolation experiments) and passive current density ( $i_{\text{pass}}$ ) were estimated, from the

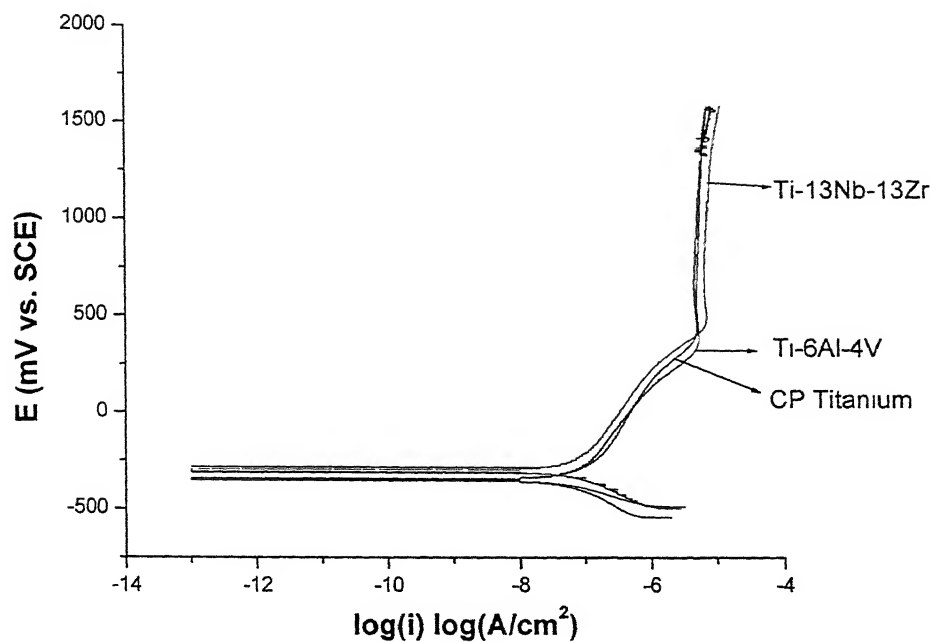


Figure 40: Potentiodynamic polarization curves for CP Titanium, Ti-6Al-4V and Ti-13Nb-13Zr after 1 Hr of immersion in Hank's solution.

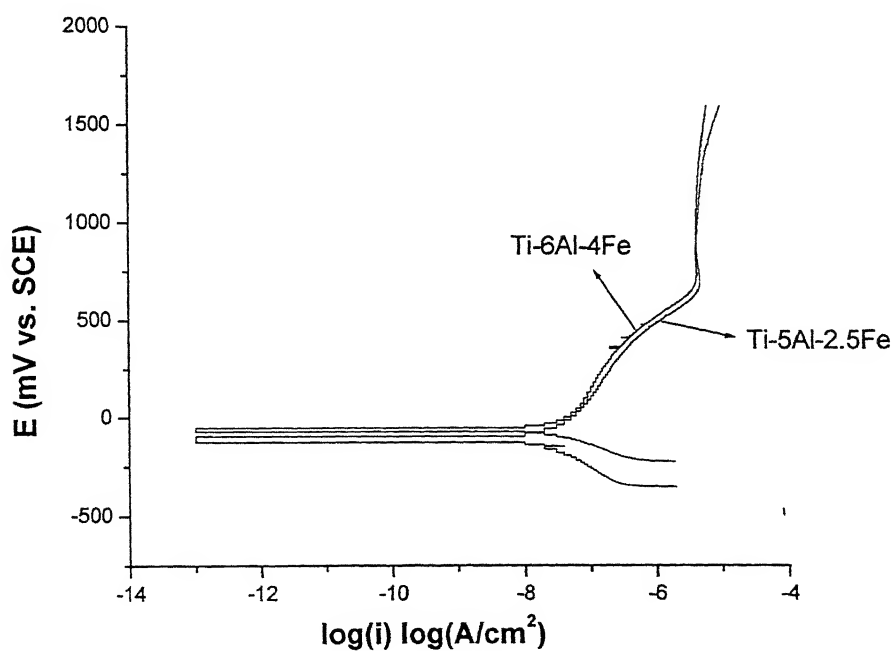


Figure 41: Potentiodynamic polarization curves for Ti-5Al-2.5Fe and Ti-6Al-4Fe after 1 Hr of immersion in Hank's solution.

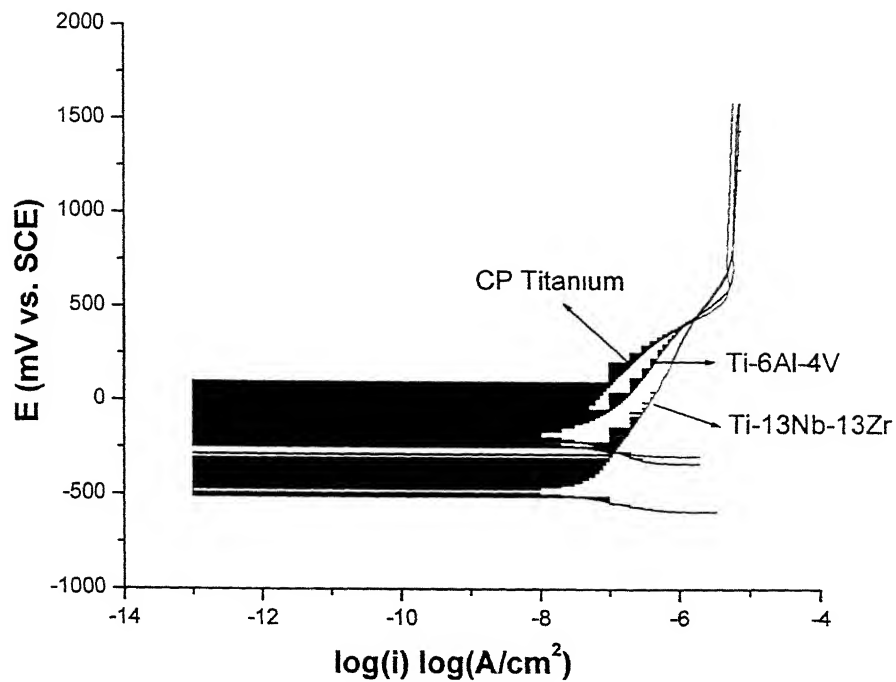


Figure 44: Potentiodynamic polarization curves for CP Titanium, Ti-6Al-4V and Ti-13Nb-13Zr after 168 Hrs of immersion in Hank's solution.

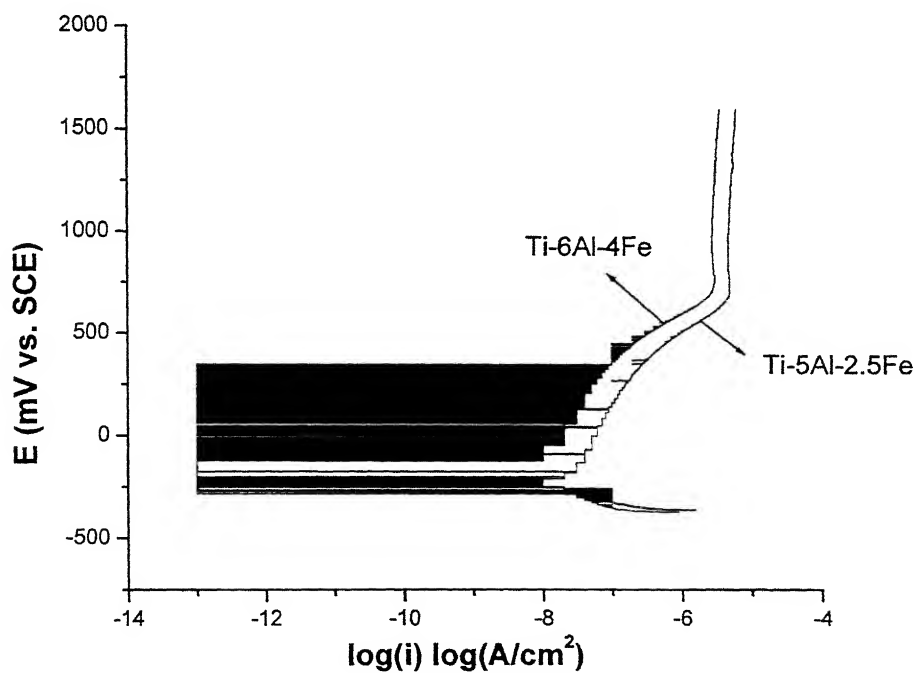


Figure 45: Potentiodynamic polarization curves for Ti-5Al-2.5Fe and Ti-6Al-4Fe after 168 Hrs of immersion in Hank's solution.

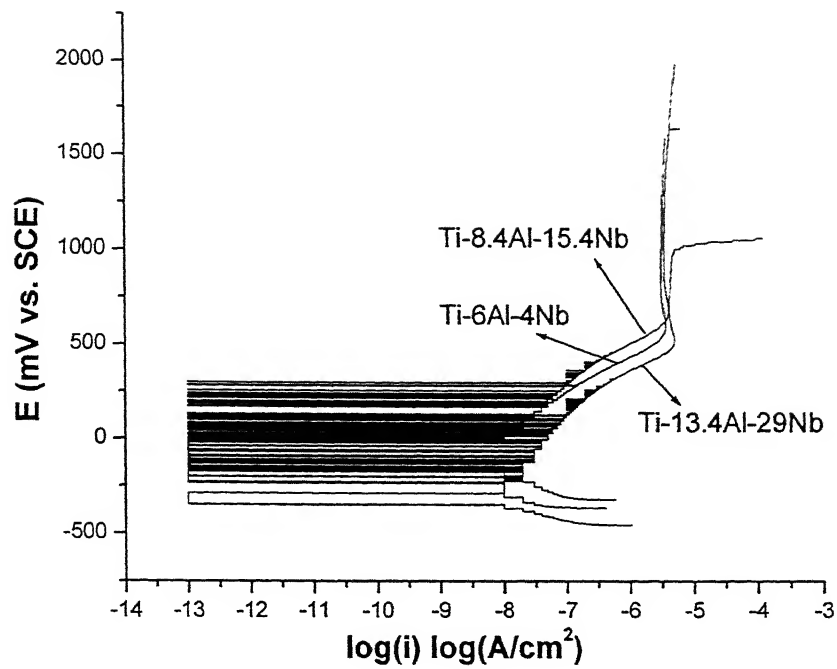


Figure 46: Potentiodynamic polarization curves for Ti-6Al-4Nb, Ti-8.4Al-15Nb and Ti-13.4Al-29Nb after 1 Hr of immersion in Hank's solution.

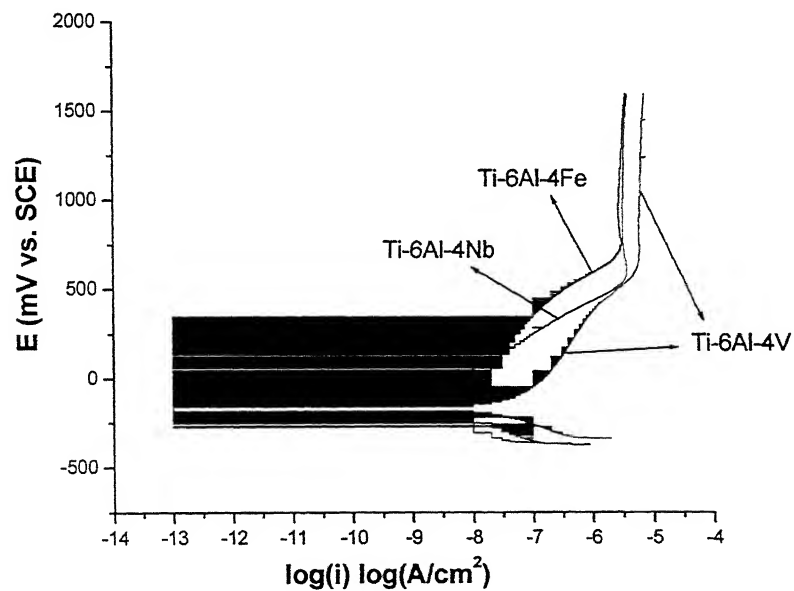


Figure 47: Potentiodynamic polarization curves for Ti-6Al-4Nb, Ti-6Al-4V and Ti-6Al-4Fe after 1 Hr of immersion in Hank's solution.

potentiodynamic polarization data of all the alloys for immersion time of 1 hr and 168 hrs, and they are tabulated in Table 12. Individual comparative potentiodynamic polarization curves collected after 1 hr and 168 hrs of immersion in Hank's solution for all the alloys are presented in Figures 48 through 55.

The nature of polarization curves indicates that the current density increased with anodic polarization and achieved a constant value ( $i_{pass}$ ) after some time without showing any active-passive behavior. This behavior was noted for all the samples for data collected after 1 hr as well as 168 hrs of immersion in Hank's solution. Animesh [226] have reported stable passivity for Ti based implant materials i.e. the alloys achieved passivation just after immersion. The difference in the passivation behavior in the two studies can be attributed to immersion time in Hank's solution. Animesh recorded potentiodynamic polarization data just after stabilization of free corrosion potential which was realized in about 15 minutes. In the present study, potentiodynamic polarization data were obtained after 1 hr and 168 hrs of immersion in Hank's solution.

Hodgson et al. [134] have showed that calcium and phosphate ions present in the Hank's solution interact with the surface film on Ti alloys and change the surface properties. Moreover, this interaction is quite predominant during first hour of immersion. The delayed passivation of Ti-alloys observed in the present study compared to instant passivation in Animesh's experiments may thus be due to interaction of calcium and phosphate ions with the surface film on Ti alloys.

The potentiodynamic polarization curves obtained after 168 hrs of immersion in Hank's solution revealed wide fluctuations in current density near the ZCP i.e. zero current potential (e.g. Figure 44). These fluctuations were caused due to the fall of current density to very low values during the potentiodynamic polarization scan. This kind of oscillation has also been reported in the literature [227-229] in the case of Fe in  $H_2SO_4$  medium and

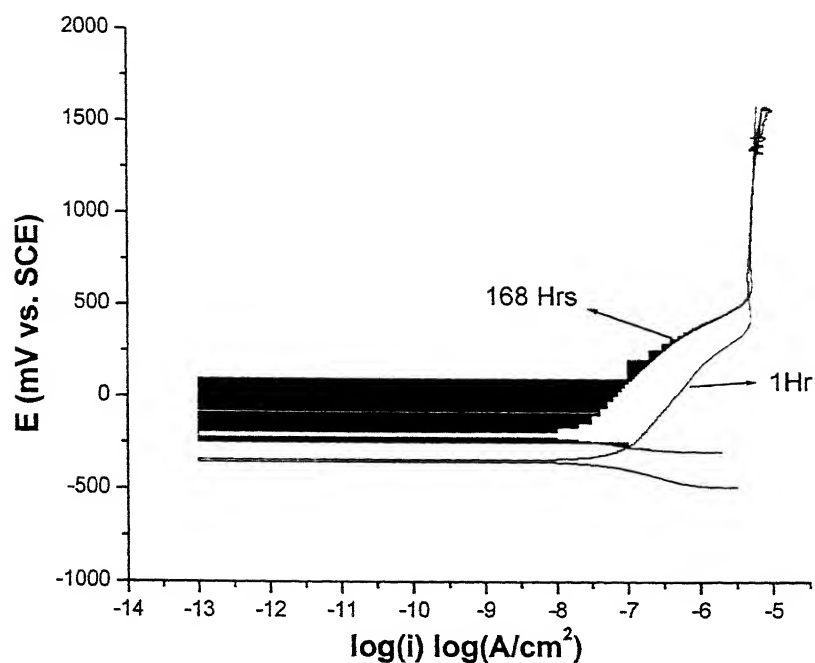


Figure 48: Potentiodynamic polarization curves for CP Titanium at immersion time of 1 Hr and 168 Hrs in Hank's solution.

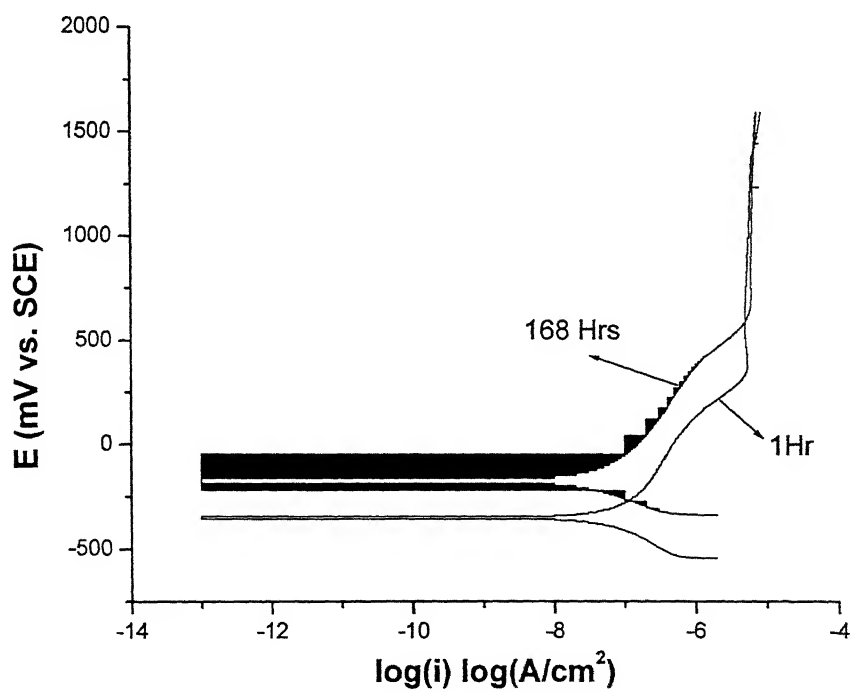


Figure 49: Potentiodynamic polarization curves for Ti-6Al-4V at immersion time of 1 Hr and 168 Hrs in Hank's solution.

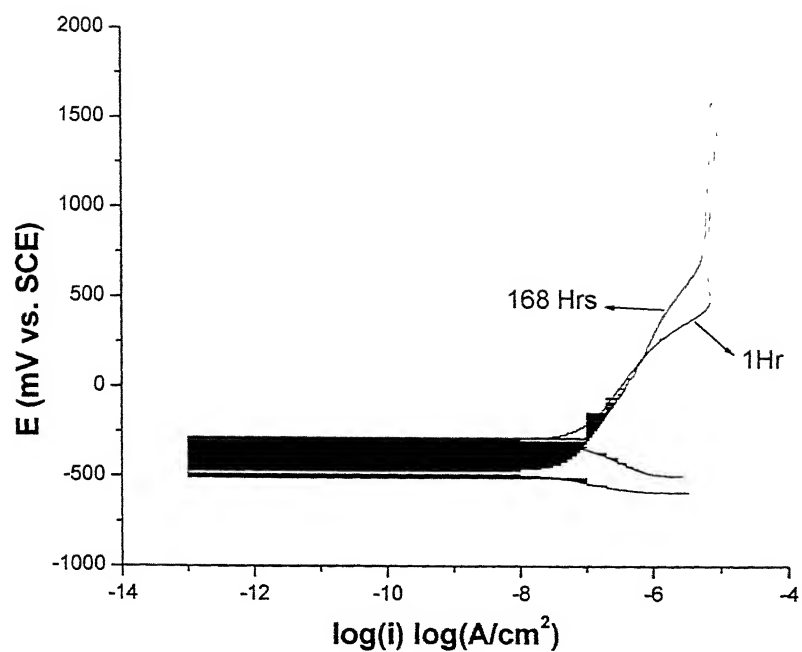


Figure 50: Potentiodynamic polarization curves for Ti-13Nb-13Zr at immersion time of 1 Hr and 168 Hrs in Hank's solution.

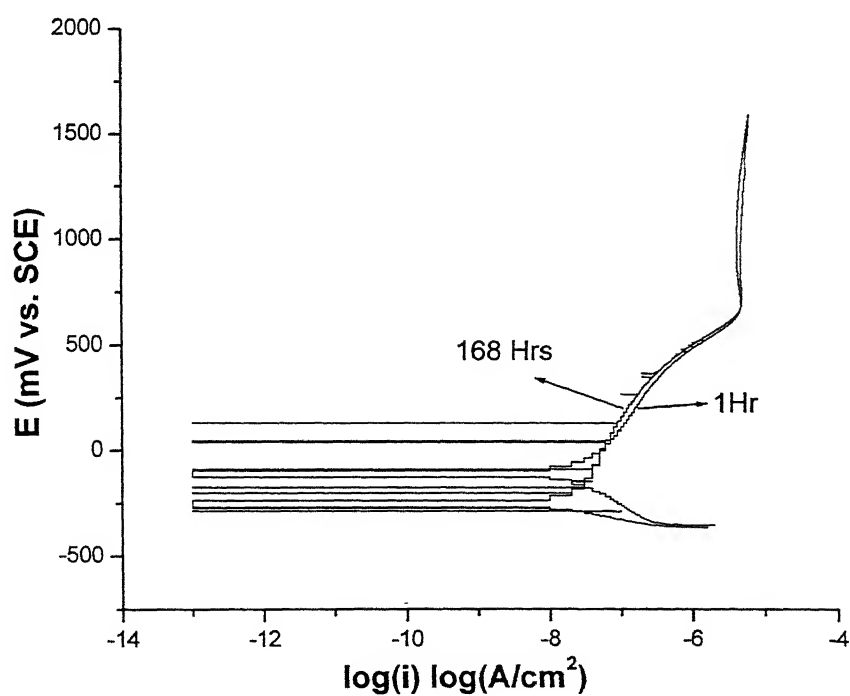


Figure 51: Potentiodynamic polarization curves for Ti-5Al-2.5Fe at immersion time of 1 Hr and 168 Hrs in Hank's solution.



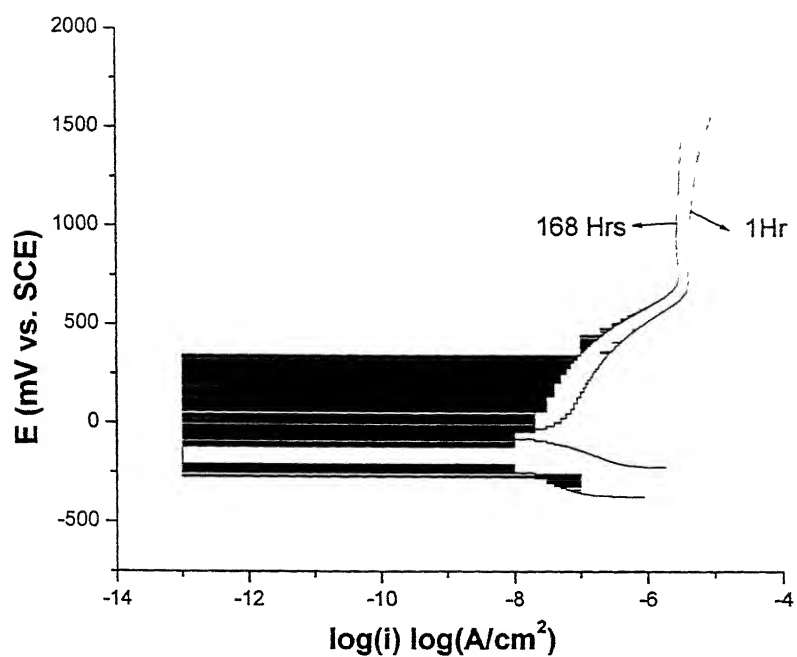


Figure 52: Potentiodynamic polarization curves for Ti-6Al-4Fe at immersion time of 1 Hr and 168 Hrs in Hank's solution.

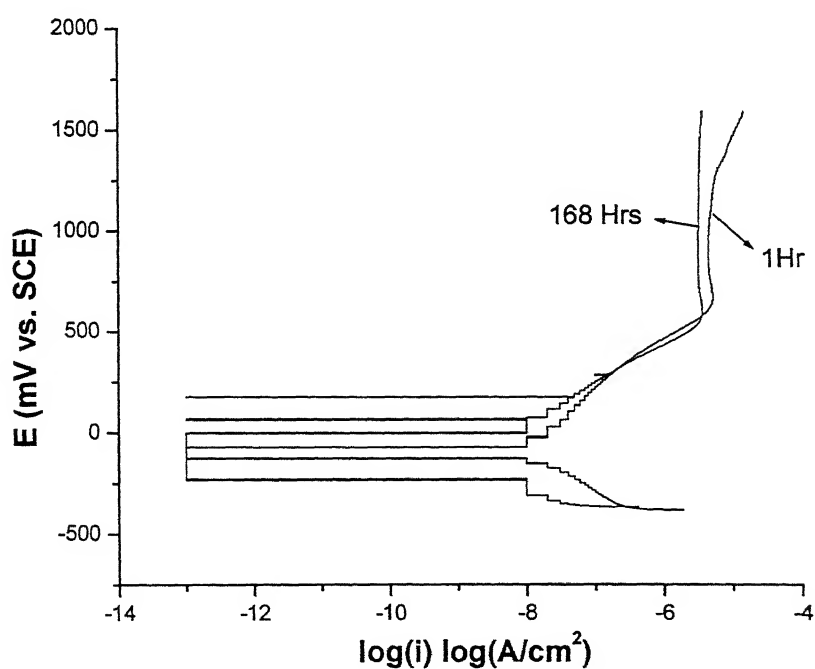


Figure 53: Potentiodynamic polarization curves for Ti-6Al-4Nb at immersion time of 1 Hr and 168 Hrs in Hank's solution.

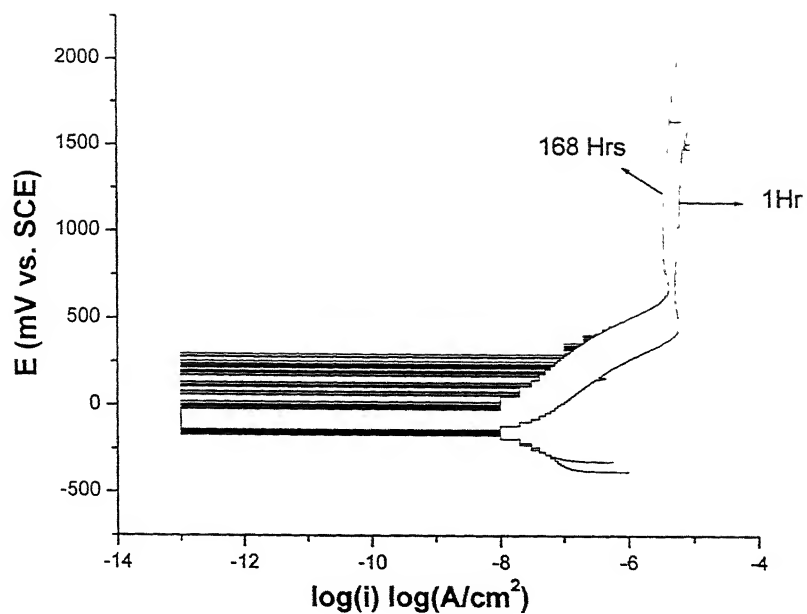


Figure 54: Potentiodynamic polarization curves for Ti-8.4Al-15.4Nb at immersion time of 1 Hr and 168 Hrs in Hank's solution.

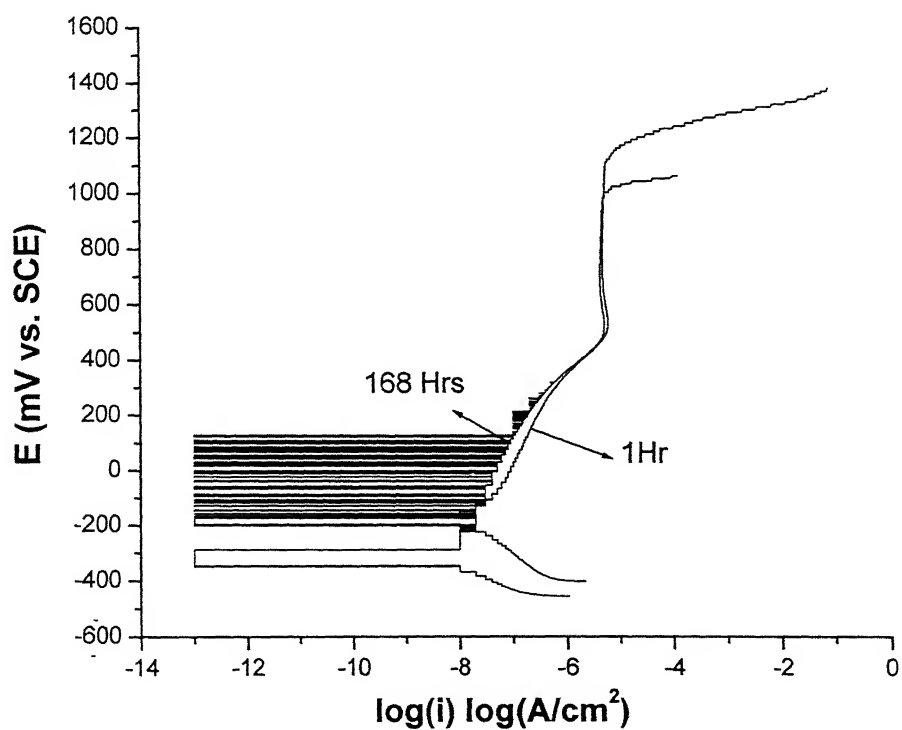


Figure 55: Potentiodynamic polarization curves for Ti-13.4Al-29Nb at immersion time of 1 Hr and 168 Hrs in Hank's solution.

was attributed to the competition between film formation and dissolution. Nelufā Ibriš et al. [230] in their study of Ti, Ti-7Al-4.5V and Ti-5Al-2.5Fe alloys in artificial saliva containing fluoride ions have also observed this feature and attributed it to dissolution of passive layer by fluoride ions. It can be seen from Figure 44 in the present study that there was an active region (just above the zero current potential) where the charge transfer reaction takes place followed by a passive region at more positive potentials. These current oscillations were predominant in the transition between active and passive region. In this region, the oxide layer is still unstable in the corrosive media i.e. Hank's solution. While the anodic reaction leads to an increase of the current, the film formation blocks the active surface of the electrode, leading to a decrease of the current. Simultaneous occurrence of these two phenomena causes fluctuations in current density [230]. With increasing potential, the anodic film becomes more stable and the passive region appears on the polarization curve. As this type of behavior was observed for potentiodynamic polarization experiments performed after 168 hrs of immersion, this can be attributed to accumulation of passivation agents near the surface and due to prolonged interaction of calcium and phosphate ions present in the Hank's solution with the surface film formed on titanium alloys [134].

CP Titanium, Ti-6Al-4V and Ti-13Nb-13Zr alloys showed similar nature of polarization behavior after 1 hr (Figure 40) as well as after 168 hrs (Figure 44) of immersion in Hank's solution. The  $i_{corr}$  for the above alloys were 0.042, 0.030 and 0.055  $\mu\text{A}/\text{cm}^2$ , respectively after 1 hr of immersion in Hank's solution and after 168 hrs of immersion these values change to 0.017, 0.022 and 0.025  $\mu\text{A}/\text{cm}^2$  (Table 12). The decrease in the  $i_{corr}$  (0.042 to 0.017  $\mu\text{A}/\text{cm}^2$ ) was higher for CP titanium (Figure 48) and Ti-13Nb-13Zr (0.055 to 0.025  $\mu\text{A}/\text{cm}^2$ ) (Figure 50) compared to Ti-6Al-4V i.e. from 0.030 to 0.022  $\mu\text{A}/\text{cm}^2$  (Figure 49). The  $i_{pass}$  for CP Titanium, Ti-6Al-4V and Ti-13Nb-13Zr alloys were 4.79, 5.75 and 7.24  $\mu\text{A}/\text{cm}^2$  respectively after 1 hr of immersion. The same values estimated after 168 hrs of immersion were

4.57, 5.50 and 5.75  $\mu\text{A}/\text{cm}^2$ . This indicated that the  $i_{\text{pass}}$  for all these three alloys were similar after 1 hr of immersion (Figure 40) and also did not change significantly after 168 hrs of immersion (Figure 44) in Hank's solution. However, the passive current density was slightly lower in all the three alloys after 168 hrs immersion. These observations suggest only a slight improvement of corrosion resistance for CP Titanium, Ti-6Al-4V and Ti-13Nb-13Zr alloys with immersion time in Hank's solution. The change in passive film nature for CP titanium can be attributed to thickening of  $\text{TiO}_2$  film which formed immediately on immersion in Hank's solution [225]. It had been reported in the literature [146] that the vanadium oxide formed on the surface of Ti-6Al-4V alloy dissolves and this dissolution of vanadium oxide is further enhanced by presence of  $\text{Cl}^-$  ions in Hank's solution. Hence, vanadium as an alloying element could not improve the surface film on Ti-6Al-4V alloy. In present study the change in passive behavior of Ti-6Al-4V alloy with immersion time in Hank's solution (contains  $\text{Cl}^-$  ions) can be attributed to same phenomena [146]. Although the presence of alloying elements Nb and Zr has been reported to improve the electrochemical behavior of Ti-13Nb-13Zr alloy [144,145], only a slight improvement in passive film behavior of this alloy was observed. Animesh also noted the varied electrochemical results for this alloy in Hank's solution [226].

The Ti-5Al-2.5Fe and Ti-6Al-4Fe alloys revealed the  $i_{\text{corr}}$  of 0.025 and 0.023  $\mu\text{A}/\text{cm}^2$  after 1 hr of immersion (Figure 41) in Hank's solution while these values decreased sharply to 0.008 and 0.005  $\mu\text{A}/\text{cm}^2$  respectively after 168 hrs of immersion (Figure 45). The  $i_{\text{pass}}$  for Ti-5Al-2.5Fe alloy decreased from 4.37 to 3.55  $\mu\text{A}/\text{cm}^2$  when experiments conducted after 1 hr and after 168 hrs of immersion were compared (Table 12). This decrease was also noted for Ti-6Al-4Fe, i.e. from 5.13 to 3.09  $\mu\text{A}/\text{cm}^2$ . This indicates improvement in the passive nature of the barrier present on these alloys with time when immersed in Hank's solution. Animesh have reported that alloying of Al in Ti based alloys has a deleterious effect on the passive film on Ti. Therefore, the decrease in corrosion rate with immersion time in Hank's

solution can be attributed to alloying of iron in the Ti alloys. Increased corrosion resistance, with immersion time in Hank's solution, of Ti-based alloys with iron as an alloying element has also been reported by Netula et al. [230].

The Ti-6Al-4Nb, Ti-8.4Al-15.4Nb and Ti-13.4Al-29Nb alloys revealed similar kind of polarization behavior after 1 hr (Figure 41) as well as after 168 hrs (Figure 46) of immersion in Hank's solution. The only exception was the breakdown of passive layer for Ti-13.4Al-29Nb alloy. This observation can be attributed to increased percentage of Al which has been reported to have a deleterious effect on passive film [226]. The  $i_{corr}$  for the above alloys were 0.017, 0.042 and 0.022  $\mu\text{A}/\text{cm}^2$ , respectively, after 1 hr of immersion in Hank's solution and after 168 hrs of immersion these values were 0.002, 0.003 and 0.006  $\mu\text{A}/\text{cm}^2$  (Table 12). The  $i_{pass}$  values for Ti-6Al-4Nb, Ti-8.4Al-15.4Nb and Ti-13.4Al-29Nb alloys were 4.79, 6.46 and 5.25  $\mu\text{A}/\text{cm}^2$  respectively after 1 hr of immersion. The same values estimated after 168 hrs of immersion were 3.24, 3.63 and 3.98  $\mu\text{A}/\text{cm}^2$ . This indicated that the  $i_{pass}$  values decreased for all these three alloys with immersion time in Hank's solution (Figures 53, 54 and 55). A sharp decrease in  $i_{corr}$  and mild decrease in  $i_{pass}$  value suggests enhanced corrosion resistance of the surface film. In the literature, it had been reported that Nb as alloying element has a stabilizing effect on surface films on Ti based alloys [139]. Metikos et al. [146], in their study on influence of Nb addition on passivity of Ti based implants in Hank's solution, concluded that the Nb cations improve the passivation properties of surface film by annihilating the stoichiometric defects present on titanium oxide film.

Comparing the polarization behavior Ti-6Al-4Nb, Ti-6Al-4V and Ti-6Al-4Fe alloys (Figures 43 and 47) it can be observed that Ti-6Al-4Nb and Ti-6Al-4Fe alloys behaved in almost similar manner which was quite different from Ti-6Al-4V. The potentiodynamic polarization data for these alloys after 1 hr and after 168 hrs of immersion in Hank's solution are presented in Figure 43

and 16. The  $i_{\text{corr}}$  estimated from polarization data for the Ti-6Al-4Nb, Ti-6Al-4V and Ti-6Al-4Fe alloys were 0.017, 0.030, and 0.023  $\mu\text{A}/\text{cm}^2$ , respectively, after 1 hr of immersion in Hank's solution. After 168 hrs of immersion, these values were 0.002, 0.022 and 0.005  $\mu\text{A}/\text{cm}^2$  (Table 12). The  $i_{\text{corr}}$  for the three alloys were comparable after 1 hr of immersion but after 168 hrs of immersion in Hank's solution, the  $i_{\text{corr}}$  for Ti-6Al-4Nb and Ti-6Al-4Fe alloys decreased sharply to 0.002 and 0.005  $\mu\text{A}/\text{cm}^2$ , respectively, while the  $i_{\text{corr}}$  for Ti-6Al-4V alloy remained almost same at 0.022  $\mu\text{A}/\text{cm}^2$ . The  $i_{\text{pass}}$  for Ti-6Al-4Nb, Ti-6Al-4V and Ti-6Al-4Fe alloys were 4.79, 5.75 and 5.13  $\mu\text{A}/\text{cm}^2$ , respectively, after 1 hr of immersion. The same values estimated after 168 hrs of immersion were 3.24, 5.50 and 3.09  $\mu\text{A}/\text{cm}^2$ . This indicated that  $i_{\text{pass}}$  for all these three alloys were similar after 1 hr of immersion (Figure 43) and after 168 hrs of immersion (Figure 44) in Hank's solution the  $i_{\text{pass}}$  decreased for Ti-6Al-4Nb and Ti-6Al-4Fe but did not drastically change for Ti-6Al-4V. These observations suggest improvement in passive film on the metal surface for Ti-6Al-4Nb and Ti-6Al-4Fe alloys. The Ti-6Al-4V alloy exhibited very minimal change in electrochemical behavior with immersion time in Hank's solution.

The potentiodynamic polarization behavior of surface film on titanium alloys revealed that passivation properties of surface films improved with immersion time in Hank's solution. While Fe and Nb additions along with Al appear to improve passive film nature, V addition along with Al revealed only minimal improvement. Increased Fe content as alloying element indicated improvement in the passive film nature.

Table 12: Values estimated from potentiodynamic polarization curves obtained at immersion time of 1 Hr and 168 Hrs in Hank's solution.

Material	ZCP (mV vs. SCE)		$i_{corr}$ ( $\mu\text{A}/\text{cm}^2$ )		$i_{pass}$ ( $\mu\text{A}/\text{cm}^2$ )	
	1Hr	168 Hrs	1Hr	168 Hrs	1Hr	168 Hrs
CP Titanium	-342	-205	0.042	0.017	4.79	4.57
Ti-6Al-4V	-266	-176	0.030	0.022	5.75	5.50
Ti-13Nb-13Zr	-348	-478	0.055	0.025	7.24	5.75
Ti-5Al-2.5Fe	-112	-253	0.025	0.008	4.37	3.55
Ti-6Al-4Fe	-161	-181	0.023	0.005	5.13	3.09
Ti-6Al-4Nb	-107	-122	0.017	0.002	4.79	3.24
Ti-8.4Al-15.4Nb	-206	-209	0.042	0.003	6.46	3.63
Ti-13.4Al-29Nb	-184	-380	0.022	0.006	5.25	3.98

#### 4.2.2 Electrochemical Impedance Spectroscopy

Electrochemical behavior of passive films on Ti based biomaterials in Hank's solution has also been investigated in this study. Electrochemical impedance spectroscopy (EIS) technique was employed to monitor passive film behavior on exposure to simulated body fluid i.e. Hank's solution. In order to study the changes in passive film properties with time, impedance spectra of all the alloys, used in present research, were collected after immersion times of 1hr, 24 hrs (1 day), 72 hrs (3 days) and 168 hrs (7 days) in Hank's solution. All the impedance experiments were conducted at open circuit potential (i.e. free corrosion potential). All the impedance data, collected for all the alloys, were fit to appropriate equivalent electrical circuit (figure 56) using a complex nonlinear least-squares fitting routine, using both the real and imaginary components of the data [231].

Impedance spectra obtained from all the experiments exhibited similar nature in the Nyquist, Bode phase and Bode magnitude plots. All these plots for each alloy has been provided in Figures 57 through 64. From these figures it can be observed that the nature of the Nyquist plots is similar for all the alloys, consisting of an arc that can be extrapolated to a semicircle, which is associated with the corrosion process. The diameter of the semicircle corresponds to the polarization resistance ( $R_p$ ). From the Bode phase plots shown in figures 57 through 64 it can be noted that, for all the alloys, the phase angle drops towards zero degree at very high frequencies, indicating that the impedance is dominated by solution resistance in this frequency range (no phase shift between current and potential results due presence of a resistor in AC circuit). Moreover, it can also be noted that the phase angle drops slightly towards lower values in the low frequency region indicating the contribution of polarization resistance to the impedance. However, the phase remains close to  $-90^\circ$  over a wide range of frequency indicating a near capacitive response for all the alloys. This behavior is indicative of a typical thin passive oxide film present on the surface [139]. Bode magnitude plots, presented in figures 57 through 64, were also similar in nature for all the



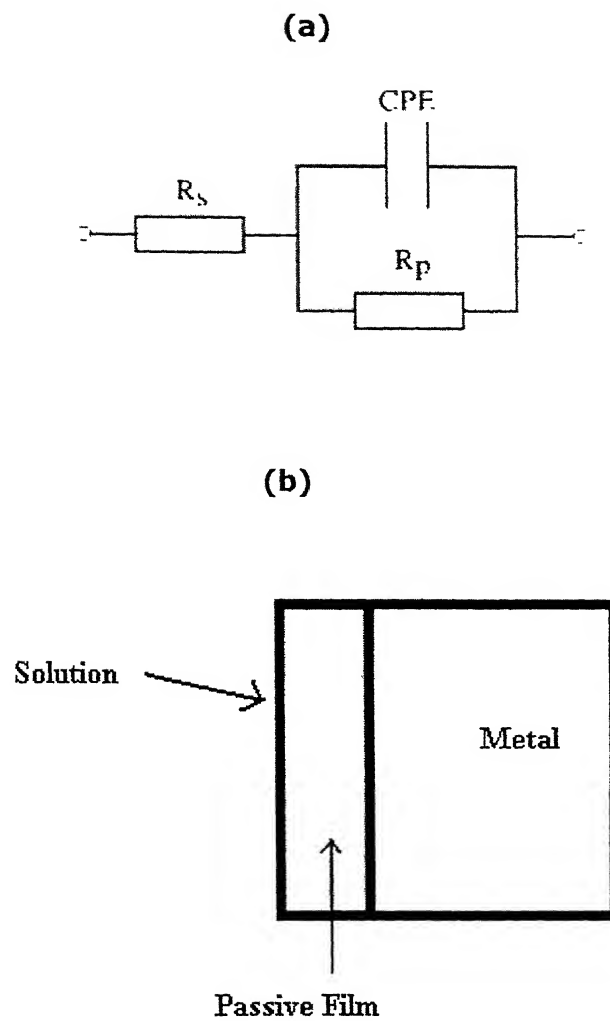


Figure 56: Model used to fit the EIS data obtained at different immersion times in hank's solution for all the Ti based alloys: (a) equivalent circuit, and (b) physical model

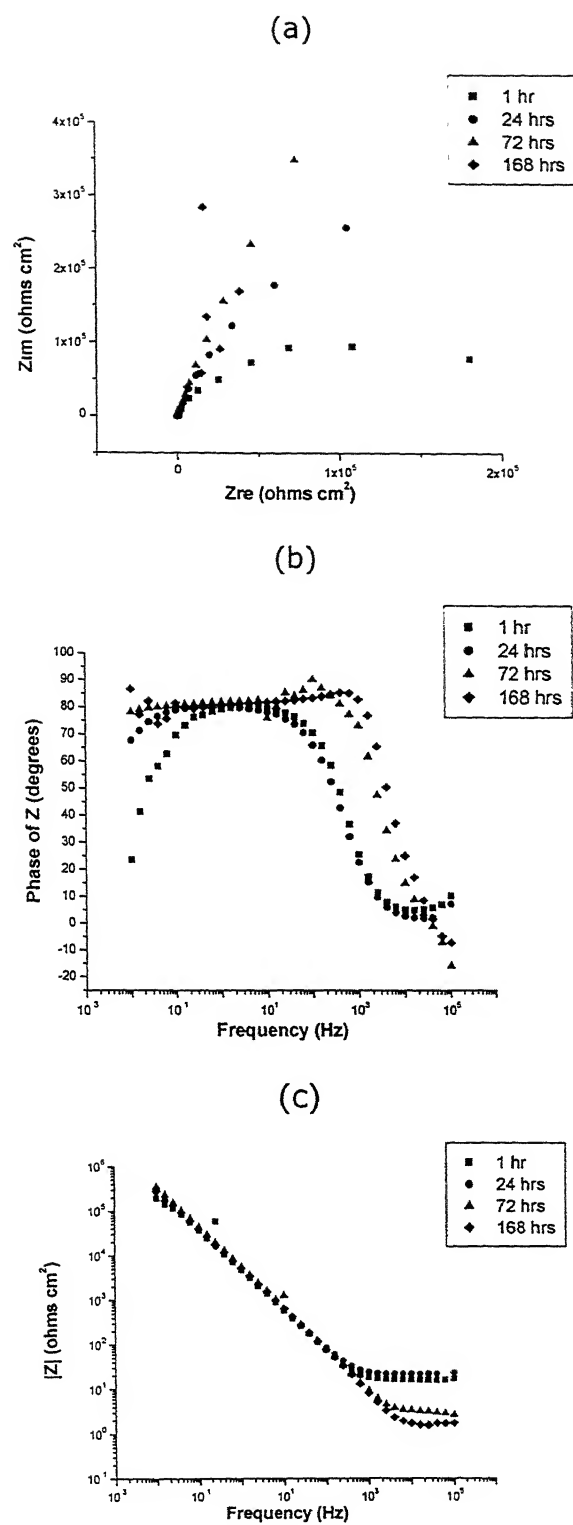


Figure 57: EIS data for CP Titanium as a function of immersion time in Hank's solution: (a) Nyquist plots (b) Bode phase plots and (c) Bode magnitude plots.

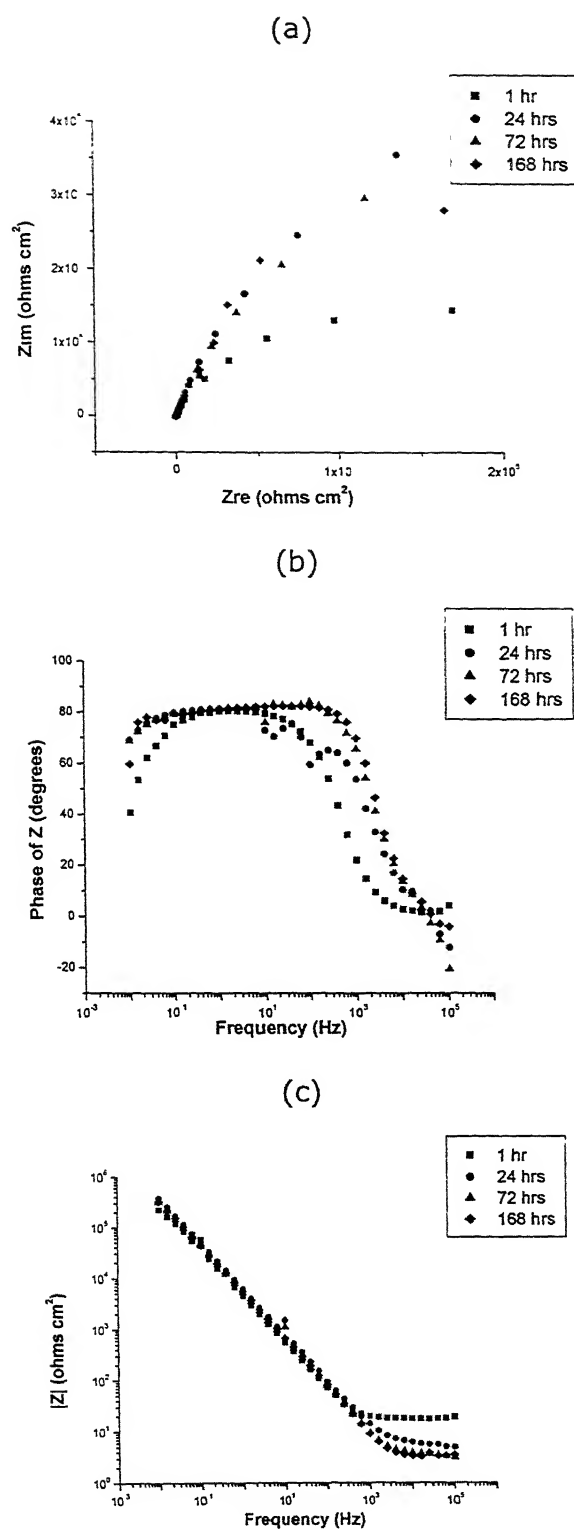


Figure 58: EIS data for Ti-6Al-4V as a function of immersion time in Hank's solution: (a) Nyquist plots (b) Bode phase plots and (c) Bode magnitude plots.

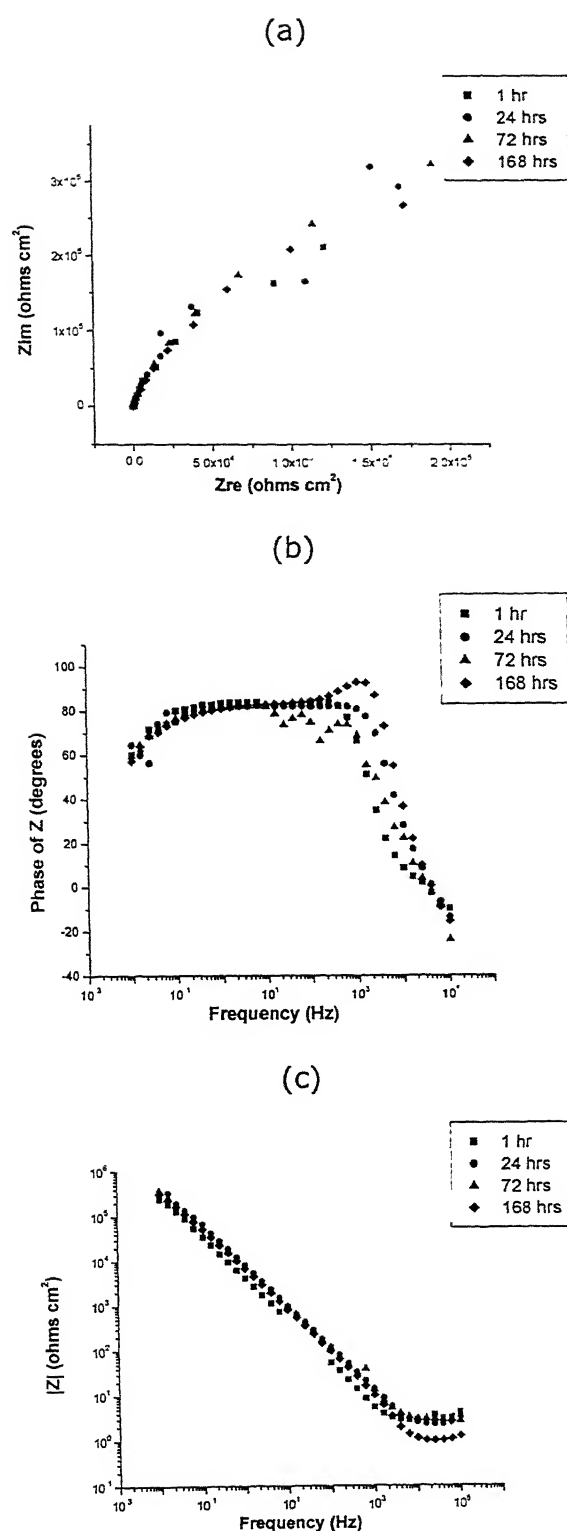


Figure 59: EIS data for Ti-13Nb-13Zr as a function of immersion time in Hank's solution: (a) Nyquist plots (b) Bode phase plots and (c) Bode magnitude plots.

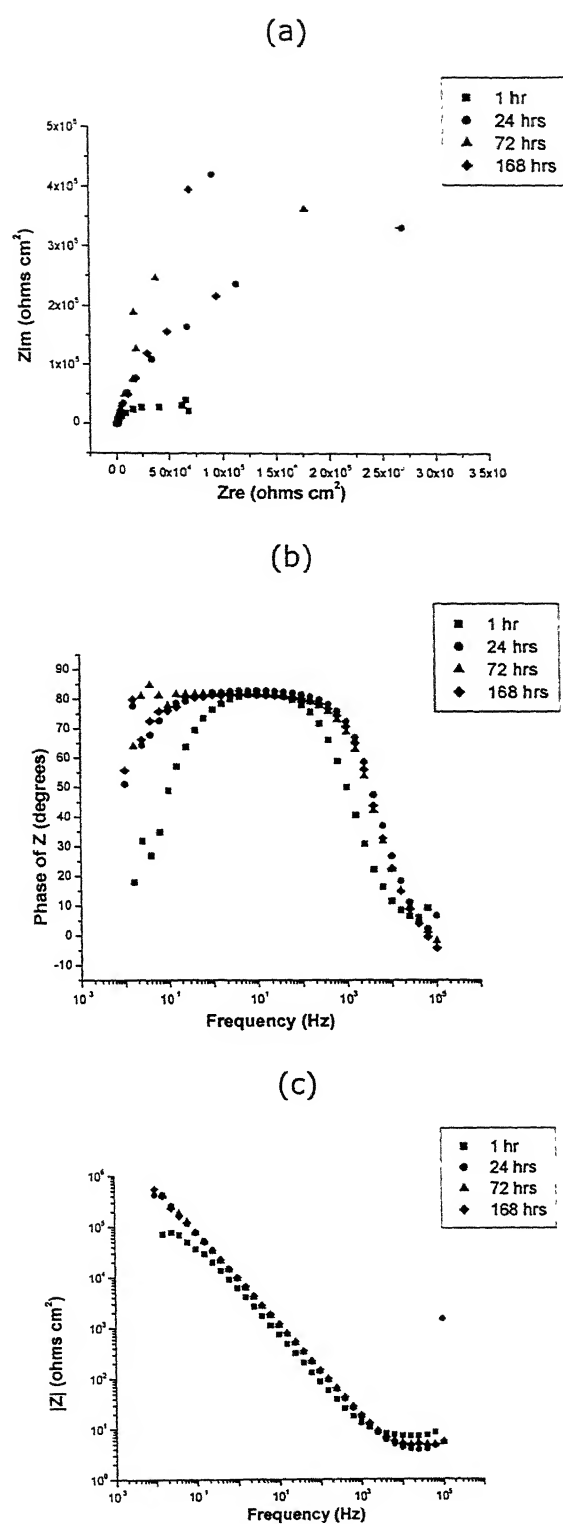


Figure 60: EIS data for Ti-5Al-2.5Fe as a function of immersion time in Hank's solution: (a) Nyquist plots (b) Bode phase plots and (c) Bode magnitude plots.

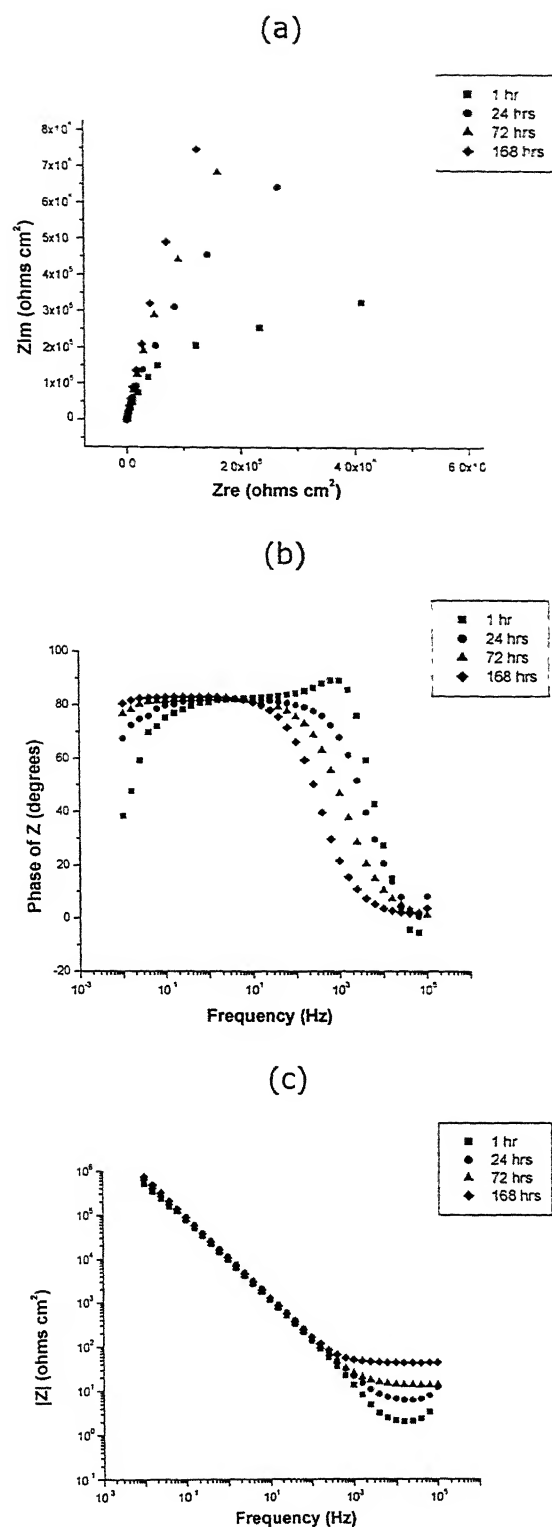
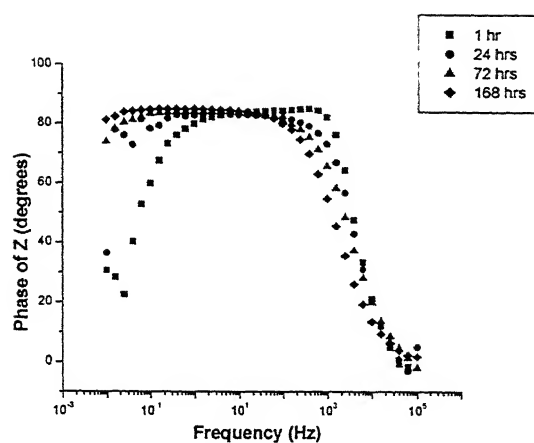
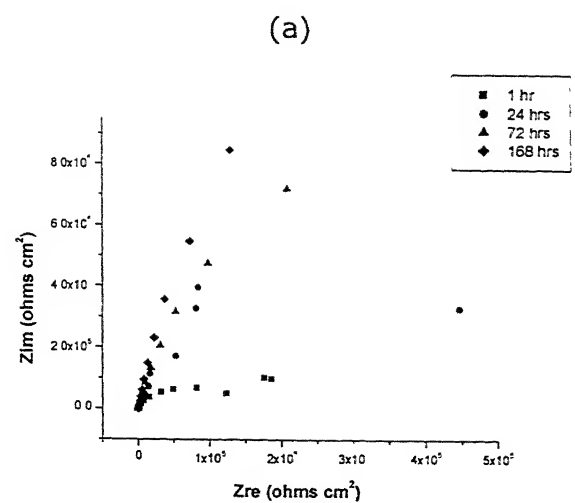


Figure 61: EIS data for Ti-6Al-4Fe as a function of immersion time in Hank's solution: (a) Nyquist plots (b) Bode phase plots and (c) Bode magnitude plots.



(b)

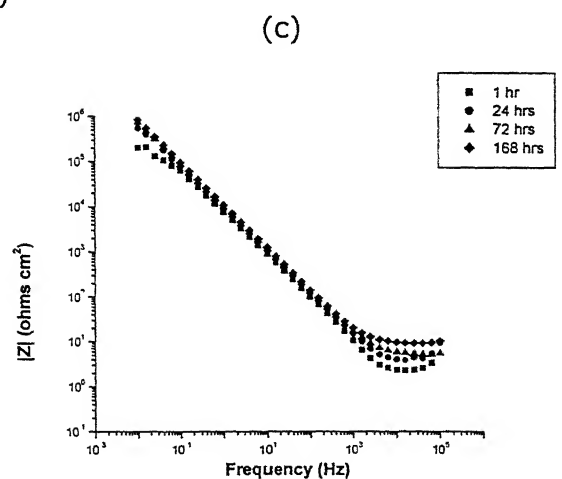


Figure 62: EIS data for Ti-6Al-4Nb as a function of immersion time in Hank's solution: (a) Nyquist plots (b) Bode phase plots and (c) Bode magnitude plots.

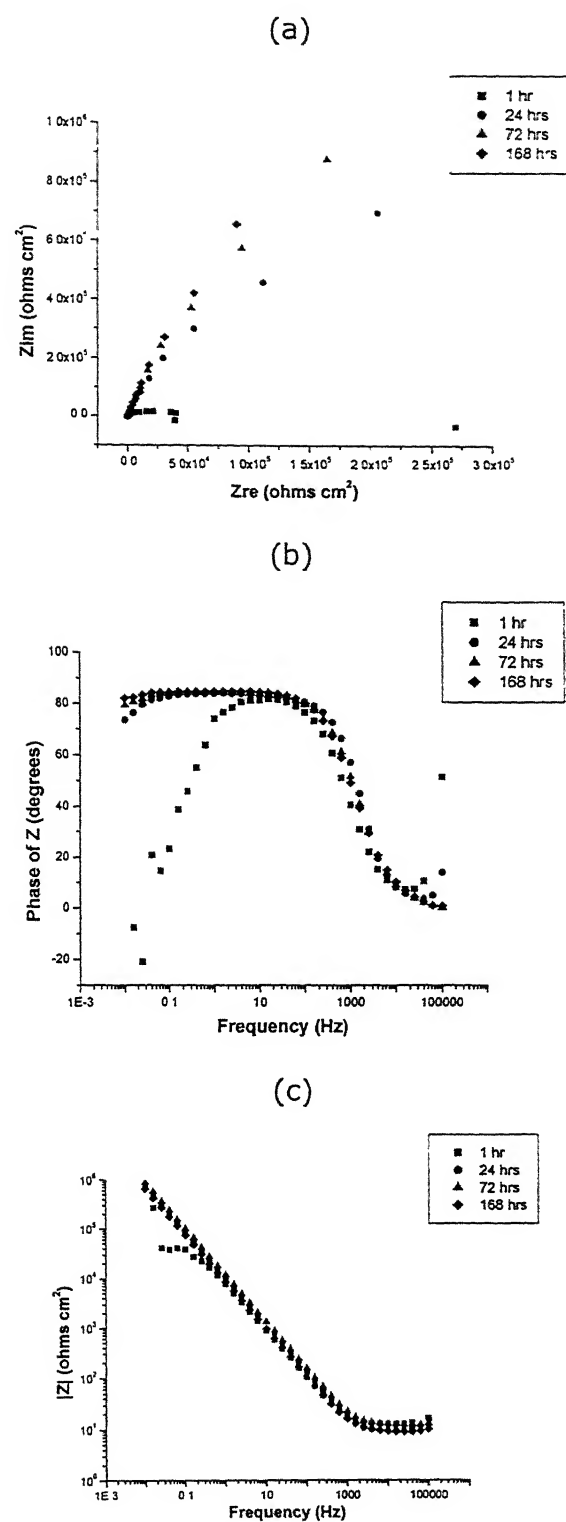


Figure 63: EIS data for Ti-8.4Al-15.4Nb as a function of immersion time in Hank's solution: (a) Nyquist plots (b) Bode phase plots and (c) Bode magnitude plots.



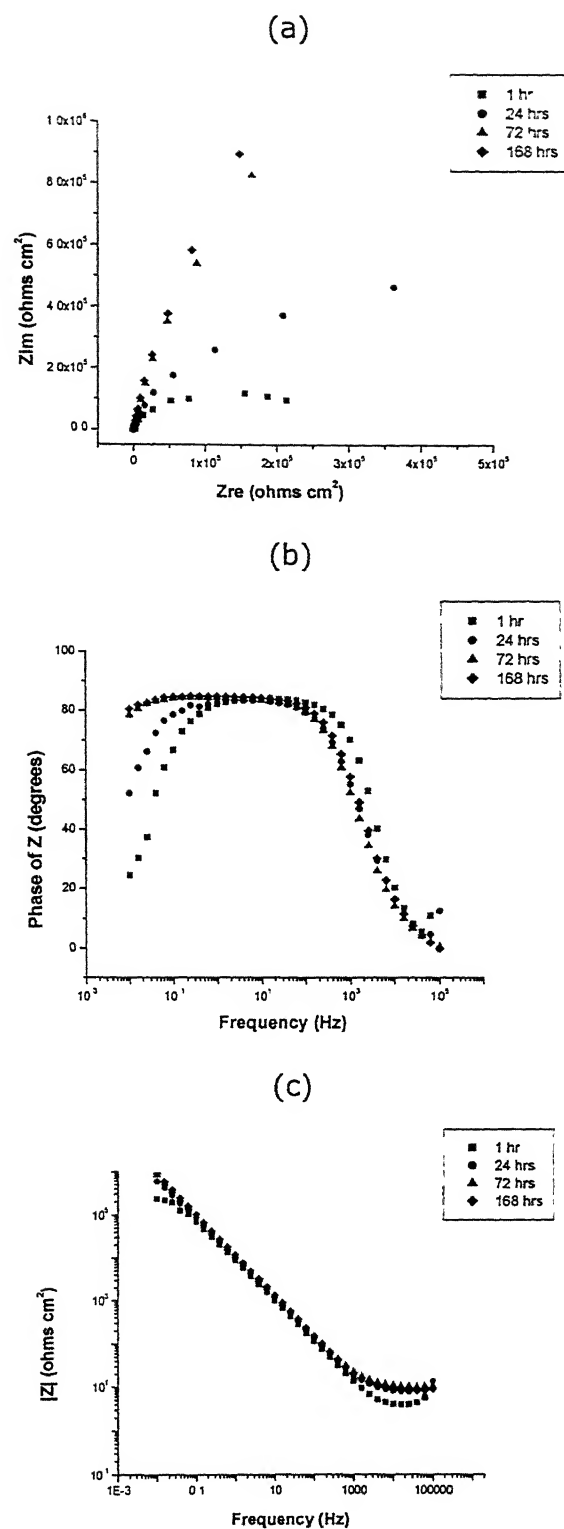


Figure 64: EIS data for Ti-13.4Al-29Nb as a function of immersion time in Hank's solution: (a) Nyquist plots (b) Bode phase plots and (c) Bode magnitude plots.

alloys. Bode magnitude plots were characterized by two distinct regions. In the higher frequency region (1-100 kHz), the Bode magnitude plots exhibited constant  $\log |Z|$  values vs.  $\log (f)$  with a phase angle near  $0^\circ$ . This was due to response of the electrolyte resistance  $R_s$  (resistive region). In the broad low and middle frequency range, the spectra displayed a linear slope of about -1. This is the characteristic response of a capacitive behavior of surface film [232].

It can be observed from the Nyquist plots that the diameter of the extrapolated semicircle (when drawn) increased with immersion time in Hank's solution. This feature was observed in Nyquist plots for all the alloys. In the case of CP Titanium, Ti-6Al-4V and Ti-13Nb-13Zr alloys, it was a little difficult to distinguish this (see Figures 57(a), 58(a) and 59(a)). However, in the other alloys, this was clearly observed. This suggests that for CP Titanium, Ti-6Al-4V and Ti-13Nb-13Zr alloys, the increase in polarization resistance was not as large as in other alloys.

It can be observed from Bode phase plots that the frequency range over which the phase angle is close to  $-90^\circ$  increases with immersion time in the Hank's solution. This feature was also present in all the spectra collected for all the alloys. Increase in frequency range over which phase angle is close to  $-90^\circ$  is indicative of film acquiring pure capacitive behavior. This observation suggested improvement in nature of surface film with immersion time. The nature of the Bode magnitude plots remained same with the immersion time in Hank's solution (Figures 57-64). The flat portion of the curve (slope  $\approx 0$ ), present in high frequency region, marginally shifted its position. This was due to minor changes in solution resistance ( $R_s$ ) with immersion time in Hank's solution for different alloys. However, the solution resistance was quite low (generally below 20 ohms-cm<sup>2</sup>) for all the alloys and also did not changed drastically with immersion time in Hank's solution.

The equivalent circuit shown in Figure 56 (a) was used to fit the experimental data, where  $R_s$  is solution resistance,  $R_p$  is polarization resistance and CPE is constant phase element. The physical model (Figure

56(b)) for this equivalent circuit, R(QR), is the presence of a single layer on metal surface possessing resistance as well as capacitance [232]. The surface film is considered to be a parallel circuit of a resistor, due to the ionic conduction through the film, and a capacitor due to its dielectric properties [219]. The fitting procedure revealed that better agreement between theoretical and experimental data was obtained if a frequency dependent constant-phase element (CPE) was used instead of pure capacitance and Warburg impedance. The impedance of a constant phase element is defined in as [219]:

$$Z_{CPE} = [Q(j\omega)^n]^{-1}$$

where Q and n are frequency independent parameters which usually depend on temperature and condition for n is:  $-1 \leq n \leq 1$  [219]. CPE describes an ideal capacitor for  $n = 1$ , an ideal resistor for  $n = 0$  and  $n = -1$  for a pure inductor [219]. Generally, the appearance of a CPE is due to the presence of inhomogeneities in the electrode-material system and it can be described in terms of a (nonnormalizable) distribution of relaxation times, or it may arise from non-uniform diffusion whose electrical analog is an inhomogeneously distributed RC transmission line. Low values of chi-squared and low % error in parameters were the main criteria while choosing the best fit model. The nature of Nyquist, Bode phase and Bode magnitude plots were also considered while choosing the best fit model.

Based on the fit of the of R(QR) model, the values of  $R_s$ ,  $Q_p$ , n and  $R_p$  were obtained. The % error, in different parameters, obtained while fitting the R(QR) model with experimental data has also been obtained. Chi-squared value was also calculated while fitting proposed R(QR) model with the experimentally measured EIS data. Chi-squared values are quite useful in judging the match of experimental curve with the curve generated by using the proposed equivalent circuit. Lower values of chi-square indicate better fit. All the parameters ( $R_s$ ,  $Q_p$ , n and  $R_p$ ) obtained for all the alloys based on the fitting procedure are tabulated separately in Tables 13 through 20. Each table provides these parameters, estimated at different immersion times in

Hank's solution, along with the chi-squared and % error values, for a single alloy.

The  $R_p$  and  $Q_p$  values for CP Titanium, Ti-6Al-4V and Ti-13Nb-13Zr alloys as a function of immersion time are plotted in Figures 65 and 66, respectively. These  $R_p$  and  $Q_p$  values for Ti-6Al-2.5Fe and Ti-6Al-4Fe alloys have been presented in Figures 67 and 68, respectively. The same values for Ti-6Al-4Nb, Ti-8.4Al-15.4Nb and Ti-13.4Al-29Nb alloys have been presented in Figures 69 and 70, respectively. To observe effect of replacement alloying element V by Nb and Fe, on passive film behavior, comparative curves of  $R_p$  and  $Q_p$  as a function of immersion time are provided in Figures 71 and 72, respectively.

The following conclusions can be derived by analyzing the data presented in Tables 13 through 20. It can be seen that the values of  $n$  were very close to one ( $n > 0.9$ ) for all the alloys for all the immersion times. This indicated a near capacitive behavior of the passive films formed on the Ti alloys. The solution resistance values did not vary notably for different alloys (Tables 13-20). The  $R_s$  values (1-50 ohms-cm<sup>2</sup>) obtained were relatively low compared to  $R_p$  values (0.1-10 Megaohms-cm<sup>2</sup>). The solution resistance did not change significantly with immersion time in Hank's solution for all the alloys (Tables 13-20).

The values of  $R_p$  and  $Q_p$  were analyzed carefully in order to study the effect of immersion time in Hank's solution on passive films on Ti based biomaterials. The  $R_p$  and  $Q_p$  values of all the alloys at all the immersions times in Hank's solution are tabulated in Table 21. It can be seen from Table 21 that passive film resistance for different alloys varied differently with immersion time in Hank's solution but  $Q_p$  did not change much with immersion time in Hank's solution. This indicates that the capacitive behavior of passive films on Ti alloys was affected by immersion time in Hank's solution.

It can be seen from Figure 65 that  $R_p$  values for CP Titanium increased steadily with immersion time in Hank's solution (see also Table 21). Figure 65 also indicates that the increase in  $R_p$  was not uniform for Ti-6Al-4V and Ti-

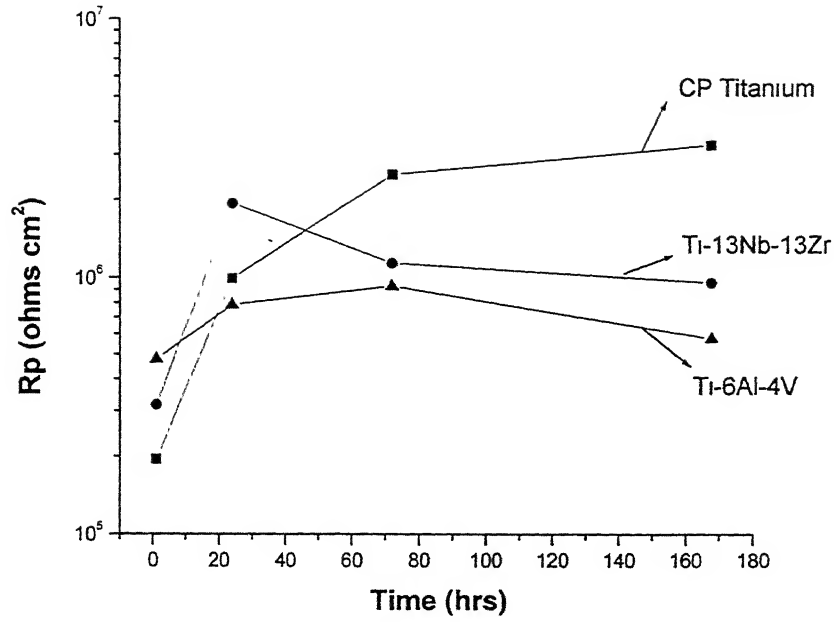


Figure 65: Polarization resistance ( $R_p$ ) as a function of immersion time in Hank's solution for CP titanium, Ti-6Al-4V and Ti-13Nb-13Zr alloys.

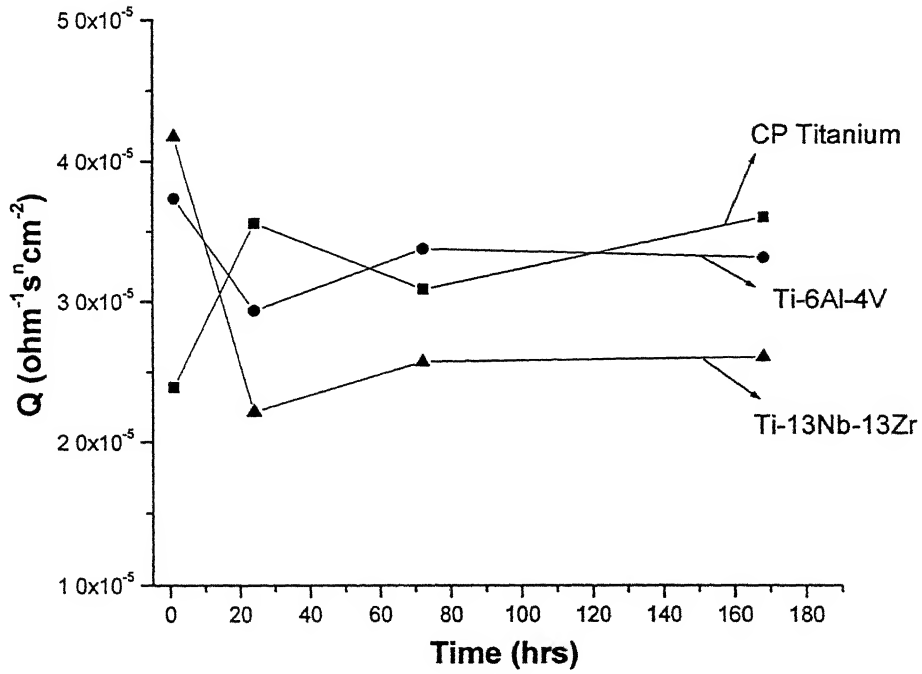


Figure 66: Constant phase element ( $Q_p$ ) as a function of immersion time in Hank's solution for CP titanium, Ti-6Al-4V and Ti-13Nb-13Zr alloys.

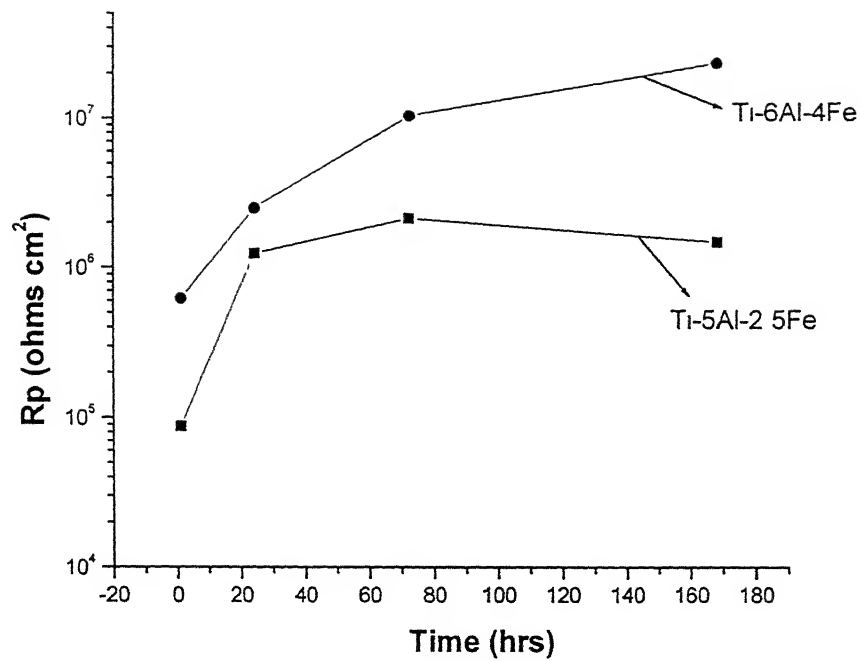


Figure 67: Polarization resistance ( $R_p$ ) as a function of immersion time in Hank's solution for Ti-5Al-2.5Fe and Ti-6Al-4Fe alloys.

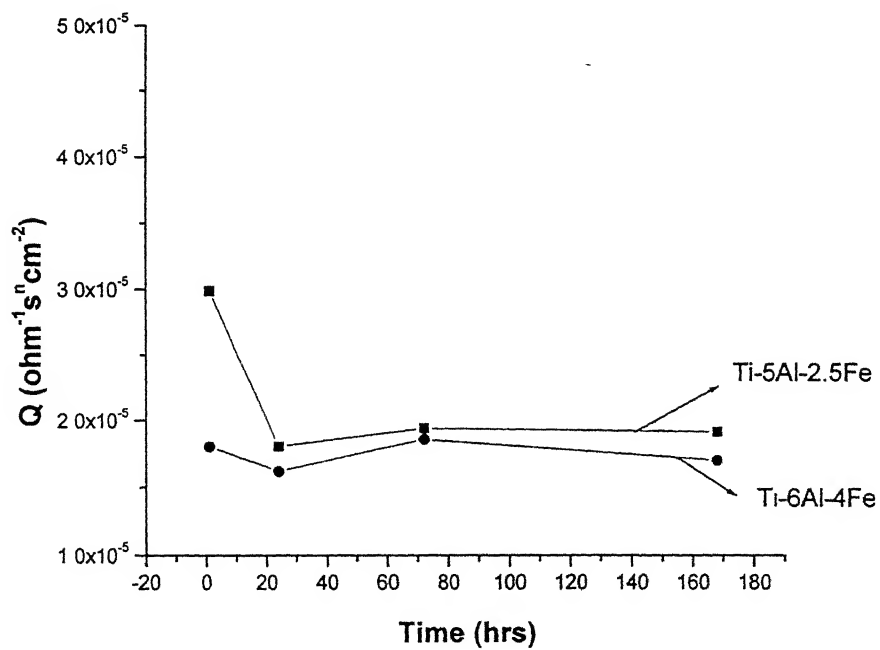


Figure 68: Constant phase element ( $Q_p$ ) as a function of immersion time in Hank's solution for Ti-5Al-2.5Fe and Ti-6Al-4Fe alloys.

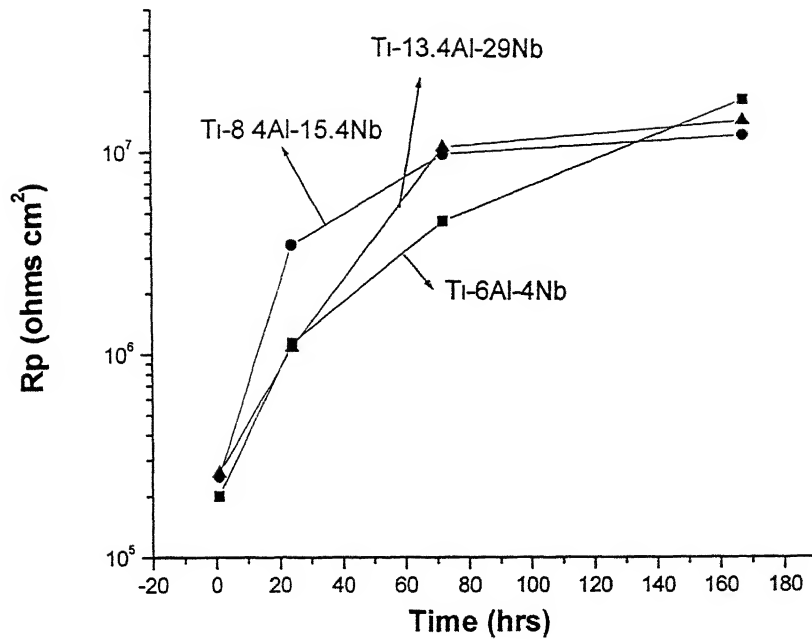


Figure 69: Polarization resistance ( $R_p$ ) as a function of immersion time in Hank's solution for Ti-6Al-4Nb, Ti-8.4Al-15.4Nb and Ti-13.4Al-29Nb alloys.

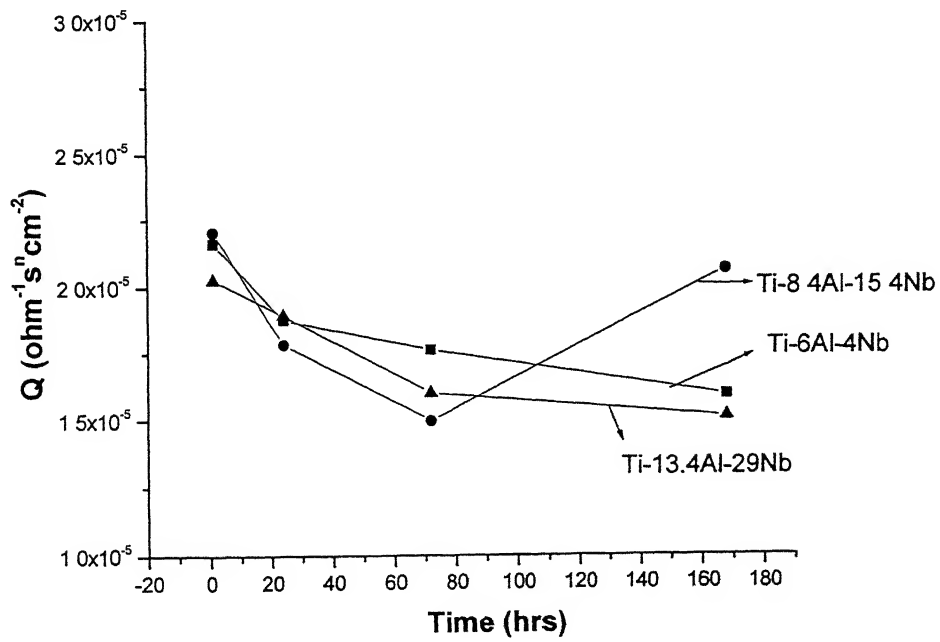


Figure 70: Constant phase element ( $Q_p$ ) as a function of immersion time in Hank's solution for Ti-6Al-4Nb, Ti-8.4Al-15.4Nb and Ti-13.4Al-29Nb alloys.

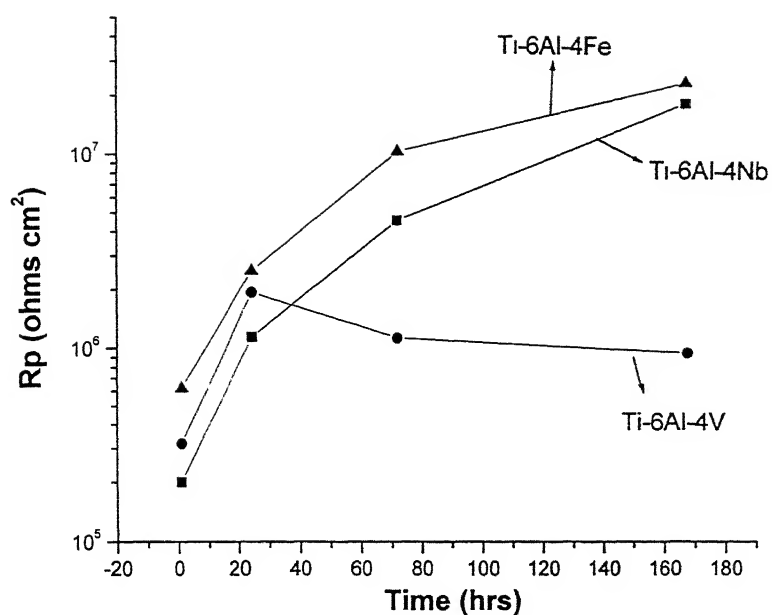


Figure 71: Polarization resistance ( $R_p$ ) as a function of immersion time in Hank's solution for Ti-6Al-4Nb, Ti-6Al-4V and Ti-6Al-4Fe alloys.

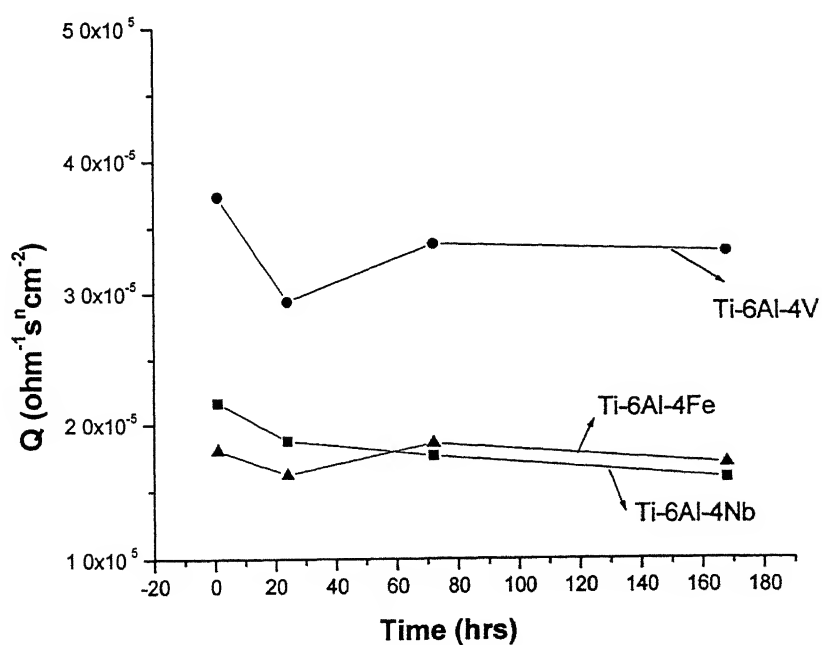


Figure 72: Constant phase element ( $Q_p$ ) as a function of immersion time in Hank's solution for Ti-6Al-4Nb, Ti-6Al-4V and Ti-6Al-4Fe alloys.



13Nb-13Zr alloys. There was an initial increase in  $R_p$  value with immersion time, but it decreased slightly after immersion time of 168 hrs in Hank's solution. The  $Q_p$  values for these alloys (Table 21) did not change significantly with time. Even though the  $R_p$  value for Ti-13Nb-13Zr alloy ( $0.477 \text{ M}\Omega \text{ cm}^2$ ) was higher than other two alloys, CP Titanium ( $0.195 \text{ M}\Omega \text{ cm}^2$ ) and Ti-6Al-4V ( $0.317 \text{ M}\Omega \text{ cm}^2$ ), after 1 hr of immersion, it did not improve significantly with immersion time in Hank's solution. After 168 hrs of immersion, the  $R_p$  value of CP Titanium ( $3.329 \text{ M}\Omega \text{ cm}^2$ ) was higher than that for Ti-6Al-4V ( $0.967 \text{ M}\Omega \text{ cm}^2$ ) and Ti-13Nb-13Zr ( $0.580 \text{ M}\Omega \text{ cm}^2$ ) alloys.

The increase in  $R_p$  for CP titanium with immersion time in Hank's solution can be attributed to increase in passive film thickness [230]. It has been reported in literature [146] that the vanadium oxide formed on the surface of Ti-6Al-4V alloy dissolves and leaves defects in surface film and also this process is further enhanced by presence of  $\text{Cl}^-$  ions. In present study, the initial increase and then decrease of  $R_p$  values of Ti-6Al-4V alloy can be related to the above phenomena as Hank's solution contains  $\text{Cl}^-$  ions. In the case of Ti-13Nb-13Zr alloy, the surface film resistance ( $R_p$ ) did not change significantly with immersion time. This suggests that the passive film of this alloy does not change significantly with immersion time in Hank's solution.

The Ti-5Al-2.5Fe and Ti-6Al-4Fe alloys revealed  $R_p$  of 0.088 and  $0.622 \text{ M}\Omega \text{ cm}^2$  after 1 hr of immersion in Hank's solution and  $R_p$  increased to 1.508 and  $24.31 \text{ M}\Omega \text{ cm}^2$  after 168 hrs of immersion (Table 21). The increase in  $R_p$  for Ti-6Al-4Fe alloy was higher than for Ti-5Al-2.5Fe alloy (Figure 67, Table 21). The  $Q_p$  values for the two alloys at different immersion time was almost same (Figure 68, Table 21). These observations indicate an improvement in the passive film behavior with immersion time in Hank's solution for these two alloys. Animesh have reported that alloying of Al in Ti based alloys has a deleterious effect on the passive film [226]. Hence, this increase in passive film resistance can be attributed to alloying of iron in these alloys. Furthermore, increased iron content showed higher passive film resistance. The increase in passive film resistance with immersion time in Hank's

solution of Ti-based alloys with iron as an alloying element has also been reported by Netula et al. [230].

The Ti-6Al-4Nb, Ti-8.4Al-15.4Nb and Ti-13.4Al-29Nb alloys revealed similar kind of nature for variation of passive film resistance ( $R_p$ ) with immersion time in Hank's solution (Figure 69).  $R_p$  increased with immersion time in Hank's solution for all these three alloys.  $R_p$  values for Ti-6Al-4Nb, Ti-8.4Al-15.4Nb and Ti-13.4Al-29Nb alloys after 1 hr of immersion were 0.201, 0.120 and 0.120  $M\Omega\text{ cm}^2$ , respectively, and the  $R_p$  values for these alloys increased to 18.99, 12.64 and 14.92 after 168 Hrs of immersion in Hank's solution (Table 21). The variation of constant phase element ( $Q_p$ ) with immersion time in Hank's solution for Ti-6Al-4Nb, Ti-8.4Al-15.4Nb and Ti-13.4Al-29Nb alloys also revealed a similar kind of nature (Figure 70). The  $Q_p$  values for all the alloys were in a very narrow region between  $1.5 \times 10^{-5}$  and  $2.3 \times 10^{-5} \Omega^{-1}\text{s}^n\text{cm}^{-2}$ . This indicated that the capacitive behavior of these alloys did not change with immersion time in Hank's solution. The increase in  $R_p$  values suggested an improvement in passive film behavior for these alloys with immersion time in Hank's solution. In the literature, it had been reported that Nb as alloying element has a stabilizing effect on surface films on Ti based alloys [139]. Metikos et al. [146], in their study on influence of Nb addition on passivity of Ti based implants in Hank's solution, concluded that the Nb cations improve the passivation properties of surface film by annihilating the stoichiometric defects present on titanium oxide film.

The variation of passive film resistance ( $R_p$ ) with immersion time for Ti-6Al-4Nb, Ti-6Al-4V and Ti-6Al-4Fe are provided in Figure 71, while the same for constant phase element ( $Q_p$ ) are shown in Figure 72. It can be observed that passive film resistance for Ti-6Al-4Nb and Ti-6Al-4Fe alloys increased steadily with immersion time in Hank's solution, while it ( $R_p$ ) increased initially and then decreased for Ti-6Al-4V alloy (Figure 71, Table 21). Constant phase element for Ti-6Al-4Nb and Ti-6Al-4Fe were almost same at different immersion times in Hank's solution and these values were different from that of Ti-6Al-4V alloy (Figure 72, Table 21).

These observations suggested that alloying elements Nb and Fe have improved the passive film resistance. In the literature, it had been reported that Nb as alloying element has a stabilizing effect on surface films on Ti based alloys [139]. Metikos et al. [146], in their study on influence of Nb addition on passivity of Ti based implants in Hank's solution, concluded that the Nb cations improve the passivation properties of surface film by annihilating the stoichiometric defects present on titanium oxide film. Netula et al. [230] also have reported the increased corrosion resistance, with immersion time in Hank's solution, of Ti-based alloys with iron as an alloying element. Netula et al. have reported similar comparative behavior of Ti-7Al-4.5V and Ti-5Al-2.5Fe in Hank's solution. In their study also passive film resistance for Ti-5Al-2.5Fe alloy increased with immersion time in Hank's solution whereas for Ti-7Al-4.5V passive film resistance initially increased and then decreased slightly with immersion time in Hank's solution. One reason for this difference in passive film nature of Ti-6Al-4V has been reported in literature [146]. Vanadium oxide formed on the surface of Ti-6Al-4V alloy dissolves. This dissolution of vanadium oxide is further enhanced by presence of  $\text{Cl}^-$  ions in Hank's solution. Hence, vanadium as an alloying element could not improve the surface film on Ti-6Al-4V alloy [146]. In present study, the changes in passive film nature of Ti-6Al-4V alloy with immersion time in Hank's solution (contains  $\text{Cl}^-$  ions) can be attributed to same phenomena. The vanadium present in Ti-6Al-4V alloy does not contribute significantly to improvement of passive film properties, whereas its replacement by elements like Nb and Fe do improve the passive surface film nature with immersion time in Hank's solution.

Table 13: Values of fitting parameters obtained by fitting R(QR) model to the EIS data obtained as a function of immersion time in Hank's solution for CP Titanium. Values in brackets are the % errors in various parameters while fitting the experimental data in to the proposed model.

<b>Material</b>	<b>Immersion Time</b>	<b>Chi-Squared</b>	<b><math>R_s</math> (ohm-cm<sup>2</sup>)</b>	<b><math>Q_p</math> (ohm<sup>-1</sup>s<sup>n</sup>cm<sup>-2</sup>)</b>	<b>n</b>	<b><math>R_p</math> (ohm-cm<sup>2</sup>)</b>
CP Titanium	1 hr	1.057e-01	16.66 (9.422)	2.392E-5 (10.22)	0.9811 (2.292)	1.949E5 (18.83)
	24 hrs	3.011e-02	21.82 (5.604)	3.559E-5 (4.581)	0.9065 (1.202)	9.933E5 (42.25)
	72 hrs	3.825e-02	3.005 (7.271)	3.092E-5 (4.983)	0.9271 (1.014)	2.516E6 (93.19)
	168 hrs	2.346e-02	1.593 (6.257)	3.606E-5 (3.879)	0.9222 (0.7522)	3.329E6 (112.7)

Table 14: Values of fitting parameters obtained by fitting R(QR) model to the EIS data obtained as a function of immersion time in Hank's solution for Ti-6Al-4V alloy. Values in brackets are the % errors in various parameters while fitting the experimental data in to the proposed model.

Material	Immersion Time	Chi-Squared	$R_s$ (ohm-cm <sup>2</sup> )	$Q_p$ (ohm <sup>-1</sup> s <sup>n</sup> cm <sup>-2</sup> )	n	$R_p$ (ohm-cm <sup>2</sup> )
Ti-6Al-4V	1 hr	1.073e-02	18.13 (3.019)	3.735E-5 (2.914)	0.9271 (0.7315)	3.174E5 (10.19)
	24 hrs	3.964e-02	5.804 (7.168)	2.938E-5 (5.155)	0.8956 (1.128)	1.937E6 (76.87)
	72 hrs	2.786e-02	3.57 (6.066)	3.38E-5 (4.32)	0.9181 (0.9028)	1.141E6 (42.09)
	168 hrs	8.232e-03	3.301 (3.305)	3.322E-5 (2.356)	0.9244 (0.4858)	9.667E5 (19.08)

Table 15: Values of fitting parameters obtained by fitting R(QR) model to the EIS data obtained as a function of immersion time in Hank's solution for Ti-13Nb-13Zr alloy. Values in brackets are the % errors in various parameters while fitting the experimental data in to the proposed model.

Material	Immersion Time	Chi-Squared	$R_s$ (ohm-cm <sup>2</sup> )	$Q_p$ (ohm <sup>-1</sup> s <sup>n</sup> cm <sup>-2</sup> )	n	$R_p$ (ohm-cm <sup>2</sup> )
<b>Ti-13Nb-13Zr</b>	1 hr	2.276e-02	3.091 (5.086)	4.177E-5 (4.113)	0.9565 (0.8638)	4.773E5 (19.71)
	24 hrs	2.467e-02	2.433 (6.406)	2.215E-5 (4.172)	0.9278 (0.7918)	7.852E5 (19.79)
	72 hrs	4.851e-02	2.951 (9.021)	2.575E-5 (5.798)	0.9002 (1.152)	9.295E5 (38.31)
	168 hrs	5.122e-02	1.069 (10.12)	2.611E-5 (6.015)	0.9434 (1.065)	5.802E5 (24.86)

Table 16: Values of fitting parameters obtained by fitting R(QR) model to the EIS data obtained as a function of immersion time in Hank's solution for Ti-5Al-2.5Fe alloy. Values in brackets are the % errors in various parameters while fitting the experimental data in to the proposed model.

Material	Immersion Time	Chi-squared	$R_s$ (ohm-cm <sup>2</sup> )	$Q_p$ (ohm <sup>-1</sup> s <sup>n</sup> cm <sup>-2</sup> )	n	$R_p$ (ohm-cm <sup>2</sup> )
Ti-5Al-2.5Fe	1 hr	1.564e-02	7.389 (4.418)	2.988E-5 (4.315)	0.9215 (0.8938)	8.75E4 (6.45)
	24 hrs	6.101e-01	8.785 (18.16)	1.804E-5 (21.7)	0.9059 (8.94)	1.239E6 (33.9)
	72 hrs	3.573e-03	4.84 (2.451)	1.942E-5 (1.631)	0.9156 (0.3291)	2.146E6 (24.23)
	168 hrs	6.709e-03	4.76 (3.16)	1.916E-5 (2.138)	0.9112 (0.433)	1.508E6 (16.26)

Table 17: Values of fitting parameters obtained by fitting R(QR) model to the EIS data obtained as a function of immersion time in Hank's solution for Ti-6Al-4Fe alloy. Values in brackets are the % errors in various parameters while fitting the experimental data in to the proposed model.

Material	Immersion Time	Chi-Squared	$R_s$ (ohm-cm <sup>2</sup> )	$Q_p$ (ohm <sup>-1</sup> s <sup>n</sup> cm <sup>-2</sup> )	n	$R_p$ (ohm-cm <sup>2</sup> )
Ti-6Al-4Fe	1 hr	2.873e-02	2.008 (8.663)	1.802E-5 (4.638)	0.9494 (0.8373)	6.219E5 (15.19)
	24 hrs	2.225e-02	7.574 (5.413)	1.619E-5 (3.891)	0.9175 (0.8106)	2.507E6 (39.49)
	72 hrs	9.705e-04	13.83 (1.029)	1.858E-5 (0.8018)	0.9125 (0.1846)	1.046E7 (38.16)
	168 hrs	5.153e-04	44.48 (0.6577)	1.702E-5 (0.5831)	0.9215 (0.1525)	2.431E7 (57.91)



Table 18: Values of fitting parameters obtained by fitting R(QR) model to the EIS data obtained as a function of immersion time in Hank's solution for Ti-6Al-4Nb alloy. Values in brackets are the % errors in various parameters while fitting the experimental data in to the proposed model

Material	Immersion Time	Chi-Squared	$R_s$ (ohm-cm <sup>2</sup> )	$Q_p$ (ohm <sup>-1</sup> s <sup>n</sup> cm <sup>-2</sup> )	n	$R_p$ (ohm-cm <sup>2</sup> )
Ti-6Al-4Nb	1 hr	2.598e-02	2.492 (6.673)	2.163E-5 (4.969)	0.9559 (0.9011)	2.005E5 (9.323)
	24 hrs	4.542e-02	5.433 (7.619)	1.875E-5 (5.612)	0.9404 (1.138)	1.14E6 (30.54)
	72 hrs	6.263e-04	5.42 (0.9142)	1.762E-5 (0.6367)	0.9338 (0.1297)	4.618E6 (12.23)
	168 hrs	1.095e-03	9.733 (1.117)	1.594E-5 (0.8391)	0.9397 (0.1802)	1.899E7 (58.31)

Table 19: Values of fitting parameters obtained by fitting R(QR) model to the EIS data obtained as a function of immersion time in Hank's solution for Ti-8.4Al-15.4Nb alloy. Values in brackets are the % errors in various parameters while fitting the experimental data in to the proposed model.

Material	Immersion Time	Chi-Squared	$R_s$ (ohm-cm <sup>2</sup> )	$Q_p$ (ohm <sup>-1</sup> s <sup>n</sup> cm <sup>-2</sup> )	n	$R_p$ (ohm-cm <sup>2</sup> )
Ti-8.4Al-15.4Nb	1 hr	1.017e-01	12.09 (10.56)	2.3E-5 (10.93)	0.9426 (2.318)	1.198E5 (16.37)
	24 hrs	1.738e-02	10.7 (4.324)	1.783E-5 (3.403)	0.9419 (0.7434)	3.489E6 (48.8)
	72 hrs	1.507e-04	12.61 (0.405)	1.498E-5 (0.3124)	0.9388 (0.06857)	9.882E6 (10.67)
	168 hrs	7.692e-04	9.268 (0.9065)	2.067E-5 (0.704)	0.9439 (0.1546)	1.264E7 (41.76)

Table 20: Values of fitting parameters obtained by fitting R(QR) model to the EIS data obtained as a function of immersion time in Hank's solution for Ti-13.4Al-29Nb alloy. Values in brackets are the % errors in various parameters while fitting the experimental data in to the proposed model.

<b>Material</b>	<b>Immersion Time</b>	<b>Chi-Squared</b>	<b><math>R_s</math> (ohm-cm<sup>2</sup>)</b>	<b><math>Q</math> (ohm<sup>-1</sup>s<sup>n</sup>cm<sup>-2</sup>)</b>	<b>n</b>	<b><math>R_p</math> (ohm-cm<sup>2</sup>)</b>
Ti-13.4Al-29Nb	1 hr	7.992e-03	4.223 (3.514)	2.026E-5 (2.707)	0.9421 (0.5195)	2.593E5 (5.65)
	24 hrs	1.471e-02	9.187 (4.092)	1.893E-5 (3.251)	0.9314 (0.6972)	1.082E6 (17.24)
	72 Hrs	1.716e-03	10.55 (1.4)	1.601E-5 (1.054)	0.9324 (0.2289)	1.071E7 (42.33)
	168 Hrs	1.429e-03	8.561 (1.31)	1.512E-5 (0.9582)	0.9386 (0.2018)	1.492E7 (49.83)

Table 21: Passive film resistance ( $R_p$ ) and constant phase element ( $Q_p$ ) values obtained by fitting R(QR) model to the EIS data for the Ti alloys used in the study as a function of immersion time in Hank's solution.

Material	$R_p$ ( $M\Omega$ $cm^2$ )				$Q_p$ ( $\times 10^5 \Omega^{-1}s^n cm^{-2}$ )			
	1 hr	24 hrs	72 hrs	168 hrs	1 hr	24 hrs	72 hrs	168 hrs
CP Titanium	0.195	0.993	2.516	3.329	2.392	3.559	3.092	3.606
Ti-6Al-4V	0.317	1.937	1.141	0.967	3.735	2.938	3.38	3.322
Ti-13Nb-13Zr	0.477	0.785	0.930	0.580	4.177	2.215	2.575	2.611
Ti-5Al-2.5Fe	0.088	1.239	2.146	1.508	2.988	1.804	1.942	1.916
Ti-6Al-4Fe	0.622	2.507	10.46	24.31	1.802	1.619	1.858	1.702
Ti-6Al-4Nb	0.201	1.140	4.618	18.99	2.163	1.875	1.762	1.594
Ti-8.4Al-15.4Nb	0.120	3.489	9.882	12.64	2.3	1.783	1.498	2.067
Ti-13.4Al-29Nb	0.259	1.082	10.71	14.92	2.026	1.893	1.601	1.512

## **4.3 Effect of NaOH treatment**

Three of the alloys investigated, namely CP Titanium, Ti-6Al-4V and Ti-13Nb-13Zr, were immersed in 5M NaOH solution at a temperature of 60°C for 24Hr. These alloys were then immersed in simulated body fluid (Hank's Solution) and the changes in the properties of passive film on these three alloys were investigated as a function of immersion time by means of electrochemical impedance spectroscopy and potentiodynamic polarization. In order to understand the possible changes in surface film nature, the surfaces of these alloys after various treatments were examined using XRD and SEM techniques.

The results obtained are presented and discussed below.

### **4.3.1 Surface characterization**

#### **4.3.1.1 X-Ray Diffraction**

In order to study the changes taking place on the surface of CP Titanium, Ti-6Al-4V and Ti-13Nb-13Zr alloys after NaOH treatment and also due to immersion in Hank's solution, X-Ray diffraction pattern was obtained from the surface. The results obtained are presented and discussed below.

X-Ray diffraction patterns of all the alloys, CP Titanium, Ti-6Al-4V and Ti-13Nb-13Zr, were obtained at three stages. The XRD patterns were obtained for these alloys without any surface treatment, after NaOH treatment and also after immersing these NaOH-treated samples in Hank's solution for 168 hrs. The XRD patterns for CP Titanium, Ti-6Al-4V and Ti-13Nb-13Zr alloys, taken at three stages, are provided in Figures 73, 74 and 75, respectively. The XRD patterns for the untreated materials have been indexed using Diffrac-Plus and presented in Appendix D. The patterns obtained after surface treatments have been superimposed with the peaks due to  $\text{Na}_2\text{TiO}_3$  and presented in Appendix D. This was again performed using

Diffraction-Plus software. The standard diffraction pattern for apatite is also provided in Appendix D.

The XRD pattern for untreated CP Titanium alloy exhibited peaks of  $\alpha$  phase (i.e. h.c.p Ti) (JCPDF 44-1294) (Figure 73(a)). No clear distinguishable peaks were observed in the XRD patterns (Figure 73(b) and 73(c)) obtained after NaOH treatment and also after 168 hrs of Immersion in Hank's solution.

The XRD pattern of untreated Ti-6Al-4V alloy exhibited peaks corresponding to both  $\alpha$  (i.e. h.c.p Ti) and  $\beta$  (i.e. b.c.c Ti) phases (Figure 74(a)). It can be observed from Figures 74(b) and 74(c) that the XRD patterns obtained of Ti-6Al-4V after NaOH treatment and also after immersion of 168 hrs in Hank's solution exhibited a small peak around two theta angle of  $58^\circ$ , which was not present in the XRD pattern obtained for untreated Ti-6Al-4V. This peak may be due to presence of  $\text{Na}_2\text{TiO}_3$  (JCPDF 28-1152).

The XRD pattern obtained for untreated Ti-13Nb-13Zr alloy exhibited peaks of  $\beta$  phase (b.c.c Ti) (JCPDF 44-1288) and  $\alpha$  phase (JCPDF 44-1294). These peaks have been marked in Figure 75(a). The relatively higher  $\beta$  phase peak intensities indicate the higher volume fraction of  $\beta$  phase in this alloy. It can be observed from Figures 75(b) and 75(c) that the XRD patterns obtained of Ti-13Nb-13Zr after NaOH treatment and also after immersion of 168 hrs in Hank's solution indicated the presence of  $\text{Na}_2\text{TiO}_3$  on the surface.

In all the cases, apatite peaks could not be firmly established in the XRD patterns obtained after immersion in Hank's solution. However, SEM studies (to be presented later) clearly indicated apatite formation on the surfaces of all the samples after NaOH treatment and subsequent immersion in Hank's solution for 168 hrs.

In the literature it has been reported [171-191] that the Ti alloys on treatment with NaOH solution produces a sodium titanate gel layer on the titanium surface. This gel layer, of sodium titanate, has the ability to induce formation of bone-like apatite during immersion in simulated body fluid. The gel layer can initiate apatite nucleation on itself. Once apatite nucleation

occurs, it spontaneously grows by taking calcium and phosphate ions from the surrounding environment (Hank's solution).

Although apatite formation has been reported in the literature, peaks due to apatite could not be clearly distinguished.

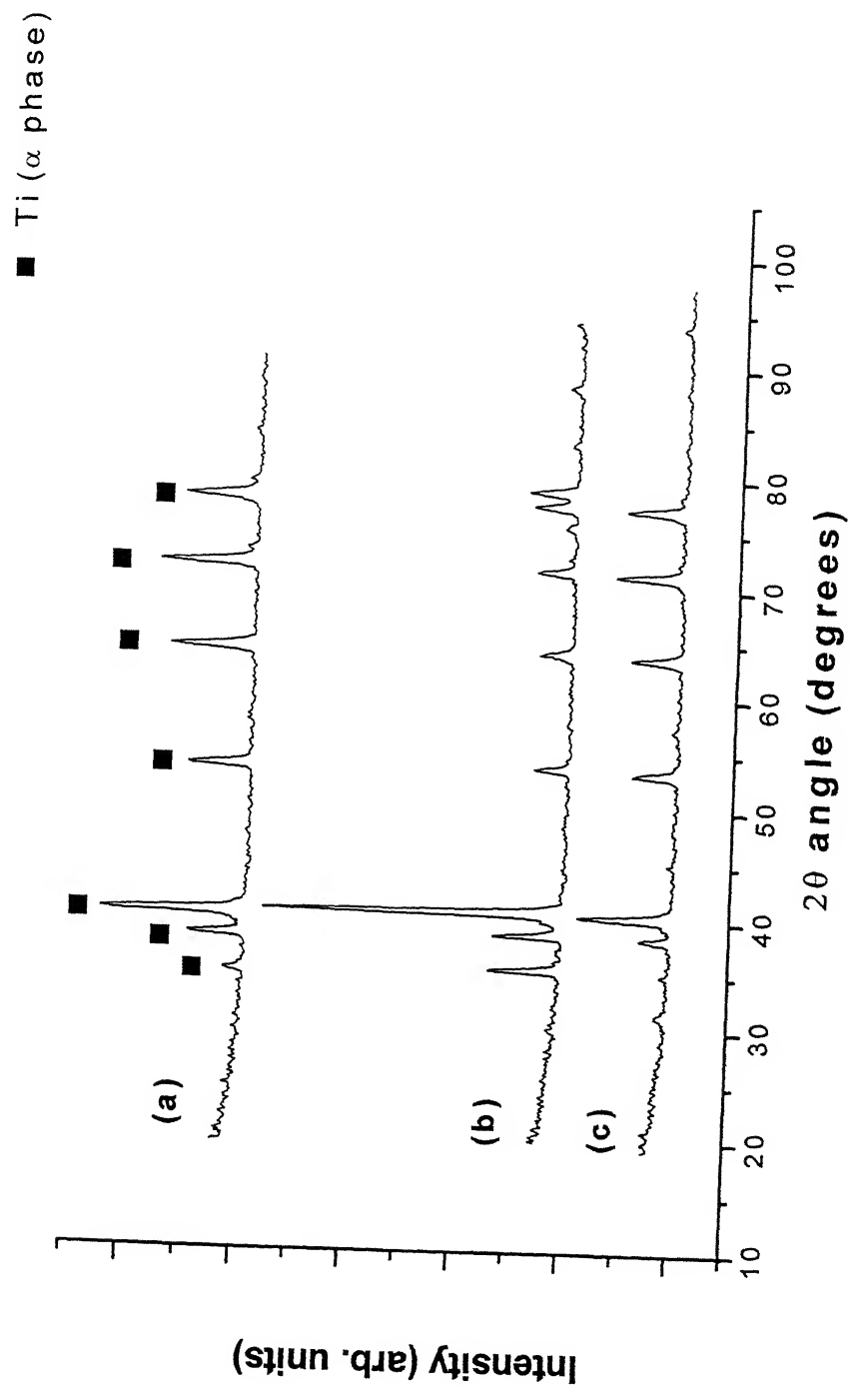


Figure 73: X-Ray Diffraction pattern obtained from the surface of CP Titanium: (a) untreated (b) treated with NaOH, and (c) Treated with NaOH and immersed in Hank's solution for 168 hrs.



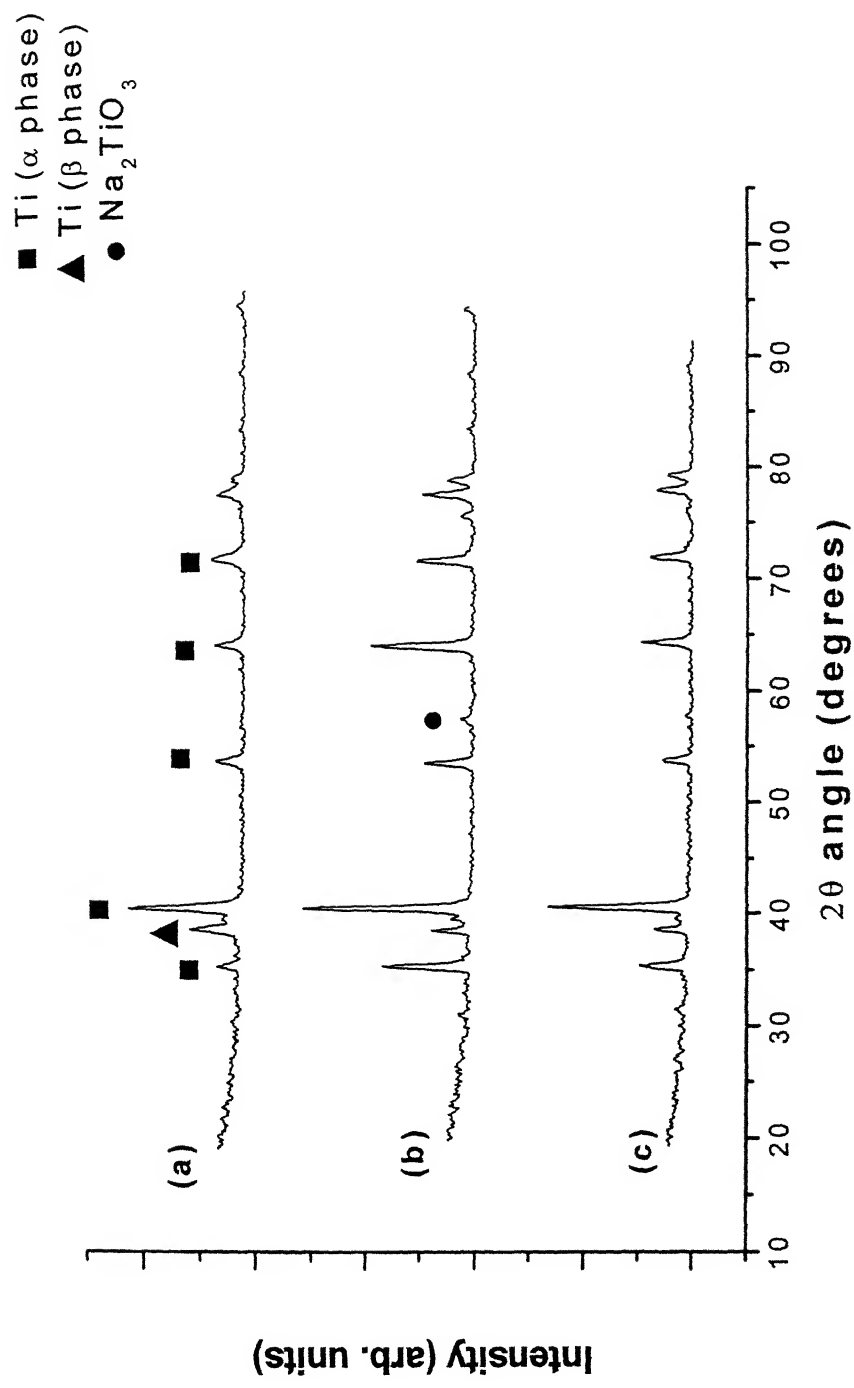


Figure 74: X-Ray Diffraction pattern obtained from the surface of Ti-6Al-4V: (a) untreated (b) treated with NaOH, and (c) treated with NaOH and immersed in Hank's solution for 168 hrs.

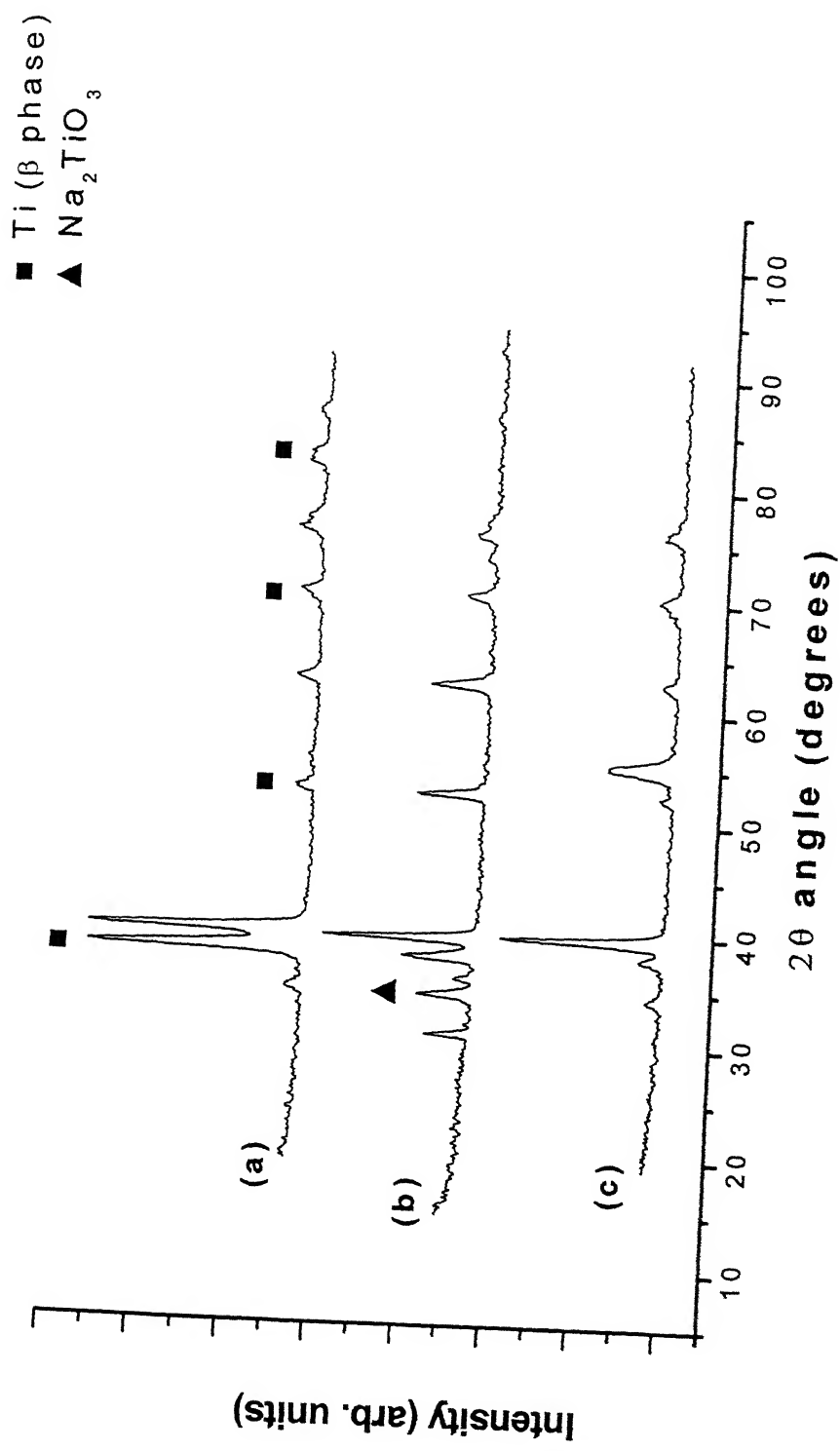


Figure 75: X-Ray Diffraction patterns obtained from the surface of Ti-13Nb-13Zr: (a) untreated (b) treated with NaOH, and (c) treated with NaOH and immersed in Hank's solution for 168 hrs.

#### 4.3.1.2 Scanning Electron Microscopy

The surfaces of the alloys, CP titanium, Ti-6Al-4V and Ti-13Nb-13Zr were observed in a scanning electron microscope (SEM), just after NaOH treatment as well as after immersing these NaOH-treated samples in Hank's solution for 168 hrs. The samples for these observations were specially treated for SEM observations and XRD studies and these were not the samples used for electrochemical studies.

The surface of NaOH-treated CP Titanium revealed a relatively porous structure at high magnifications (Figures 76). A similar porous layer on NaOH-treated CP Titanium surface was also reported by Wang et al. [201]. Layer formation was clearly indicated on the surfaces of Ti-6Al-4V and Ti-13Nb-13Zr (Figure 77 and 78). Cracks observed on these surfaces indicated relatively thicker layer on the surface. It has been reported in the literature that sodium titanate gel layer forms on the Ti alloys on reaction with NaOH [201,202]. As these micrographs were obtained after drying the NaOH treated samples for 24 hrs, the gel layer dried up and developed cracks on the layer surface. These cracked surface layers on NaOH-treated Ti-6Al-4V and Ti-13Nb-13Zr alloys, in contrast to porous layer on NaOH-treated CP Titanium surface, can be attributed to enhanced interaction of Ti-6Al-4V and Ti-13Nb-13Zr alloys with NaOH solution.

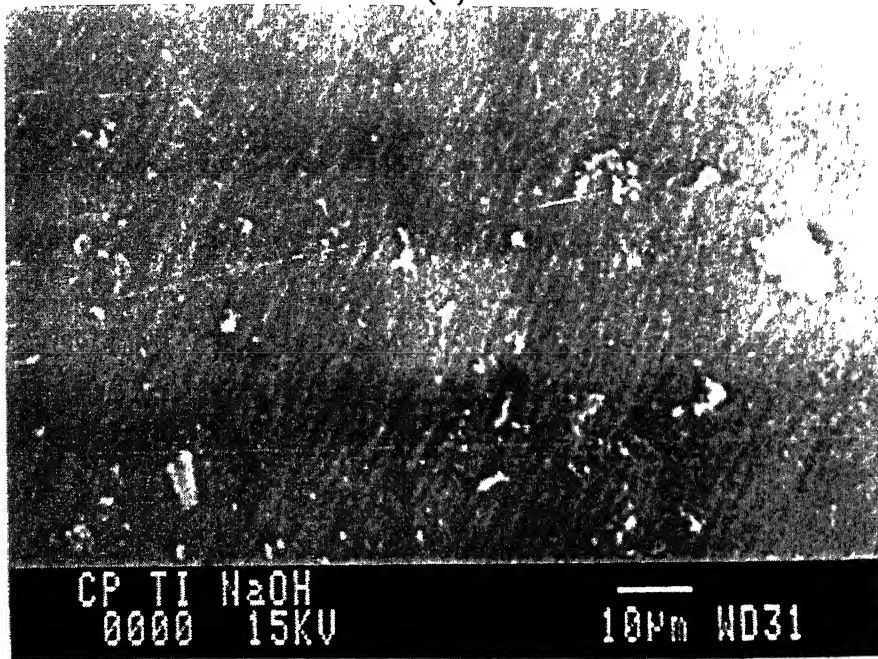
The SEM micrographs obtained after immersing the NaOH-treated CP Titanium, Ti-6Al-4V and Ti-13Nb-13Zr alloys in Hank's solution for 168 hrs are provided in figures 79, 80 and 81, respectively. All the surfaces exhibited similar features namely a product phase was present on a porous network structure. It has been reported by Wang et al. [202] that this porous network was composed of calcium titanate which formed on reaction of sodium titanate with calcium ions of Hank's solution. Moreover, the island type of product phase was identified as apatite which grew with immersion time in Hank's solution and covered the whole surface (see Figure 11). The results of

the present study are in agreement with earlier studies.

For the NaOH-treated CP Titanium, the XRD analysis could not detect any change on the surface and SEM also showed a porous passive layer. These observations suggest that there was a limited reaction of NaOH with the titanium surface and product of this reaction i.e. sodium titanate could not form a uniform layer on the CP titanium surface. However, on the surface of NaOH-treated CP titanium porous network of calcium titanate and nuclei of apatite were observed by SEM after 168 hrs of immersion in Hank's solution. This suggests formation of a new layer (second layer apart from first passive layer of  $\text{TiO}_2$ ) on NaOH-treated CP titanium surface after 168 hrs of immersion in Hank's solution.

The XRD patterns obtained of surfaces of NaOH-treated Ti-6Al-4V and Ti-13Nb-13Zr alloys revealed a small peak of sodium titanate and SEM analysis also showed a cracked layer on the surface of these alloys after NaOH treatment. These two observations suggest a new layer (second layer apart from first passive layer of  $\text{TiO}_2$ ) of sodium titanate on the surface of Ti-6Al-4V and Ti-13Nb-13Zr alloys. SEM analysis showed porous network of calcium titanate and apatite nuclei on the surface of these two alloys also. This suggests formation of an extra layer (third layer) on NaOH-treated Ti-6Al-4V and Ti-13Nb-13Zr surfaces after 168 hrs of immersion in Hank's solution.

(a)



(b)

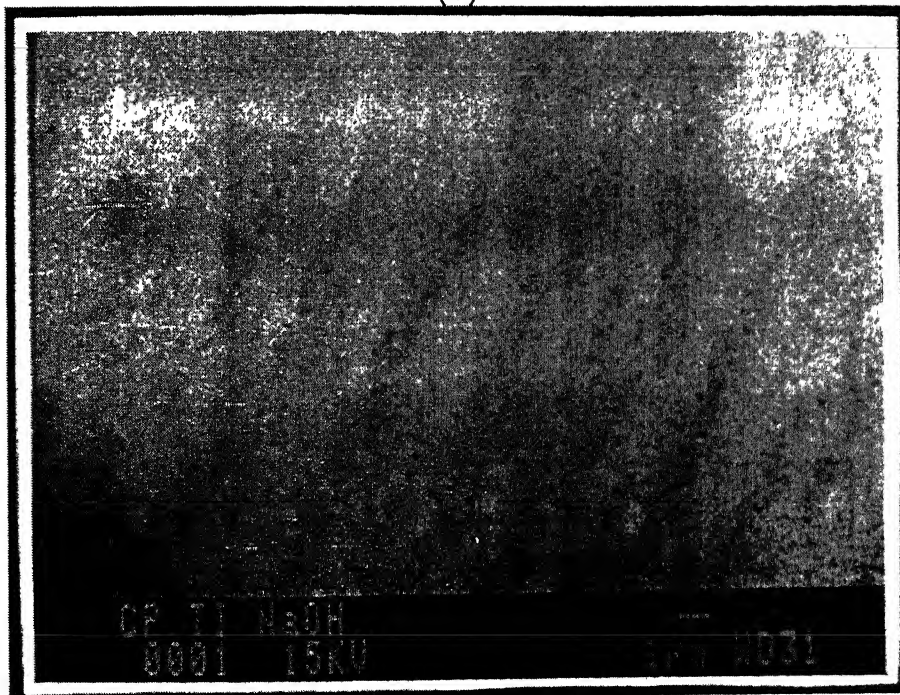
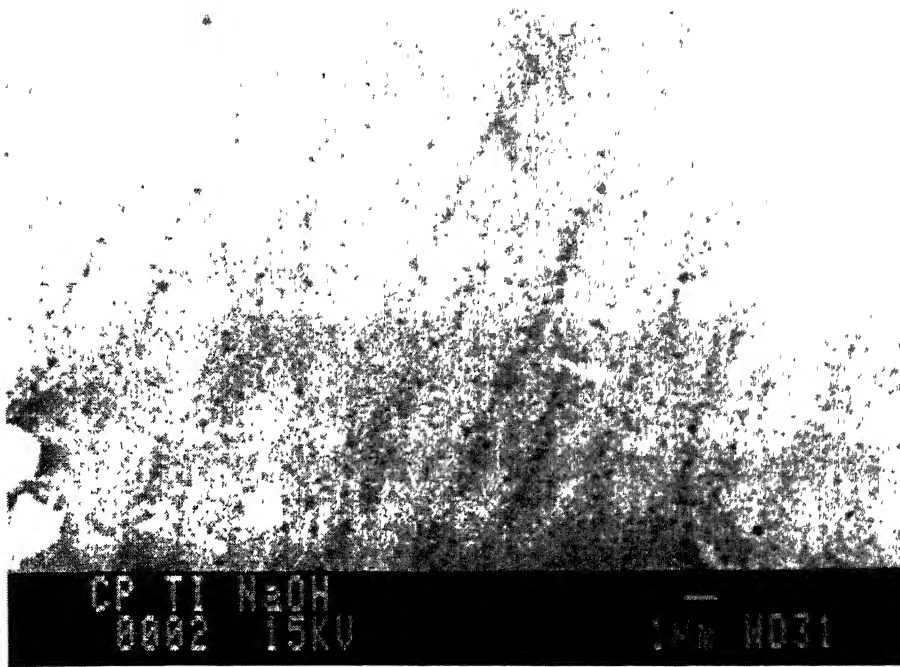


Figure 76: SEM micrographs of NaOH treated surface of CP Titanium.

(c)



(d)

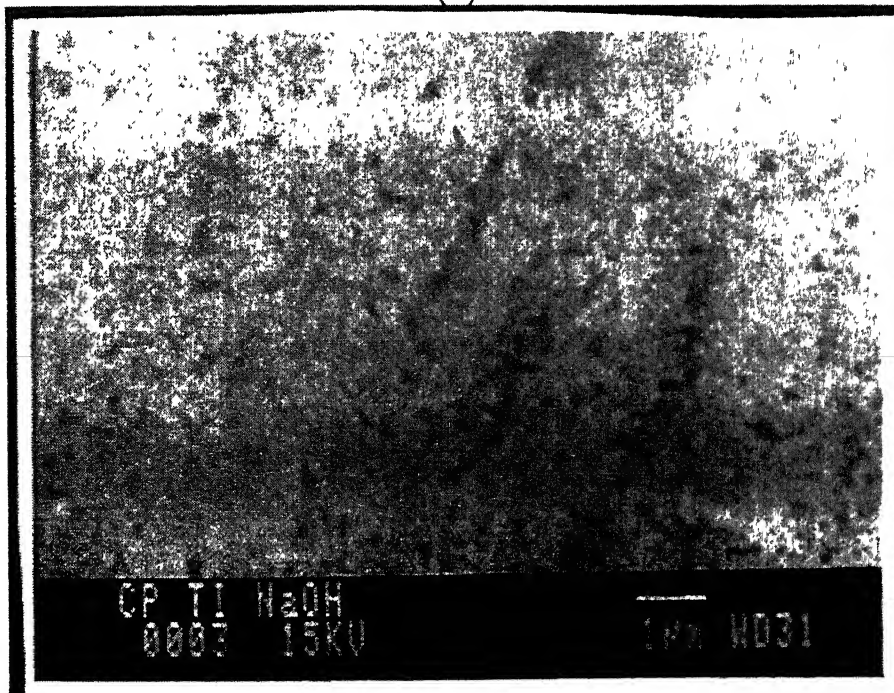


Figure 76(contd.): SEM micrographs of NaOH treated surface of CP Titanium.

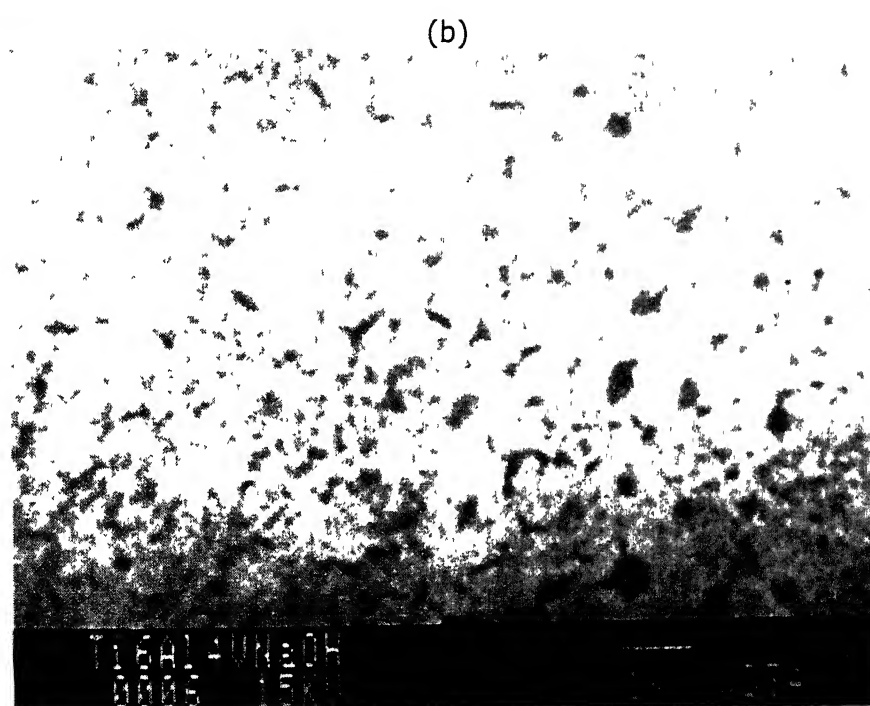
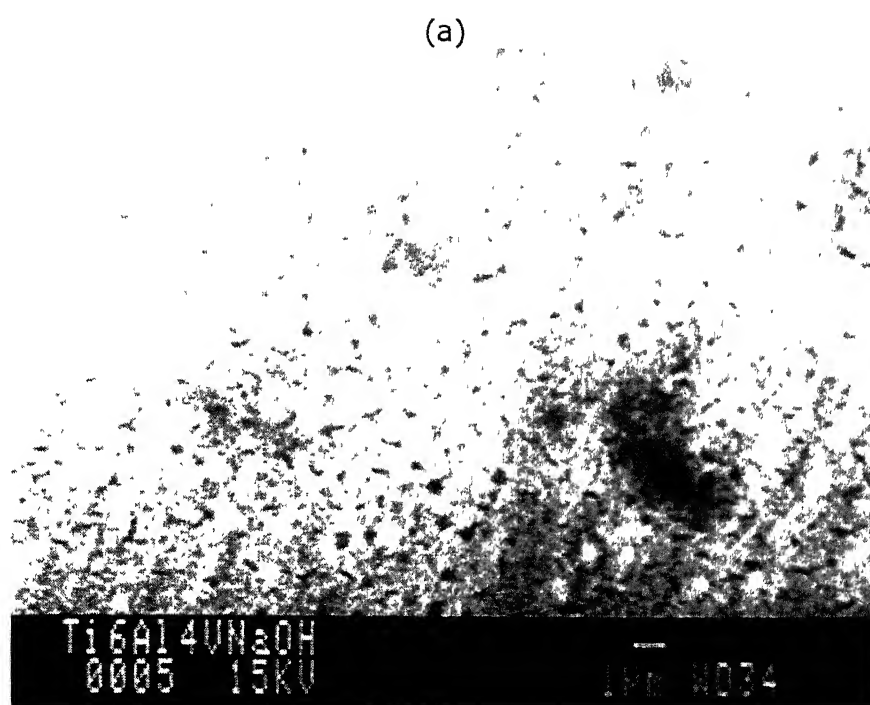


Figure 77: SEM micrographs of surface of NaOH-treated Ti-6Al-4V alloy.

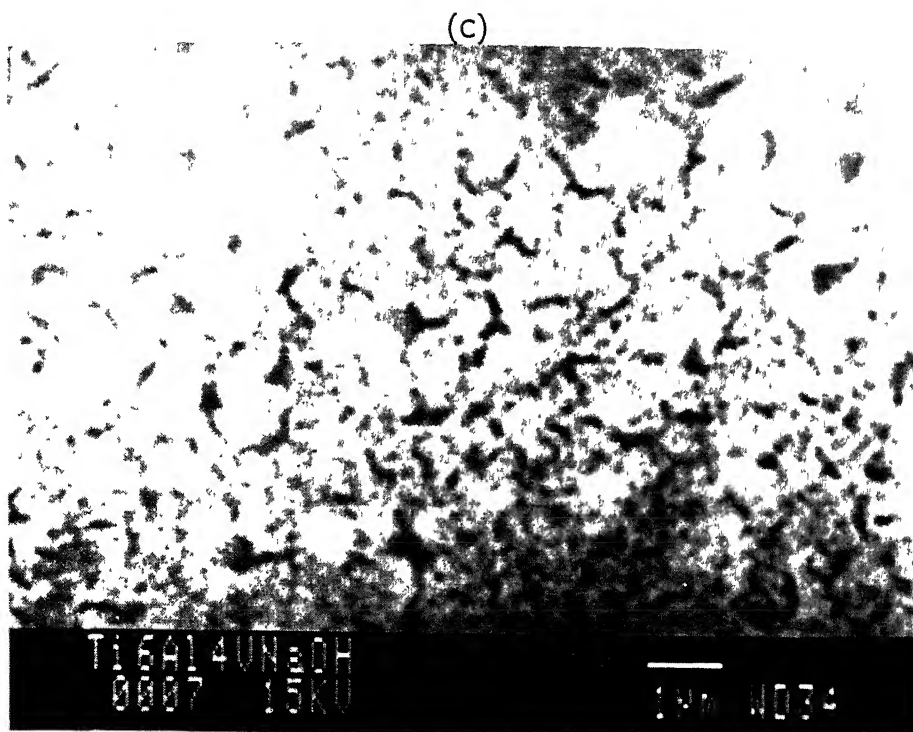


Figure 77(contd.): SEM micrographs of surface of NaOH-treated Ti-6Al-4V alloy.



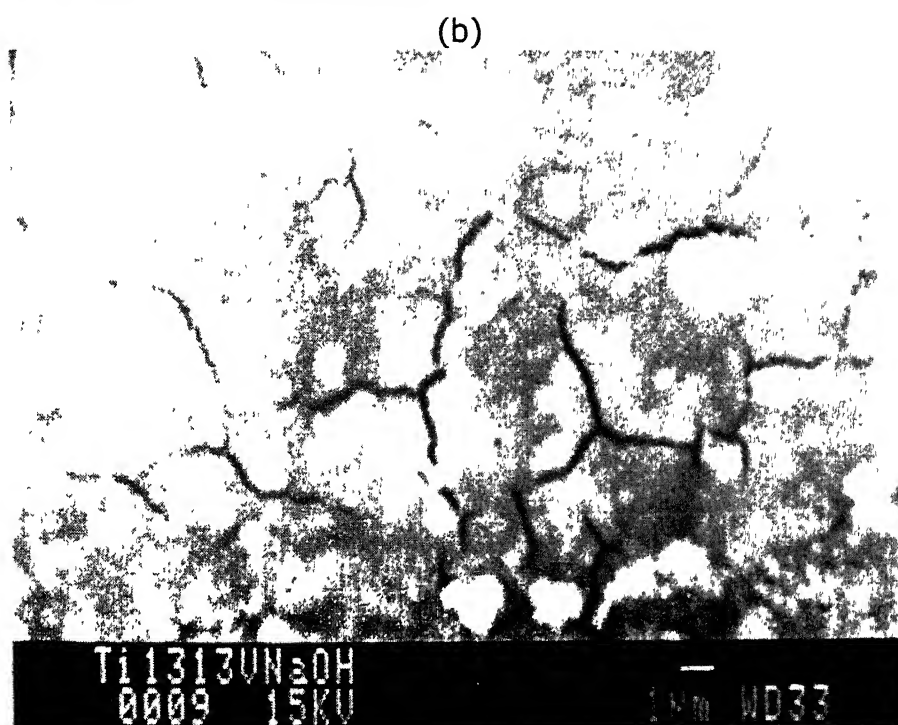
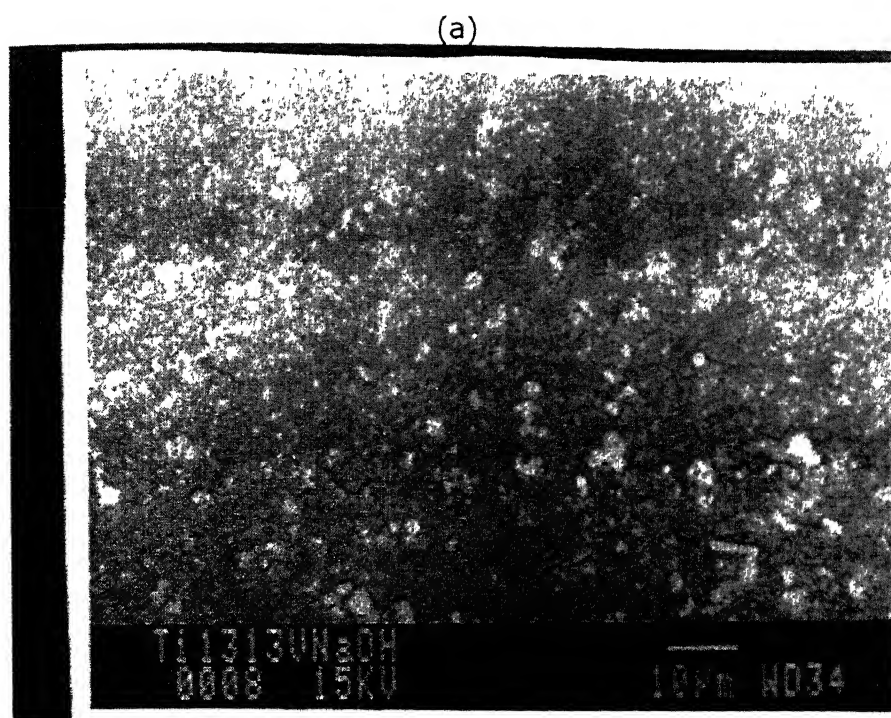


Figure 78: SEM micrographs of surface of NaOH-treated Ti-13Nb-13Zr alloy.

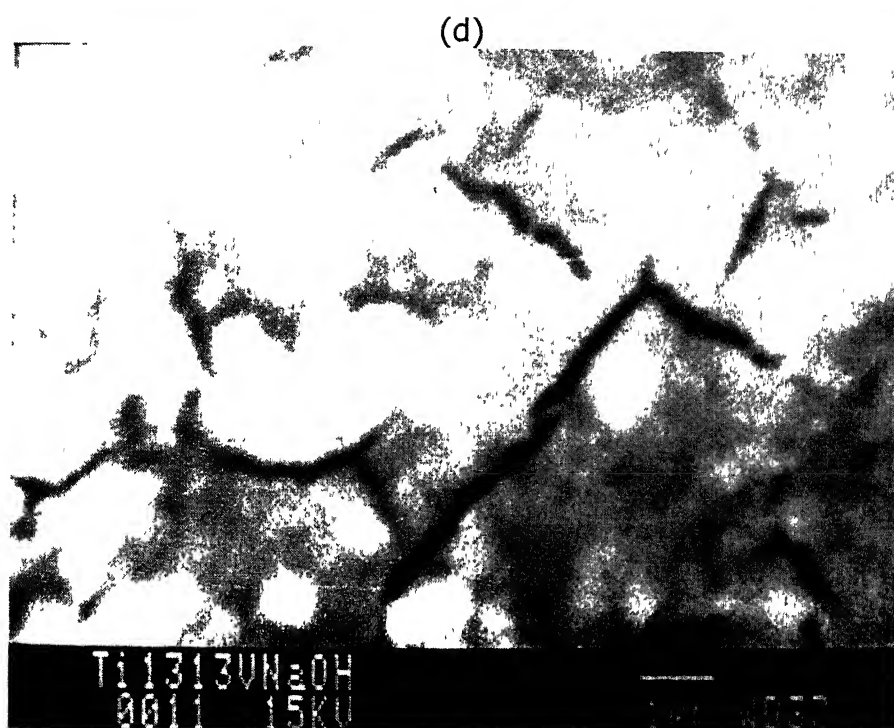
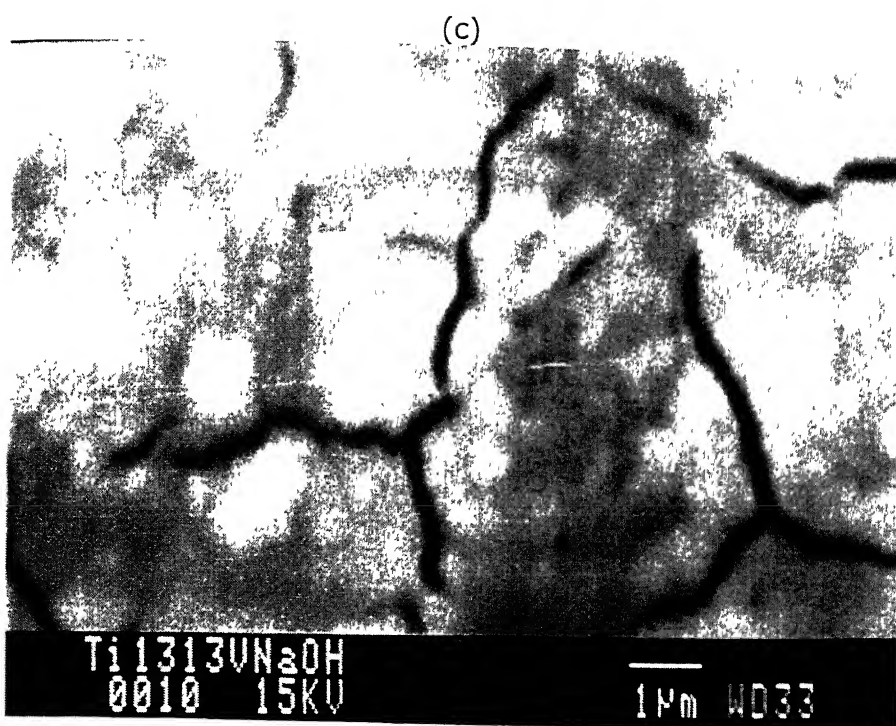
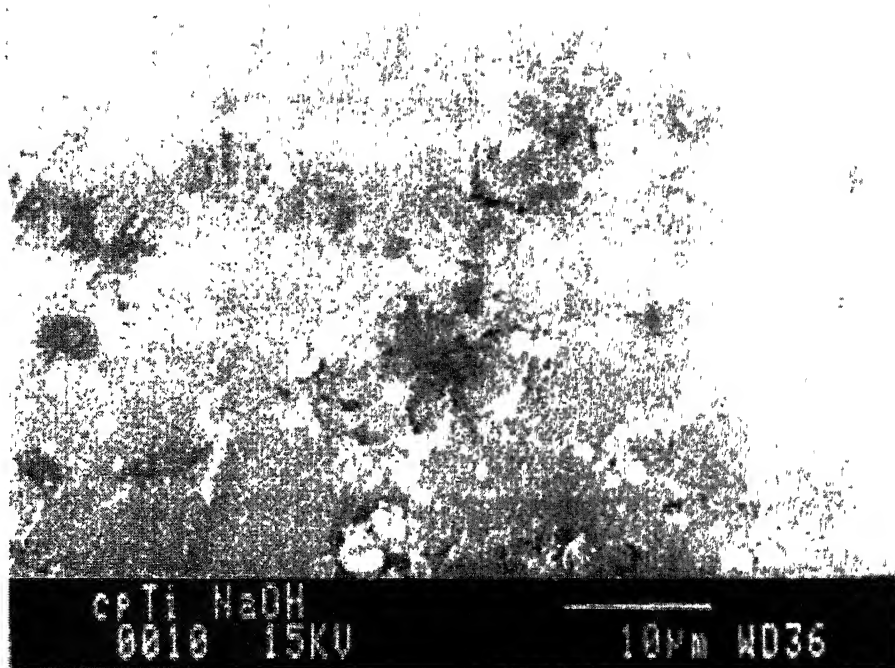


Figure 78(contd.): SEM micrographs of surface of NaOH-treated Ti-13Nb-13Zr alloy.

(a)



(b)

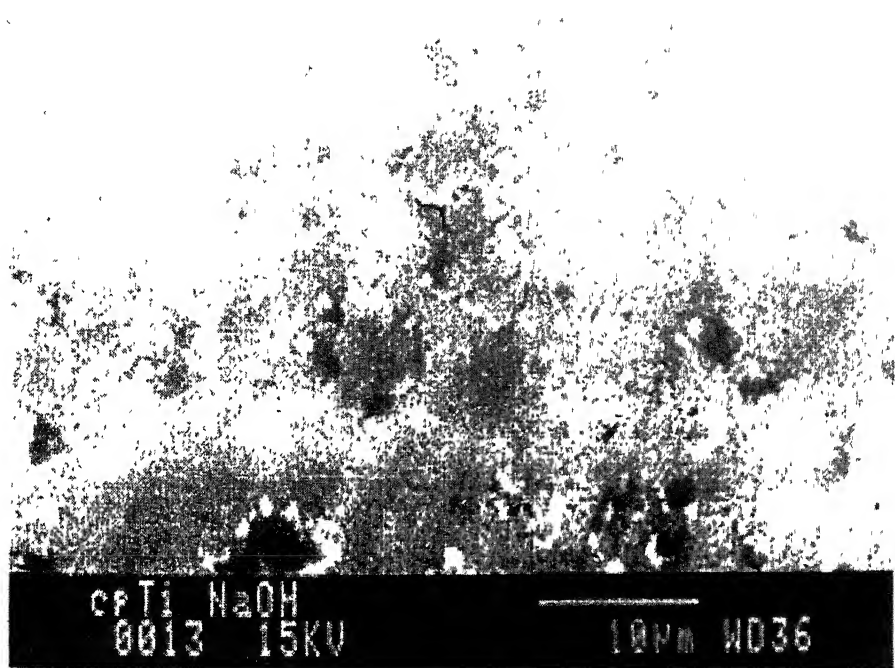
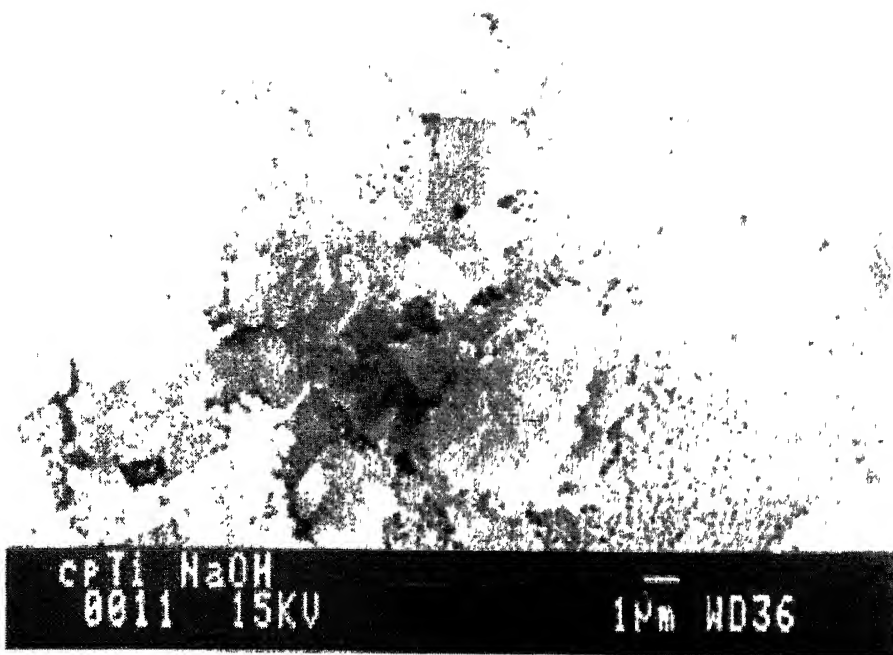


Figure 79: SEM micrographs of surface of NaOH-treated CP titanium after immersion of 1week in Hank's Solution.

(c)



(d)

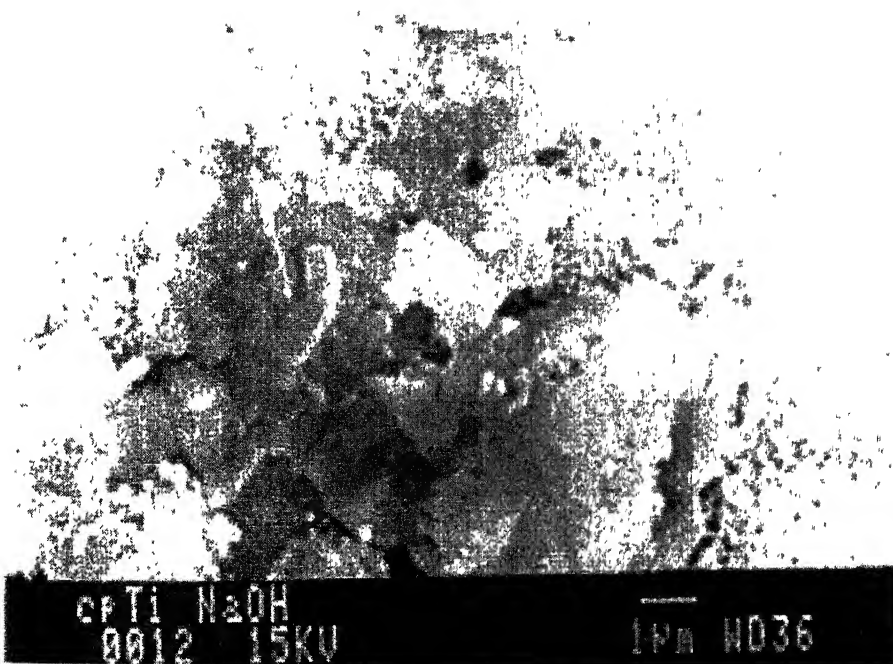
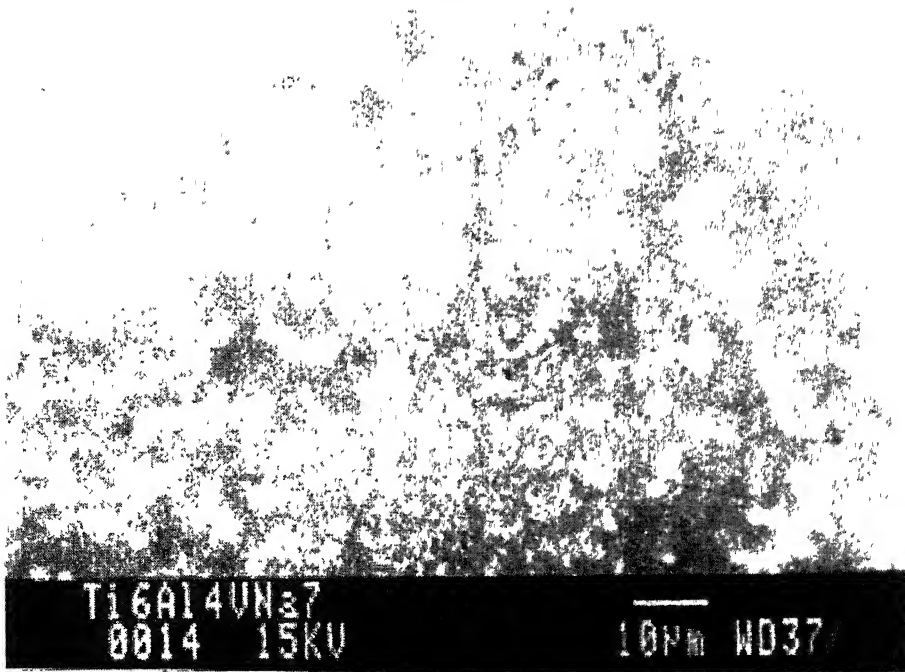


Figure 79(contd.): SEM micrographs of surface of NaOH-treated CP titanium after immersion of 1week in Hank's Solution.

(a)



(b)

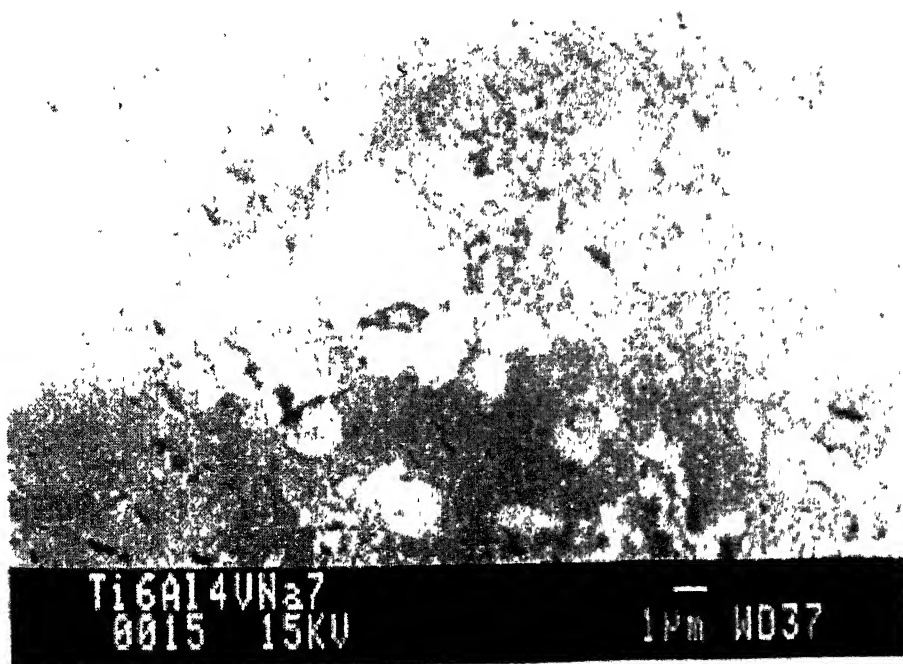
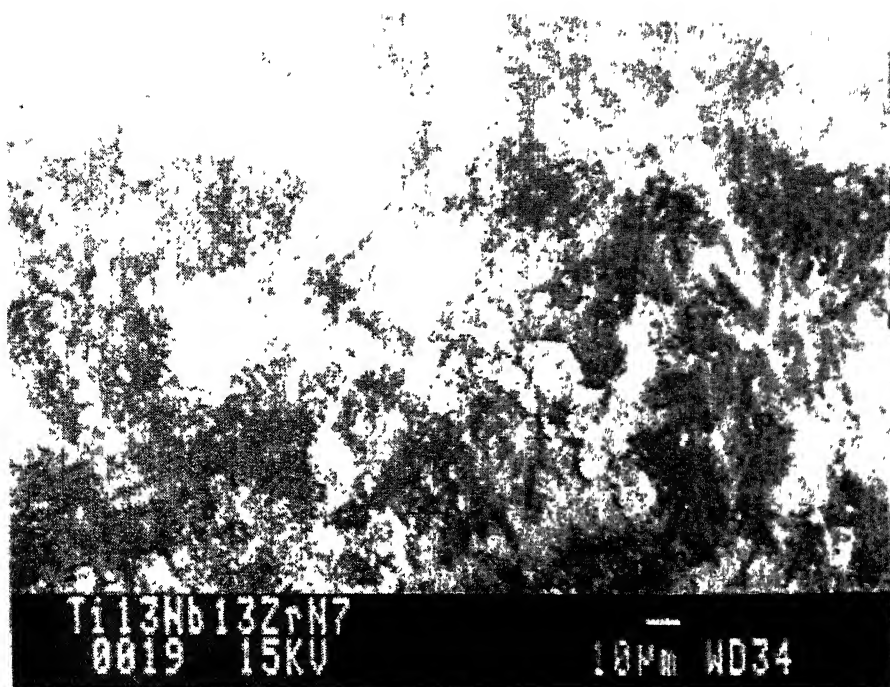


Figure 80: SEM micrographs of the surface of NaOH-treated Ti-6Al-4V alloy after immersion of 1week in Hank's Solution.

(a)



(b)

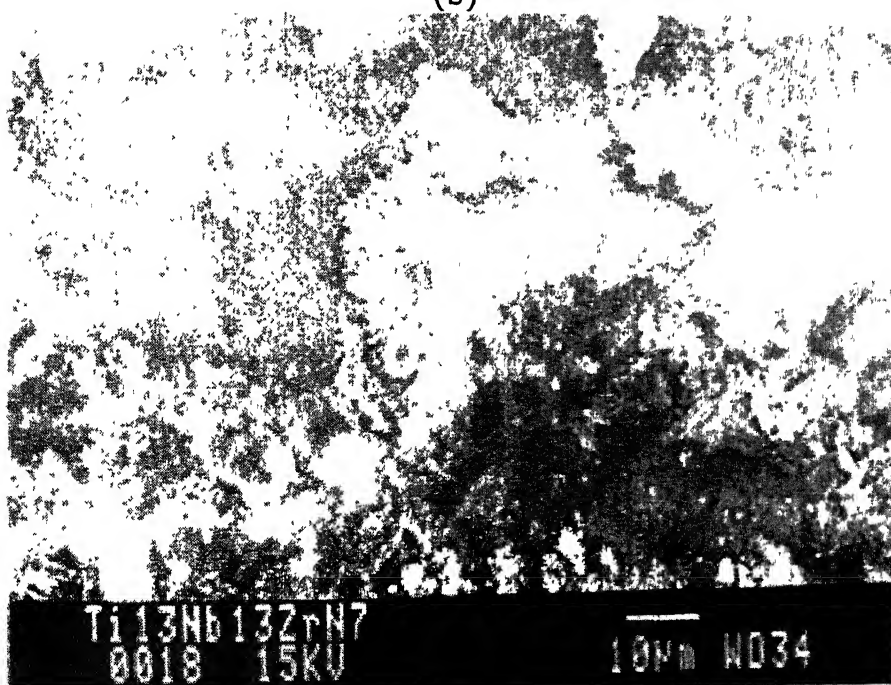


Figure 81: SEM micrographs of surface of NaOH-treated Ti-13Nb-13Zr alloy after immersion of 1 week in Hank's Solution.



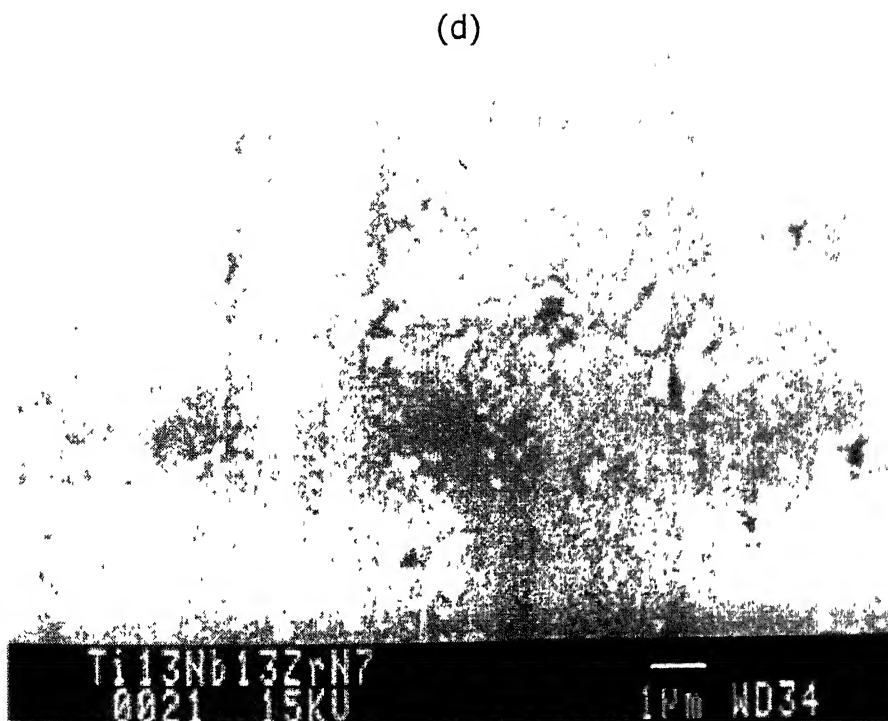
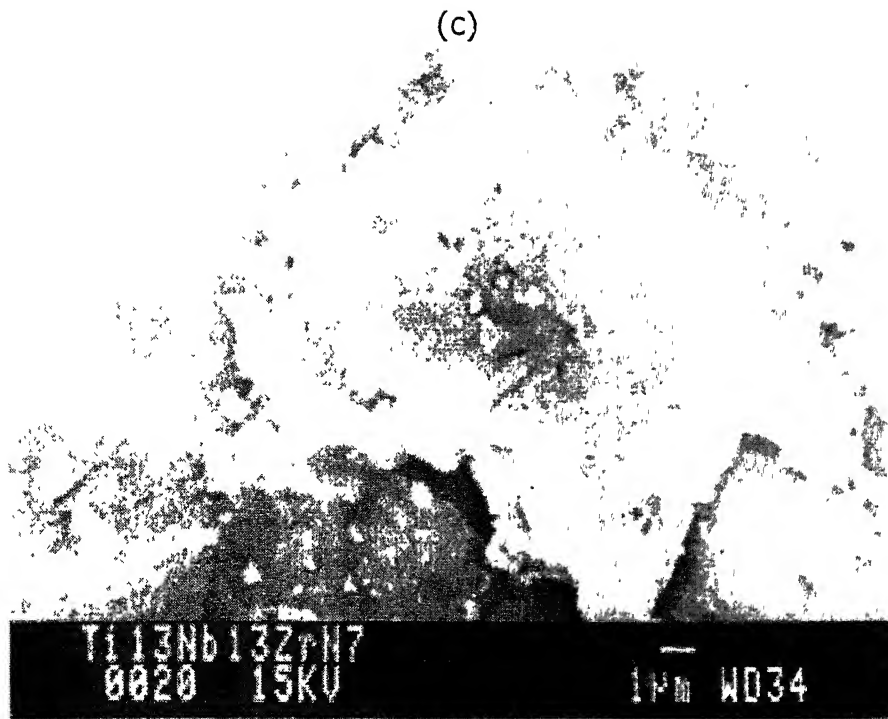


Figure 81(contd.): SEM micrographs of surface of NaOH-treated Ti-13Nb-13Zr alloy after immersion of 1week in Hank's Solution.

### 4.3.2 Potentiodynamic Polarization

Potentiodynamic polarization data for NaOH-treated CP Titanium, Ti-6Al-4V and Ti-13Nb-13Zr, was collected after 1 hr of immersion and also after 168 hrs (1 week) of immersion in the Hank's solution. Potentiodynamic polarization curves for all the three alloys (NaOH-treated CP Titanium, Ti-6Al-4V and Ti-13Nb-13Zr) after 1 hr of immersion in Hank's solution are presented in Figure 82 (a). The same data collected after 168 hrs of immersion in Hank's solution are provided in Figure 82 (b). The potentiodynamic curves have also been compared after immersion of 1 hr and 168 hrs individually for each alloy in Figures 83 through 85. Zero current potential and passive current density ( $i_{pass}$ ) were estimated, from the potentiodynamic polarization data of all the NaOH-treated alloys for immersion time of 1 hr and 168 hrs, and they are tabulated in Table 22.

The nature of polarization curves indicates that the current density increased with anodic polarization and achieved a constant value ( $i_{pass}$ ) after some time without showing any active-passive behavior. All the three NaOH-treated alloys exhibited similar nature of potentiodynamic polarization curve after 1 hr of immersion in Hank's solution (Figure 82 (a)). After 168 hrs of immersion, the potentiodynamic polarization curves of NaOH-treated Ti-6Al-4V and Ti-13Nb-13Zr alloys were similar but these were different from that of NaOH-treated CP Titanium (Figure 82 (b)). Figure 83 reveals that there was a change in the polarization behavior of NaOH-treated CP Titanium with immersion time in Hank's solution. Figures 84 and 85 indicate that there were minor changes in polarization behavior of NaOH treated Ti-6Al-4V and Ti-13Nb-13Zr alloys with immersion time in Hank's solution. It can be observed that the zero current potential for NaOH-treated CP Titanium decreased with immersion time in Hank's solution (-511 to -734 mV vs. SCE) (Table 22). However, the zero current potential for NaOH-treated Ti-6Al-4V and Ti-13Nb-13Zr alloys increased with immersion time in Hank's solution (Table 22). This indicated that passive film acquired more noble character



with immersion time in Hank's solution for these alloys. The passive current densities for all the three NaOH-treated alloys showed a slight decrease with immersion time in Hank's solution (Table 22). The decrease in passive current density for all the NaOH-treated alloys after immersion in Hank's solution can be attributed to change in passive film behavior.

The potentiodynamic polarization results indicated only an improvement in passive film behavior for all the alloys. However, these experiments were not conclusive in predicting whether surface film itself improved or a new film formed on the surface of NaOH-treated Ti alloys with immersion time in Hanks solution. To study the nature of passive film more elaborately, electrochemical impedance spectroscopy technique was used. The change in passive film behavior of NaOH-treated CP Titanium, Ti-6Al-4V and Ti-13Nb-13Zr with immersion time in Hank's solution is discussed in next section using EIS data.

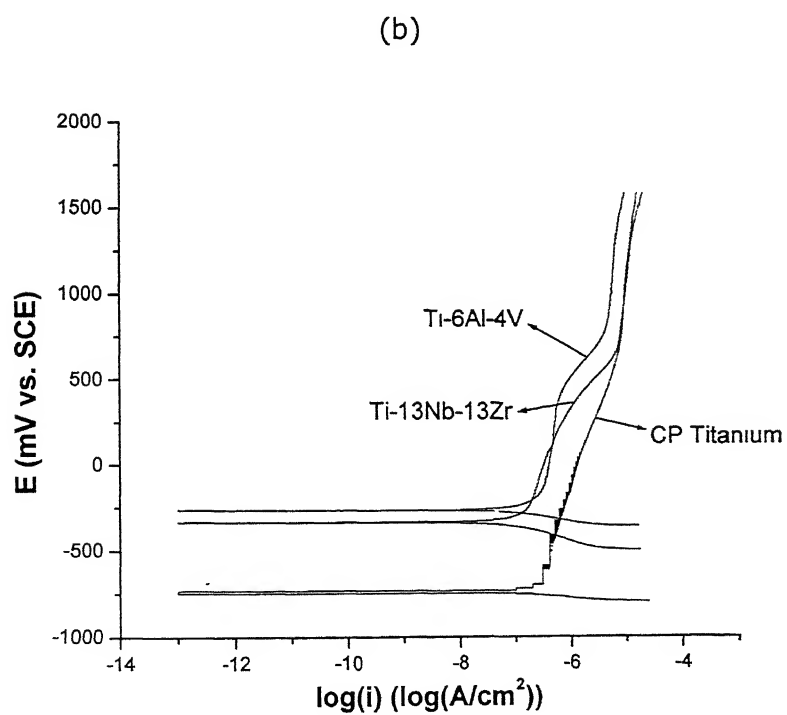
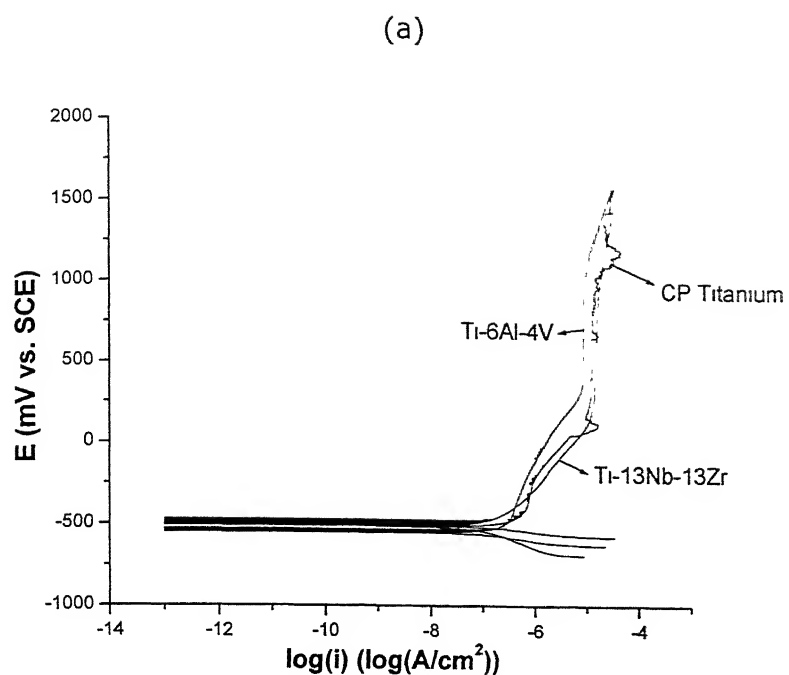


Figure 82: Potentiodynamic curves for NaOH-treated CP Titanium, Ti-6Al-4V and Ti-13Nb-13Zr after immersion time of (a) 1 hr and (b) 168 hrs in Hank's solution

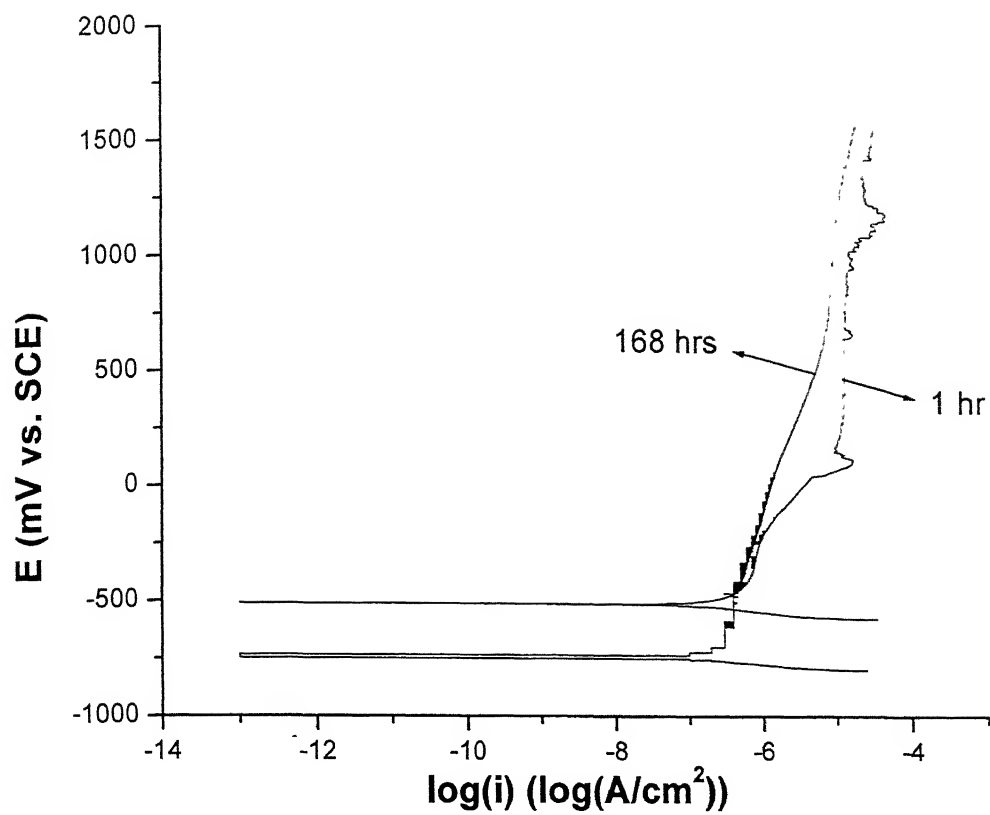


Figure 83: Potentiodynamic polarization curves of NaOH-treated CP Titanium after immersion in Hank's solution for 1 hr and 168 hrs.

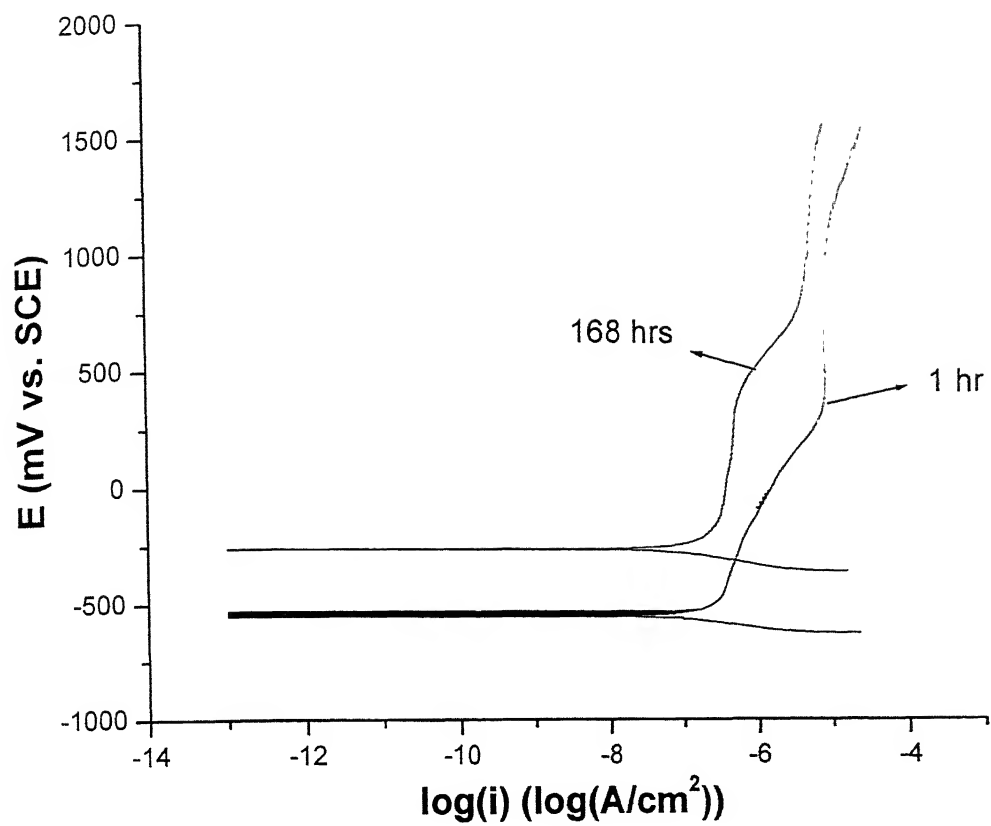


Figure 84: Potentiodynamic polarization curves of NaOH-treated Ti-6Al-4V alloy after immersion in Hank's solution for 1 hr and 168 hrs.

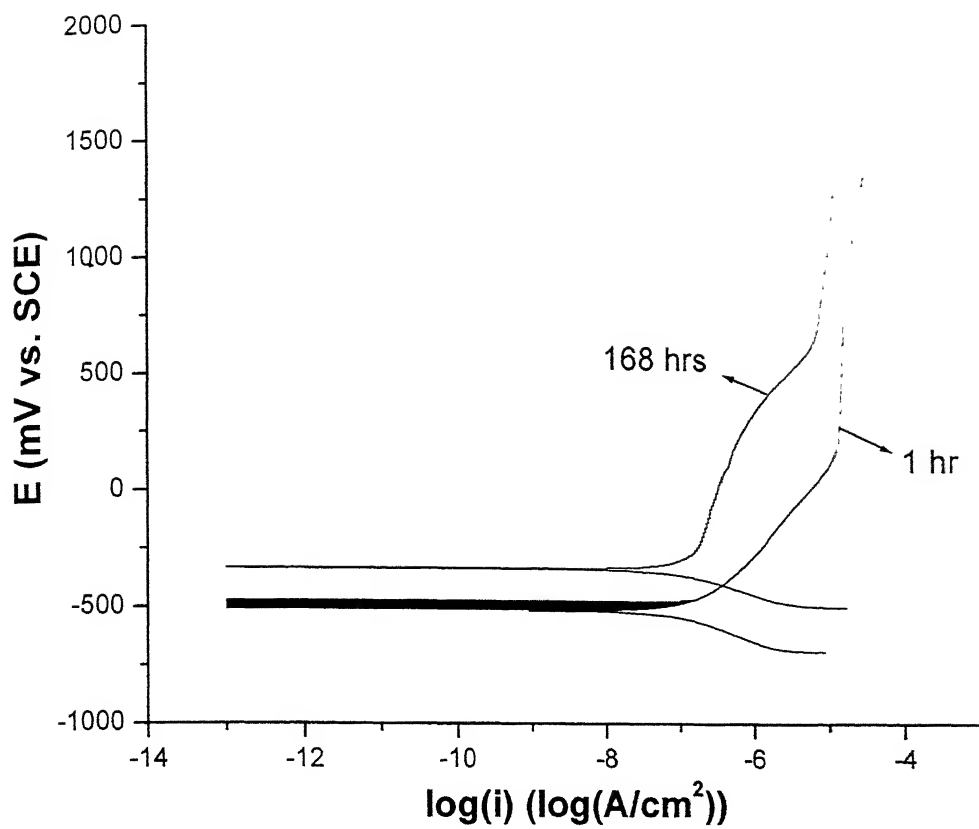


Figure 85: Potentiodynamic polarization curves of NaOH-treated Ti-13Nb-13Zr alloy after immersion in Hank's solution for 1 hr and 168 hrs.

Table 22: Values estimated from Potentiodynamic polarization curves obtained for NaOH-treated samples at immersion time of 1 Hr and 168 Hrs in Hank's solution.

Material	ZCP (mV vs. SCE)		$i_{\text{pass}}$ ( $\mu\text{A}/\text{cm}^2$ )	
	1 hr	168 hrs	1 hr	168 hrs
CP Titanium	-511	-734	12.56	9.33
Ti-6Al-4V	-387	-264	8.31	5.62
Ti-13Nb-13Zr	-485	-327	15.13	10.23

### 4.3.3 Electrochemical Impedance Spectroscopy

The impedance spectra of the three alloys, which were treated with NaOH, were obtained after immersion times of 1 hr, 24 hrs, 72 hrs and 168 hrs in Hank's solution. All the impedance data were fit to appropriate equivalent circuits using a complex nonlinear least-squares fitting routine, using both the real and imaginary components of the data [231]. The results obtained are presented and discussed below.

#### 4.3.3.1 Models used to fit EIS data

In the literature it has been reported [171-191] that the Ti alloys on treatment with NaOH solution produces a sodium titanate gel layer on the titanium surface. This gel layer, of sodium titanate, has the ability to induce formation of bone-like apatite during immersion in simulated body fluid. The gel layer can initiate apatite nucleation on itself. Once apatite nucleation occurs, it spontaneously grows by combining with calcium and phosphate ions from the surrounding environment (Hank's solution).

The possible mechanism of nucleation and growth of apatite on alkaline treated titanium immersed in SBF solution has been proposed as following [171]. The sodium titanate layer releases its  $\text{Na}^+$  ions into the surrounding fluid via an ion exchange with  $\text{H}_3\text{O}^+$  in the fluid to form Ti-OH groups as early as 0.5 h after immersion. The Ti-OH groups then immediately interact with the calcium ions in the fluid to form calcium titanate. The calcium titanate incorporates the phosphate ions, as well as the calcium ions, in the surrounding fluid to form apatite nuclei. Once formed, the apatite nuclei grow by consuming the calcium and phosphate ions in the SBF solution.

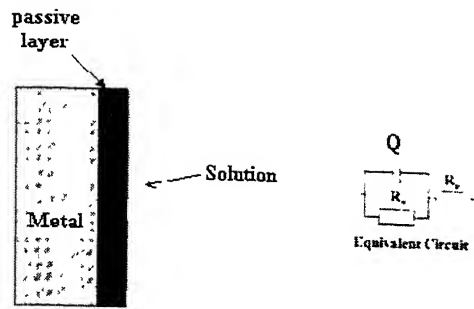
It was concluded by the XRD and SEM analysis that there was a limited reaction of NaOH with the CP titanium surface and product of this reaction i.e. sodium titanate could not form a uniform layer on the CP titanium. Hence, there would only be passive oxide layer of  $\text{TiO}_2$  which form on titanium surface just after immersion in aqueous solutions [225].

Gonzalez et al. have proposed  $R(QR)$  as the equivalent circuit model to fit the EIS data in the case of single passive film present on the metal surface (Figure 86 (a)). Hence,  $R(QR)$  model was used to fit the EIS data obtained for NaOH-treated CP titanium after 1 hr of immersion in Hank's solution. It has also been reported that nucleation and growth of bone like apatite takes place on NaOH treated titanium surfaces [201]. Hence, the  $R(QR)(CR)$  model, which is generally used in case two layers, was used to fit the EIS data obtained after immersion time of 24 hrs, 72 hrs and 168 hrs in Hank's solution (Figure 86(b)). Low values of chi-square obtained by fitting the equivalent circuits with the EIS data indicated a good fit (Table 23).

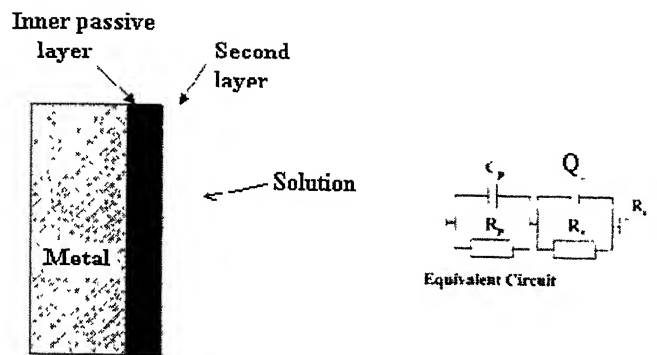
The XRD patterns obtained of surfaces of NaOH-treated Ti-6Al-4V and Ti-13Nb-13Zr alloys revealed a small peak of sodium titanate and SEM analysis also showed a cracked layer on the surface of these alloys after NaOH treatment. These two observations suggested a new layer of sodium titanate on the surface of Ti-6Al-4V and Ti-13Nb-13Zr alloys. Hence, equivalent circuit model  $R(QR)(CR)$  was used to fit EIS data obtained for these alloys after 1 hr of immersion in Hank's solution. As it was reported and also observed by SEM analysis that apatite nucleates and grows on the NaOH treated titanium surfaces [201,202]. Hence, equivalent circuit model of  $R(QR)(QR)(CR)$  was used to fit with EIS data obtained for NaOH-treated Ti-6Al-4V and Ti-13Nb-13Zr alloys after immersion time of 24 hrs, 72 hrs and 168 hrs in Hank's solution (Figure 86(c)). Wang et al. also used the same model to fit the EIS data obtained at prolonged immersion times in Hank's solution for NaOH-treated Ti-6Al-4V alloy [202]. They argued that the layers were an inner passive layer (mainly  $TiO_2$ ), hydrogel layer of sodium titanate and outermost layer of apatite.



(a)



(b)



(c)

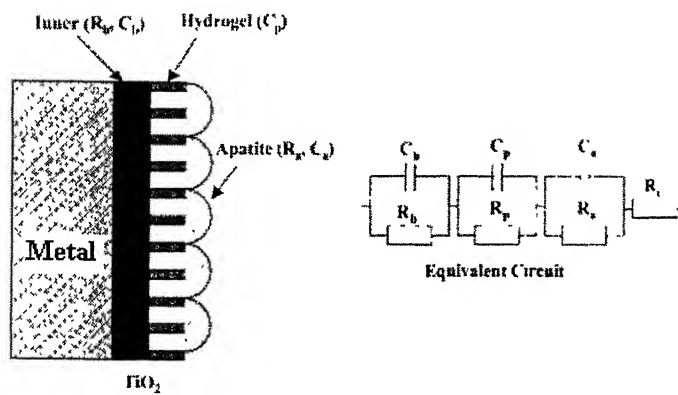


Figure 86: Models used to fit the EIS data: (a)  $R(QR)$  model, (b)  $R(QR)(CR)$  and (c)  $R(QR)(QR)(CR)$  model [201].

### 4.3.3.2 EIS data analysis

The Nyquist, Bode phase and Bode magnitude plots for NaOH-treated CP Titanium obtained after immersion time of 1 hr, 24 hrs, 72 hrs and 168 hrs in Hank's solution are provided in Figure 87. The same plots for Ti-6Al-4V and Ti-13Nb-13Zr alloys are shown in Figures 88 and 89, respectively. Nyquist plots for all the pretreated samples were similar in nature. On observing Figures 87(a), 88(a) and 89(a), it can be noticed that Nyquist plots were similar in nature for all the alloys (NaOH-treated CP Titanium, Ti-6Al-4V and Ti-13Nb-13Zr) for different immersion times in Hank's solution. This indicated that the passive film on the three alloys were similar at different immersion times in Hank's solution. However, the Bode phase plots revealed different behavior with immersion time for these alloys (Figures 87(b), 88(b) and 89(c)). For CP Titanium, at immersion time of 1 hr, phase angle was quite low (below  $10^{\circ}$ ) at high frequencies (10-100 kHz) but increased rapidly to values near  $65^{\circ}$  and remained almost constant (Figure 87(b)). This type of Bode phase plot is characteristic of a single capacitor in the equivalent circuit [219]. Its physical interpretation would be the presence of a single passive film on the metal surface. Bode phase plots for NaOH-pretreated Ti-6Al-4V and Ti-13Nb-13Zr alloys, after 1 hr of immersion in Hank's solution, was different compared to that of CP Titanium for the same immersion time. It can be seen that in Bode phase plots (Figures 88(b) and 89(b)), for NaOH-pretreated Ti-6Al-4V and Ti-13Nb-13Zr alloys after 1 hr of immersion in Hank's solution, there was a small additional peak emerging at the low frequency region (0.01-0.1 Hz) other than the peak present at mid frequency region (Figures 88(b) and 89(b)). This indicates the presence of two layers at the metal-solution interface for these alloys.

Observing Bode phase plots for all the three alloys, NaOH-treated CP Titanium, Ti-6Al-4V and Ti-13Nb-13Zr, at immersion times of 24 hrs, 72 hrs and 168 hrs (Figures 87(b), 88(b) and 89(b)) it can be seen that the plots at high frequencies (10-100 KHz) were different compared to what was observed at 1 hr immersion for the same alloys. The presence of an extra peak, i.e. an extra layer at metal-solution interface, was indicated by the

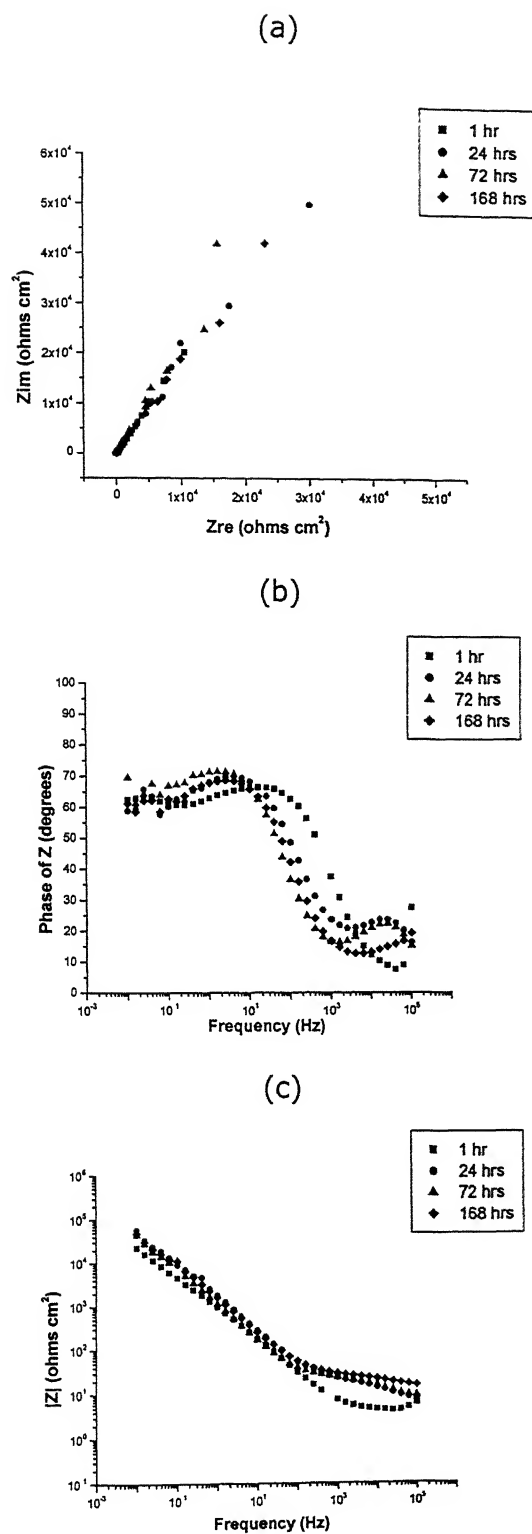


Figure 87: EIS data for NaOH-treated CP Titanium as a function of immersion time in Hank's solution: (a) Nyquist plots (b) Bode phase plots and (c) Bode magnitude plots.

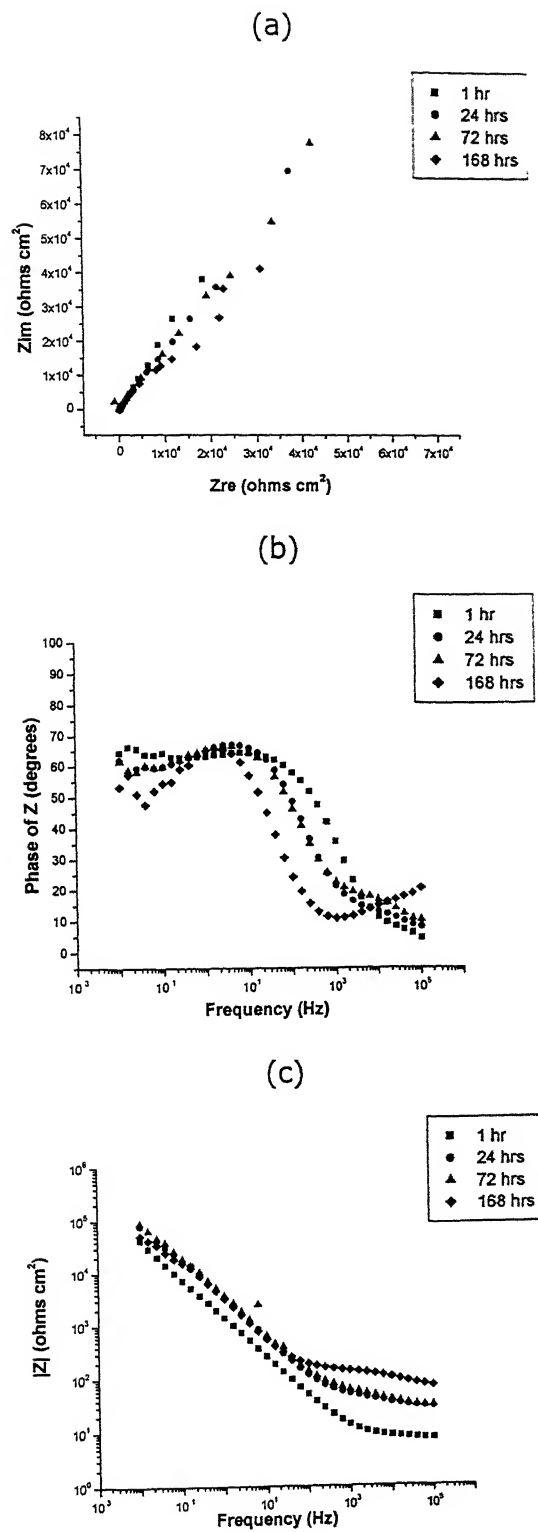


Figure 88: EIS data for NaOH-treated Ti-6Al-4V as a function of immersion time in Hank's solution: (a) Nyquist plots (b) Bode phase plots and (c) Bode magnitude plots.

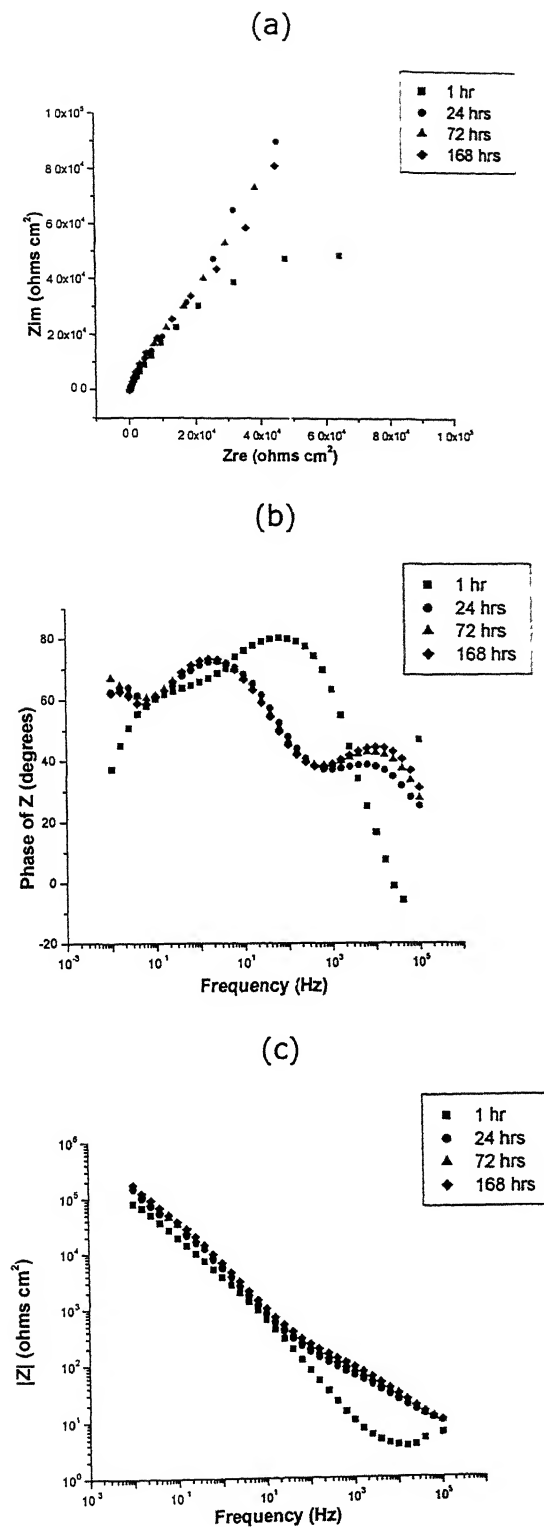


Figure 89: EIS data for NaOH-treated Ti-13Nb-13Zr as a function of immersion time in Hank's solution: (a) Nyquist plots (b) Bode phase plots and (c) Bode magnitude plots.

frequency response in that region (Figures 87(b), 88(b) and 89(b)). Thus two layers were present at the metal-solution interface for immersion time of 24 hrs, 72 hrs and 168 hrs in Hank's solution for NaOH-treated CP Titanium. In contrast, three layers were indicated at metal-solution interface at immersion time of 24 hrs, 72 hrs and 168 hrs in Hank's solution for NaOH-treated Ti-6Al-4V and Ti-13Nb-13Zr alloys. These observations are in accordance with the results of XRD and SEM studies on these alloys.

The Bode magnitude plots for all the alloys investigated showed near capacitive response in the lower and middle frequency region (0.01-100 Hz) which was characterized by slope  $\approx -1$  in the  $\log |z|$  vs.  $\log(f)$  curve (Figures 87(c), 88(c) and 89(c)). It can also be observed that the  $|z|$  values in high frequency region (0.1-100 kHz) increased with immersion time in Hank's solution.

As mentioned earlier, the EIS data for CP titanium collected from impedance spectra was fit to the R(QR) model (Figure 86(a)) for immersion time of 1hr, the R(QR)(CR) model (Figure 86(b)) for the other three immersion times, i.e. 24 hrs, 72 hrs and 168 hrs. This assumes that an additional layer was present at the metal-solution interface for longer immersion times in Hank's solution. In the case for Ti-6Al-4V and Ti-13Nb-13Zr alloys, the R(QR)(CR) model was used to fit EIS data obtained after immersion of 1 hr and the R(QR)(QR)(CR) model (Figure 86(c)) for three other immersion times, i.e. 24 hrs, 72 hrs and 168 hrs. The parameters obtained, by fitting various models to the EIS data collected at different immersion time, are tabulated in Tables 23 through 25. Tables 23, 24 and 25 presents the values of all the parameters, estimated by fitting proposed models in EIS data collected at immersion time of 1 hr, 24 hrs, 72 hrs and 168 hrs in Hank's solution, for NaOH-treated CP Titanium, Ti-6Al-4V and Ti-13Nb-13Zr alloys, respectively. The variation of  $R_p$  and constant phase element as a function of immersion time in Hank's solution has been plotted, for different layers, for all the three alloys used in the present study in Figures 90 through 95.

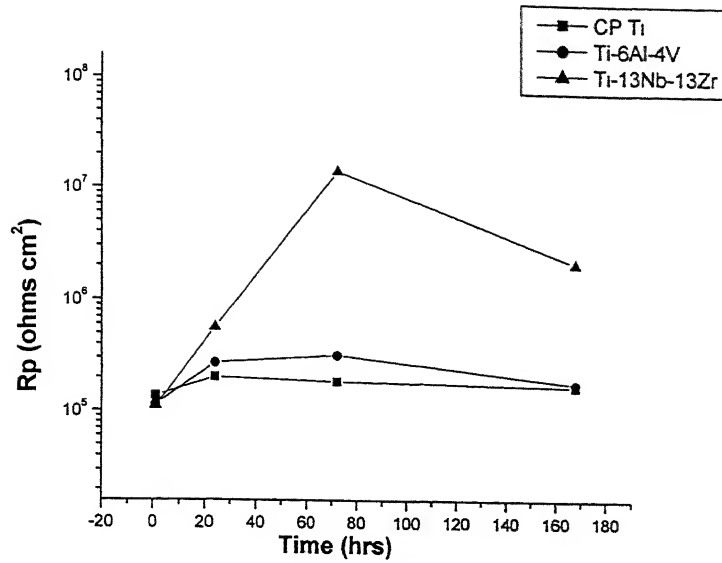


Figure 90: Inner passive layer resistance as a function of immersion time in Hank's solution for NaOH-treated CP Titanium, Ti-6Al-4V and Ti-13Nb-13Zr alloys.

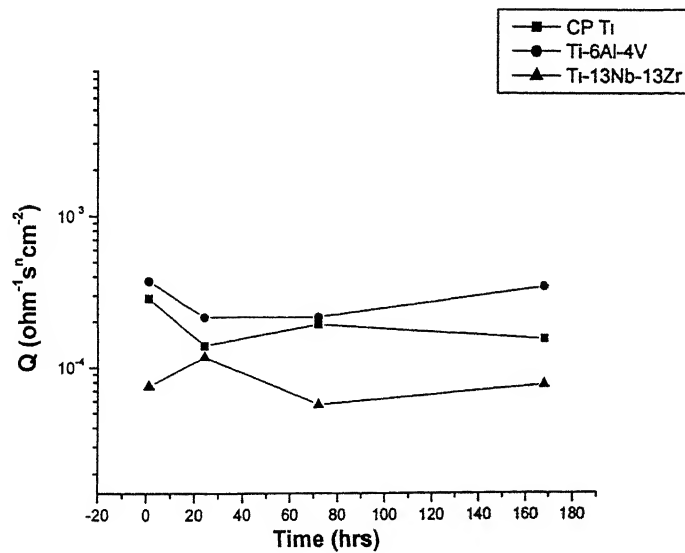


Figure 91: Constant phase element of inner passive layer as a function of immersion time in Hank's solution for NaOH-treated CP Titanium, Ti-6Al-4V and Ti-13Nb-13Zr alloys

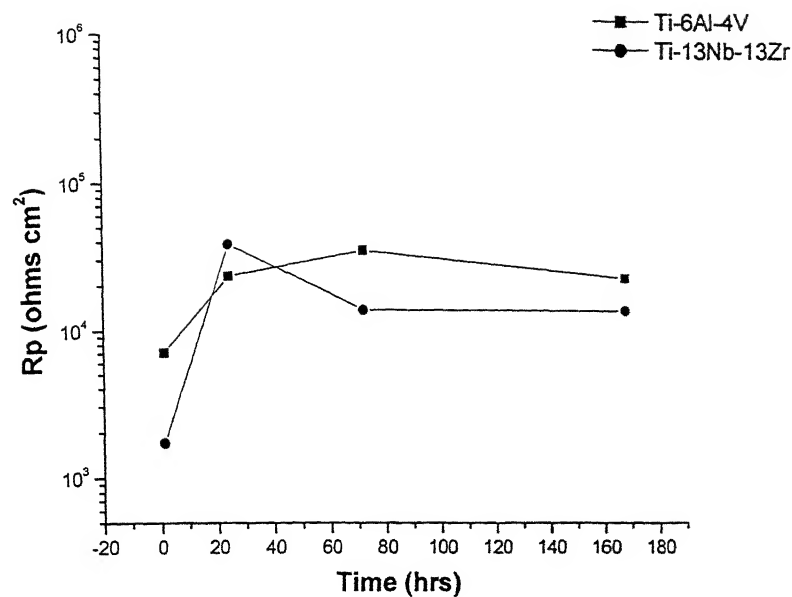


Figure 92: Hydrogel layer resistance as a function of immersion time in Hank's solution for NaOH-treated Ti-6Al-4V and Ti-13Nb-13Zr alloys.

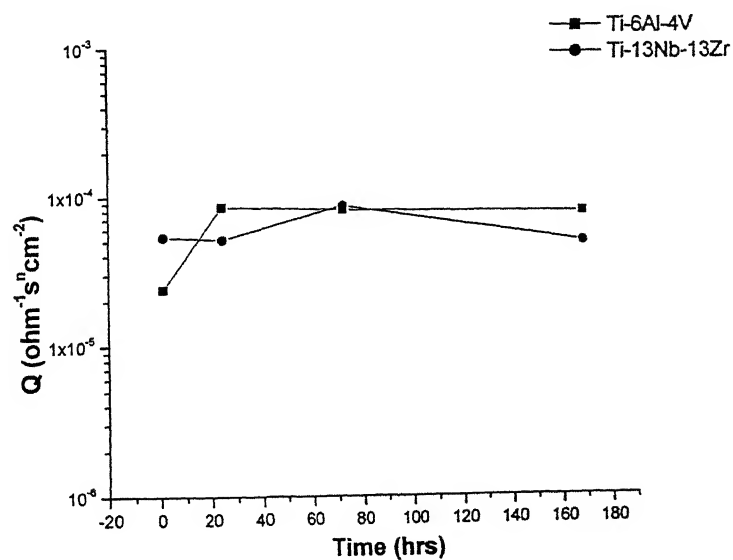


Figure 93: Constant phase element of hydrogel layer as a function of immersion time in Hank's solution for NaOH-treated Ti-6Al-4V and Ti-13Nb-13Zr alloys.



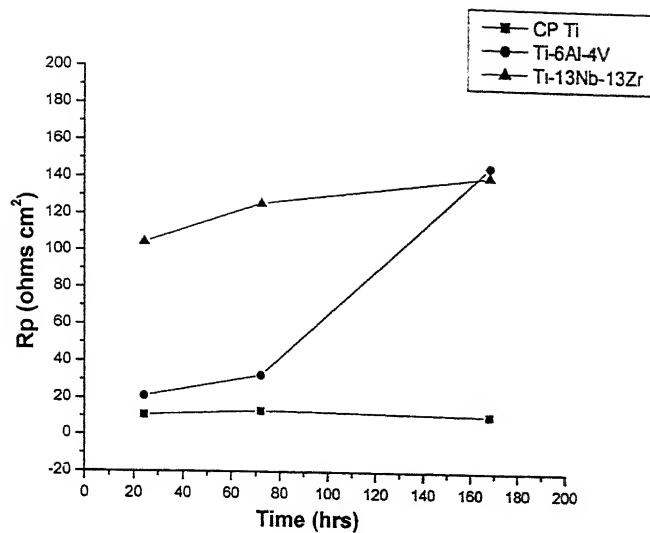


Figure 94: Apatite layer resistance as a function of immersion time in Hank's solution for NaOH-treated CP Titanium, Ti-6Al-4V and Ti-13Nb-13Zr alloys

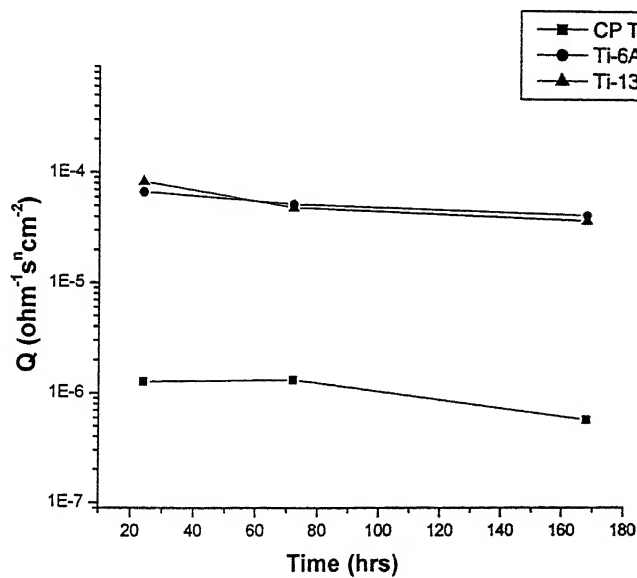


Figure 95: Constant phase element of apatite layer as a function of immersion time in Hank's solution for NaOH-treated CP Titanium, Ti-6Al-4V and Ti-13Nb-13Zr alloys.

From Figure 90, it can be observed that the inner passive layer resistance was unaffected with immersion time for CP Titanium and Ti-6Al-4V alloys but increased for Ti-13Nb-13Zr. The constant phase element for this layer was almost similar for all the alloys and it did not change significantly with immersion time in Hank's solution (Figure 91). This indicates that capacitive behavior of the inner layer was similar for all the alloys as a function of immersion time in Hank's solution.

It was discussed earlier that sodium titanate gel layer was absent on the NaOH CP Titanium surface. Hence, the sodium titanate gel layer resistance and constant phase element were plotted as a function of immersion time in Hank's solution for NaOH-treated Ti-6Al-4V and Ti-13Nb-13Zr alloys (Figures 92 and 93). A slight increase in gel layer resistance was observed with immersion time in Hank's solution for NaOH-treated Ti-6Al-4V and Ti-13Nb-13Zr alloys (Figure 92). Whereas, from Figure 93 it can be observed that constant phase element of the gel layer was almost similar for the two alloys for all the immersion times in Hank's solution. The increase in gel layer resistance can be attributed to its interaction with calcium and phosphate ions present in the electrolyte. It has been reported that these ions interact with sodium titanate gel layer to produce calcium titanate apart from apatite which nucleates and grows to form a new layer [202].

From Figure 94 it can be observed that the apatite layer resistance increased for Ti-6Al-4V and Ti-13Nb-13Zr alloys but was constant for CP Titanium. This observation can be attributed to the formation of sodium titanate gel layer on Ti-6Al-4V and Ti-13Nb-13Zr and not on the CP Titanium surface. The Ti-6Al-4V and Ti-13Nb-13Zr showed enhanced reaction towards NaOH solution producing a thicker sodium titanate gel layer. This also aided apatite formation. The constant phase element for the apatite layer on Ti-6Al-4V and Ti-13Nb-13Zr alloys was almost similar at all the immersion times. Even though the constant phase element for CP titanium also did not change with immersion time (Figure 95), its values were different than that for Ti-6Al-4V and Ti-13Nb-13Zr alloys. This indicates that apatite layer

possessed almost similar nature on Ti-6Al-4V and Ti-13Nb-13Zr alloys, while this must have been different on CP Titanium.

Table 23: Parameters obtained by fitting R(QR) model for immersion time of 1 hr and R(CR)(QR) model for immersion time of 24 hrs, 72 hrs and 168 hrs in Hank's solution for NaOH-treated CP Titanium. Values in brackets are the % errors in various parameters while fitting the experimental data in to the proposed model

NaOH-treated CP Titanium		Immersion time in Hank's solution			
Layers		1 hr	24 hrs	72 hrs	168 hrs
Solution	Chi-squared	2.320e-02	1.197e-02	1.948e-02	9.459e-03
	$R_s$ (ohm-cm <sup>2</sup> )	4.615 (5.545)	7.705 (6.754)	9.254 (7.752)	14.07 (7.483)
Apatite layer	$C_a$ (ohm <sup>-1</sup> s <sup>n</sup> cm <sup>-2</sup> )	Layer absent	1.27E-6 (16.5)	1.326E-6 (19.45)	5.787E-7 (25.86)
	$R_a$ (ohm-cm <sup>2</sup> )		10.64 (9.023)	13.13 (9.752)	10.97 (11.09)
Inner Passive layer	$Q_i$ (ohm <sup>-1</sup> s <sup>n</sup> cm <sup>-2</sup> )	2.885e-04 (4.348)	1.398e-04 (3.129)	1.935e-04 (3.876)	1.556e-04 (2.801)
	$n_i$	0.7318 (1.32)	0.7725 (1.056)	0.8176 (1.384)	0.7701 (0.9899)
	$R_i$ (ohm-cm <sup>2</sup> )	1.372E5 (67.6)	2.022E5 (32.32)	1.857E5 (45.41)	1.71E5 (27.57)



Table 25: Parameters obtained by fitting R(QR)(CR) model for immersion time of 1 hr and R(QR)(QR)(CR) model for immersion time of 24 hrs, 72 hrs and 168 hrs in Hank's solution for NaOH-treated Ti-13Nb-13Zr. Values in brackets are the % errors in various parameters while fitting the experimental data in to the proposed model

NaOH-treated Ti-13Nb-13Zr		Immersion time in Hank's solution			
Layers		1 hr	24 hrs	72 hrs	168 hrs
<b>Solution</b>	<b>Chi-squared</b>	4.866e-02	1.808e-03	3.501e-04	3.831e-04
<b>Apatite Layer</b>	<b>Rs</b> (ohm-cm <sup>2</sup> )	4.508 (8.568)	5.592 (10.26)	5.16 (4.642)	4.75 (5.297)
	<b>Q</b> (ohm <sup>-1</sup> s <sup>n</sup> cm <sup>-2</sup> )	<b>Layer absent</b>	8.238E-5 (25.1)	4.88E-5 (10.18)	3.827E-5 (9.645)
	<b>N</b>		0.5783 (4.25)	0.6147 (1.654)	0.6239 (1.495)
	<b>R</b> (ohm-cm <sup>2</sup> )		104.4 (10.28)	125.8 (5.871)	141.8 (3.778)
<b>Sodium titanate Layer</b>	<b>Q</b> (ohm <sup>-1</sup> s <sup>n</sup> cm <sup>-2</sup> )	5.359E-5 (26.15)	5.143E-5 (2.904)	8.739E-5 (7.003)	5.008E-5 (1.288)
	<b>N</b>	0.87 (2.553)	0.8208 (1.171)	0.9353 (4.087)	0.7847 (0.4215)
	<b>R</b> (ohm-cm <sup>2</sup> )	1711 (37.28)	3.864E4 (10.95)	1.387E4 (16.99)	1.407E4 (5.983)
	<b>C</b> (farad-cm <sup>-2</sup> )	7.549E-5 (9.279)	1.175E-04 (4.741)	5.712E-5 (3.98)	7.786E-5 (3.998)
<b>Inner Passive layer</b>	<b>R</b>	1.106E5 (20.73)	5.669E5 (21.23)	1.429E7 (198.9)	2.207E6 (28.29)

## 4.4 Mechanical properties

In the present study differences in the electrochemical behavior of Ti-alloys in Hank's solution were studied. As these alloys are to be used as biomedical implants, mechanical properties are also important. Two alloys Ti-6Al-4Nb and Ti-6Al-4Fe, where the alloying element V in the Ti-6Al-4V was replaced by Nb and Fe, were experimented. Tensile testing was performed for these samples and their fracture surface was observed. The results obtained are tabulated and discussed below.

The duplicate tensile stress-strain curves are presented in Figure 96 and 97, for alloys Ti-6Al-4Nb and Ti-6Al-4Fe, respectively. The dimensions of tensile test samples before and after fracture are tabulated in Table 26. Table 27 lists the different parameters of the sample used for tests. These parameters include gauge length, width and thickness of the samples. Two samples were tested for both Ti-6Al-4Nb and Ti-6Al-4Fe alloys. In Ti-6Al-4Fe alloy no yielding was present. This alloy showed brittle fracture (to be discussed later). Hence, yield stress was equal to ultimate tensile stress. Wide variation was observed in duplicated experiments for Ti-6Al-4Fe alloy (Table 27). The duplicated values for ultimate tensile stress, yield stress and elastic modulus from the two experiments were similar in case of Ti-6Al-4Nb alloy (Table 27).

The fracture surfaces were observed using scanning electron microscope (SEM). SEM micrographs of the fractured surface for Ti-6Al-4Fe and Ti-6Al-4Nb alloys are provided in Figure 98 and 99, respectively.

The fractured surface for Ti-6Al-4Fe alloy showed cleavage near the surface as can be seen in Figure 98(a). Flat cleaved facets were also observed at the fractured surface for this alloy (Figure 98(b)). Ductile/mixed mode failure was observed mostly in the inner region of the fractured surface (Figure 98(c) and 98(d)). Based on these observations, the following mechanism for fracture may be proposed. A brittle crack nucleated near the

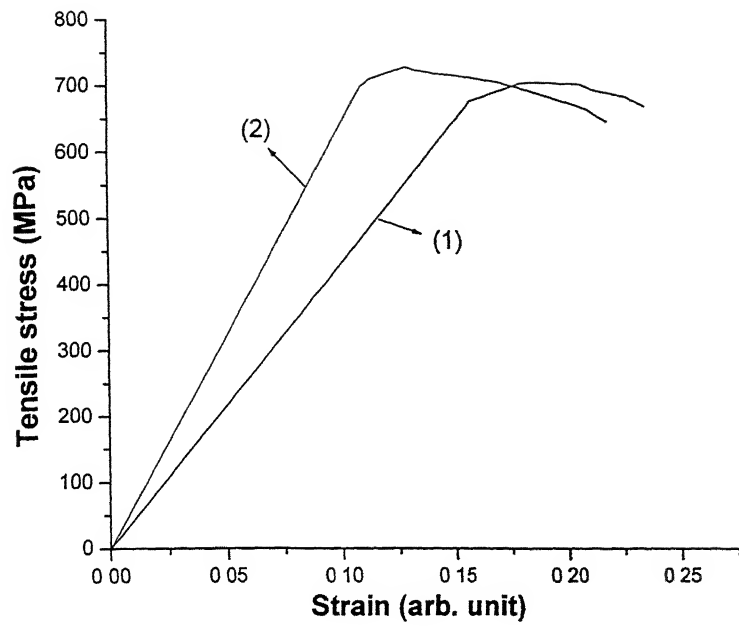


Figure 96: Stress vs. strain curves for Ti-6Al-4Nb alloy.

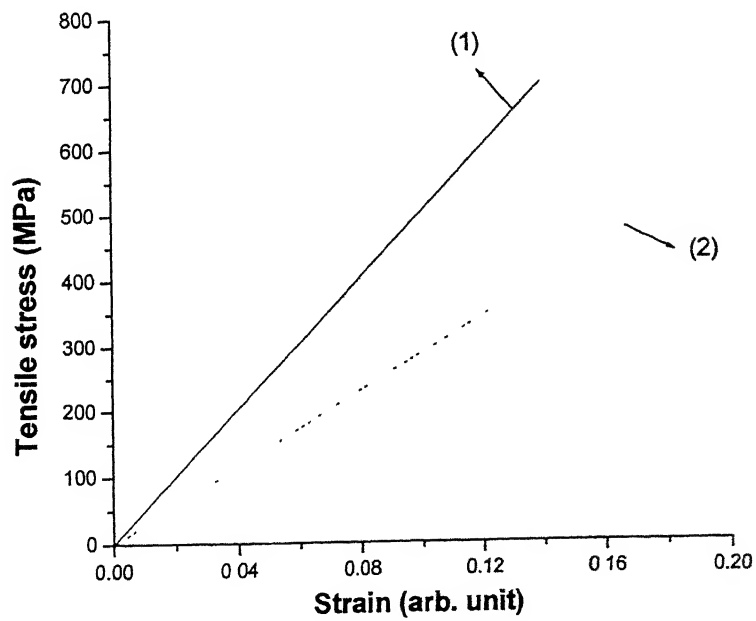
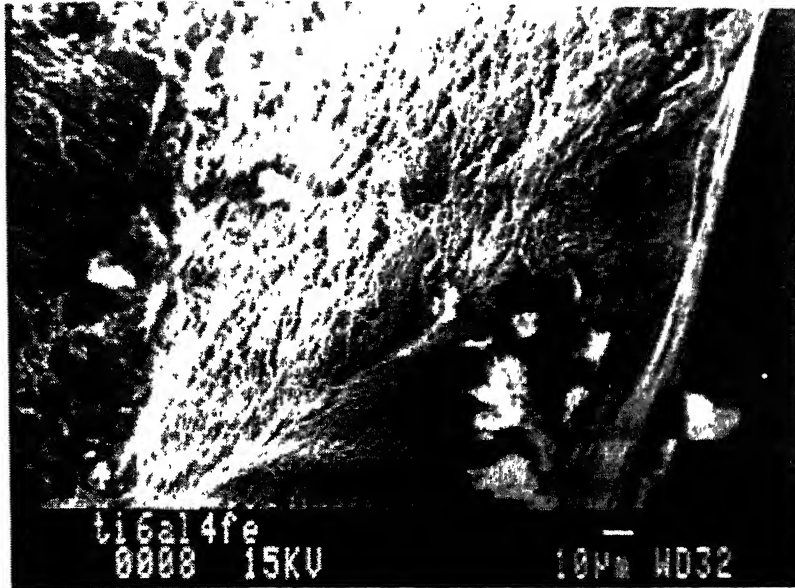


Figure 97: Stress vs. strain curves for Ti-6Al-4Nb alloy.



(a)



(b)

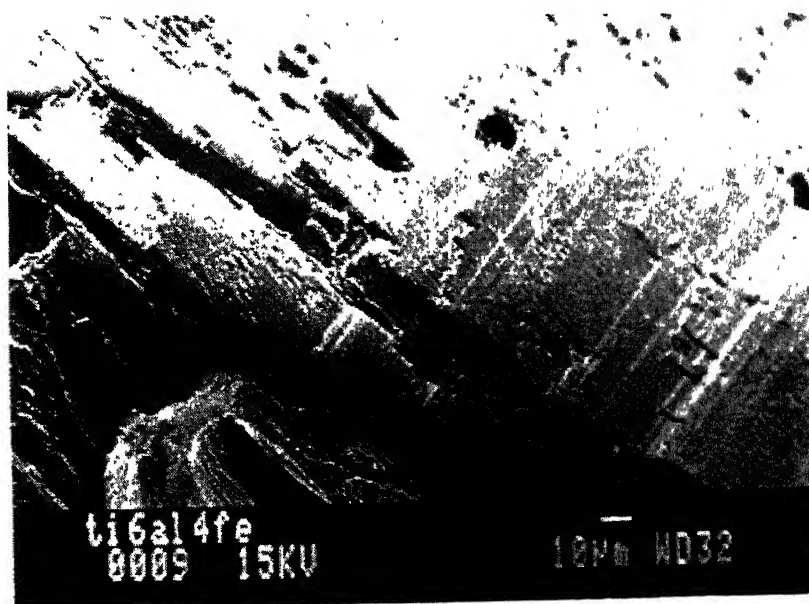
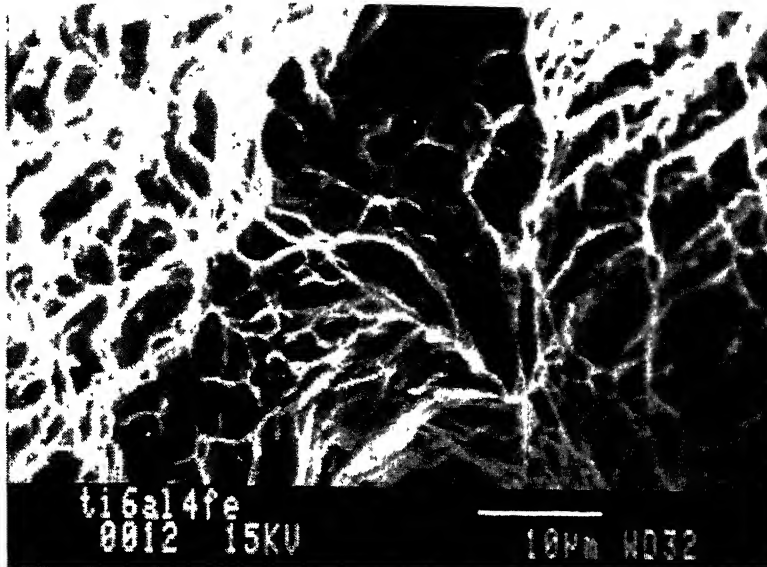


Figure 98: SEM micrographs of fracture surface of Ti-6Al-4Fe alloy: (a), (b), (c) and (d).

(c)



(d)

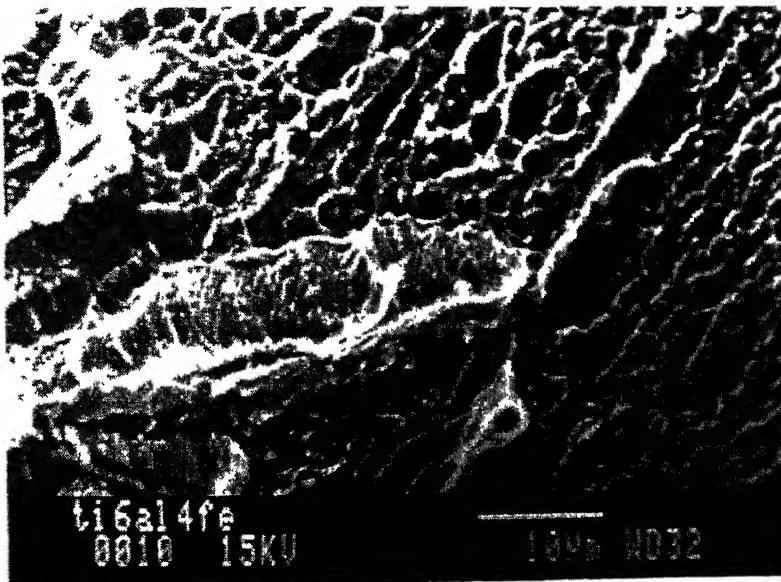
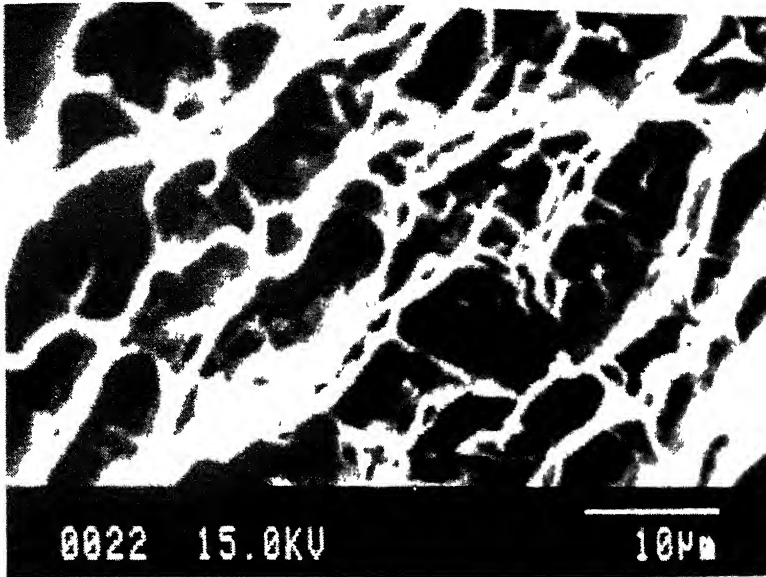


Figure 98: SEM micrographs of fracture surface of Ti-6Al-4Fe alloy: (a), (b), (c) and (d)

(a)



(b)

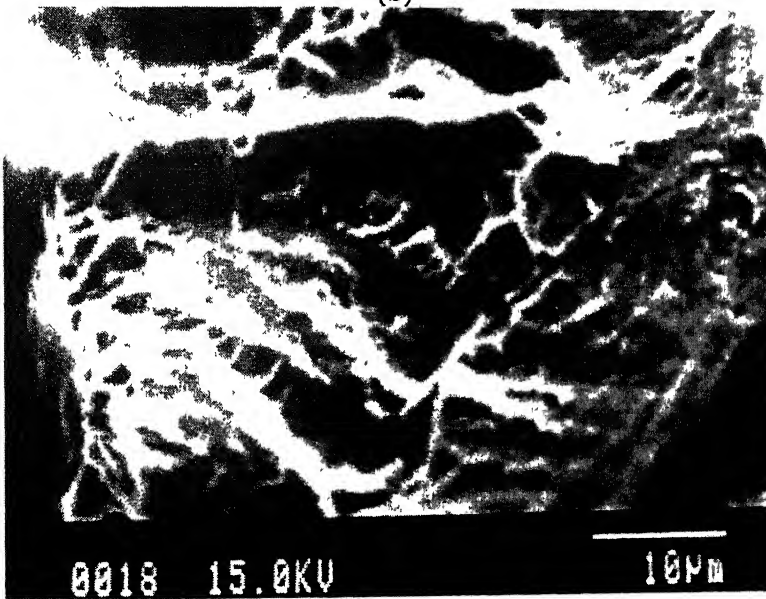


Figure 99(contd.): SEM micrographs of fracture surface of Ti-6Al-4Nb alloy (a) and (b)

surface and cleaved across the material and in the last stages some ductile failure took place. The large variation in the duplicate experiments can be attributed to the brittle failure mode.

On the surface of Ti-6Al-4Nb alloy, flat cleaved facets like those seen on the other alloy were not observed (Figure 99). Feature typical of ductile type of failures were observed across the surface for this alloy. This indicated a predominantly ductile fracture for Ti-6Al-4Nb alloy. The higher ductility obtained for this alloy (Table 27) can also be explained by these observations.

Various Ti alloys are reported to possess tensile strength (UTS) around 900 MPa [233]. In the present study the tensile strengths for Ti-6Al-4Nb and Ti-6Al-4Fe alloys were around 700 MPa. The lower values of tensile strength for these alloys may be due to the cast structure of the two alloys (the microstructures will be discussed later). Microstructural conditions play a major role in determining mechanical properties of Ti based alloys. The effect of microstructure on mechanical properties was not attempted.

The microstructural variation in the pancake, from which these samples were cut, was observed from centre of the pancake to edge. The grains were even visible even by naked eye (Figures 100). The microstructures were observed at various locations. The schematic of the locations from where microstructures were recorded is shown in Figure 101. The microstructures obtained at these locations for the two alloys are provided in Figures 102 and 103. Microstructures showed cast structure for the two alloys (discussed later in detail).

These micrographs indicated presence of relatively large grains. The tensile test samples were also obtained along the same plane as shown in Figure 100. These relatively large grains could provide paths of weakness and failure could take place.

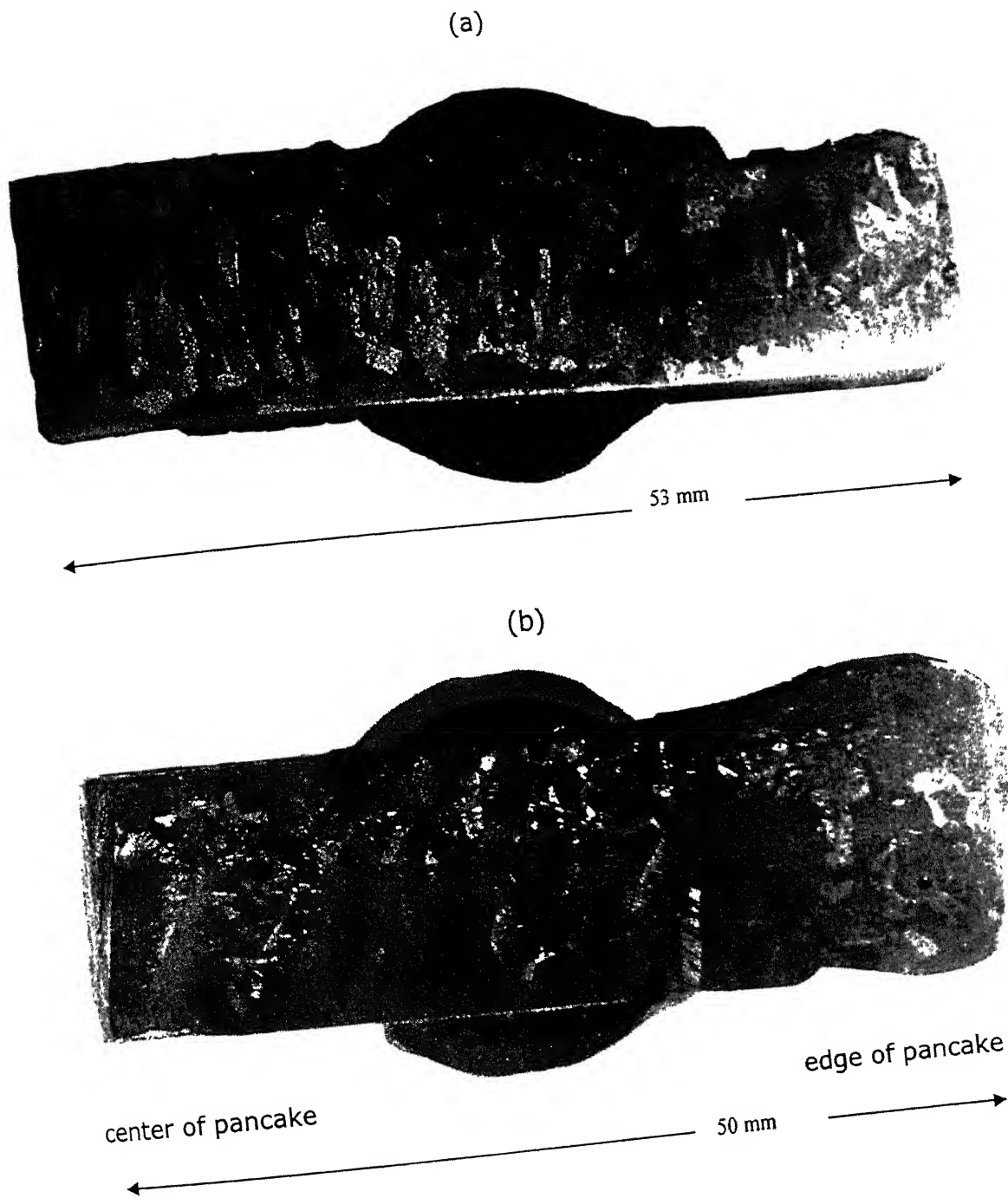


Figure 100: Optical micrograph showing microstructural variation in pancake for (a) Ti-6Al-4Fe and (b) Ti-6Al-4Nb alloys.

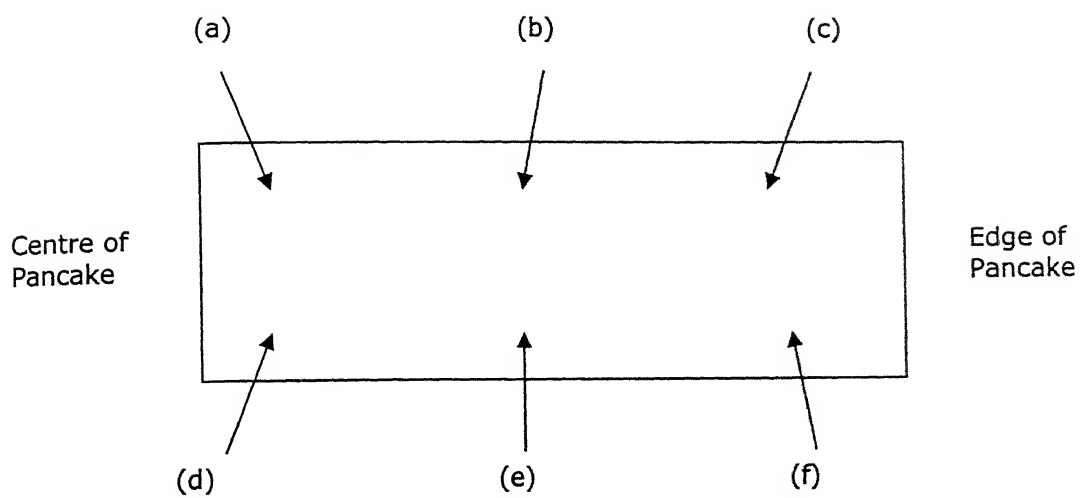


Figure 101: Schematic showing the locations where micrographs were obtained.

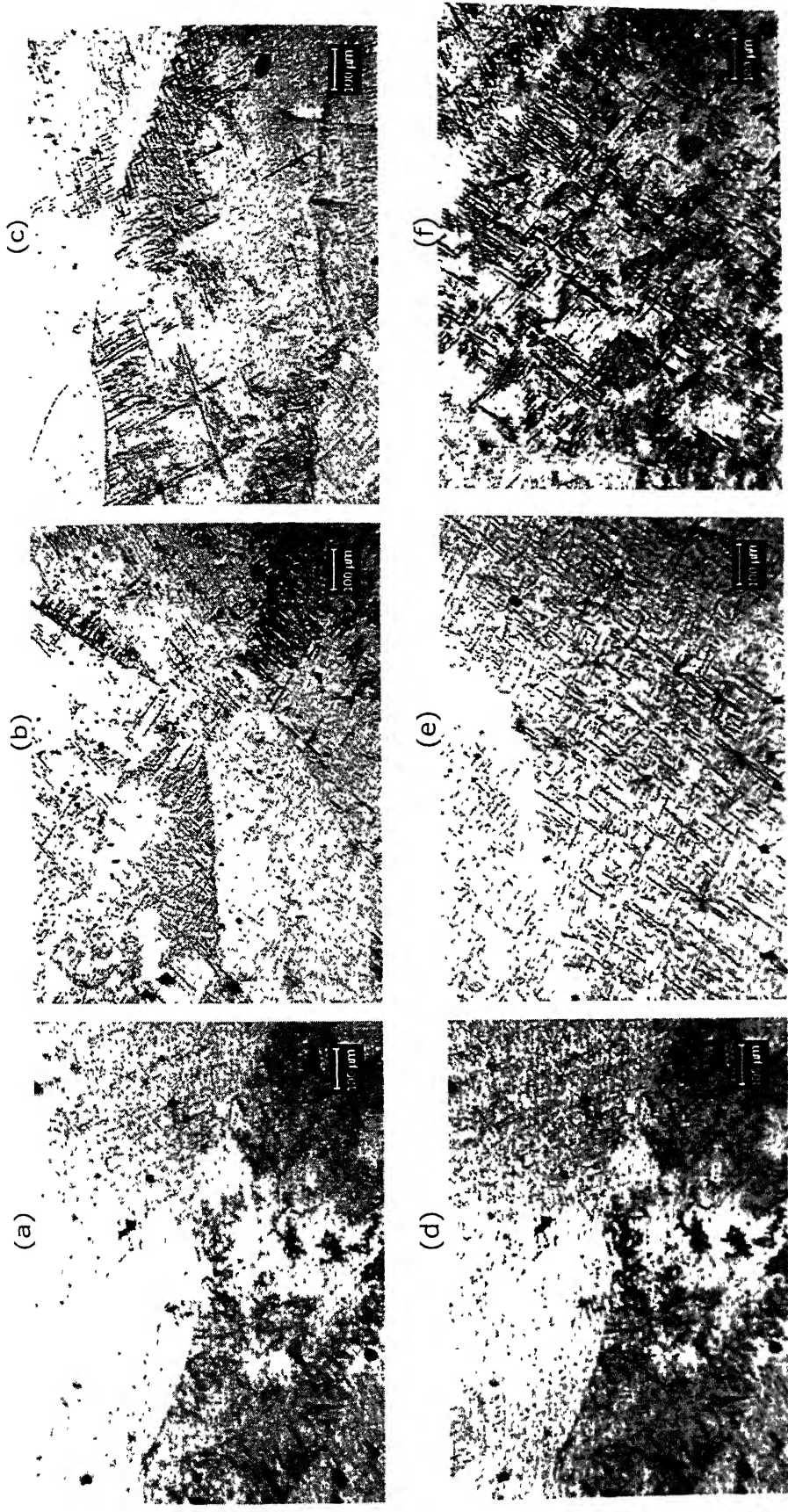


Figure 102: Optical micrographs of the surface of Ti-6Al-4Fe alloy.



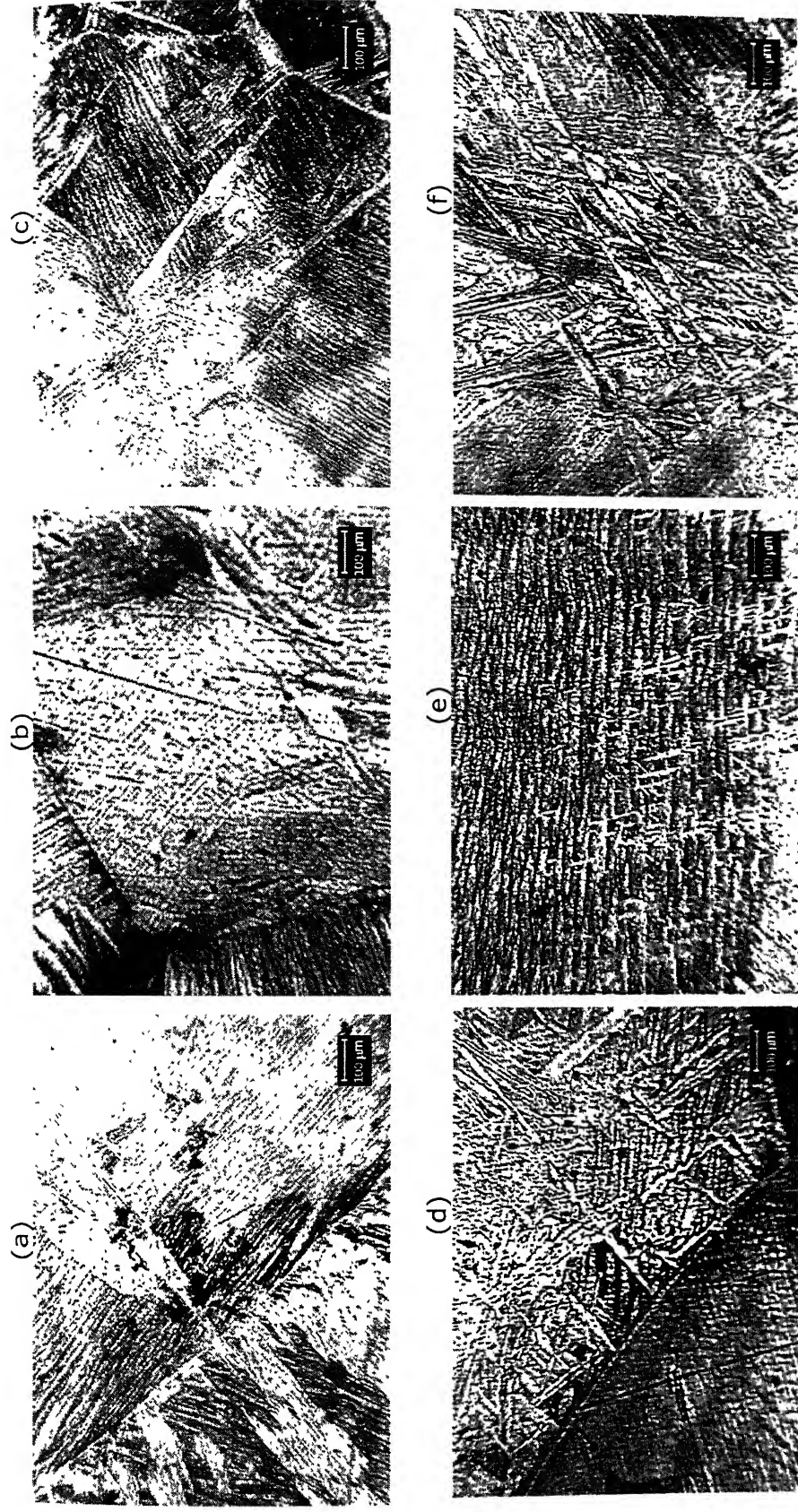


Figure 103: Optical micrographs of the surface of Ti-6Al-4Nb alloy.



Material	Exp. No.	Dimensions before fracture			Dimensions after fracture		
		Length (Cms)	Width (Cms)	Thickness (Cms)	Length (Cms)	Width (Cms)	Thickness (Cms)
Ti-6Al-4Nb	1	15.34	5.66	2.24	-	5.14	2.08
	2	14.26	5.80	2.86	-	5.26	2.86
Ti-6Al-4Fe	1	13.32	5.90	2.28	-	5.90	2.2
	2	12.24	5.24	3.24	-	5.22	3.2

Table 26: Dimensions of tensile test samples before and after fracture for Ti-6Al-4Nb and Ti-6Al-4Fe alloys.

Material	Exp. No.	Ultimate Tensile Stress(MPa)	Yield stress, (MPa)	% elongation	Elastic Modulus (GPa)
Ti-6Al-4Nb	1	709.86	678.32	8.14	4.34
	2	729.44	699.3	11.2	6.24
Ti-6Al-4Fe	1	706.21	706.21	0	5.17
	2	518.19	518.19	0	2.89

Table 27: Values of different material properties obtained from tensile test experiments for Ti-6Al-4Nb and Ti-6Al-4Fe alloys.

## 4.5 Microstructural Characterization

Titanium can exist in two allotropic modifications; that is, it exists in more than one crystallographic form. At room temperature, titanium possesses a hexagonal close-packed (hcp) crystal structure, which is referred to as “alpha” phase. This structure transforms to a body-centered cubic (bcc) crystal structure, called beta phase, at 888°C (1621°F). It is common to separate Ti alloys into four categories, referring to the phases normally present. The alloy categories generally are called alpha, near alpha (which contains little or no beta stabilizers), alpha-beta and beta (which contains substantial volumes fraction of beta phase, typically 0.05 to 0.40 or which can be quenched in thin sections to completely retain the metastable beta phase). Sometimes a category of near beta alloys is also considered [234].

These categories denote the general type of microstructure after processing. The microstructures of titanium are complex. They are often the direct result of composition, processing and post processing heat treatments. The most important beta stabilizing elements are the so-called beta isomorphous elements such as V, Nb, Mo, Fe and Ta, while the alpha stabilizing elements are Al, O and N. Other common alloying additions are Sn and Zr, which are neutral because they have minimal effect on beta transus [234][133].

Microstructural characterization of the materials in this study was undertaken after the electrochemical testing. This ensured that the reported microstructure was for the surface used in the electrochemical tests. The cast pancake was expected to reveal differences in structure and therefore, the surfaces that were tested were taken up for microstructural analysis. In the microstructures, beta phase appeared as dark and alpha as white phase. In addition, the microstructural variation to be noted could also result due to different composition utilized.

#### 4.5.1 Alpha and Near Alpha Phase Titanium Alloys

Pure titanium is single-phase alpha at room temperature. As with any single-phase alloy, the microstructure of CP titanium depends on whether or not it has been cold worked and the specific type of annealing employed. In addition, upon cooling from the beta region which begins at 882°C, the structure depends on the cooling process followed because the process directly affects the progression of the beta-to-alpha transition and the final alpha grain size shape. The microstructures of CP titanium are provided in Figure 104(a) and (b). Alpha grain boundaries as seen in the microstructure of CP titanium are quite elongated which suggested that the material was cold rolled in the alpha region. Customarily CP titanium is selected for its excellent corrosion resistance, especially in application where high strength is not required. Yield strength of commercially pure grades vary from about 170 MPa to 480 MPa simply as a result of variation in interstitial and impurity levels, with strength increasing as the oxygen/nitrogen (and iron) content increases [235].

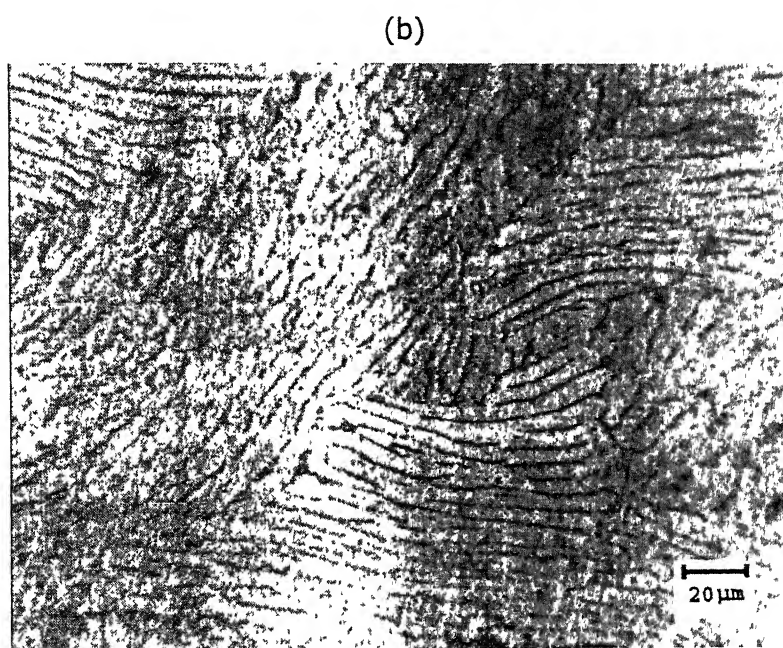
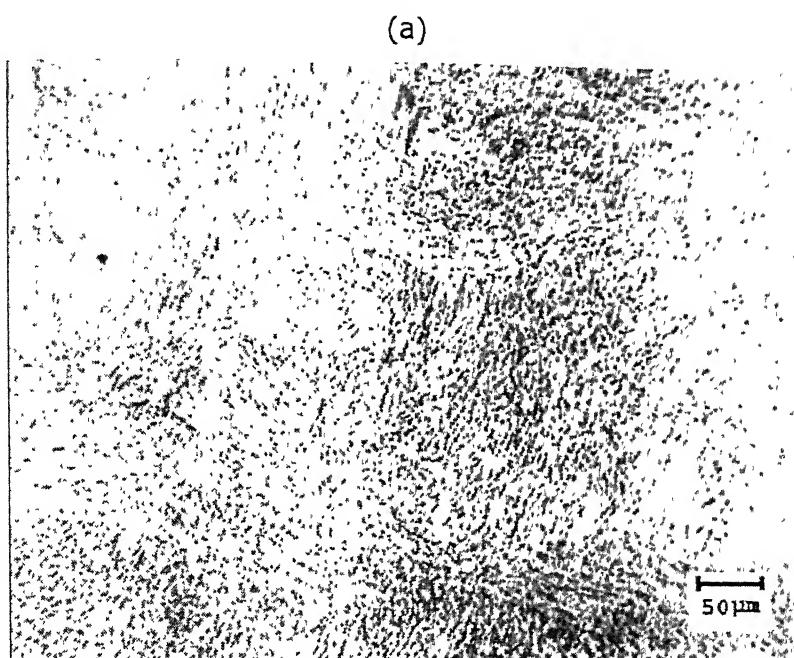


Figure 104: Optical micrographs of the surface of CP titanium. The microstructures were obtained on the area used for electrochemical testing in simulated body fluid solution at 37°C and 7.4 pH.

## 4.5.2 Alpha-Beta Titanium Alloys

The alloys Ti-6Al-4V, Ti-6Al-4Nb, Ti-5Al-2.5Fe and Ti-6Al-4Fe possess a two-phase alpha-beta structure owing to addition of vanadium, niobium and iron which are beta stabilizers. Aluminum is an alpha stabilizer. Alpha is the dominant phase in all these alloy combinations as evident from the microstructures (Figures 105 through 108). Ti-5Al-2.5Fe and Ti-6Al-4Fe are in near alpha-beta class; the alpha phase dominates the properties of this alloy to greater extent as compared to Ti-6Al-4V and Ti-6Al-4Nb.

Owing to two-phase equiaxed microstructure (Figure 105), Ti-6Al-4V is more susceptible to corrosion as the compositional difference across the grain boundaries increases which leads to the galvanic cell formation. This equiaxed structure may have resulted by extensive mechanical working (>75% reduction) of the material in alpha-beta phase field, where the breakup of lamellar alpha into equiaxed alpha depends on the exact deformation procedure. This equiaxed structure can also be obtained by recrystallization annealing followed by slow cooling [236].

In figure 106 white plates are alpha and dark plates are beta. This is a typical Widmanstatten type of structure. Grain boundary alpha can also be seen in the microstructure in a transformed beta matrix. The plate like alpha precipitates that nucleate and grow below the beta transus producing a Widmanstatten structure [237]. The plates often precipitate in colonies of the same crystallographic orientation (Figure 106), presumably because of autocatalytic nucleation. This is a high strength alloy developed for femoral component in hip prosthesis.

Figures 107 and 108 show the micrographs for Ti-5Al-2.5Fe and Ti-6Al-4Fe alloys, respectively. Fairly fine lamellar structure of alpha phase can be seen in the microstructures of both the alloys. However, in the microstructure of Ti-5Al-2.5Fe alloy a fairly fine lamellar, colony structure can be observed along the grain boundary (Figure 106(a, b)). In the

microstructure of Ti-6Al-4Fe, very fine needle like (acicular alpha) can be observed in the transformed beta matrix. Ti-5Al-2.5 Fe alloy was designed for permanent implants in human body. Cast implant devices, such as sockets of hip prosthesis, are readily produced. A special application of this alloy is porous implant devices. Pore size ( $>50\mu\text{m}$ ) makes it possible to secure implants via tissue growth into the pores. Examples for such devices are heart pacemaker electrodes and dental implants [238]. The fine lamellar Widmanstätten alpha beta structure for this alloy (Figure 106(a, b)), which is formed by solutionizing over beta transus followed by air cooling has been reported to give greatest fracture toughness [237]. Blocky and fine plate like acicular alpha and transformed beta (dark) and alpha at prior beta grain boundaries are also seen in the micrograph of Ti-5Al-2.5Fe.

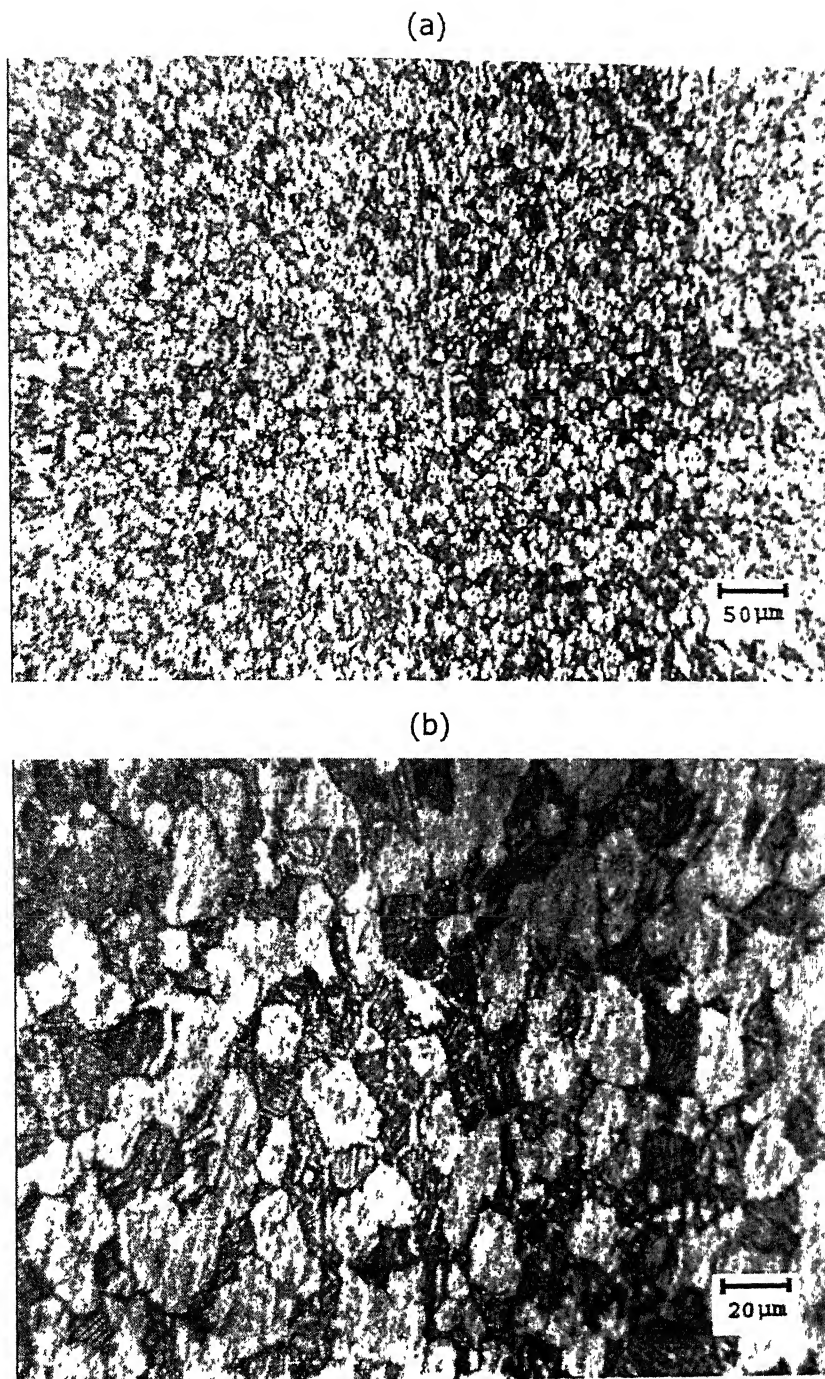


Figure 105: Optical micrographs of the surface of Ti-6Al-4V. The microstructures were obtained on the area used for electrochemical testing in simulated body fluid solution at 37°C and 7.4 pH.

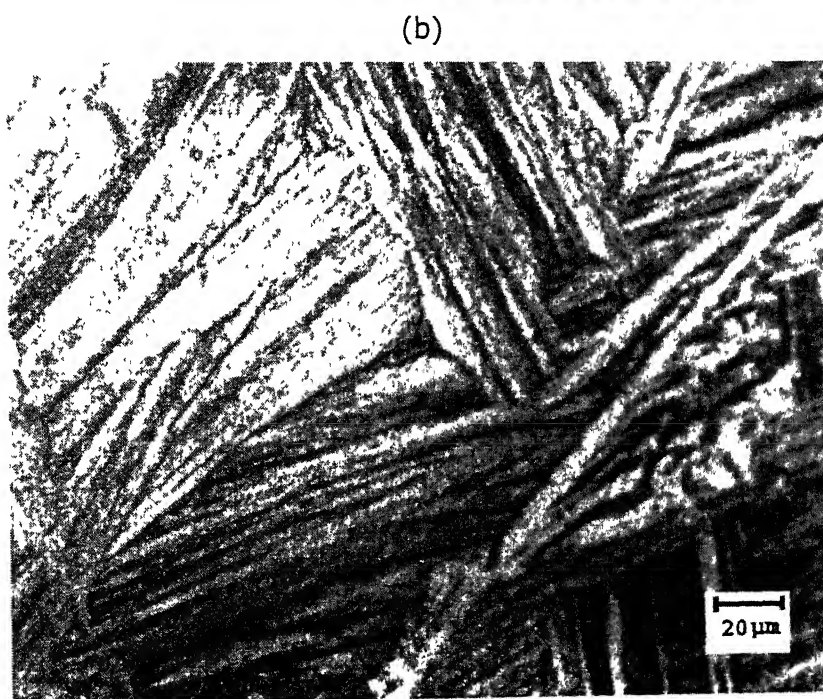
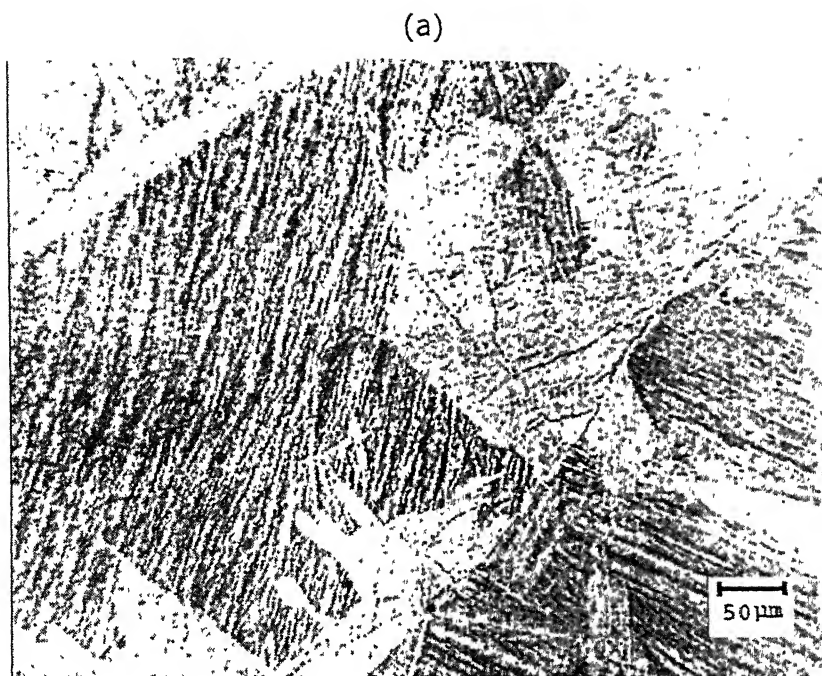


Figure 106: Optical micrographs of the surface of Ti-6Al-4Nb. The microstructures were obtained on the area used for electrochemical testing in simulated body fluid solution at 37°C and 7.4 pH.



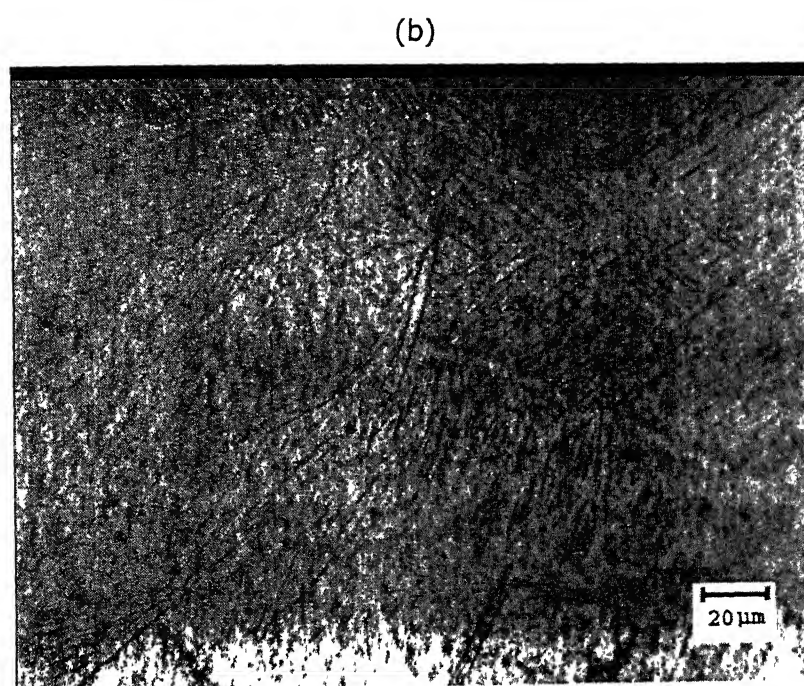
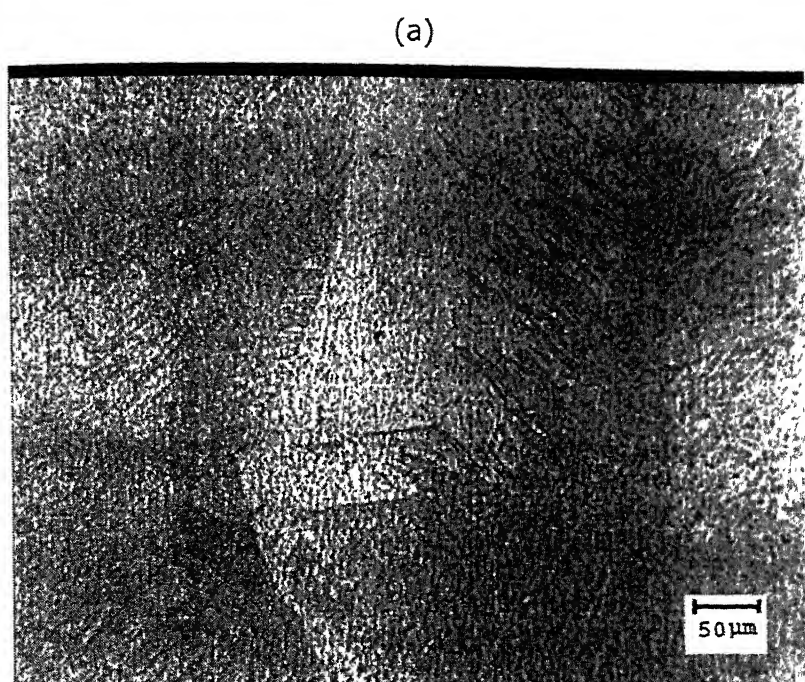
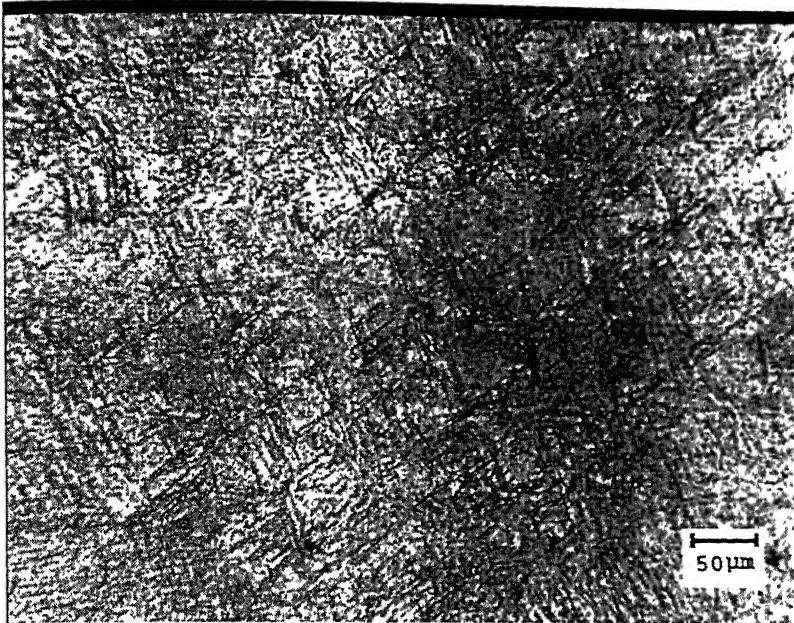


Figure 107: Optical micrographs of the surface of Ti-5Al-2.5Fe. The microstructures were obtained on the area used for electrochemical testing in simulated body fluid solution at 37°C and 7.4 pH.

(c)



(d)

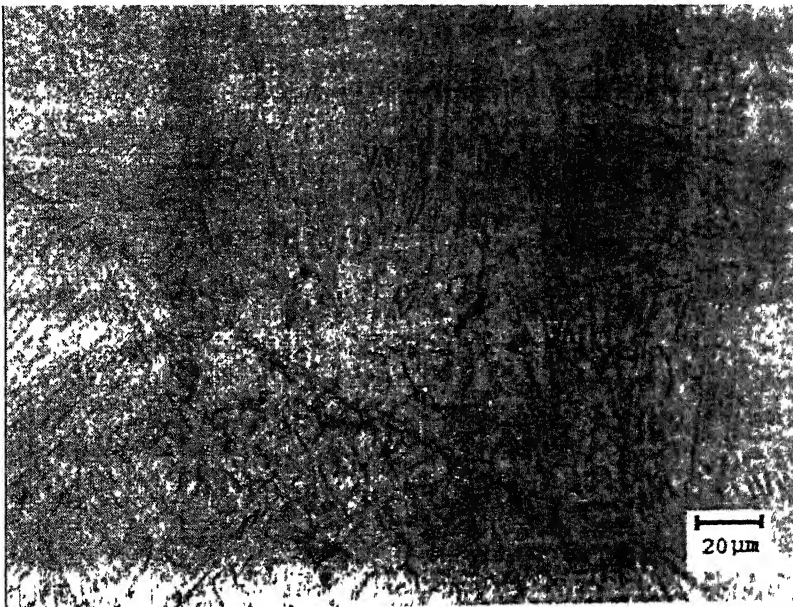


Figure 108: Optical micrographs of Ti-6Al-4Fe (c, d). The microstructures were obtained on the area used for electrochemical testing in simulated body fluid solution at 37°C and 7.4 pH.

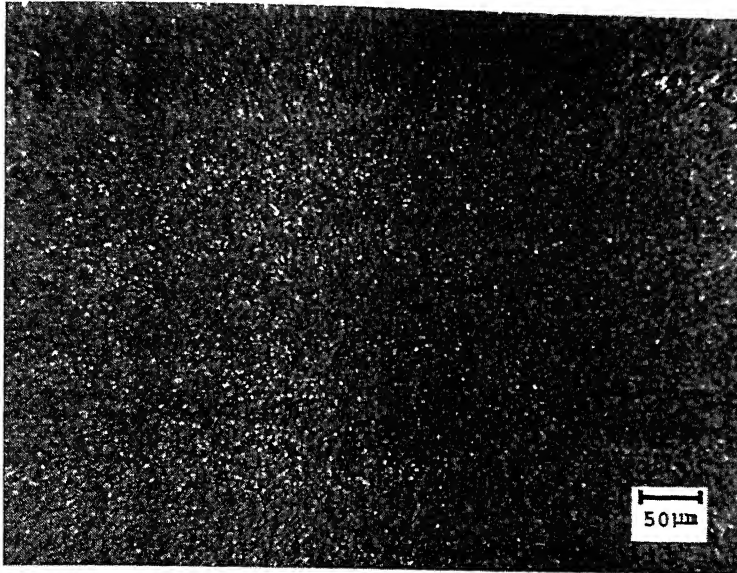
### 4.5.3 Beta and Near Beta Titanium Alloys

Ti-8.4Al-15.4Nb and Ti-13.4Al-29Nb alloys contain aluminum in addition to niobium (which is a beta stabilizer), in order to strengthen the alpha phase. It has been reported in literature that minimum 3% aluminum addition is needed to suppress the omega phase transformation effectively at lower temperature and longer times [237]. Very fine precipitates of alpha phase in beta phase were evident from the microstructure of Ti-8.4Al-15.4Nb and Ti-13.4Al-29Nb alloys (Figures 109 and 110). Uniform distribution of this alpha phase was also seen (Figure 109). Also there is no evidence of occurrence of extensive grain boundary alpha (as was seen in Figures 106 and 107), there is a precipitate free zone along the grain boundary.

Ti-13Nb-13Zr contains sufficient beta phase stabilizer in the form of niobium to retain the beta phase at room temperature and zirconium is a neutral element added which strengthens and stabilizes the beta phase and prevents the formation of alpha phase on cooling through the transformation temperature range. The microstructure of Ti-13Nb-13Zr (presented in Figure 111) exhibited extremely fine primary alpha in beta matrix.

It also enhances the corrosion resistance above the level achieved by molybdenum and suppresses omega transformation to prevent embrittlement [237]. This beta titanium alloy is developed specifically for use in biomedical applications. Titanium, niobium and zirconium are highly resistant to corrosion reported by Steineman as causing minimal negative tissue response [91].

(a)



(b)

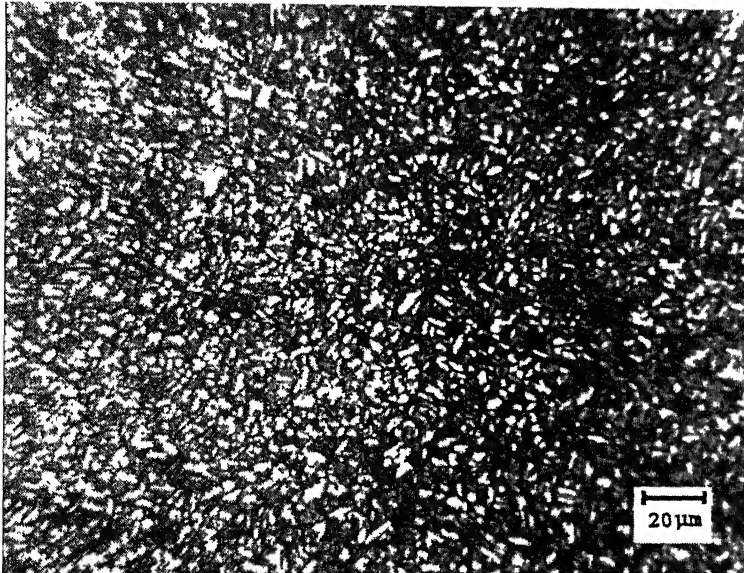
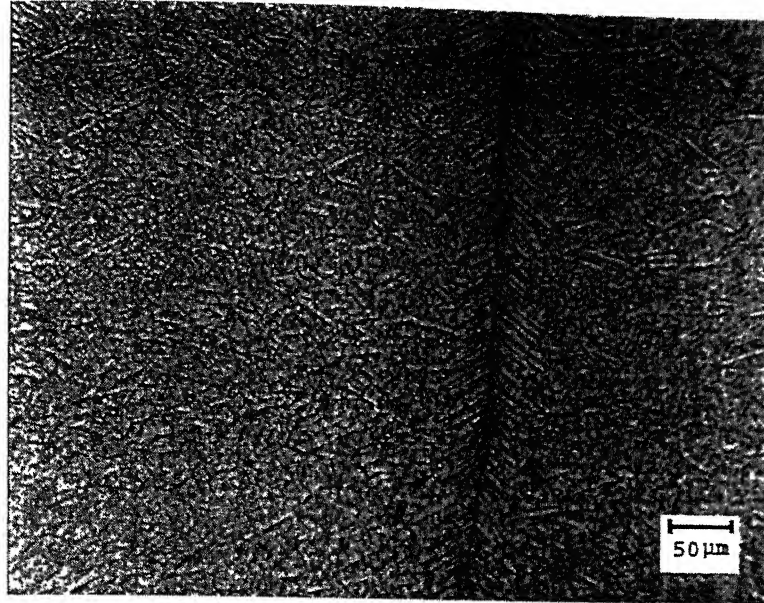


Figure 109: Optical micrographs of the surface of Ti-8.4Al-15.4Nb. The microstructures were obtained on the area used for electrochemical testing in simulated body fluid solution at 37°C and 7.4 pH.

(c)



(d)

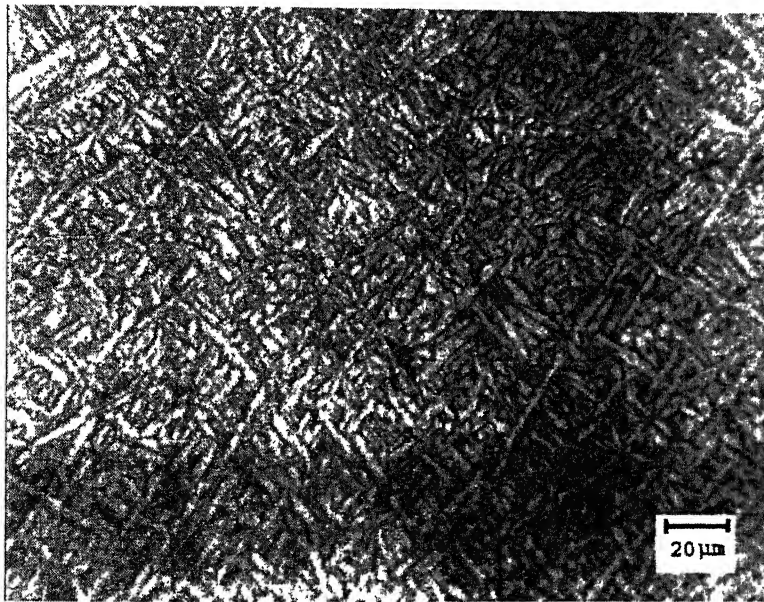
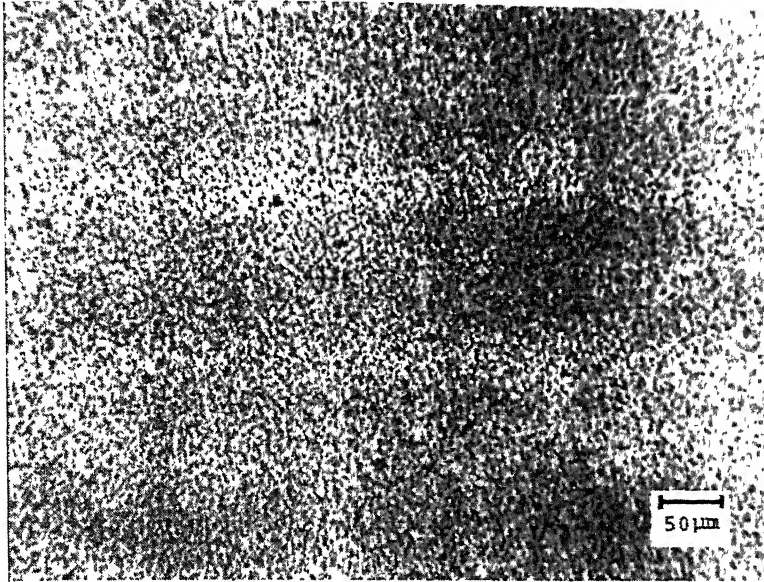


Figure 110: Optical micrographs of the surface of Ti-13.4Al-29Nb. The microstructures were obtained on the area used for electrochemical testing in simulated body fluid solution at 37°C and 7.4 pH.



(e)



(f)

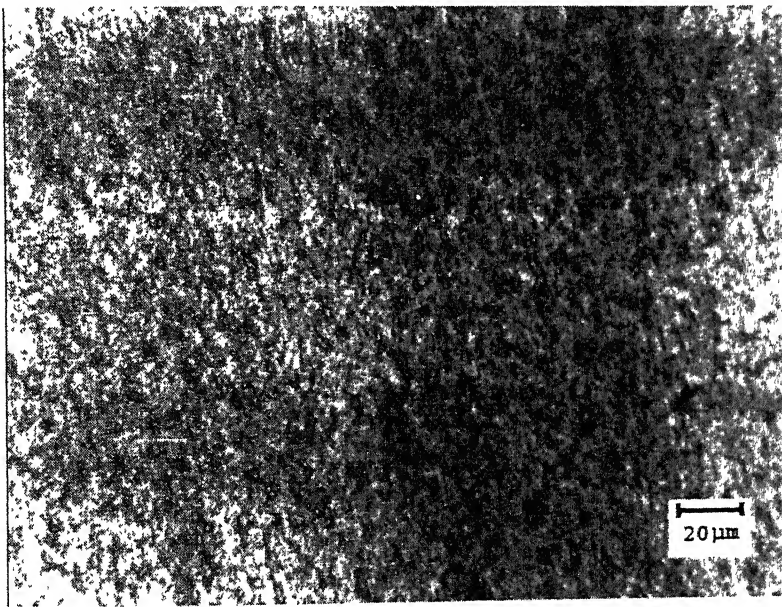


Figure 111: Optical micrographs of the surface of Ti-13Nb-13Zr. The microstructures were obtained on the area used for electrochemical testing in simulated body fluid solution at 37°C and 7.4 pH.

## Chapter 5

---

### SUMMARY

#### 5.1 Conclusions

The behavior of passive film on Ti-based alloys formed in Hank's solution was studied using Tafel extrapolation, potentiodynamic polarization and electrochemical impedance spectroscopy (EIS) techniques. The alloys studied were CP Titanium, Ti-6Al-4V, Ti-13Nb-13Zr, Ti-5Al-2.5Fe, Ti-6Al-4Fe, Ti-6Al-4Nb, Ti-8.4Al-15.4Nb and Ti-13.4Al-29Nb (all compositions are in wt %). All the experiments were carried out in simulated body fluid solution (Hank's solution of pH 7.4 and at 37°C). The effect of immersion time in Hank's solution on passive film on Ti-alloys was studied without any surface treatment. Three samples (CP Titanium, Ti-6Al-4V and Ti-13Nb-13Zr) were treated with 5M NaOH solution (for 24 hrs at 60°C temperature) and the effect of immersion time in Hank's solution on the passive film was studied using potentiodynamic polarization and EIS techniques. The surface film was characterized using SEM and XRD techniques. Tensile testing and subsequently fractography of fractured tensile samples was performed for two alloys i.e. Ti-6Al-4Nb and Ti-6Al-4Fe. All the results were analyzed in detail.

Following conclusions were drawn in the current study.

1. All the Ti alloys exhibited  $i_{\text{corr}}$  (i.e. corrosion rate) in a narrow region between 0.025 and 0.090  $\mu\text{A}/\text{cm}^2$ . The corrosion rate was not drastically affected by addition of alloying elements like aluminum, niobium, iron, zirconium and vanadium to CP titanium ( $i_{\text{corr}}$  of 0.047  $\mu\text{A}/\text{cm}^2$ ).

2. Comparing, Ti-6Al-4Fe and Ti-5Al-2.5Fe alloys,  $i_{\text{corr}}$  of these alloys were 0.045 and 0.028  $\mu\text{A}/\text{cm}^2$ , respectively. This indicated lowering of corrosion rate with higher amount Fe as alloying element. However, this change is quite low. Passive film resistance for both the iron-containing titanium alloys increased with immersion time in Hank's solution. This indicated improvement in passive film behavior with Fe as an alloying element. However, the increase in passive film resistance, with immersion time in Hank's solution, for Ti-6Al-4Fe was much higher than Ti-5Al-2.5Fe. This suggests that increased percentage of Fe improves passive film behavior.
3. All the Ti alloys showed improvement in passive film resistance with immersion time in Hank's solution. This indicated that passive film on Ti-alloys becomes more protective with immersion in Hank's solution.
4. The increase in passive film resistance was quite high for Ti-6Al-4Nb, Ti-8.4Al-15.4Nb and Ti-13Al-28Nb alloys when immersed in Hank's solution. This indicated that alloying element Nb along with Al improved the passive film resistance on immersion in Hank's solution.
5. Surface characterization (XRD and SEM) and subsequently EIS studies of NaOH-treated samples indicated that Ti alloys react with NaOH solution to form sodium titanate gel layer, which further initiated apatite nucleation and growth on subsequent immersion in Hank's solution.
6. EIS studies showed that the apatite layer resistance, after 168 hrs of immersion, was highest for NaOH-treated Ti-13Nb-13Zr alloy. This indicated enhance rate of apatite growth on NaOH-treated Ti-13Nb-13Zr compared to NaOH-treated CP titanium and Ti-6Al-4V alloys.



7. The as-cast Ti-6Al-4Nb and Ti-6Al-4Fe alloys exhibited similar tensile strength. The effect of alloying element on tensile strength was not clearly understood due to cast structure of tensile test samples. The SEM micrographs of the fractured samples showed brittle fracture (presence of flat cleaved facets) in Ti-6Al-4Fe alloy, in contrast to ductile mode of fracture for Ti-6Al-4Nb alloy. The Ti-6Al-4Nb alloy exhibited higher ductility compared to Ti-6Al-4Fe alloy.

## 5.2 suggestions for future work

- Cyclic voltammetry experiments can be used to examine the effect of various alloying elements on the passivation behavior of titanium alloys.
- An alloy with higher Fe content can be used to ascertain the effect of alloying element Fe on passive film behavior of titanium alloys.
- A more detailed study including electrochemical, tribological and heat treatment experiments can be performed to examine effect of Fe as alloying element to titanium alloys.
- Electrochemical noise experiments can be performed to study passive film behavior.
- Surface sensitive techniques like XPS can be used for surface characterization of titanium alloys after NaOH treatment and after immersion in Hank's solution.
- Effect of heat treatment on localized corrosion resistance and passivity can be examined.
- Heat treatment can also be performed on Ti-6Al-4Fe alloy to improve its ductility.
- Effect of thermomechanical processing on the microstructures of the Ti alloys can be investigated

## REFERENCES

---

1. Galante J.O., Laing P.G., Lautenschlager E., *BIOMATERIALS AAOS Instr. Course Lect.*, 24:1, (1975).
2. Friedman R.J., Black J., Galante J.O., Jacobs J.C., Skinner H.B., Correct Concepts in Orthopedic BIOMATERIALS and Implant fixation, *J Bone Joint Surg. (Am)*, 75A, 1086-1090, (1993).
3. William D.F., Critical Reviews in BIOCOMPATIBILITY CRC Press Inc.; Boca Raton, FL, USA; (1996).
4. Mathieson E.B., Ahlbohm A., Berman, Linggrn J.O., Total Hip Replacement and Cancer, (Br) 77B, 345-350, (1992).
5. Wickstrom J.K., Surgical Implants-The Mechanical and Environmental Problems, *Journal of Materials*, 1,366-372, (1966).
6. Bardos D.I., Stainless Steels in Medical Devices, in *Handbook of Stainless Steels*, (Eds) D. Peckner and I.M. Bernstein, 42.1-42.10. McGraw-Hill, New York (1977).
7. Luckey H.A., Kubli Jr. F., Editors Introduction in, Titanium Alloys in Surgical Implants, *ASTM Publication STP 796-800*,1-3,Philadelphia (1983).
8. Lemons J.E., Venugopalan R. and Lucas L.C.: Corrosion and Biodegradation, In: *Handbook of Biomaterials Evaluation*, Ed: A. Von Recum, Taylor Francis, Inc., 2,155-170, (1999).
9. ASTM G5: Standard reference test method for making Potentiostatic and Potentiodynamic anodic polarization measurements. In: *Metals, Test Methods and Analytical Procedures*, PA: *American Society for Testing and Materials*, 03.02.Philadelphia, 48-58, (1995).
10. Brown S.A. and Meritt K., Electrochemical Corrosion in Saline and Serum, *Journal of Biomedical Materials Research*, 14,173-175, (1980).
11. Kruger, Jerome, Fundamental Aspects of the Corrosion of Metallic Implants, *Corrosion and Degradation of Implant Materials*, B.C. Syrett

and A. Acharya, Eds, *American Society for Testing and Materials*, ASTM STP 684,107-127, (1979).

12. Litsky A.S., Spector M., Biomaterials-Orthopaedic basic science, American academy of orthopaedic surgeons, Simon SR (ed), 470-473, (1994).
13. Jacobs J.J., Gilbert J.L., Urban R.M., Corrosion of metal orthopaedic implants. *Journal of Bone and Joint Surgery*, 80A, 268 – 282, (1998).
14. Atkinson J.R., Jobbins B. Properties of Engineering materials for use in the body, In Dowson D., Wright V. (eds). *Introduction to the Biomechanics of Joints and Joint Replacement*, London, Mechanical Engineering Publications Ltd, (1981).
15. Williams D.F., The Deterioration of Materials in used in Implants in Surgery, (Eds) D.F. Williams and R. Roaf, W.B. Saunders, Philadelphia, 137-183, (1973).
16. Pourbaix M., Electrochemical Corrosion of Metallic Biomaterials, *Biomaterials*, 5, 122-134 (1984).
17. Bardos D.I., Stainless Steels in Medical Devices, in *Handbook of Stainless Steels*, (Eds) D. Peckner and I. M. Bernstein, 42.1-42.10 McGraw-Hill, New York (1977).
18. Zapffe C.A., Human Body fluids affect Stainless Steel, *Metal Progress*, 67, 95-98, (1965).
19. Hughes A.N., Jordan B.A. and Orman S., The Corrosion Fatigue Properties of Surgical Implant Materials. Third Progress Report-May 1973, *Engineering in Medicine*, 7, 135-141 (1978).
20. Walker G.D., *Journal of Biomedical Materials Research* (Symposium), 5, 11-26 (1974).
21. Jacobson B., and Webster J.B., Chapter 10. Surgery in Medicine and Clinical Engineering, (Eds) Jacobson and Webster Prentice-Hall Inc., New Jersey, 525-532, (1977).
22. Guyton A.C., Chapter 33, Partition of the Body Fluids Osmotic Equilibria between Extracellular and Intracellular Fluids, in *Textbook of*

Medical Physiology (5<sup>th</sup> Edition), (Ed.) Guyton A.C., W.B. Saunders, Philadelphia, 424-437, (1976).

23. Greene N.D., Corrosion of surgical implant alloys: A few basic ideas, in Corrosion and Degradation of Implant materials, Second Symposium, (Eds) A.C. Fraker and C.D. Griffin, ASTM Publication STP 859, Philadelphia (1985).
24. Laing P.G., Compatibility of Biomaterials, Orthopaedic Clinics of North America, 4, 249-273 (1973).
25. Pazzaglia U.E., Minola C., Gualtieri G., Gualtieri, Riccardi C., Cecillani L., Metal ions in body fluids after arthroplasty. *Acta Orthop Scand*, 57, 415 – 418, (1986).
26. Dorr L.D., Bloebaum R., Emmanuel J., Meldrum R., Histologic, Biochemical, and ion analysis of tissue and fluids retrieved during Total Hip Arthroplasty. *Clin Orthop*, 261, 82 – 95, (1990).
27. Urban R.M., Jacobs J.J., Gilbert J.L., Galante J.O., Migration of corrosion products, from modular hip prostheses. Particle microanalysis and histopathological findings. *Journal of Bone and Joint Surgery*, 76A, 1345–1359, (1994).
28. Park J.B., Lakes R.S., Metallic Implant Materials, In Biomaterials-an Introduction, and ed, New York, Plenum Press, 75-115, (1992).
29. Black J., Metallic Ion Release and its relationship to Oncogenesis, In Fitzgerald RH Jr (ed): The Hip, St. Louis, Mosby, 199-213, (1985).
30. Hoar T.P., and Mears D.C., Corrosion Resistant Alloys in Chloride Solutions, *Proceedings of Royal Society-Series A*, 294, 486-510 (1966).
31. Lucas L.C., Buchanan R.A., Lemons J.E., and Griffin C.D., Susceptibility of Surgical Cobalt-base Alloy to Pitting Corrosion, *Journal of Biomedical Materials Research*, 1, 405-414 (1967).
32. Svare C.W., Belton G., and Korostoffe E., The Role of Organics in Metallic Passivation, *Journal of Biomedical Materials Research*, 457-467 (1970).

33. Revie R. and Greene N.D., Comparison of the In-Vivo and In-Vitro Corrosion of 18-8 Stainless Steel and Titanium, *Journal of Biomedical Materials Research*, 3,465-470 (1969).
34. Colangelo V.T., Greene N.D., Kettelkamp D.B., Alexander H., and Campbell, C.J., Corrosion Rate Measurement In-Vivo, *Journal of Biomedical Materials Research*, 1, 405-414 (1967).
35. Steinemann S.G., Corrosion of Surgical Implants- In-Vivo and In-Vitro Tests, in Evaluation of Biomaterials, (Eds) G.D. Winter, J.L. Leray and K. deGroot, *Advanced Biomaterials*, 1,1-34 (1980).
36. Buchanan R.A. and Lemons J.E., In-Vivo Corrosion-Polarization Behaviour of Titanium-Base and Cobalt-Base Surgical Alloys, Transactions of the 8<sup>th</sup> Annual Meeting of the Society of Biomaterials, 5,110 (1982).
37. Brown S.A. and Merritt K., Fretting Corrosion in Saline and Serum, *Journal of Biomedical Materials Research*, 15, 867-878 (1981).
38. Thull R. and Schaldach M., Corrosion of Highly Stressed Orthopaedic Joint Replacements, in Engineering Medicine: Advances in Artificial Hip and Knee Joint Technology, (Eds) M. Schaldach and D. Hohmann, Springer Verlag, Berlin, Heidelberg, New York, 242-256, (1976).
39. Bundy K.J., Vogelbaum M.A. and Desai V.H., The influence of Static Stress on the Corrosion Behaviour of 316L Stainless Steel in Ringer's Solution, *Journal of Biomedical Material's Research*, 20,493-505, (1986).
40. Semlitsch M., and Willert H.G., Properties of Implant alloys for artificial Hip Joints, *Medical and Biological Engineering and Computing*, 18, 511-520 (1980).
41. Revie R.W., Greene N.D., Corrosion Behaviour of Surgical Implant Materials1: Effect of Sterilisation, *Corrosion Science*, 9,755-761, (1969).
42. Revie R.W., Greene N.D., Corrosion Behaviour of Surgical Implant Materials 2: Effect of Surface Preparation, *Corrosion Science*, 9, 763-770 (1969).

43. Mueller H.J. and Greener E.H., Polarization Studies of Surgical Materials in Ringer's Solution, *Journal of Biomedical Materials research*, 4, 29-41 (1970).
44. Ogundele G.I., and White W.E., Polarization Studies on Surgical- Grade Stainless Steels in Hank's Physiological Solution, in Corrosion and Degradation of Implant Materials, second symposium, (Eds) Fraker A.C. and Griffin C.D., *ASTM Publication STP 859*, Philadelphia 117-135, (1985).
45. White W.E., Postlethwaite J. and LeMay I., in Microstructural Science, *American Elsevier*, New York, 4,145-157 (1976).
46. Black J., Corrosion and degradation in Orthopaedic biomaterials in research and practice, New York, Churchill, Livingstone, 235-266, (1988).
47. Griffin C.D., Buchanan R.A., Lemons J.E., In vivo electrochemical corrosion study of coupled surgical implant materials. *Journal of Biomedical Materials Research*, 17,489-500, (1983).
48. Syrett B.C. and Wing S.S., Pitting Resistance of New and Conventional Orthopaedic Implant Materials-Effect of Metallurgical Condition, *Corrosion*, 34A, 138-145, (1978).
49. Syrett B.C., and Davis E.E., Crevice Corrosion of Implant Alloys-A comparison In-Vitro and In-Vivo Studies, Presented at Spring Meeting of ASTM, Kansas City, MO. (1978).
50. Sury P., Corrosion Behaviour of Case and Forged Implant Materials for Artificial Joints, Particularly with Respect to Compound Designs. Research and Development Department, Sulzer Brothers Ltd., CH-8401, Winterthur, Switzerland.
51. Cohen J., Clinical failure Caused by Corrosion of a Vitalium Plate, *Journal of Bone and Joint Surgery*, 54A, 617-628 (1972).
52. Rose R.M., Schiller A.L. and Radin E.L., Corrosion-Accelerated Mechanical Failure of Vitalium Nail-Plate, *Journal of Bone and Joint Surgery*, 54A, 854-862 (1972).

53. Cahoon J.R., Bandyopadhyaya R. and Tennese L., The Concept of Protection Potential Applied to the Corrosion of Metallic Orthopaedic Implants, *Journal of Biomedical Materials Research*, 9, 259-264, (1975).
54. Morral F.R., Crevice Corrosion of Cobalt Based Surgical Alloys, *Journal of Materials*, 1, 384 (1966).
55. Rostoker W., Pretzel C.W. and Galante J.O., Couple Corrosion Among Alloys for skeletal Prostheses, *Journal of Biomedical Materials Research*, 8, 407-419 (1974).
56. Syrett B.C., and Wing S.S., An Electrochemical Investigation of Fretting Corrosion of Surgical Implant Materials, *Corrosion*, 34, 379-386 (1978).
57. Cohen J., Corrosion Testing of Orthopaedic Implants, *Journal of Bone and Joint Surgery*, 44A, 307-316 (1962).
58. Lucas L.C., Buchanan R.A., Lemons J.E., and Griffin C.D., Susceptibility of Surgical Cobalt-base Alloy to Pitting Corrosion, *Journal of Biomedical Materials Research*, 16, 799-810 (1982).
59. Bowden F.P., Williamson J.B.P., Laing P.G., The Significance of Metal Transfer Orthopaedic Surgery, *Journal of Bone and Joint Surgery*, 37B, 676-690, (1955).
60. Gilbert T.L., Buckley C.A., Jacobs J.J., In vivo Corrosion of Modular Hip Prosthesis components in mixed and similar combinations. The effect of crevice, stress, motion and stress coupling, *Journal of Biomedical Materials Research*, 27, 1533 – 1544, (1993).
61. Pugh J., Dee R., Properties of Musculoskeletal tissues and Biomaterials, In Dee R, Mango E, Hurst LC (eds); *Principles of Orthopaedic Practice*, New York, McGraw Hill, (1988).
62. Greener E., Lauten Schlager E., Materials for Bioengineering Applications, In: Brown JHV, Jacobs JE and Stuart L (eds): *Biomedical Engineering*, Philadelphia, FA Davis, (1971).



63. Colangelo V.J., and Greene N.D., Corrosion and Fracture of Type 316 SMO Orthopaedic Implants, *Journal of Biomedical Materials Research*, 3, 247-265, (1969).
64. Cahoon J.R., and Paxton H.W., Metallurgical Analyses of Failed Orthopaedic Implants, *Journal of Biomedical Materials Research*, 2, 1-22, (1968).
65. Sheehan J.P., Morin C.R. and Packer K.F., Study of Stress Corrosion Cracking Susceptibility of Type 316L Stainless Steel In-Vitro, in Corrosion and Degradation of Implant Materials, Second Symposium, (Eds) A.C. Fraker and C.D. Griffin, *ASTM Publication STP 859*, 57-72, Philadelphia (1985).
66. Bundy K.J., and Desai V.H., Studies of Stress-Corrosion Cracking Behaviour of Surgical Implant Materials Using a Fracture Mechanics Approach, in Corrosion and Degradation of Implant Materials, Second Symposium, (Eds) A.C. Fraker and C.D. Griffin, *ASTM Publication STP 859*, 73-90, Philadelphia (1985).
67. Leclerc M.F., A Review of the Factors Influencing the Mechanical Failure of the Femoral Component used in Total Hip Replacement, Proceedings: *Engineering in Orthopaedic Surgery and Rehabilitation*, published by Bioengineering Unit, Princess Margaret Rose Hospital, 36-48, Edinburgh (1982).
68. Bechtol C.O., Failure of Femoral Implant Components in Total Hip Replacement Operations, *Orthopaedic Review*, 4, 23-29, (1975).
69. Hughes A.N., Jordan B.A. and Orman S., The Corrosion Fatigue Properties of Surgical Implant Materials, Third Progress Report-May 1973, *Engineering in Medicine*, 7, 135-141 (1978).
70. Rollins V., Arnold B. and Lardner E., Corrosion Fatigue in High Carbon Steel, *British Corrosion Journal*, 5,33 (1970).
71. Piehler H.R., Portnoff M.A., Slotter L.E., Vegdahl E.J., Gilbert J.L. and Weber M.J., Corrosion-Fatigue Performance of Hip Nails: The Influence of Materials Selection and Design, in Corrosion and Degradation of

Implant Materials, Second Symposium, (Eds) Fraker A.C. and Griffin C.D., *ASTM Publication STP 859*, 93-104, Philadelphia (1985).

72. Hille G.H., *Journal of Materials*, 1:2, 373, (1966).
73. McMaster J.A., Titanium for Prosthetic Devices, presented at IMD Dental-Medical Committee, *American Institute of Mechanical Engineers*, Cleveland, 21 Oct. (1974).
74. Greene N.D., Onkelinx C., Richelle L.J., Ritland G.D. and Ward P.A., Biomaterials: Improved Implant Alloys, presented in Brighton Implant Meeting, Brighton, Utah, 8-9 Nov. (1972).
75. Hochman R. and Mark M., In-Vivo Evaluation of Mechanical and Corrosion Characteristics of Ti and Ti-6Al-4V ELI, presented at MATCON ' 74, *ASM/TMS-AIME*, Detroit, 22 Oct. (1974).
76. Titanium Alloys Handbook MCIC-HB02, MCIC (1972).
77. ASTM: Standard specification for unalloyed and alloyed titanium for surgical implant applications. In: Medical Devices and Services, Philadelphia, PA: *American Society for Testing and Materials*, 13.01, 1-20, (1998).
78. Farthing T.W., The Development of Titanium and its Alloys, *Clinical Materials*, 1-2, Feb. (1987).
79. Agins H.J., Alcock N.W. Metallic Wear in Failed Titanium - Alloy Total Hip Replacements. Arthrological and Quantative Analysis, *Journal of Bone and Joint Surgery. (Am)*, 70A, 347-356, (1988).
80. Titanium as a metal for implantation – Part 2: Biological properties and Clinical applications. *Journal of Medical Engineering Technology*, 1, 266-270, (1977).
81. Bluementhal N.C., Cosma V. Inhibition of Apatite formation by Titanium and Vanadium ions. *Journal of Biomedical Materials Research*, 23, 13-22, (1989).
82. Torgerson S., Gjerdet N.R., Retrieval study of Stainless Steel and Titanium miniplates and screws used in Maxillofacial Surgery, *Journal of Material Science: Mater Med*, 5, 256-262, (1994).

83. Scales J.T., Black J., Staining around Titanium alloy Prosthesis—an orthopaedic enigma. *Journal of Bone and Joint Surgery*, 73B, 534-536, (1991).
84. Mirza Rosca J.C., Gonzalez S., Llorente M.L., Popa M.V., Vasilescu E. and Drob P. In: 7th European Conference on Applications of Surface and Interface Analysis Wiley, New York, 377-380, (1997).
85. Popa M.V., Vasilescu E., Mirza Rosca J.C., Rodrigues J.J.S., Gonzalez S., Drob P. in: M. Andritschky (Ed.), *Advances in Materials and Processing Technologies*, 2-AMPT'97, 737, (1997).
86. Popa M.V., Radovici O., Vasilescu E., Mirza Rosca J.C., Gonzalez S., Drob P., *9th Proceedings of the International Metallurgy and Materials Congress*, 1, p.209, (1997).
87. Yu S.Y. and Scully J.R., *Corrosion*, 12, 965, (1997).
88. Bandyopadhyaya R. and Cahoon J.R., Effect of composition on the Electrochemical behaviour of Austenitic Stainless Steel in Ringer's solution, *Corrosion*, 33, 204-208, (1977).
89. Cahoon J.R., Chaturvedi M.C., and Tennese L., Corrosion studies on metallic implant materials, *JAAMI* 7, 131-135, (1973).
90. Donachie M.J., Titanium—a technical guide. OH, USA: *ASM International*, (1988).
91. Steinemann S.G. et al., Beta Titanium Alloy for Surgical Implants, *Titanium 92 Science and Technology*, 3, 2689-2696, TMS, (1993).
92. Hoar T.P. and Mears D.C., Corrosion-resistant alloys in chloride solutions: materials for surgical implants, *Proc Royal Soc* 294A, 486-510, (1966).
93. Kovacs P., Davidson J.A., The electrochemical behaviour of a new titanium alloy, Ti-13Nb-13Zr. Presented at the 19th Annual meeting of the Society for Biomaterials. Davidson JA, Mishra AK, Kovacs P, Poggie RA. New surfacehardened, low modulus, corrosion resistant Ti-13Nb-13Zr alloy for total hip arthroplasty. *Biomedical Materials Engineering*, 4, 231-243, (1994).

94. Sousa S.R., Barbosa M.A., Corrosion resistance of titanium CP in saline physiological solutions with calcium phosphate and proteins. *Clinical Materials*, 12, 1-4, (1993).
95. Gurappa I., Characterization of Different Materials for Corrosion Resistance under Simulated Body Fluid Conditions, *Materials Characterization*, 49, 73-79, (2002).
96. Kovacs P., Davidson J.A., The electrochemical behaviour of a new titanium alloy, Ti-13Nb-13Zr. Presented at the 19<sup>th</sup> Annual meeting of the Society for Biomaterials, (1993-88).
97. Williams D.F., Physiological and Microbiological Corrosion, *Critical Reviews on Biocompatibility*, 1, 1-24, (1985).
98. Khan M.A. et al., The Corrosion behaviour of Ti-6Al-4V, Ti-6Al-7Nb and Ti-13Nb-13Zr in Protein Solutions, *Biomaterials*, 20, 631-637, (1999).
99. Andreeva V. and Kazarin V., *Proceedings of third International Congress on Metallic Corrosion*, Mir Publications, Moscow, 1, 464, (1969).
100. Fraker A.C., Ruff A.W., and Yeager M.P., *Proceedings, Second International Titanium Conference*, Plenum, New York, (1976) (preprint).
101. Tomashov N.D., *Corrosion*, 20, 7t, (1964).
102. Bomberger H.B., Alloying to Improve Crevice Corrosion Resistance of Titanium, *presented at MATCON '74, ASM/TMS-AIME*, Detroit, 22 Oct. (1974).
103. Sousa S.R., Barbosa M.A. Corrosion Resistance of Titanium CP in saline physiological solutions with calcium phosphate and proteins, *Clinical Materials*, 12, 1-4, (1993).
104. B.D. Ratner, A.B. Johnston and T.J. Lenk J. *Biomed. Mat. Res.*, 21, 59, (1987).
105. J. Breme and P. Lacombe , *Sixth World Conference on Titanium*, Cannes, 533, (1988).
106. K.J. Bundy, *Crit. Rev. Biomed. Eng.*, 22,139, (1994).

107. A.C. Fraker, C.D. Griffin (Eds.), Corrosion and Degradation of Implant Materials, *Second International Symposium, American Society for Testing and Materials*, Philadelphia, PA, 384, (1985).
108. H. Zitter and H.P. Lenk, Jr. *J. Biomed. Mat. Res.* 21, 881, (1987).
109. L.L. Hench *Anal. Quim., Int. Ed.*, 93, S3, (1997).
110. J.A. Hunt and M. Stoichet *Curr. Op. Sol. State Mat. Sci.*, 5 (2001)
111. R.J. Solar, A. Syrett, A. Acharya (Eds.), Corrosion and Degradation of Implant Materials, *First International Symposium, American Society for Testing and Materials*, Philadelphia, PA, 259, (1979).
112. E.J. Sutow and S.R. Pollack, *Biocompatibility of Clinical Implant Materials*, CRC Press, Boca Raton, FL, 45, (1981).
113. D.F Williams, *Biocompatibility of Clinical Implant Materials*, CRC Press, Boca Raton, FL, 99 (1981).
114. K.E. Healy and P. Ducheyne, *J. Biomed. Mat. Res.* 26, 319, (1992).
115. D.J. Blackwood, L.M. Peter and D.E. Williams *Electrochim. Acta*, 33, 1143 (1988)
116. M.A. Khan, R.L. Williams and D.F. Williams, *Biomaterials*, 20, 765, (1999).
117. R.J. Solar and E. Korostoff *J. Biomed. Mat. Res.*, 13, 217, (1979).
118. R.J. Solar, S.R. Pollack., E. Korostoff, B.C. Syrett, A. Acharya (Eds.), Corrosion and Degradation of Implant Materials, *First International Symposium of American Society for Testing and Materials*, Philadelphia, PA, 161, (1979)
119. M.A. Khan, R.L. Williams and D.F. Williams, *Biomaterials*, 20, 631, (1998)

120. M. Wieland, C. Sittig, M. Textor, V. Schenk, S.W. Ha, B.A. Keller, E. Wintermantel, N.D. Spencer, *ECASIA 97*, Göteborg, 122, (1997).
121. S.R. Sousa and M.A. Barbosa *Clin. Mat.*, 14, 287, (1993).
122. W. Wu and G. Nancollas *J. Coll. Int. Sci.* 199, 206, (1998).
123. T. Hanawa and M. Ota, *Biomaterials*, 12, 767, (1991).
124. S.R. Sousa and M.A. Barbosa *Biomaterials*, 17, 397, (1996).
125. P. Li and P. Ducheyne *J. Biomed. Mat. Res.*, 41, 341, (1998).
126. L. Frauchiger, M. Taborelly, B.O. Aronsson and P. Descouts, *Appl. Surf. Sci.* 143, 57, (1999).
127. B.C. Yang, J. Weng, X.D. Li and X.D. Zhang *J. Biomed. Mat. Res.*, 47, 213, (1999)
128. K.E. Healy and P. Ducheyne, *Biomaterials*, 13, 552, (1993).
129. J.E. Ellingsen *Biomaterials*, 12, 593, (1991).
130. J.E. Sundgren, P. Bodo and I. Lundstrom *J. Colloid. Int. Sci.*, 110, 9, (1986).
131. J.E. Sundgren, P. Bodo, B. Ivarsson and I. Lundstrom, *J. Colloid. Int. Sci.*, 113, 530, (1986).
132. T. Hanawa, K. Asami and K. Asaoka *J. Biomed. Mat. Res.*, 40, 530, (1998)
133. L.I. Panjian and P. Ducheyne *J. Biomed. Mat. Res.*, 41, 341, (1997).
134. Alexia W. E. Hodgson, Yves Mueller, Dominic Forster and Sannakaisa Virtanen, *Electrochimica Acta*, 47, 913-1923, (2002).
135. J.E. Ellingsen and K. Videm, *Mat. Clin. Appl.*, 543, (1995).

136. J. Pan, D. Thierry and C. Leygraf *J. Biomed. Mat. Res.*, 28, 113, (1994).
137. J. Pan, D. Thierry and C. Leygraf, *J. Biomed. Mat. Res.*, 30, 393, (1996).
138. J.P. Bearinger, C.A. Orme and J.L. Gilbert, Direct observation of hydration of TiO<sub>2</sub> on Ti using electrochemical AFM: freely corroding versus potentiostatically held conditions, *Surf Sci*, 491, 370–387, (2001).
139. E. Kobayashi, T.J. Wang, H. Doi, T. Yoneyama and H. Hamanaka, Mechanical properties and corrosion resistance of Ti–6Al–7Nb alloy dental casting, *Mater Sci: Mater Med*, 9, 567–574, (1998).
140. C. Sittig, G. Hahner, A. Marti, M. Textor, N.D. Spencer and R. Hauert, The implant material, Ti6Al7Nb: surface microstructure, composition and properties, *J Mater Sci: Mater Med*, 10, 191–199, (1999).
141. D. Rogers, D.W. Howie, S.E. Graves, M.J. Pearcy and D.R. Haynes, In vitro human monocyte response to wear particles of titanium alloy containing vanadium or niobium, *J Bone Joint Surg*, 79-B, 311–315 (1997).
142. D.G. Kolman and J.R. Scully, Electrochemistry and passivity of Ti–15V–3Cr–3Al–3Sn b-titanium alloy in ambient temperature aqueous chloride solution. *J Electrochem Soc*, 142, 2633–2641, (1994).
143. S.Y. Yu, J.R. Scully and C.M. Vitus, Influence of niobium and zirconium alloying additions on the anodic dissolution behavior of activated titanium in HCl solutions, *J Electrochem Soc*, 148, B68–B78, (2001).
144. S.Y. Yu and J.R. Scully, Corrosion and passivity of Ti-13% Nb-13%Zr in comparison to other biomedical implant alloys, *Corrosion*, 53, 965–976, (1997).

145. Yu SY, Scully JR., Enhanced resistance to steady state active dissolution and passivity of alloyed with Nb and Zr, *Electrochemical Society Proceedings*, Pennington, NJ, 96, 18, (1996).
146. M. Metikoš-Huković, A. Kwokal and J. Piljac, *Biomaterials*, 24, 3765-3775, (2003).
147. Lide DR, *Handbook of Chemistry and Physics*. 76<sup>th</sup> ed., (1995-1996).
148. R. Adell, U. Lekholm, B. Rockler and P.I. Branemark, A 15-year study of osseointegrated implants in the treatment of the edentulous jaw, *Int J Oral Surg*, 10, 387-461, (1981).
149. B.D. Ratner, New ideas in biomaterials science-a path to engineered biomaterials. *J Biomed Mater Res*, 27, 837-850 (1993).
150. M.S. Block, I.M. Finger, M.G. Fontenot and J.N. Kent, Loaded hydroxyapatite-coated and grit-blasted titanium implants in dogs, *Int J Oral Maxillofac Implants*, 4, 219-225, (1989).
151. A. Nanci, J.D. Wuest, L. Peru, P. Brunet, V. Sharma, S. Zalzal *et al.*, Chemical modification of titanium surfaces for covalent attachment of biological molecules, *J Biomed Mater Res*, 40, 324-335, (1998).
152. L.L. Hench, Bioceramics: from concept to clinic, *J Am Ceram Soc*, 74 1485-1510, (1991).
153. E.J. McPherson, L.D. Dorr, T.A. Gruen and M.T. Saberi, Hydroxyapatite-coated proximal ingrowth femoral stems. A matched pair control study. *Clin Orthop*, 315, 223-230 (1995).
154. H. Kurzweg, R.B. Heimann, M. Troczynski and M.L. Wayman, Development of plasma-sprayed bioceramic coatings with bond coats based on titania and zirconia, *Biomaterials*, 19, 1507-1511, (1998).



155. J. Pan, D. Thierry and C. Leygraf, Electrochemical impedance spectroscopy study of the passive oxide film on titanium for implant application, *Electrochim Acta*, 41, 1143–1153, (1996).
156. Solar RJ. In: Syrett BC, Acharya A, editors. Corrosion, degradation of implant materials, *American Society for Testing and Materials*, Philadelphia, (1979).
157. M. Cabrini, A. Cigada, G. Rondelli and B. Vicentini, Effect of different surface finishing and of hydroxyapatite coatings on passive and corrosion of Ti6Al4V alloy in simulated physiological solution. *Biomaterials*, 18, 783–787 (1997).
158. R. R Brown, M.N. Alias and R. Fontana, Effect of composition and thickness on corrosion behavior of TiN and ZrN thin films, *Surf Coat Technol*, 62, 467–473, (1993).
159. I. Vaquila, L.I. Vergara, M.C.G. Passeggi Jr, R.A. Vidal and J. Ferron, Chemical reactions at surfaces: titanium oxidation, *Surf Coat Technol* 122, 67–71, (1991).
160. H. Ishizawa and M. Ogino, Formation and characterization of anodic titanium oxide films containing Ca and P. *J Biomed Mater Res* 29, 65–72, (1995).
161. D.B. Haddow, S. Kothari, P.F. James, R.D. Short, P.V. Hatton and R. van Noort, Synthetic implant surfaces: The formation and characterization of sol-gel titania films, *Biomaterials*, 17 501–507, (1996).
162. S.C. Dieudonne, J. van den Dolder, J.E. de Ruijter, H. Paldan, T. Peltola, M.A. van't Hof, R.P. Happonen and J.A. Jansen, Osteoblast differentiation of bone marrow stromal cells cultured on silica gel and sol-gel derived titania, *Biomaterials*, 23, 3041–3051, (2002).

163. M. Jokinen, M. Patsi, H. Rahiala, T. Peltola, M. Ritala and J.B. Rosenholm, Influence of sol and surface properties on in vitro bioactivity of sol-gel-derived TiO<sub>2</sub> and TiO<sub>2</sub>-SiO<sub>2</sub> films deposited by dip-coating metho, *J Biomed Mater Res*, 42, 295-302 (1998).
164. Hae-Won Kim, Young-Hag Koh, Long-Hao Li, Sook Lee and Hyoun-Ee Kim, *Biomaterials*, 25, 2533-2538, (2004).
165. Kim HW, Kong YM, Bae CJ, Noh YJ, Kim HE. Sol-gel derived fluor-hydroxyapatite biocoatings on zirconia substrate. *Biomaterials*, in press.
166. L. Cleries, In vitro studies of calcium phosphate coatings obtained by laser ablation, PhD Thesis, University of Barcelona, Spain, 1999.
167. H. Hero, H. Wie, R.B. Jorgensen and I.E. Ruyter , Hydroxyapatite coating on titanium produced by isostatic pressing, *J. Biomed. Mater. Res.*, 28, 344-348 (1994).
168. K. De Groot, C.P. Klein, J.G. Wolke and J.M. Blieck-Hogervorst , Plasma sprayed coatings of calcium phosphate. In: T. Yamamuro, L. Hench and J. Wilson, Editors, *CRC Handbook of Bioactive Ceramics Calcium phosphate and hydroxyapatite ceramics*, CRC Press, Boca Raton, FL, 2, 133-142, (1990).
169. A.S. Posner, N.C. Blumenthal and F. Betts In: C. Eon, Editor, *Proceedings of the 2nd International Conference on Phosphorous Compounds*, Imphos, Paris, 25, (1980).
170. E. Park, S.R. Condrate, D.T. Hoelzer and G.S. Fischman , Interfacial characterisation of plasma-spray coated calcium phosphate on Ti6Al4V. *J. Mater. Sci. Med.* 9, 643-649, (1998).
171. H. Takadama, H.M. Kim, T. Kokubo and T. Nakamura, An X-ray photoelectron spectroscopy study of the process of apatite formation on bioactive titanium metal. *J Biomed Mater Res*, 55, 185-193, (2001).

172. S. Nishiguchi, H. Kato, M. Neo, M. Oka, H.M. Kim, T. Kokubo and T. Nakamura, Alkali- and heat-treated porous titanium for orthopedic implants, *J Biomed Mater Res* 54, 198–208, (2001).
173. Y. Han, T. Fu, J. Lu and K.W. Xu, Characterization and stability of hydroxyapatite coatings prepared by an electrodeposition and alkaline-treatment process. *J Biomed Mater Res* 54, 96–101, (2001).
174. K. Nishio, M. Neo, H. Akiyama, S. Nishiguchi, H.M. Kim, T. Kokubo and T. Nakamura, The effect of alkali- and heat-treated titanium and apatite-formed titanium on osteoblastic differentiation of bone marrow cells, *J Biomed Mater Res*, 52, 652–661, (2000).
175. H.M. Kim, T. Kokubo, S. Fujibayashi, S. Nishiguchi and T. Nakamura, Bioactive macroporous titanium surface layer on titanium substrate, *J Biomed Mater Res*, 52, 553–557, (2000).
176. S. Nishiguchi, T. Nakamura, M. Kobayashi, H.M. Kim, F. Miyaji and T. Kokubo, The effect of heat treatment on bone-bonding ability of alkali-treated titanium. *Biomaterials* 48, 689–696, (1999).
177. B.C. Yang, J. Weng, X.D. Li and X.D. Zhang, The order of calcium and phosphate ion deposition on chemically treated titanium surfaces soaked in aqueous solution, *J Biomed Mater Res*, 47, 213–219, (1999).
178. M.C. de Andrade, M.R.T. Filgueiras and T. Ogasawara, Nucleation and growth of hydroxyapatite on titanium pretreated in NaOH solution: experiments and thermodynamic explanation, *J Biomed Mater Res*, 46 441–446, (1999).
179. S. Nishiguchi, H. Kato, H. Fujita, H.M. Kim, F. Miyaji, T. Kokubo and T. Nakamura, Enhancement of bone-bonding strengths of titanium alloy implants by alkali and heat treatments. *J Biomed Mater Res (Appl Biomater)* 48, 689–696, (1999).

180. H.M. Kim, F. Miyaji, T. Kokubo, S. Nishiguchi and T. Nakamura, Graded surface structure of bioactive titanium prepared by chemical treatment, *J Biomed Mater Res*, 45 ,100–107, (1999).
181. H.M. Kim, F. Miyaji, T. Kokubo and T. Nakamura, Bonding strength of bonelike apatite layer to Ti metal substrate, *J Biomed Mater Res (Appl Biomater)* 38, 121–127, (1997).
182. W.Q. Yan, T. Nakamura, M. Kobayashi, H.M. Kim and F. Miyaji, Bonding of chemically treated titanium implants to bone. *J Biomed Mater Res* 37, pp. 267–275,(1997).
183. T. Kokubo, F. Miyaji and H.M. Kim, Spontaneous formation of bone-like apatite layer on chemically treated titanium metals. *J Am Ceram Soc* 79, pp. 1127–1129,(1996).
184. H.M. Kim, F. Miyaji, T. Kokubo and T. Nakamura, Preparation of bioactive Ti and its alloys via simple chemical surface treatment. *J Biomed Mater Res* 32, pp. 409–417, (1996).
185. W.Q. Yan, T. Nakamura, K. Kawanabe, S. Nishiguchi, M. Oka and T. Kokubo, Apatite layer-coated titanium for use as bone bonding implants. *Biomaterials* 18, pp. 1185–1190, (1997).
186. H.M. Kim, F. Miyaji, T. Kokubo and T. Nakamura, Effect of heat treatment on apatite-forming ability of Ti metal induced by alkali treatment. *J Mater Sci: Mater Med* 8, pp. 341–347, (1997).
187. C. Ohtsuki, H. Iida, S. Hayakawa and A. Osaka, Bioactivity of titanium treated with hydrogen peroxide solution containing metal chloride. *J Biomed Mater Res* 35, pp. 39–47, (1997).
188. X.X. Wang, S. Hayakawa, K. Tsuru and A. Osaka, Improvement of the bioactivity of H<sub>2</sub>O<sub>2</sub>/TaCl<sub>3</sub>-treated titanium after a subsequent heat treatment. *J Biomed Mater Res* 52, pp. 171–176, (2000).

189. X.X. Wang, S. Hayakawa, K. Tsuru and A. Osaka, A comparative study of in vitro apatite deposition on heat-, H<sub>2</sub>O<sub>2</sub>-, and NaOH-treated titanium surfaces. *J Biomed Mater Res* 54, pp. 172–178, (2001).
190. H.B. Wen, J.R. de Wijn, F.Z. Cui and K. de Groot, Preparation of bioactive Ti6Al4V surface by a simple method. *Biomaterials* 19, pp. 215–221, (1998).
191. H.B. Wen, J.R. de Wijn, F.Z. Cui and K. de Groot, Preparation of calcium phosphate coatings on titanium implant materials by simple chemistry. *J Biomed Mater Res* 41, pp. 227–236, (1998).
192. F. J. Gil' , A. Padrós, J. M. Manero, C. Aparicio, M. Nilsson and J. A. Planell Materials Science and Engineering: C Volume 22, Issue 1 , Pages 53-60, October 2002
193. T. Kokubo, F. Miyaji and H.-M. Kim , Spontaneous formation of bonelike apatite layer on chemically treated titanium metals. *J. Am. Ceram. Soc.* 79, pp. 1127–1129. (1996).
194. T. Hurlen and W. Wihelmsen , Passive behaviour of titanium. *Electrochim. Acta* 31, pp. 1139–1146, (1986).
195. K.E. Healy and P. Ducheyne , Passive dissolution kinetics of titanium in vitro. *J. Mater. Sci.: Mater. Med.* 4, pp. 117–126, (1993).
196. K.E. Healy and P. Ducheyne , The mechanism of passive dissolution kinetics of titanium in a model physiological environment. *J. Biomed. Mater. Res.* 36, pp. 319–338, (1992).
197. L.D. Arsov, C. Kormman and W. Plieth , In situ Raman spectra of anodically formed titanium dioxide layer in solution of H<sub>2</sub>SO<sub>4</sub>, KOH, and HNO<sub>3</sub>. *Electrochem. Soc.* 138, pp. 2964–2970, (1991).
198. H.M. Kim, F. Miyaji, T. Kokubo and T. Nakamura , Preparation of bioactive Ti and its alloys via simple surface treatment. *J. Biomed. Mater. Res.* 32, pp. 409–417, (1996).

199. J. Gamble *Chemical Anatomy Physiology and Pathology of Extracellular Fluid* (6th edn. ed.), Harvard University Press, Cambridge, MA (1967).
200. W. Neuman and M. Neuman *The Chemical Dynamics of Bone Mineral*, University of Chicago Press, Chicago, IL (1958).
201. C. X. Wang and M. Wang C. X. Wang and M. Wang, Electrochemical impedance spectroscopy study of the nucleation and growth of apatite on chemically treated pure titanium, *Materials Letters, Volume 54, Issue 1, , Pages 30-36, May 2002.*
202. C. X. Wang, M. Wang and X. Zhou, Nucleation and growth of apatite on chemically treated titanium alloy: an electrochemical impedance spectroscopy study *Biomaterials, Volume 24, Issue 18, Pages 3069-3077 August 2003*
203. Jones D.A., *Principles and Prevention of Corrosion*, Maxwell Macmillan, New York (1992).
204. Bockris J.O'M., *Modern Aspects of Electrochemistry*, Butterworths, (1954).
205. Tomashov N.D., *Theory of Corrosion and protection of Metals*, Macmillan, (1966).
206. Baboian R., Ed., *Electrochemical Techniques for Corrosion, National Association of Corrosion Engineers*, (1977).
207. Bertocci U. and Mansfield F., Ed., *Electrochemical Corrosion Testing, STP 727, American Society for Testing and Materials*, (1979).
208. Bard A.J. and Faulker L.R., *Electrochemical methods: Fundamentals and Applications*, p.19, John Wiley and Sons, Inc., (1980).
209. Hoare J.P., *Passivity of Metals*, Frankenthal R.P. and Kruger J., editors, *Electrochemical Society monograph series*, Princeton, NJ, p. 505, (1978).
210. Martin R.L., *Application of Electrochemical Polarization to Corrosion Problems*, Petrolite Corp., St. Louis, MO (1977).

211. Hack H. and Scully J.R., Crevice Corrosion behavior of 45 molybdenum containing Steels in sea water, *Corrosion*, 42, 79, (1986).
212. Mansfeld F., Electrochemical Methods, edited by Baboian R., *National Association of Corrosion Engineers*, Houston, TX, 67-71, (1996).
213. Anand R. R., *21<sup>st</sup> Annual Conference of NACE*, St. Louis, MO (1965).
214. Kaesche H., Metallic Corrosion, *National Association Corrosion Engineers*, Houston TX, p. 92, (1985).
215. Martin R.L., Application of Electrochemical Polarization to Corrosion Problems, Petrolite Corp., St. Louis, MO (1977).
216. A.J. Bard, L.R. Faulkner, *Electrochemical Methods; Fundamentals and Applications*, Wiley Interscience publications, 1980.
217. J.R. Scully, D.C. Silverman, and M.W. Kendig, *Electrochemical Impedance: Analysis and Interpretation*, ASTM, 1993.
218. Cottis and Stephen Turgoose, *Electrochemical Impedance and Noise*, Robert NACE International, 1440 South Creek Drive, Houston, TX 77084-4906.
219. J.R. Macdonald, *Impedance Spectroscopy; Emphasizing Solid Materials and Systems*, Wiley Interscience publications, 1987.
220. A.V. Oppenheim and A.S. Willsky, *Signals and Systems*, Prentice-Hall, 1983.
221. J.A.L. Dobbelaar, *The Use of Impedance Measurements in Corrosion Research; The Corrosion Behavior of Chromium and Iron Chromium Alloys*, PhD thesis TU-Delft, 1990.
222. F. Geenen, *Characterization of Organic Coatings with Impedance Measurements; A Study of Coating Structure, Adhesion and Underfilm Corrosion*, PhD thesis, TU-Delft, 1990.
223. C. Gabrielle, *Identification of Electrochemical Processes by Frequency Response Analysis*, Solartron Instrumentation Group, 1980.

- 235. Margolin H. and Farrar P., The physical Metallurgy of Titanium Alloys, *Ocean Engineering*, 1, 329-343, (1969).
- 236. Murakami Y., Critical Review: Phase Transformations and Heat Treatment, *Titanium 80*, The Metallurgical Society of AIME, Warrendale, PA, 153-167, (1981).
- 237. Mathew Donachie J., Jr., Titanium a Technical Guide, *ASM International*, 2<sup>nd</sup> Edition, 143-282, (2000).
- 238. Solar R.J., Corrosion Resistance of Titanium surgical implant Alloys, A Review, Corrosion and Degradation of Implant Materials, *American Society for Testing of Materials*, STP 684, 259-273, (1979).



## Appendix (A)

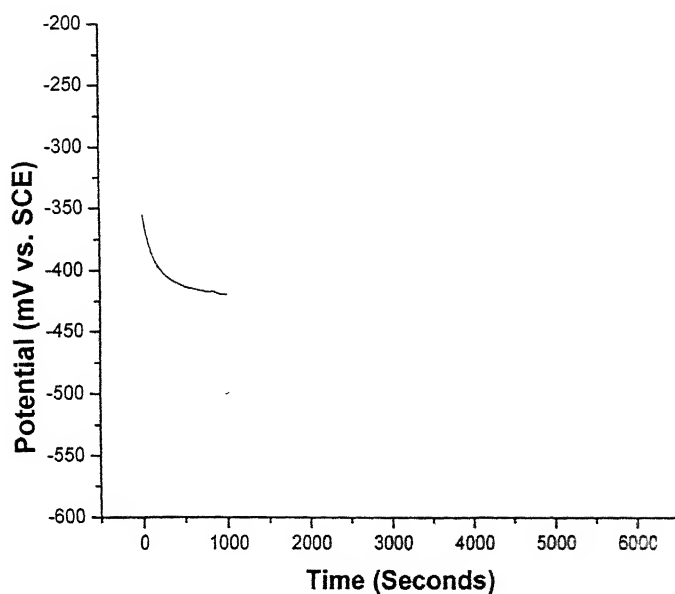


Figure A-1: Free corrosion potential as function of time for CP Titanium in Hank's solution at 37°C temperature and 7.4 pH.

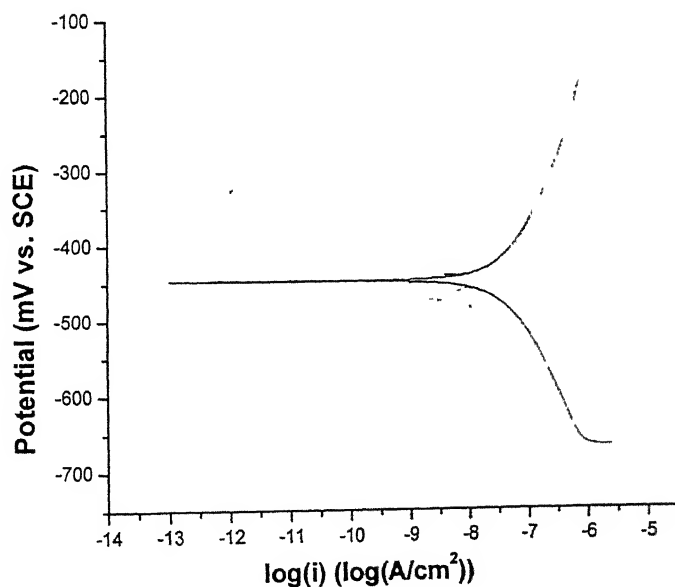


Figure A-2: Tafel extrapolation curve for CP Titanium in Hank's solution at 37°C temperature and 7.4 pH.

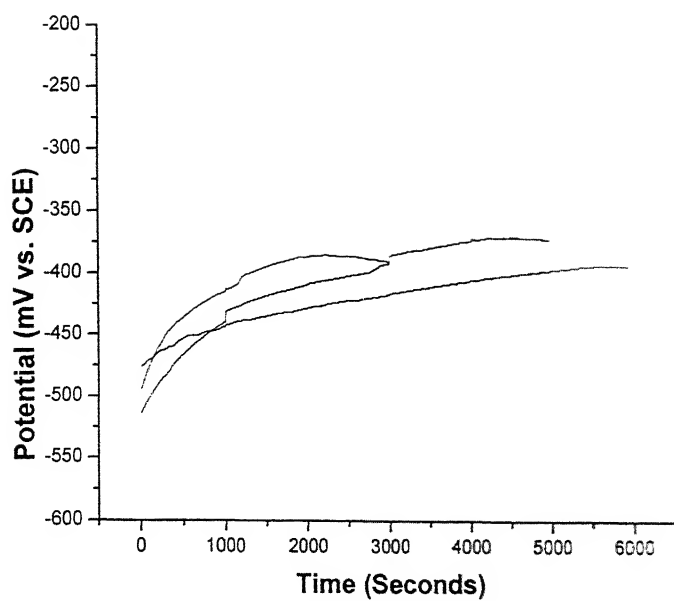


Figure A-3: Free corrosion potential as function of time for Ti-6Al-4Nb in Hank's solution at 37°C temperature and 7.4 pH.

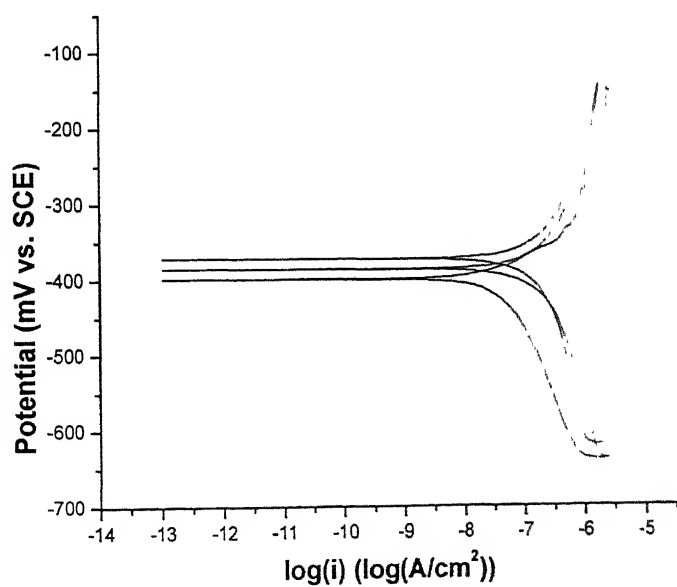


Figure A-4: Tafel extrapolation curve for Ti-6Al-4Nb in Hank's solution at 37°C temperature and 7.4 pH.

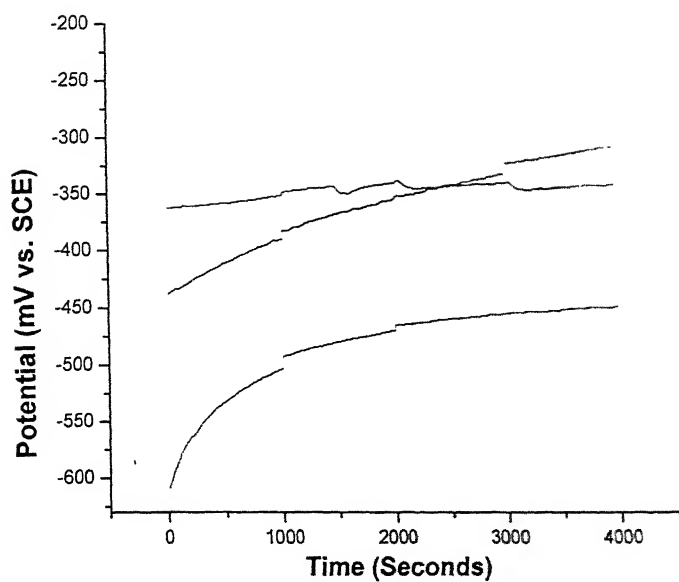


Figure A-5: Free corrosion potential as function of time for Ti-6Al-4V in Hank's solution at 37°C temperature and 7.4 pH.

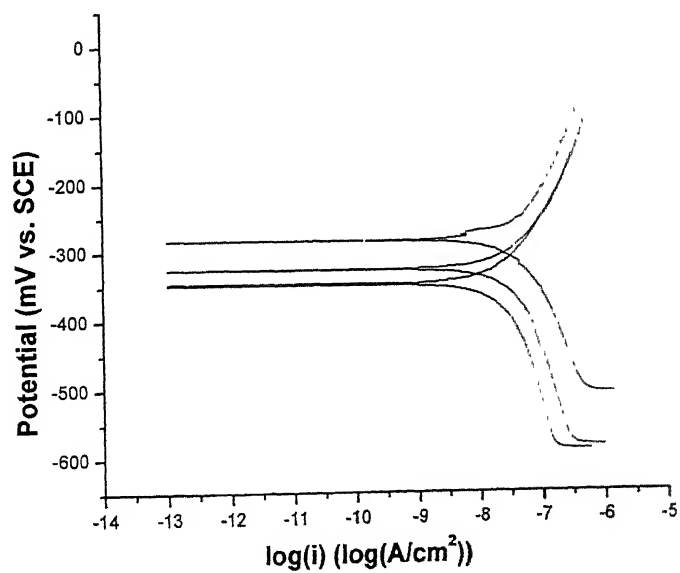


Figure A-6: Tafel extrapolation curve for Ti-6Al-4V in Hank's solution at 37°C temperature and 7.4 pH.

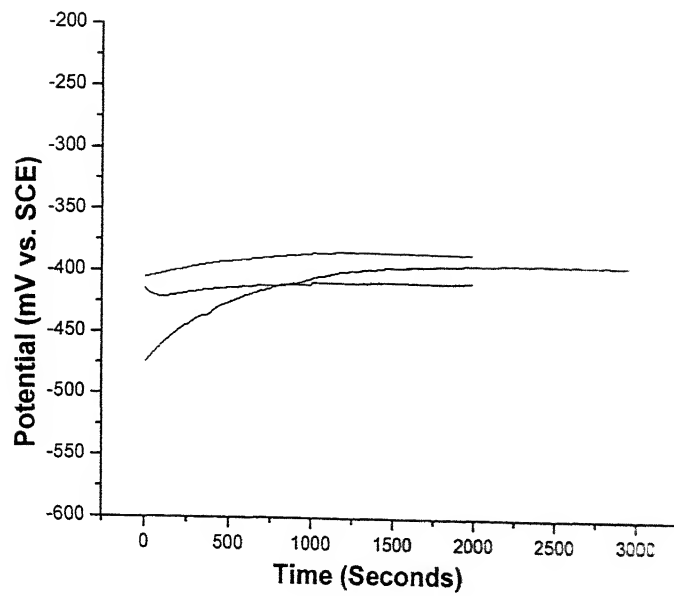


Figure A-7: Free corrosion potential as function of time for Ti-6Al-4Fe in Hank's solution at 37°C temperature and 7.4 pH.

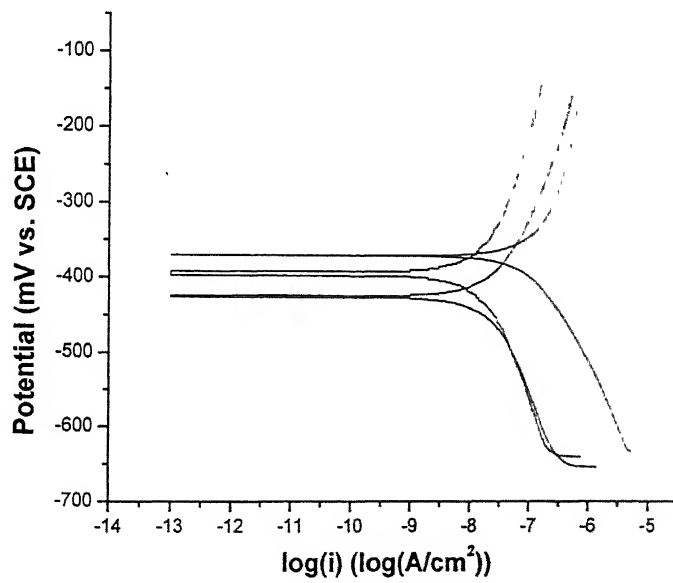


Figure A-8: Tafel extrapolation curve for Ti-6Al-4Fe in Hank's solution at 37°C temperature and 7.4 pH.

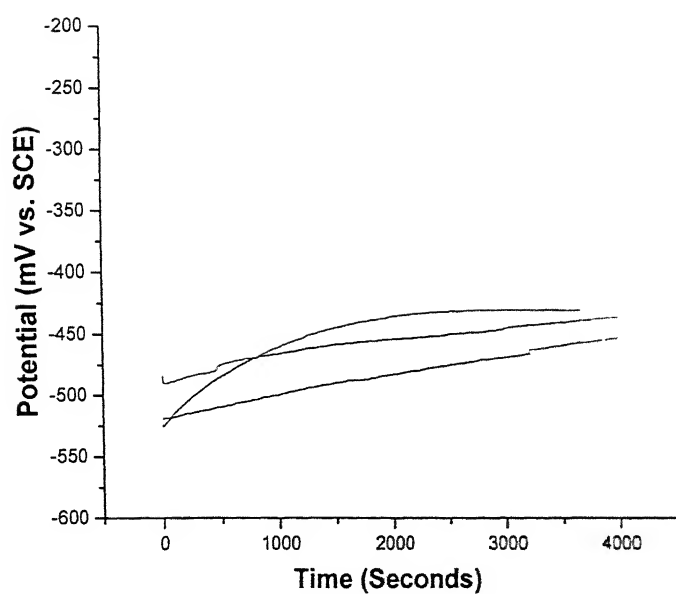


Figure A-9: Free corrosion potential as function of time for Ti-5Al-2.5Fe in Hank's solution at 37°C temperature and 7.4 pH.

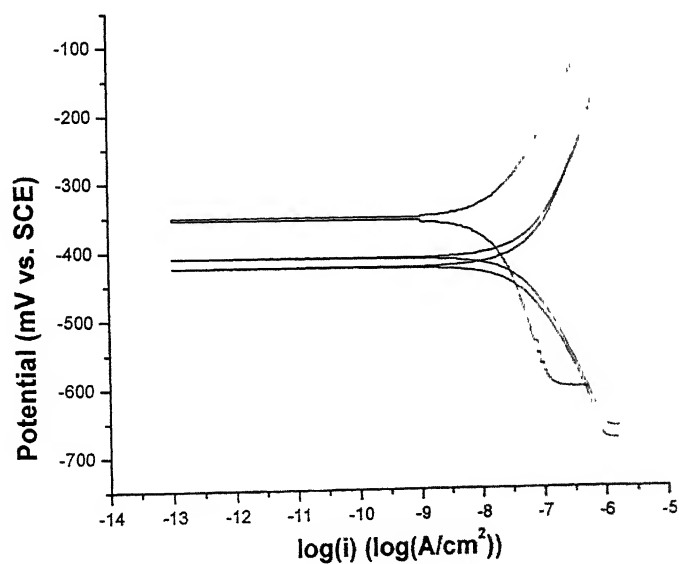


Figure A-10: Tafel extrapolation curve for Ti-5Al-2.5Fe in Hank's solution at 37°C temperature and 7.4 pH.

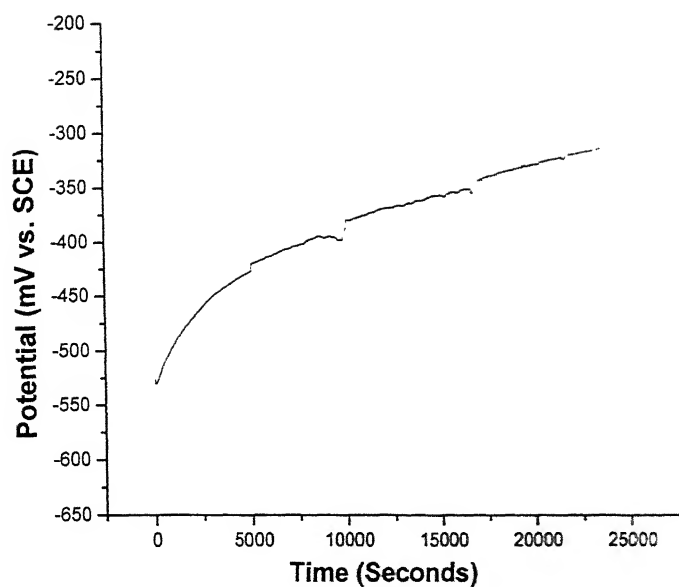


Figure A-11: Free corrosion potential as function of time for Ti-8.4Al-15.4Nb in Hank's solution at 37°C temperature and 7.4 pH.

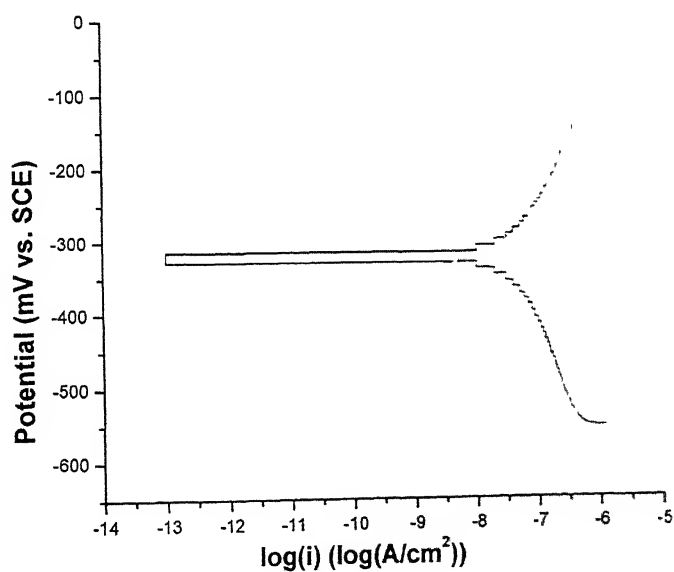


Figure A-12: Tafel extrapolation curve for Ti-8.4Al-15.4Nb in Hank's solution at 37°C temperature and 7.4 pH.

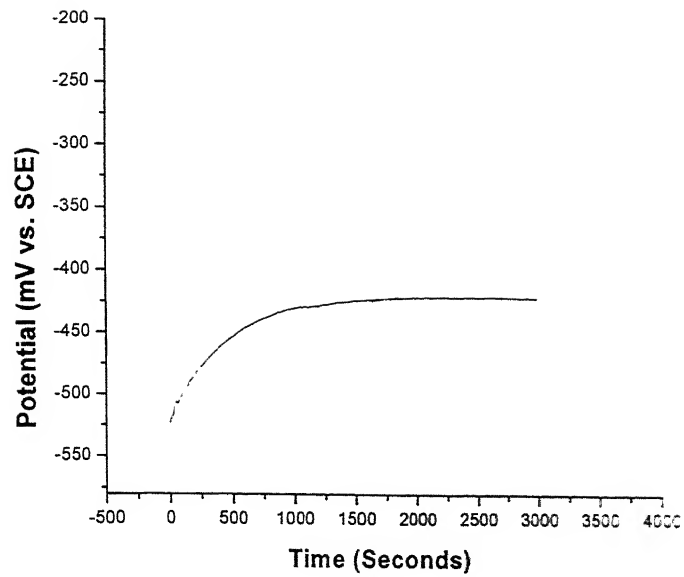


Figure A-13: Free corrosion potential as function of time for Ti-13.4Al-29Nb in Hank's solution at 37°C temperature and 7.4 pH.

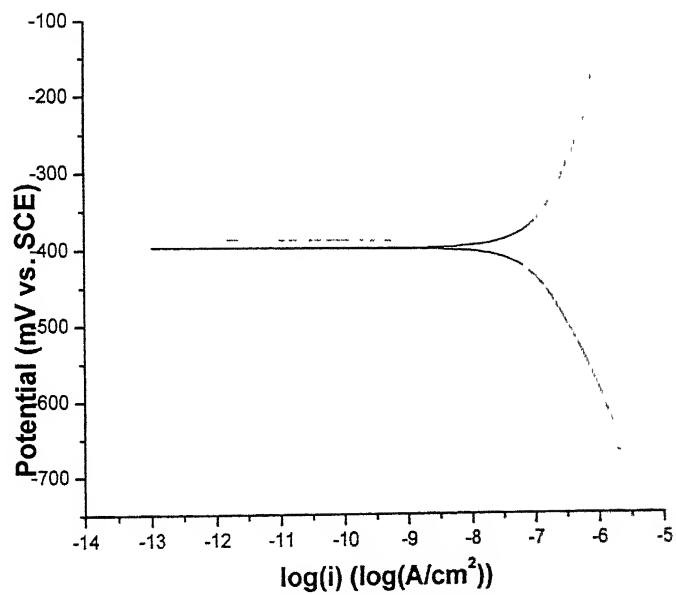


Figure A-14: Tafel extrapolation curve for Ti-13.4Al-29Nb in Hank's solution at 37°C temperature and 7.4 pH.

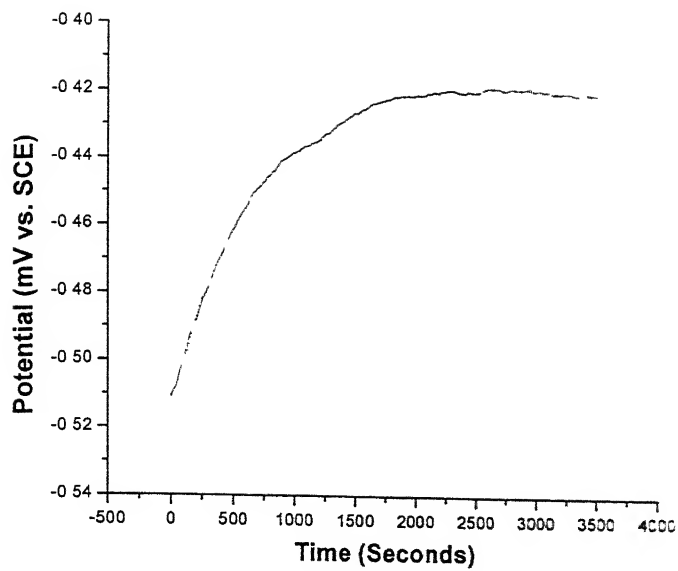


Figure A-15: Free corrosion potential as function of time for Ti-13Nb-13Zr in Hank's solution at 37°C temperature and 7.4 pH.

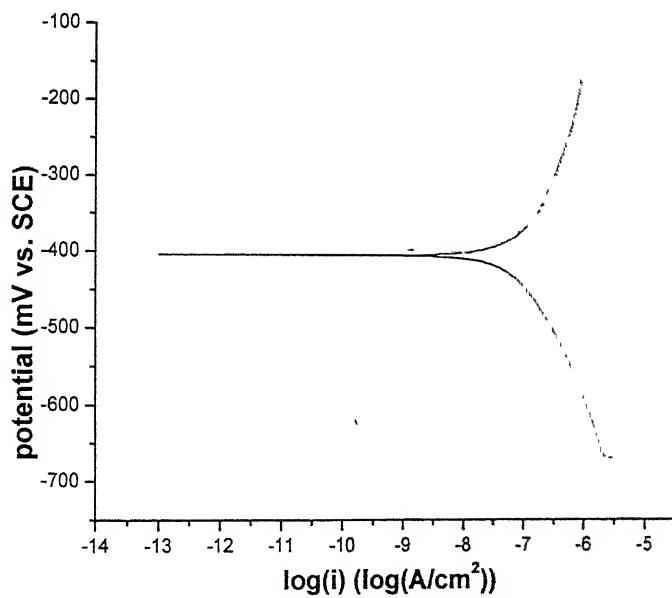


Figure A-16: Tafel extrapolation curve for Ti-13Nb-13Zr in Hank's solution at 37°C temperature and 7.4 pH.



## Appendix (B)

Table B-1: Duplicate test results of Tafel extrapolation experiment on the samples in Hank's solution at pH 7.4 and 37°C temperature.

Material		ZCP (mV vs. SCE)	$\beta_c$ (mV/dec)	$\beta_a$ (mV/dec)	Log(i)	$i_{corr}$ ( $\mu A/cm^2$ )
CP Ti	Exp1	-448	-176	207	-7.33	0.0468
	Exp2	-468	-191	182	-7.53	0.0295
Ti-6Al-4V	Exp1	-347	-343	193	-7.50	0.0316
	Exp2	-325	-284	193	-7.42	0.0380
Ti-13Nb-13Zr	Exp1	-403	-173	207	-7.06	0.0871
	Exp2	-397	-148	183	-7.10	0.0794
Ti-5Al-2.5Fe	Exp1	-424	-197	221	-7.23	0.0589
	Exp2	-410	-181	190	-7.35	0.0447
Ti-6Al-4Fe	Exp1	-425	-214	200	-7.56	0.0275
	Exp2	-397	-231	269	-7.71	0.0195
Ti-6Al-4Nb	Exp1	-372	-352	240	-7.48	0.0331
	Exp2	-386	-301	255	-7.12	0.0758
Ti-8.4Al-15.4Nb	Exp1	-322	-219	184	-7.41	0.0389
	Exp2	-334	-251	177	-7.59	0.0257
Ti-13.4Al-29Nb	Exp1	-397	-166	194	-7.10	0.0794
	Exp2	-388	-186	192	-7.19	0.0646

## Appendix (C)

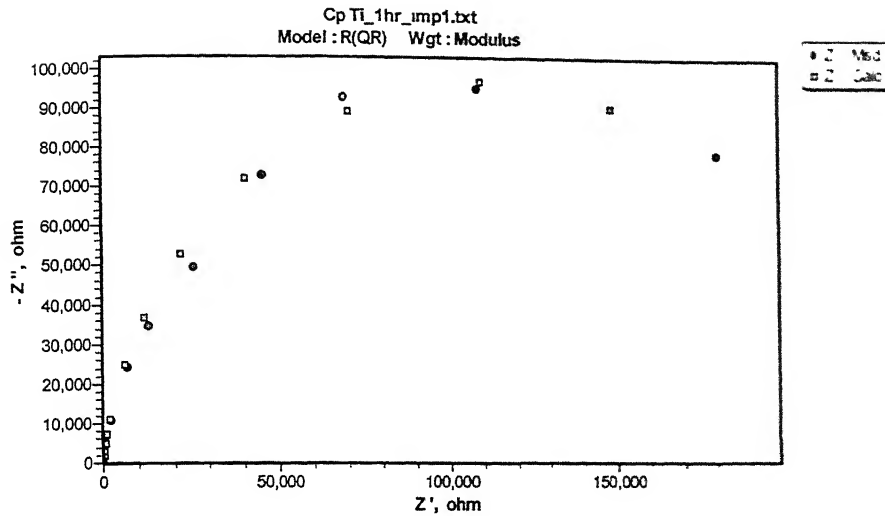


Figure C-1 Experimental (Msd.) and simulated (Calc.) Nyquist plots for CP Titanium after 1 hr of immersion in Hank's solution.

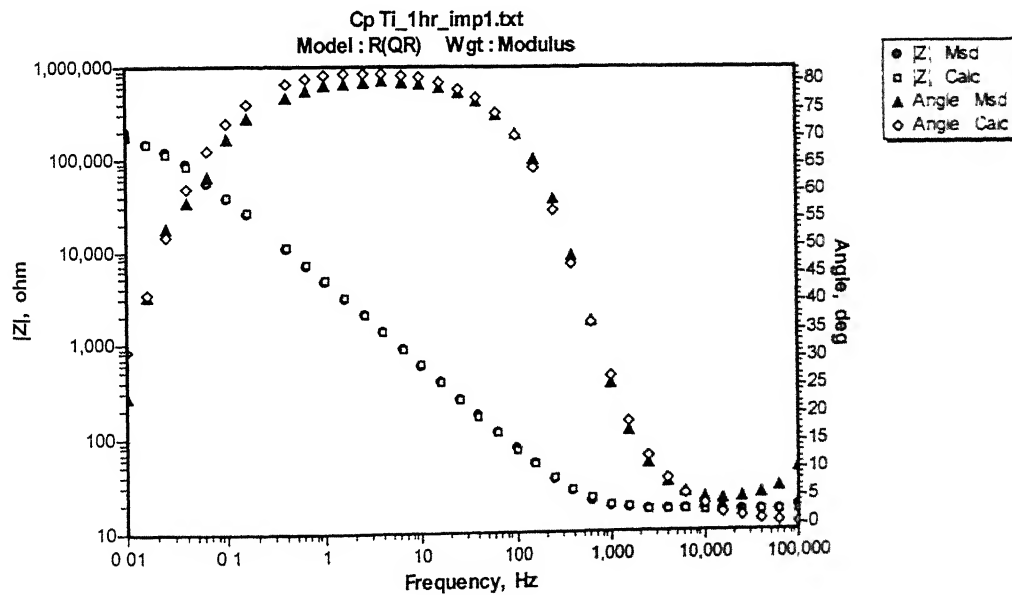


Figure C-2 Experimental (Msd.) and simulated (Calc.) Bode phase and magnitude plots for CP Titanium after 1 hr of immersion in Hank's solution.

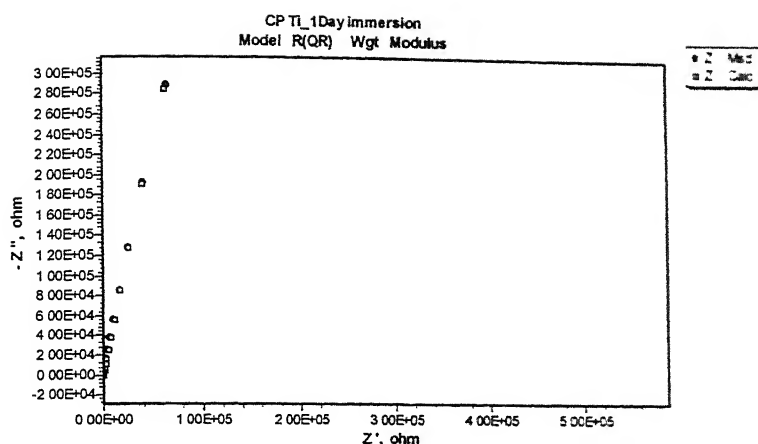


Figure C-3 Experimental (Msd.) and simulated (Calc.) Nyquist plots for CP Titanium after 24 hrs of immersion in Hank's solution.

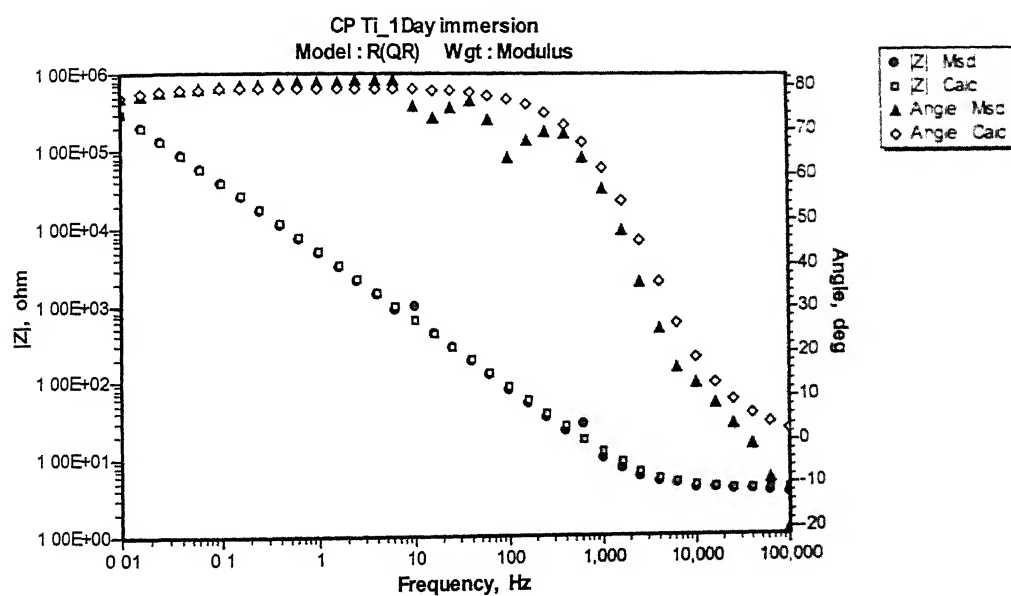


Figure C-4 Experimental (Msd.) and simulated (Calc.) Bode phase and magnitude plots for CP Titanium after 24 hrs of immersion in Hank's solution.

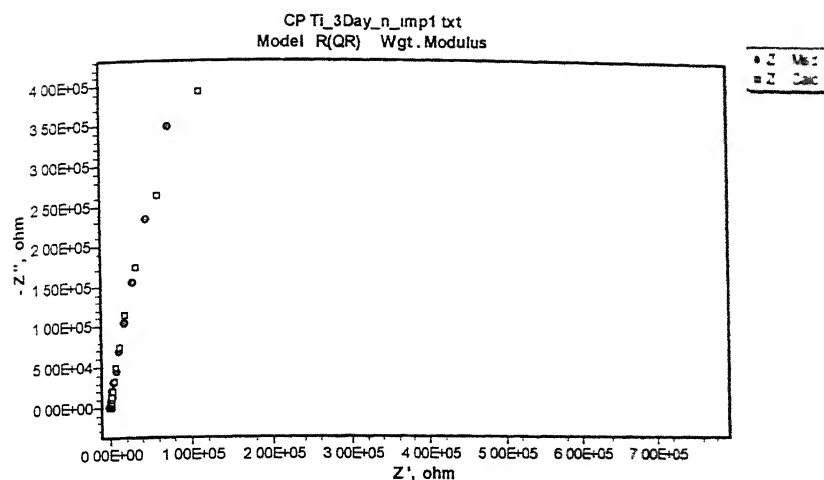


Figure C-5 Experimental (Msd.) and simulated (Calc.) Nyquist plots for CP Titanium after 72 hrs of immersion in Hank's solution.

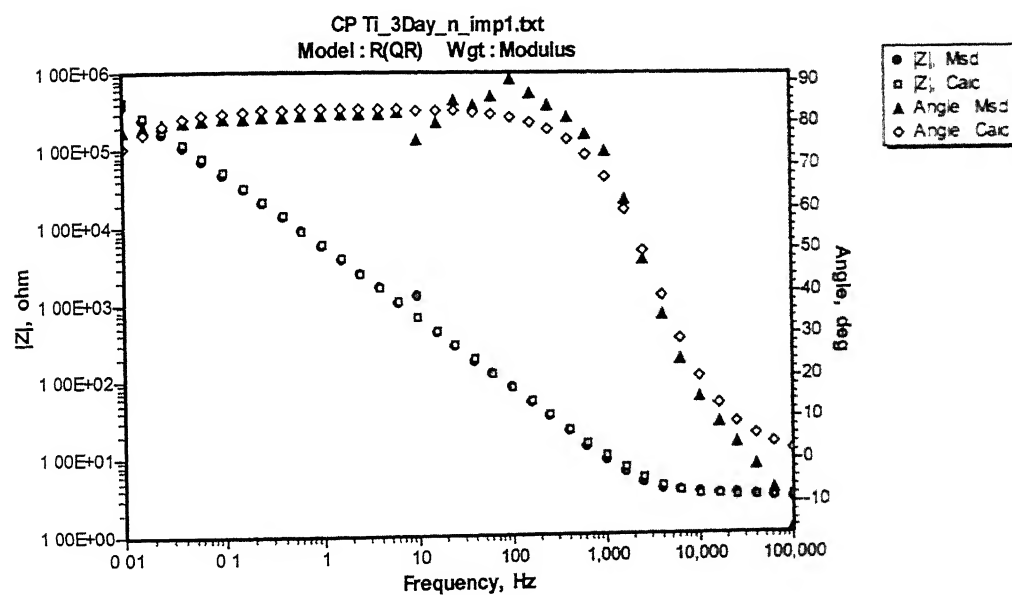


Figure C-6 Experimental (Msd.) and simulated (Calc.) Bode phase and magnitude plots for CP Titanium after 72 hrs of immersion in Hank's solution.

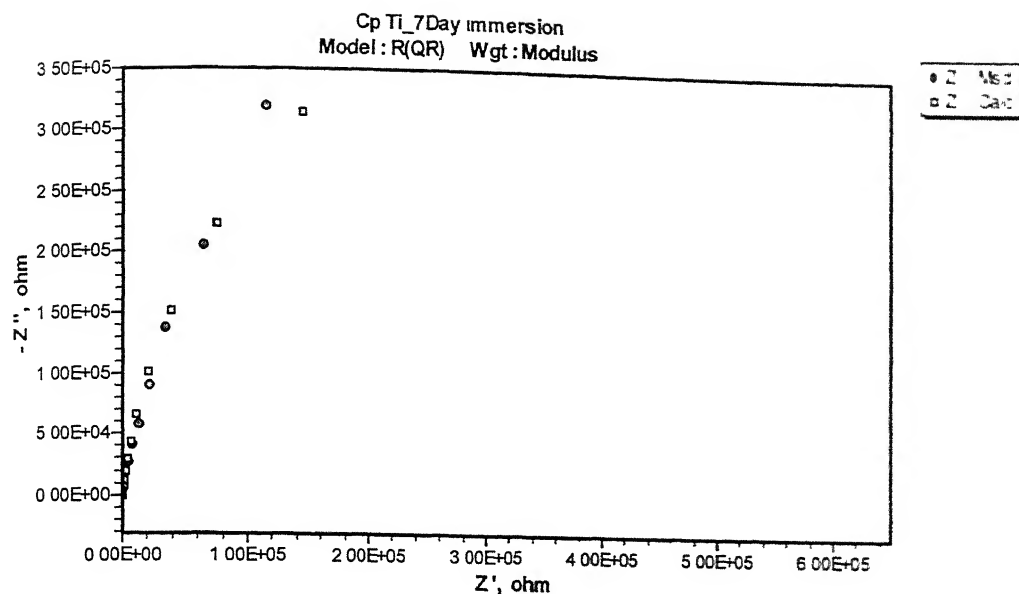


Figure C-7 Experimental (Msd.) and simulated (Calc.) Nyquist plots for CP Titanium after 168 hrs of immersion in Hank's solution.

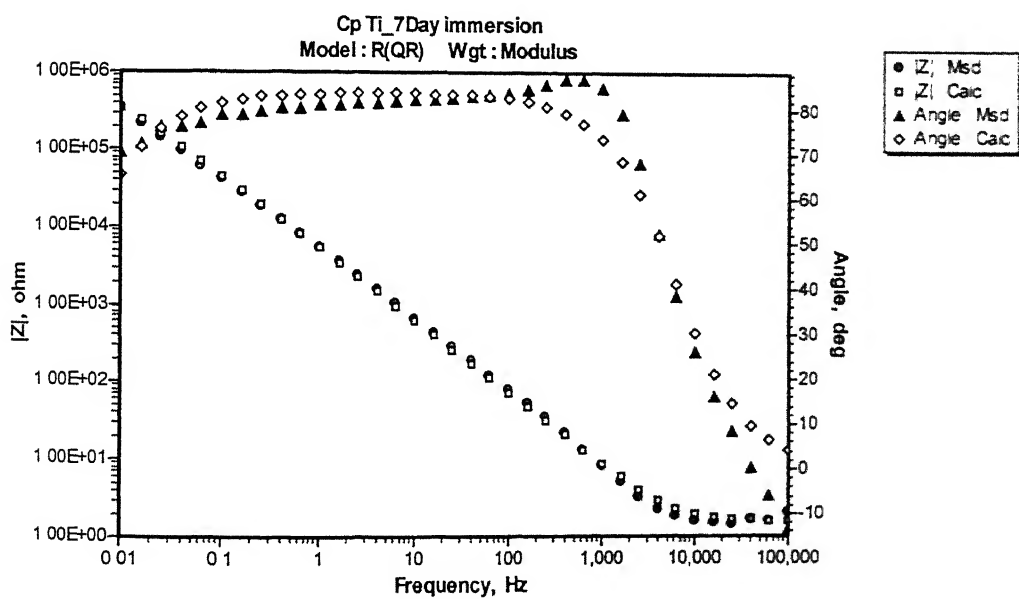


Figure C-8 Experimental (Msd.) and simulated (Calc.) Bode phase and magnitude plots for CP Titanium after 168 hrs of immersion in Hank's solution.

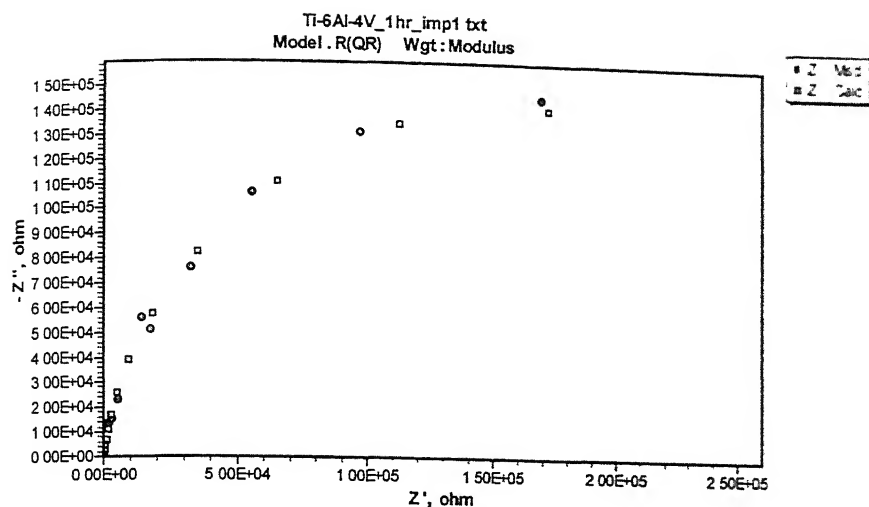


Figure C-9 Experimental (Msd.) and simulated (Calc.) Nyquist plots for Ti-6Al-4V after 1 hr of immersion in Hank's solution.

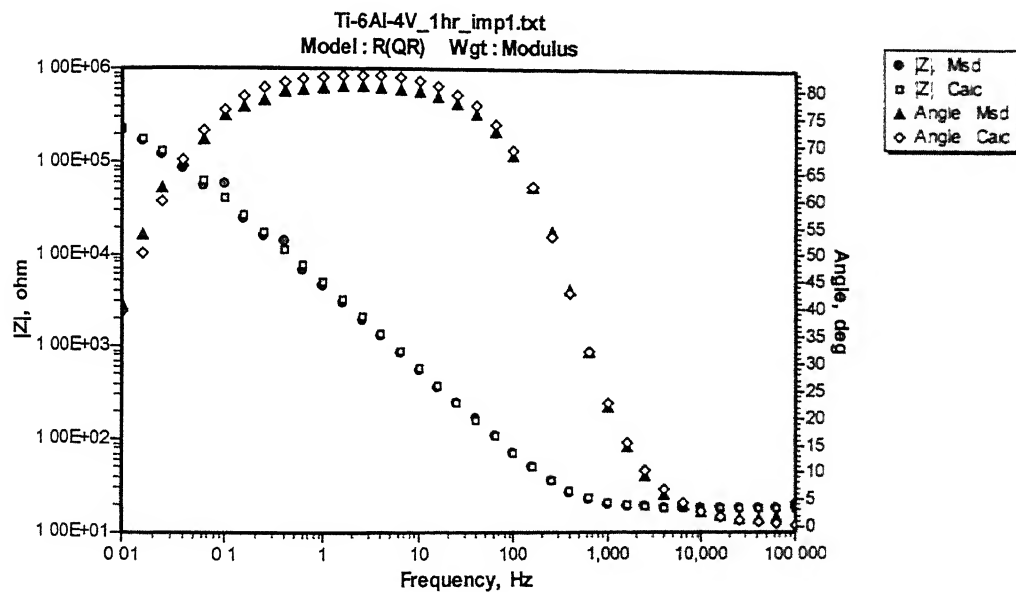


Figure C-10 Experimental (Msd.) and simulated (Calc.) Bode phase and magnitude plots for Ti-6Al-4V after 1 hr of immersion in Hank's solution.

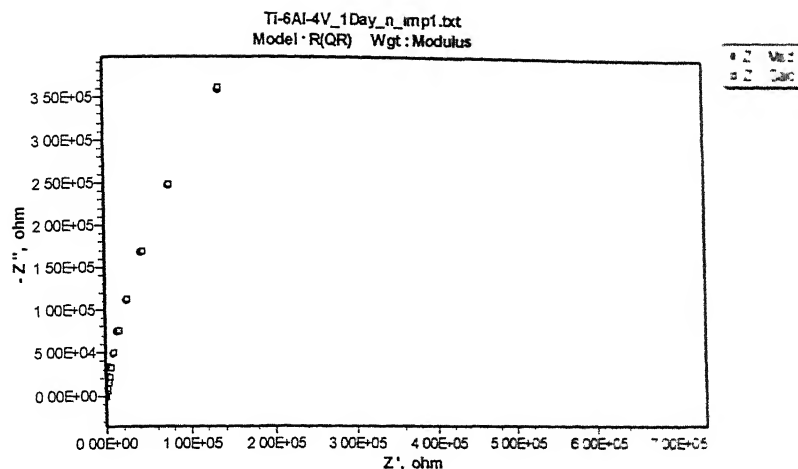


Figure C-11 Experimental (Msd.) and simulated (Calc.) Nyquist plots for Ti-6Al-4V after 24 hrs of immersion in Hank's solution.

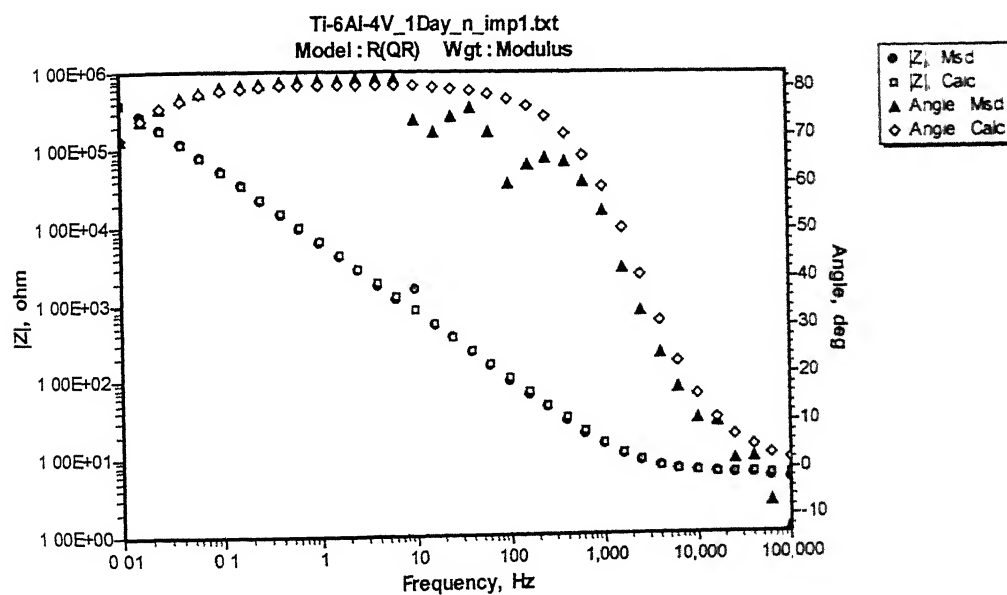


Figure C-12 Experimental (Msd.) and simulated (Calc.) Bode phase and magnitude plots for Ti-6Al-4V after 24 hrs of immersion in Hank's solution.

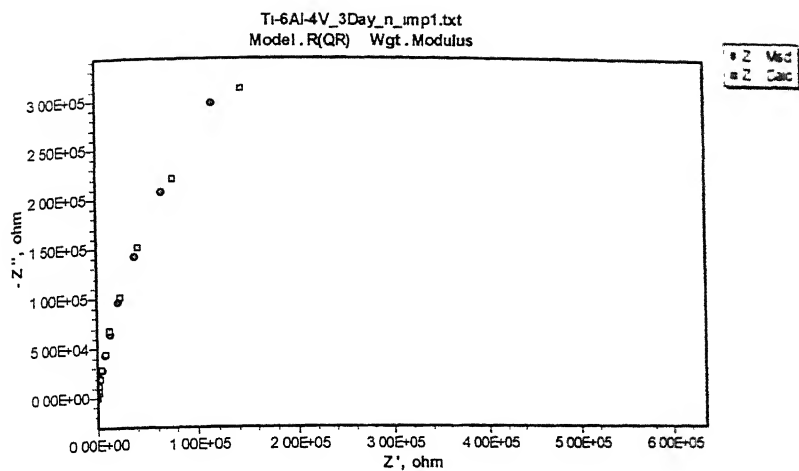


Figure C-13 Experimental (Msd.) and simulated (Calc.) Nyquist plots for Ti-6Al-4V after 72 hrs of immersion in Hank's solution.

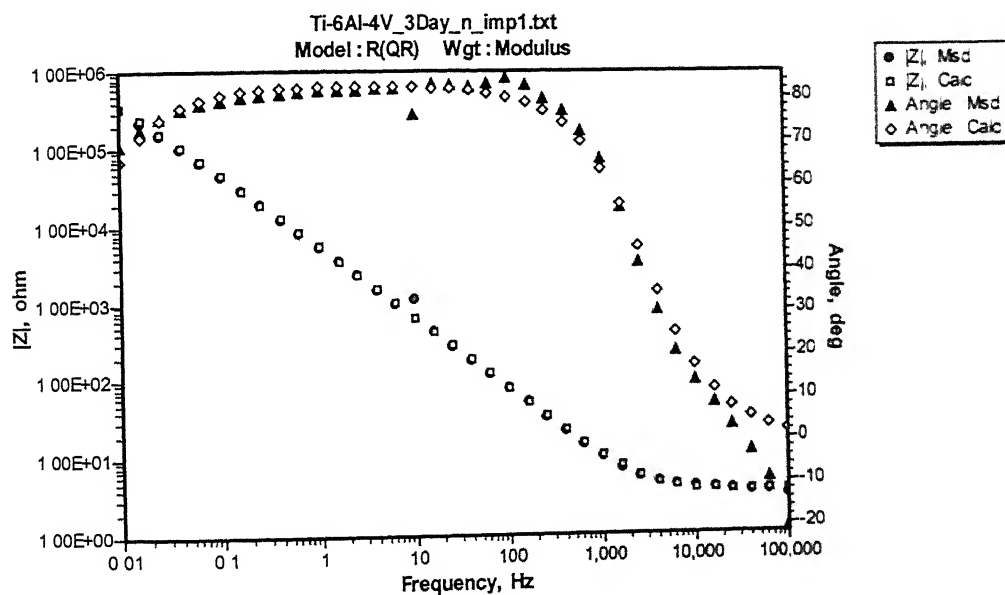


Figure C-14 Experimental (Msd.) and simulated (Calc.) Bode phase and magnitude plots for Ti-6Al-4V after 72 hrs of immersion in Hank's solution.



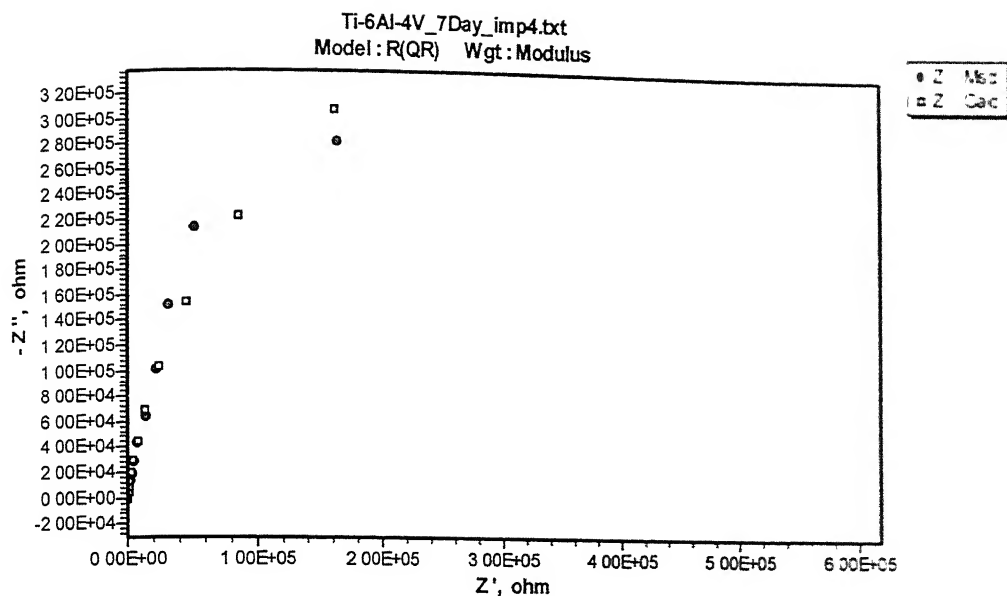


Figure C-15 Experimental (Msd.) and simulated (Calc.) Nyquist plots for Ti-6Al-4V after 168 hrs of immersion in Hank's solution.

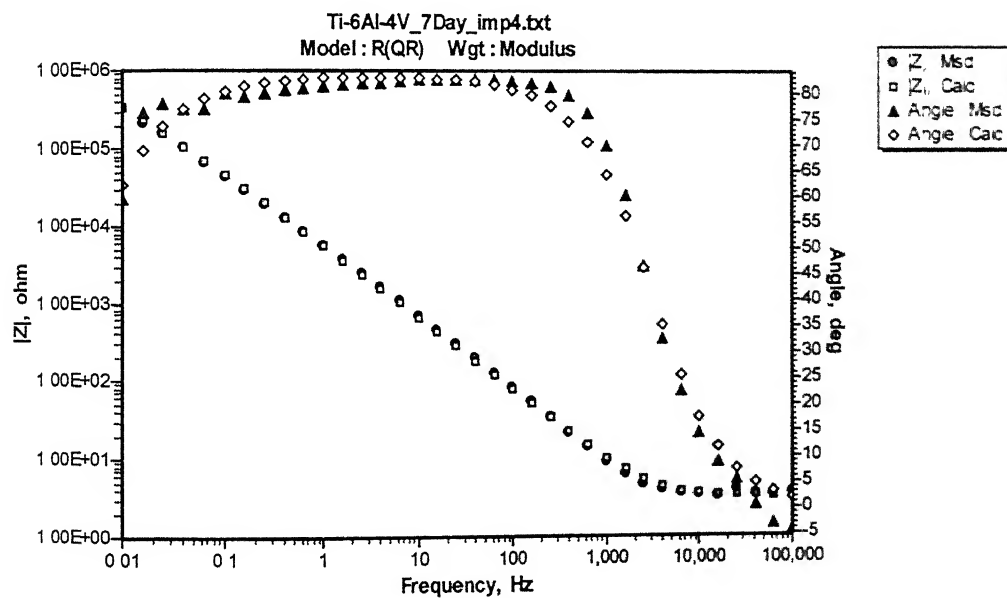


Figure C-16 Experimental (Msd.) and simulated (Calc.) Bode phase and magnitude plots for Ti-6Al-4V after 168 hrs of immersion in Hank's solution.

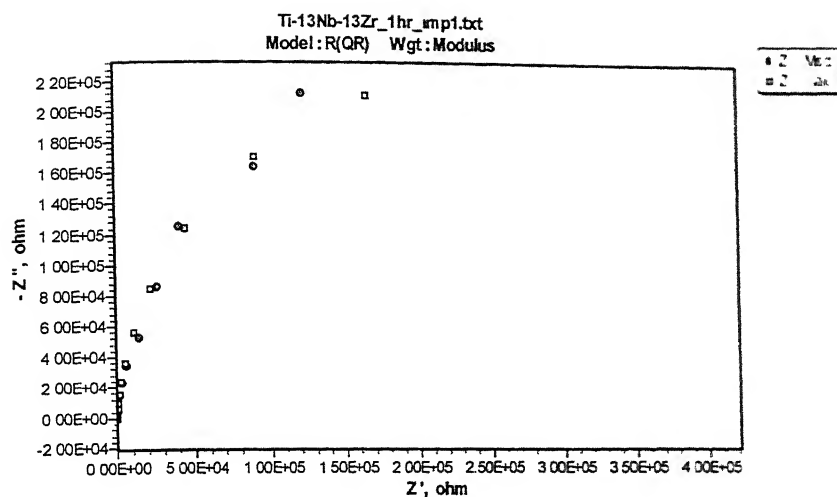


Figure C-17 Experimental (Msd.) and simulated (Calc.) Nyquist plots for Ti-13Nb-13Zr after 1 hr of immersion in Hank's solution.

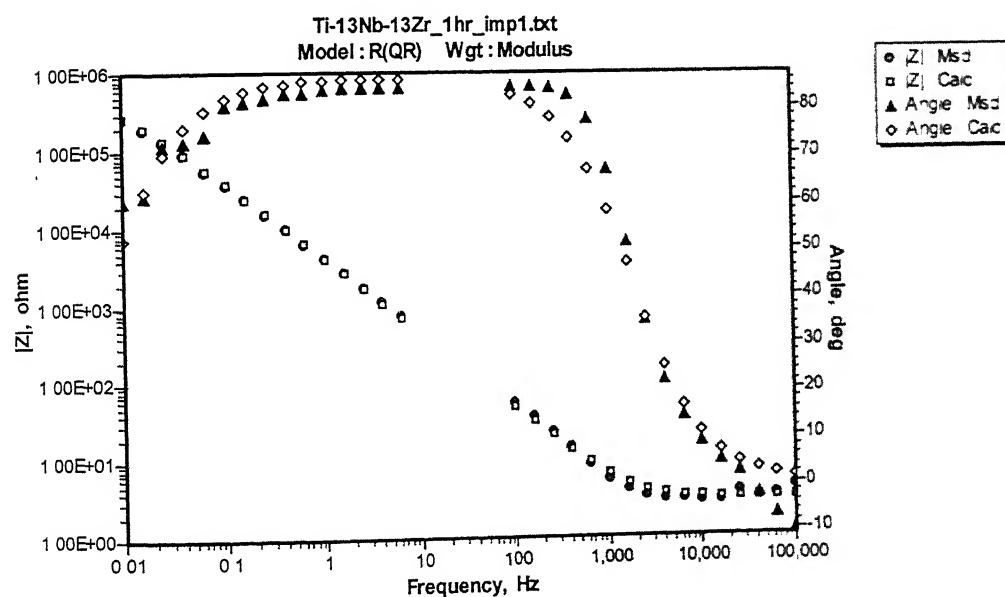


Figure C-18 Experimental (Msd.) and simulated (Calc.) Bode phase and magnitude plots for Ti-13Nb-13Zr after 1 hr of immersion in Hank's solution.

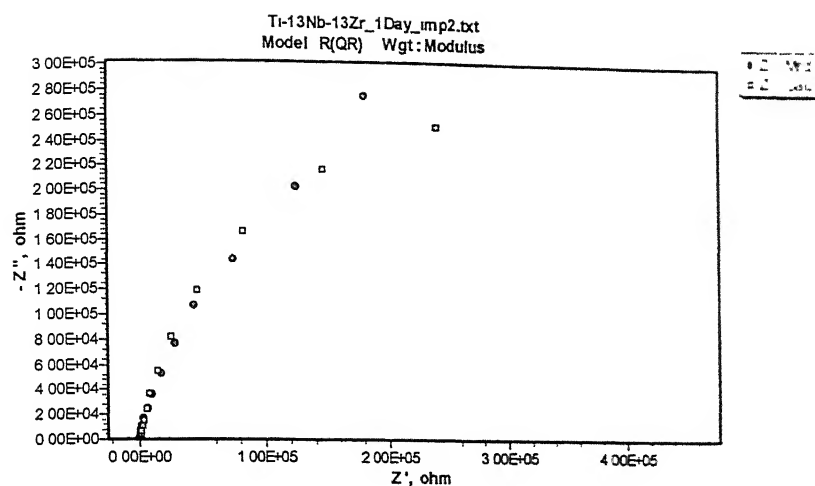


Figure C-19 Experimental (Msd.) and simulated (Calc.) Nyquist plots for Ti-13Nb-13Zr after 24 hrs of immersion in Hank's solution.

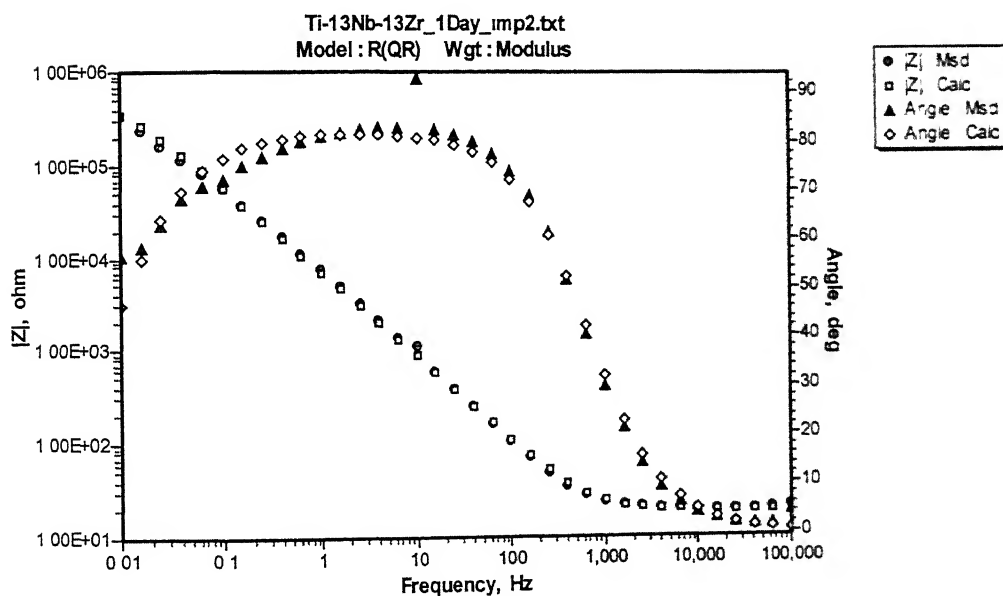


Figure C-20 Experimental (Msd.) and simulated (Calc.) Bode phase and magnitude plots for Ti-13Nb-13Zr after 24 hrs of immersion in Hank's solution.

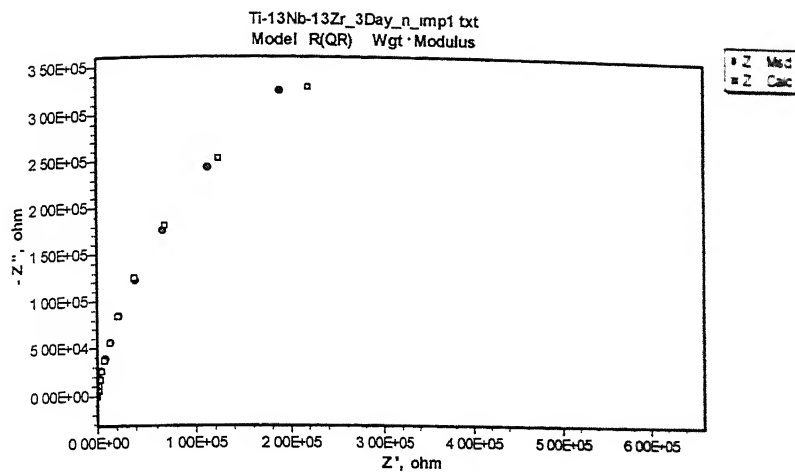


Figure C-21 Experimental (Msd.) and simulated (Calc.) Nyquist plots for Ti-13Nb-13Zr after 72 hrs of immersion in Hank's solution.

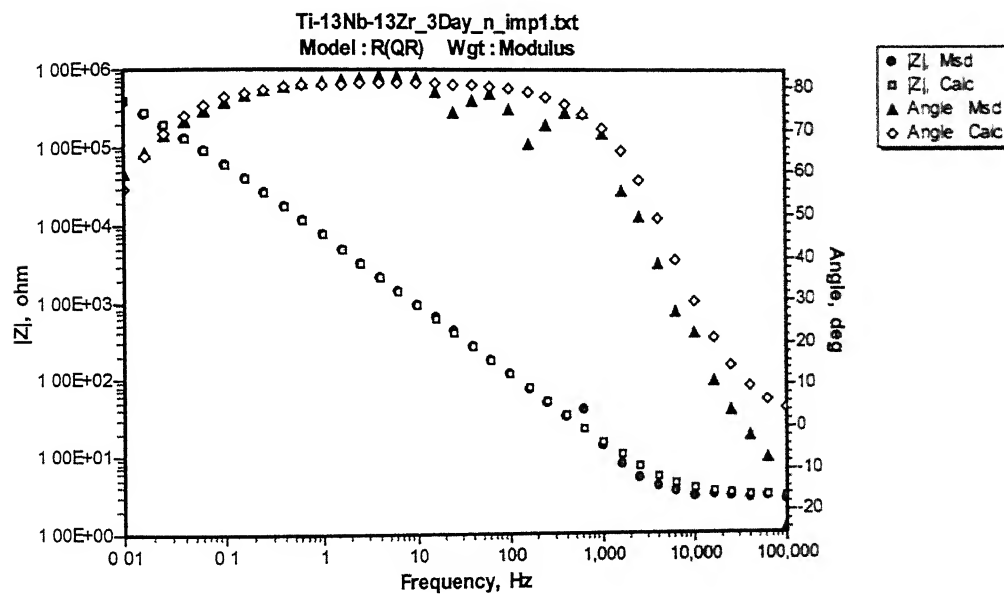


Figure C-22 Experimental (Msd.) and simulated (Calc.) Bode phase and magnitude plots for Ti-13Nb-13Zr after 72 hrs of immersion in Hank's solution.

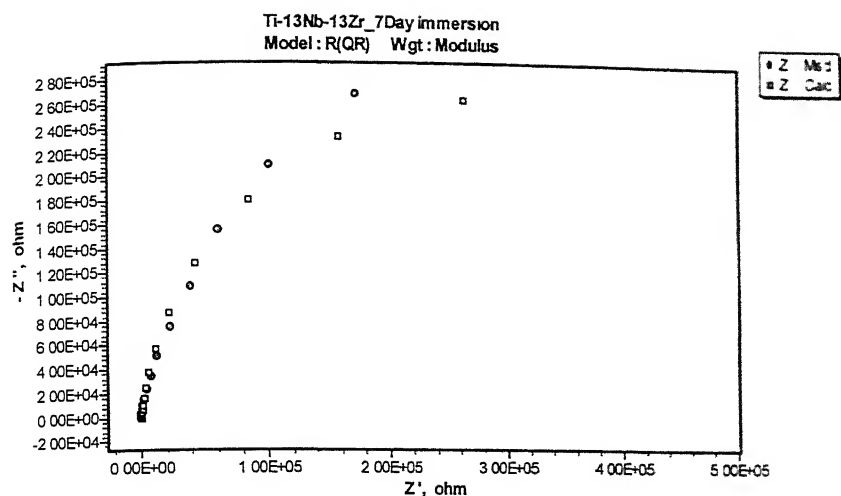


Figure C-23 Experimental (Msd.) and simulated (Calc.) Nyquist plots for Ti-13Nb-13Zr after 168 hrs of immersion in Hank's solution.

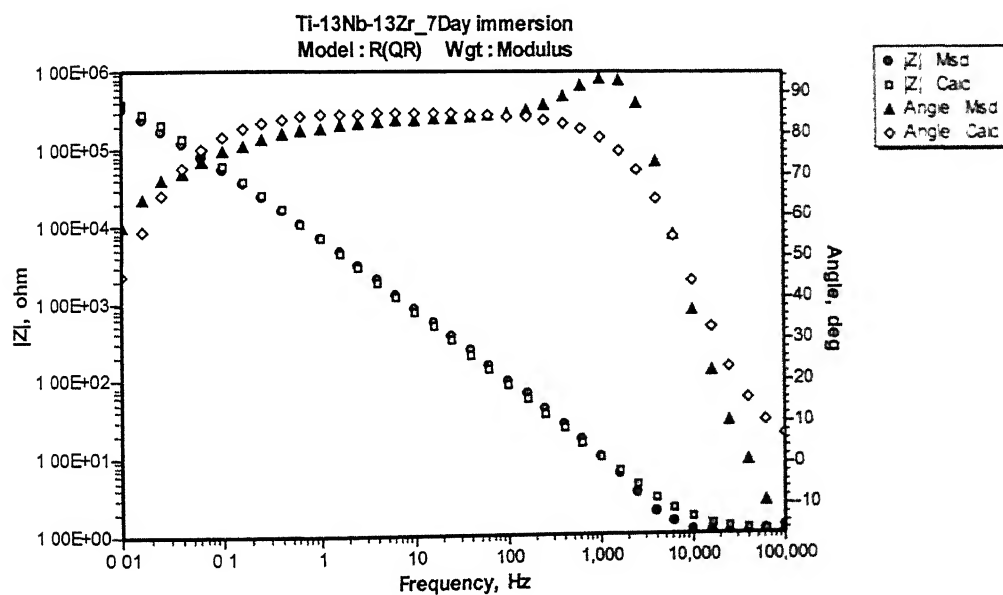


Figure C-24 Experimental (Msd.) and simulated (Calc.) Bode phase and magnitude plots for Ti-13Nb-13Zr after 168 hrs of immersion in Hank's solution.

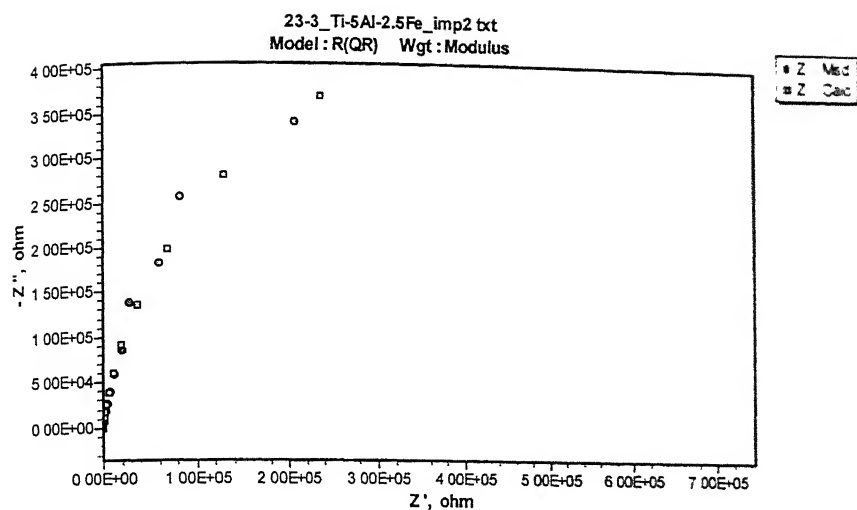


Figure C-25 Experimental (Msd.) and simulated (Calc.) Nyquist plots for Ti-5Al-2.5Fe after 1 hr of immersion in Hank's solution.

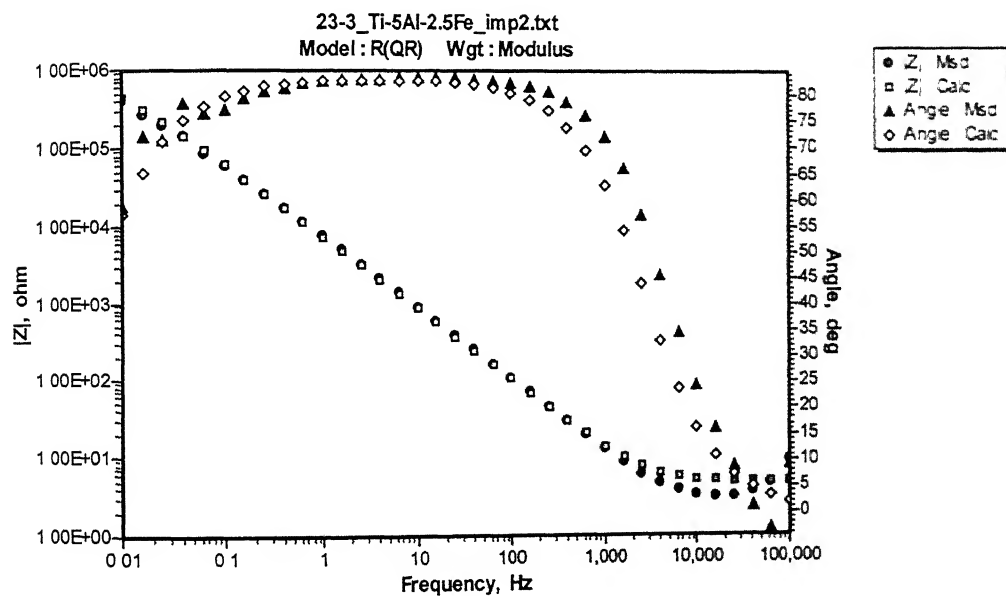


Figure C-26 Experimental (Msd.) and simulated (Calc.) Bode phase and magnitude plots for Ti-5Al-2.5Fe after 1 hr of immersion in Hank's solution.

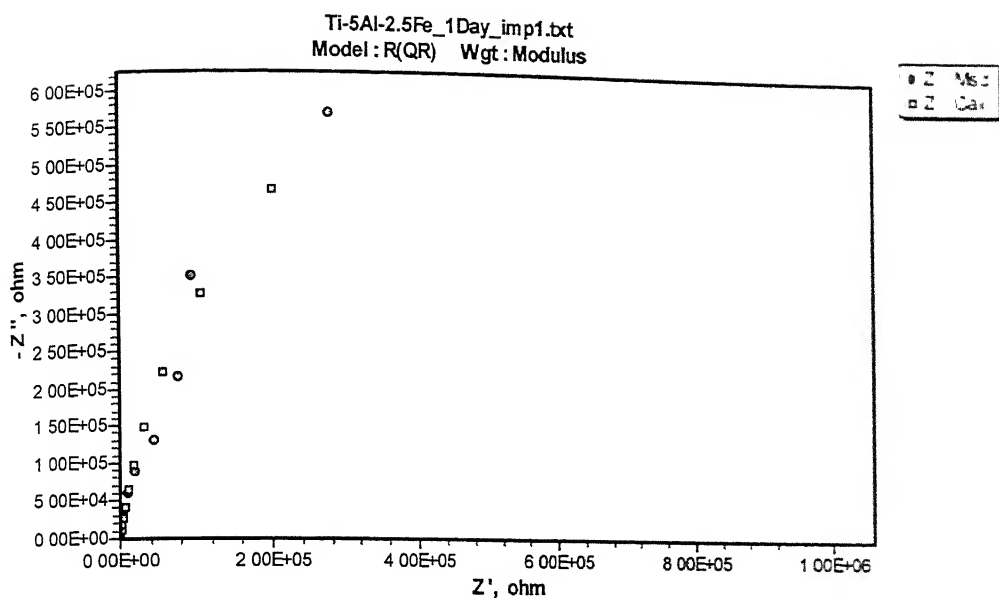


Figure C-27 Experimental (Msd.) and simulated (Calc.) Nyquist plots for Ti-5Al-2.5Fe after 24 hrs of immersion in Hank's solution

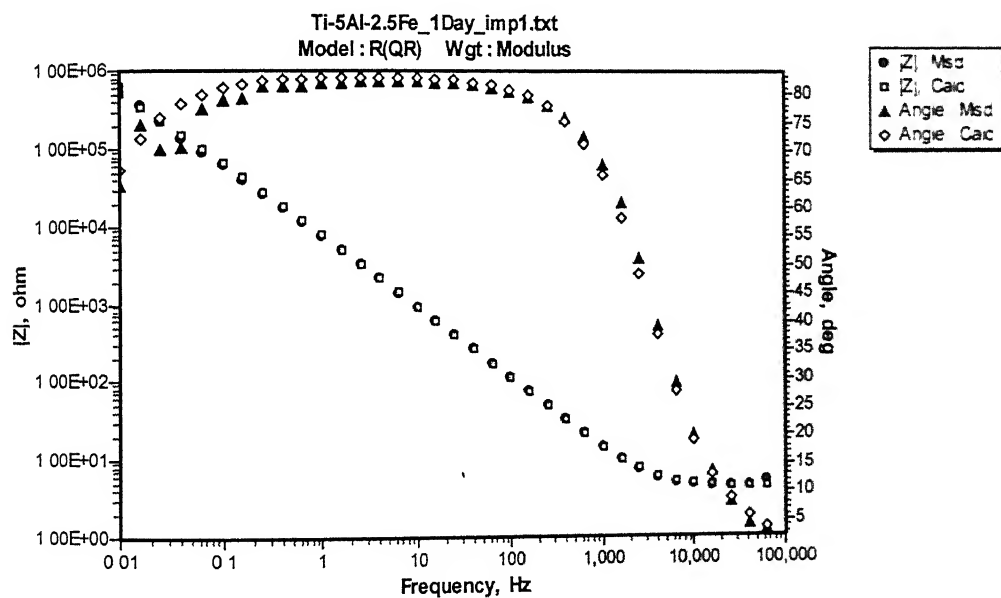


Figure C-28 Experimental (Msd.) and simulated (Calc.) Bode phase and magnitude plots for Ti-5Al-2.5Fe after 24 hr of immersion in Hank's solution.

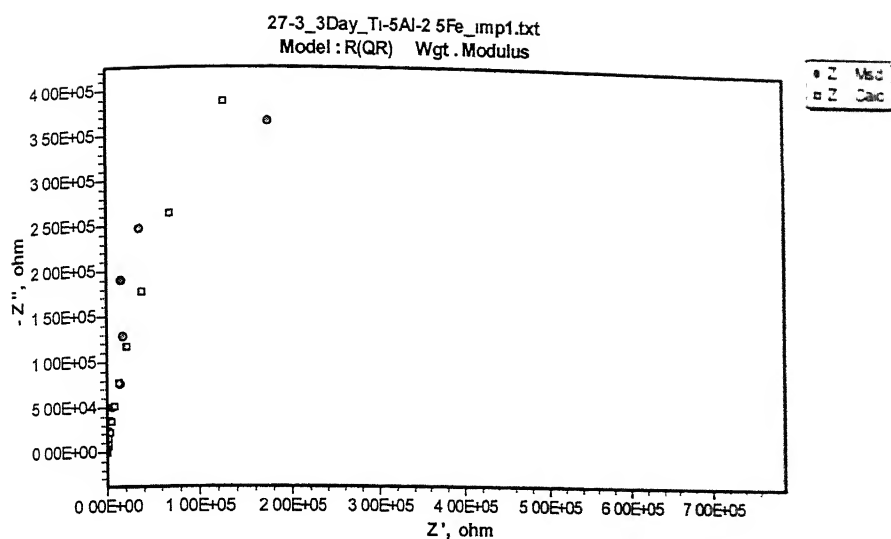


Figure C-29 Experimental (Msd.) and simulated (Calc.) Nyquist plots for Ti-5Al-2.5Fe after 72 hrs of immersion in Hank's solution.

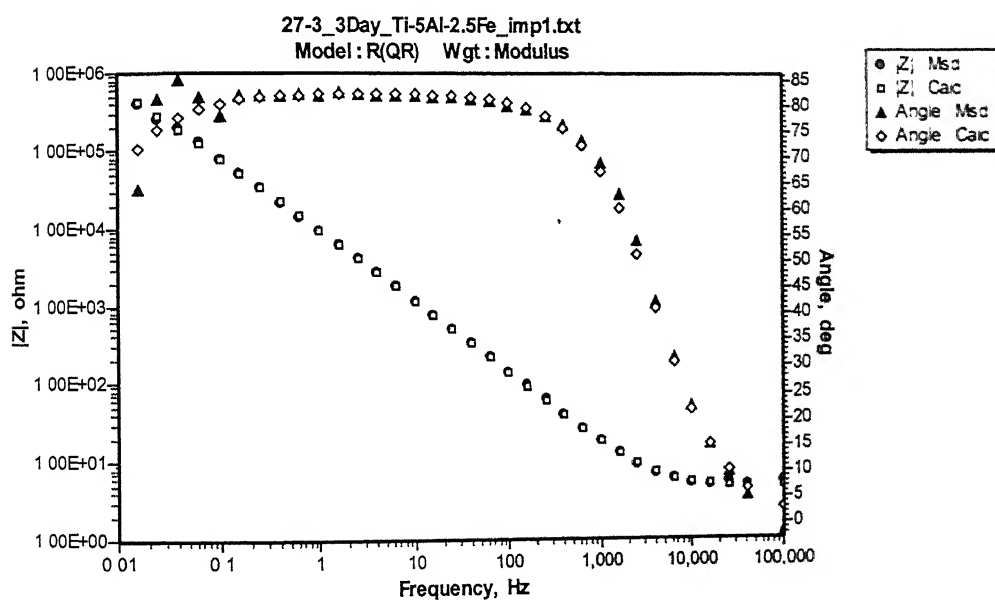


Figure C-30 Experimental (Msd.) and simulated (Calc.) Bode phase and magnitude plots for Ti-5Al-2.5Fe after 72 hrs of immersion in Hank's solution.



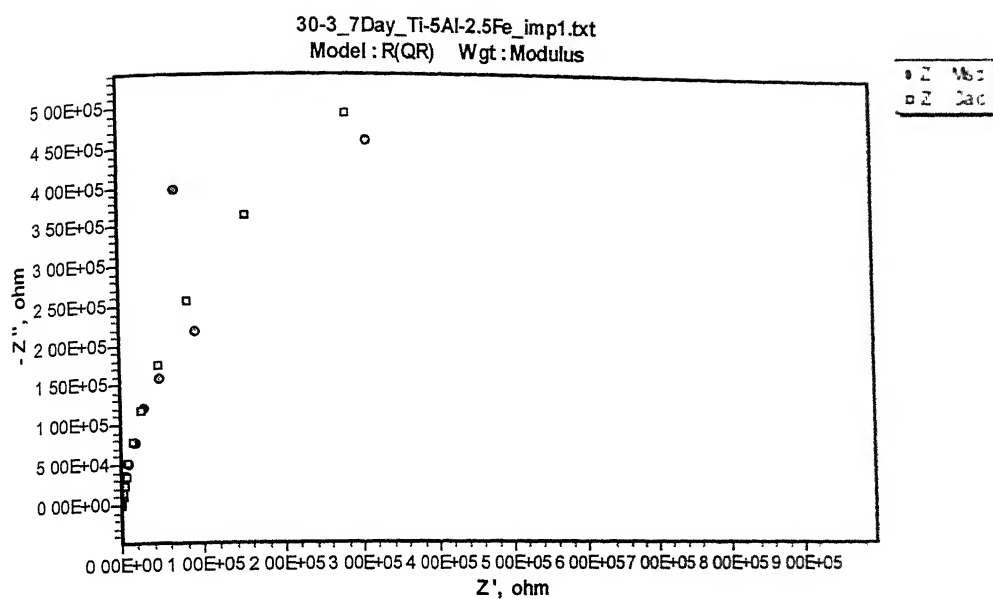


Figure C-31 Experimental (Msd.) and simulated (Calc.) Nyquist plots for Ti-5Al-2.5Fe after 168 hrs of immersion in Hank's solution.

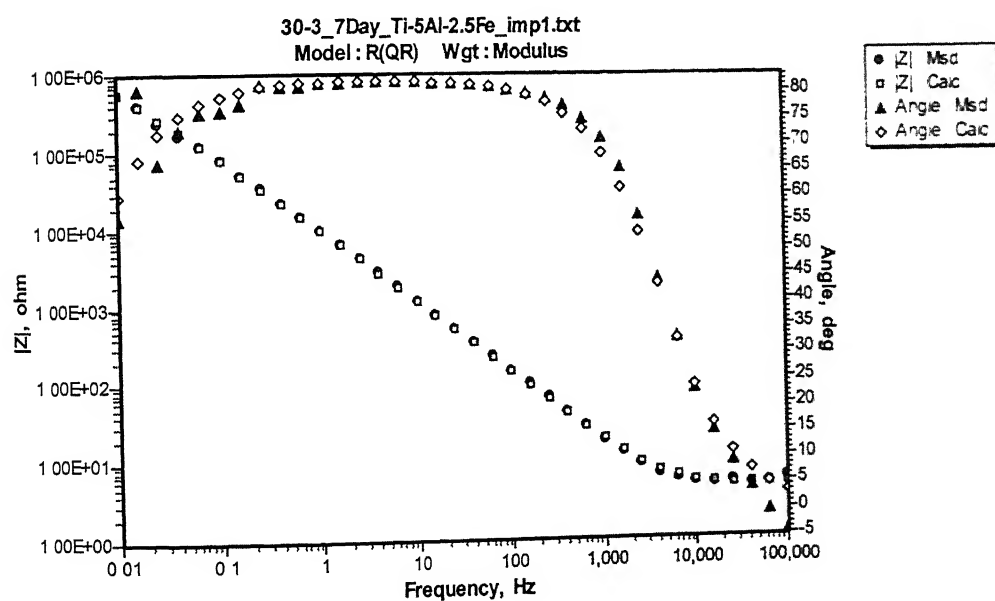


Figure C-32 Experimental (Msd.) and simulated (Calc.) Bode phase and magnitude plots for Ti-5Al-2.5Fe after 168 hrs of immersion in Hank's solution.

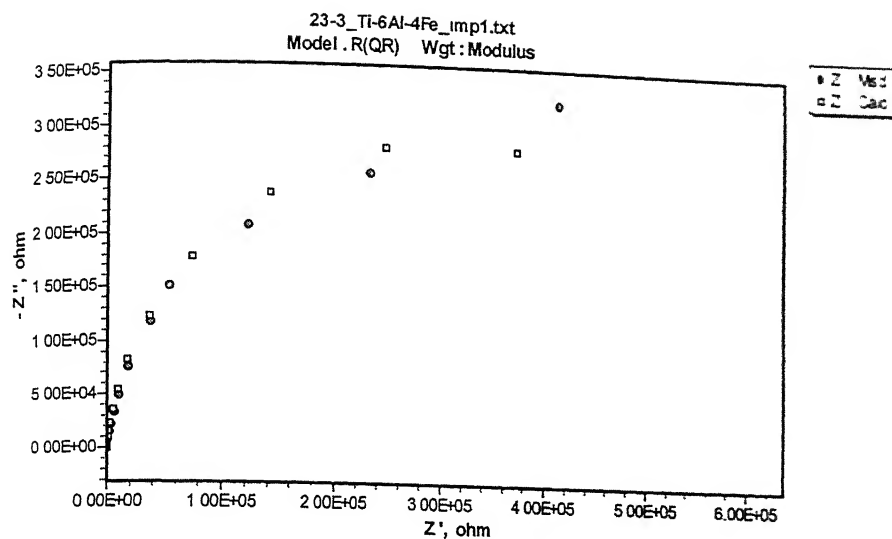


Figure C-33 Experimental (Msd.) and simulated (Calc.) Nyquist plots for Ti-6Al-4Fe after 1 hr of immersion in Hank's solution.

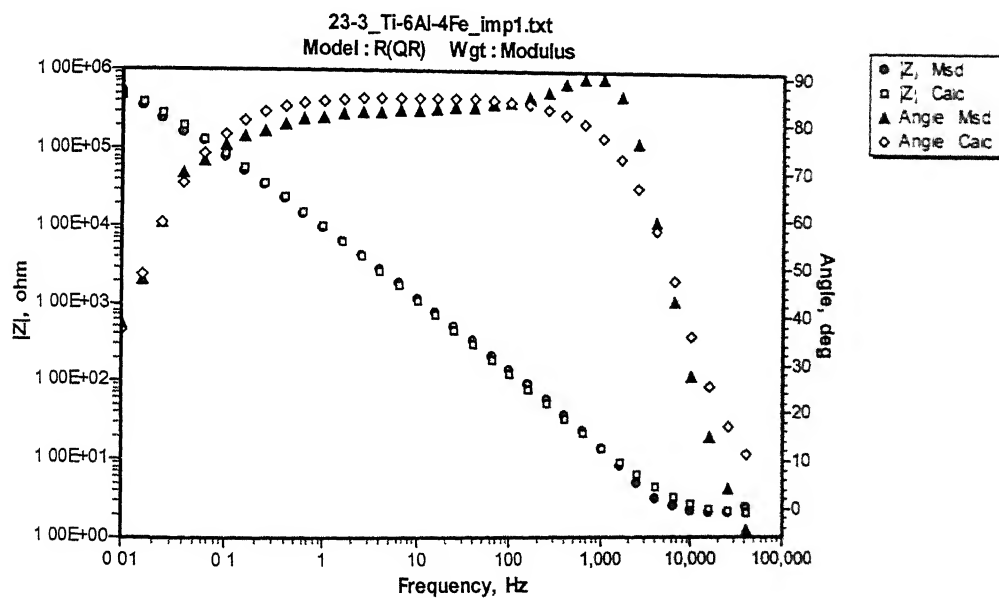


Figure C-34 Experimental (Msd.) and simulated (Calc.) Bode phase and magnitude plots for Ti-6Al-4Fe after 1 hr of immersion in Hank's solution.

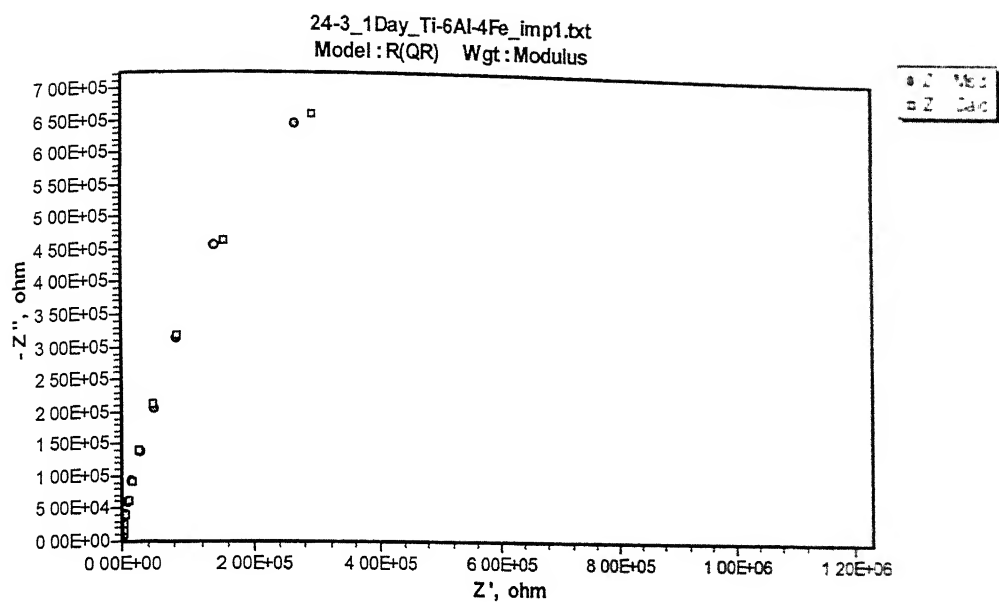


Figure C-35 Experimental (Msd.) and simulated (Calc.) Nyquist plots for Ti-6Al-4Fe after 24 hrs of immersion in Hank's solution.

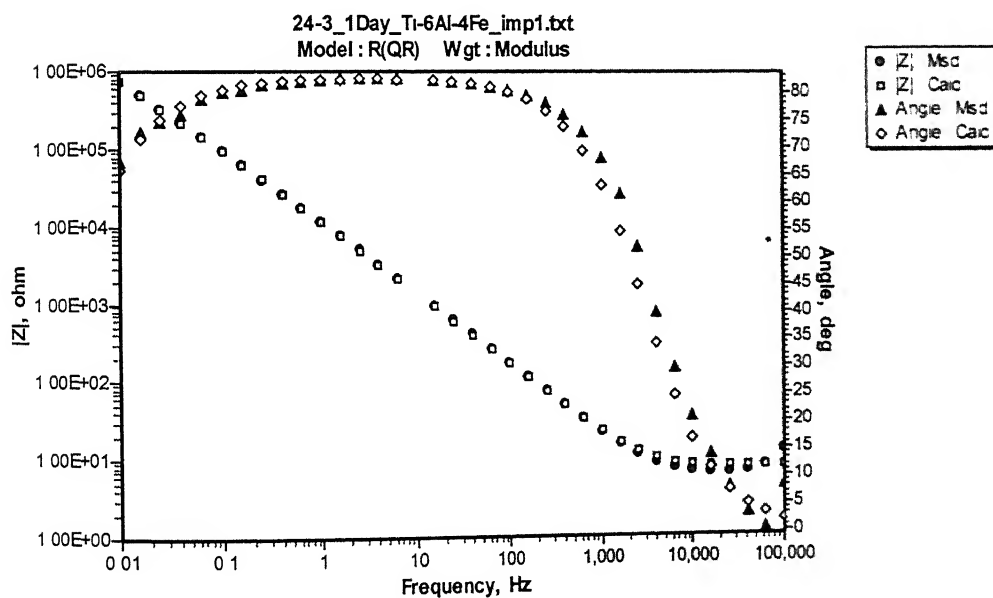


Figure C-36 Experimental (Msd.) and simulated (Calc.) Bode phase and magnitude plots for Ti-6Al-4Fe after 24 hrs of immersion in Hank's solution.

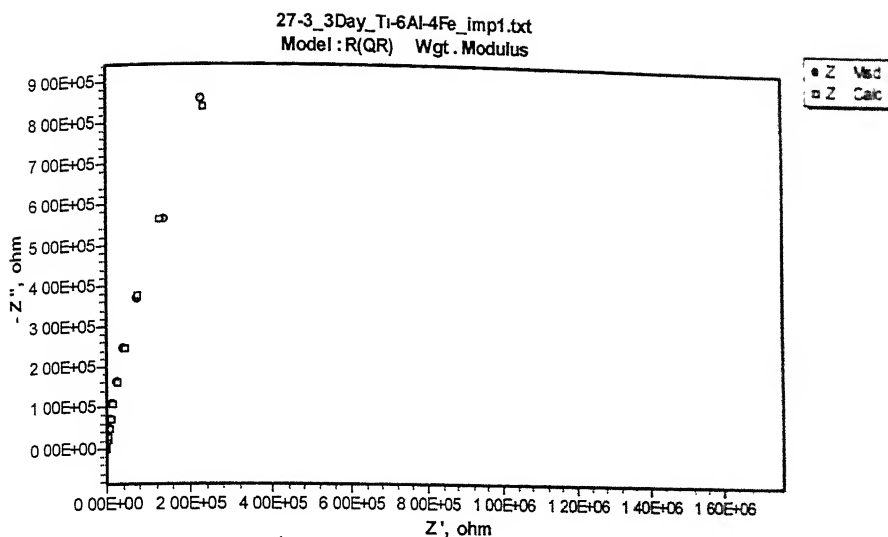


Figure C-37 Experimental (Msd.) and simulated (Calc.) Nyquist plots for Ti-6Al-4Fe after 72 hrs of immersion in Hank's solution.

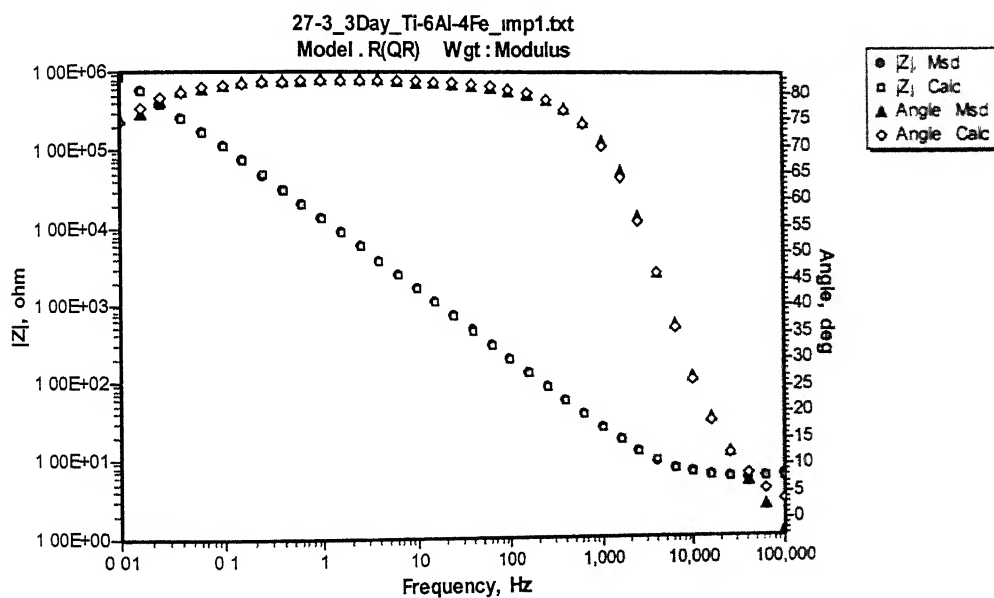


Figure C-38 Experimental (Msd.) and simulated (Calc.) Bode phase and magnitude plots for Ti-6Al-4Fe after 72 hrs of immersion in Hank's solution.

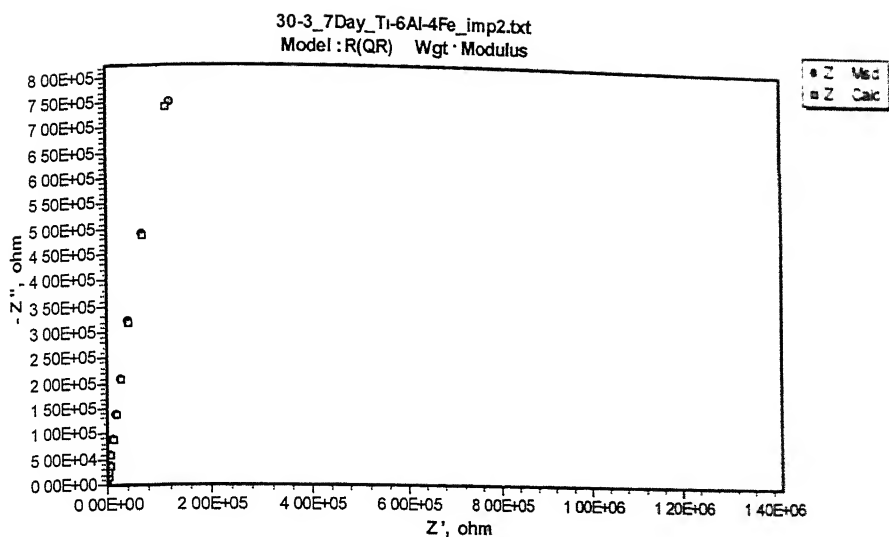


Figure C-39 Experimental (Msd.) and simulated (Calc.) Nyquist plots for Ti-6Al-4Fe after 168 hrs of immersion in Hank's solution.

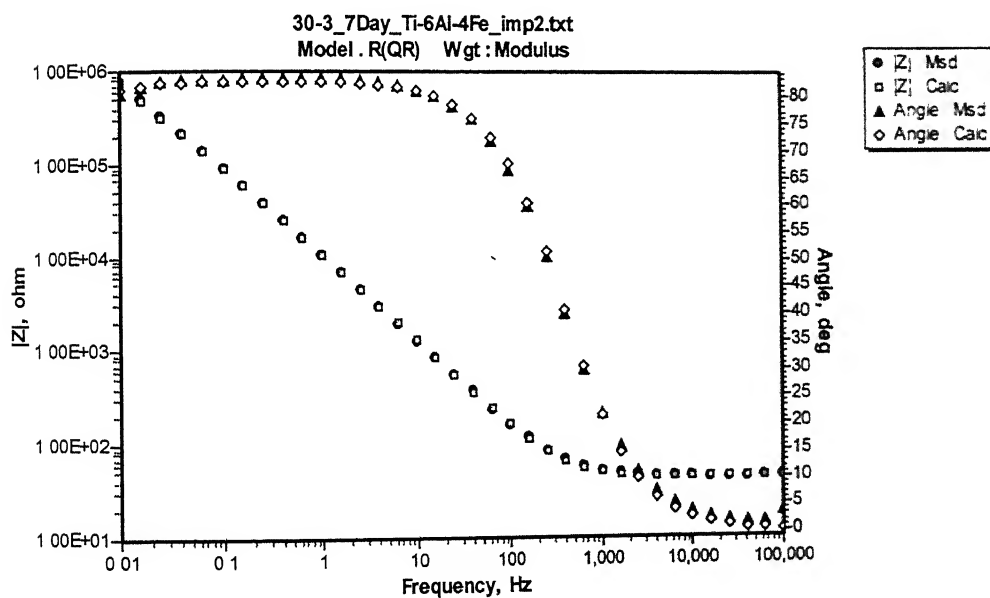


Figure C-40 Experimental (Msd.) and simulated (Calc.) Bode phase and magnitude plots for Ti-6Al-4Fe after 168 hrs of immersion in Hank's solution.

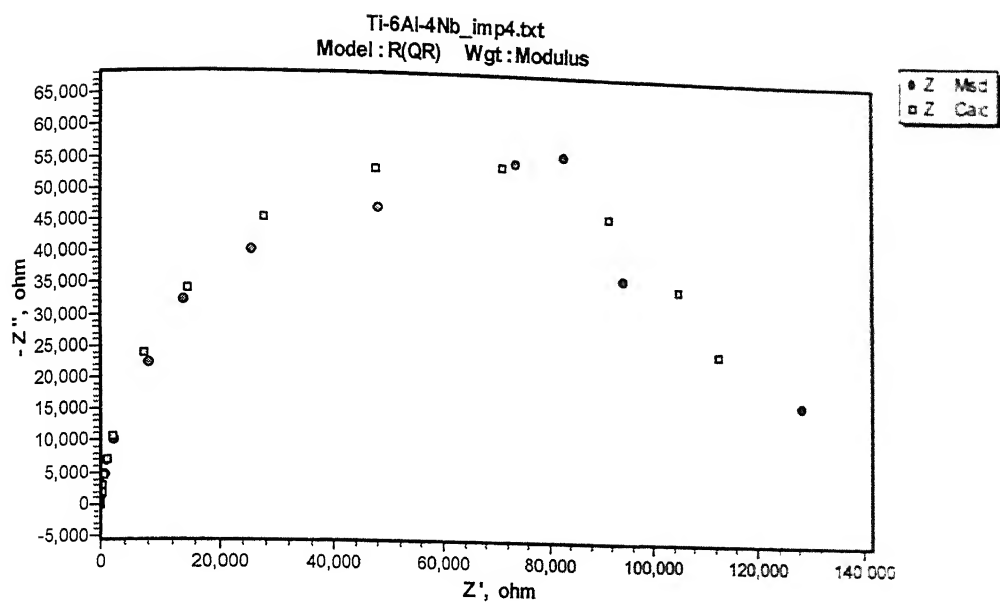


Figure C-41 Experimental (Msd.) and simulated (Calc.) Nyquist plots for Ti-6Al-4Nb after 1 hr of immersion in Hank's solution.

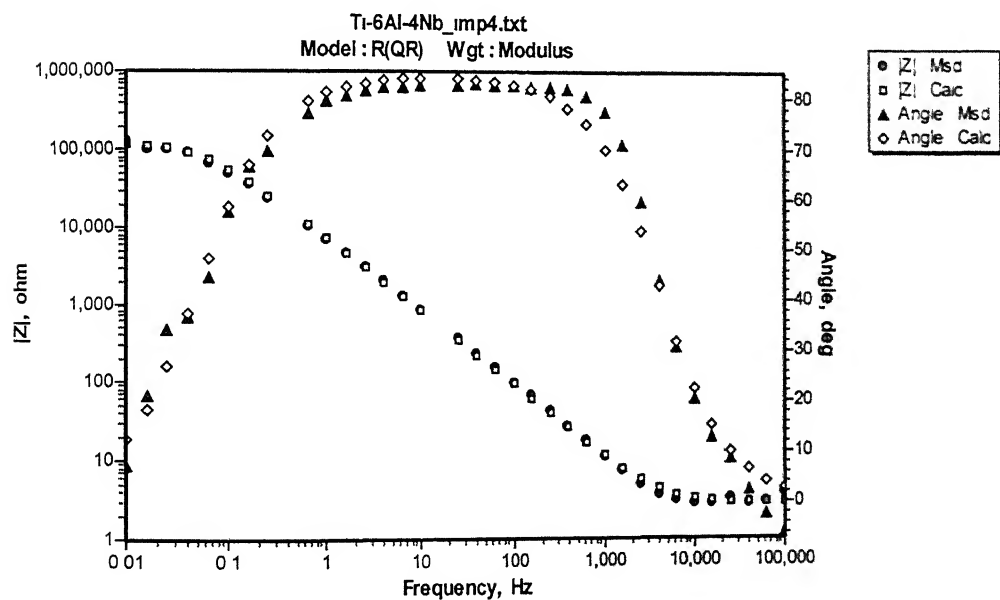


Figure C-42 Experimental (Msd.) and simulated (Calc.) Bode phase and magnitude plots for Ti-6Al-4Nb after 1 hr of immersion in Hank's solution.

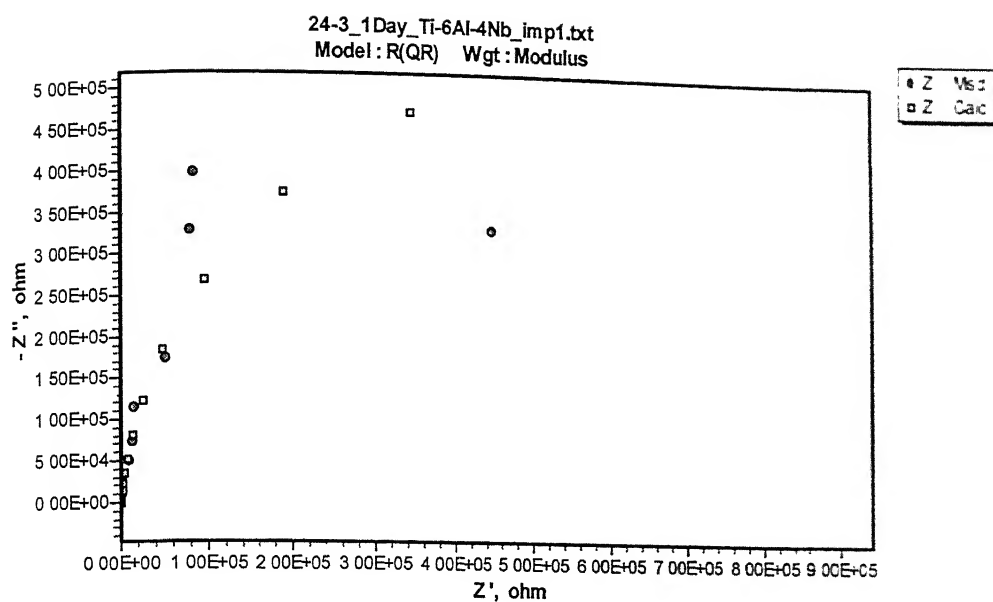


Figure C-43 Experimental (Msd.) and simulated (Calc.) Nyquist plots for Ti-6Al-4Nb after 24 hrs of immersion in Hank's solution.

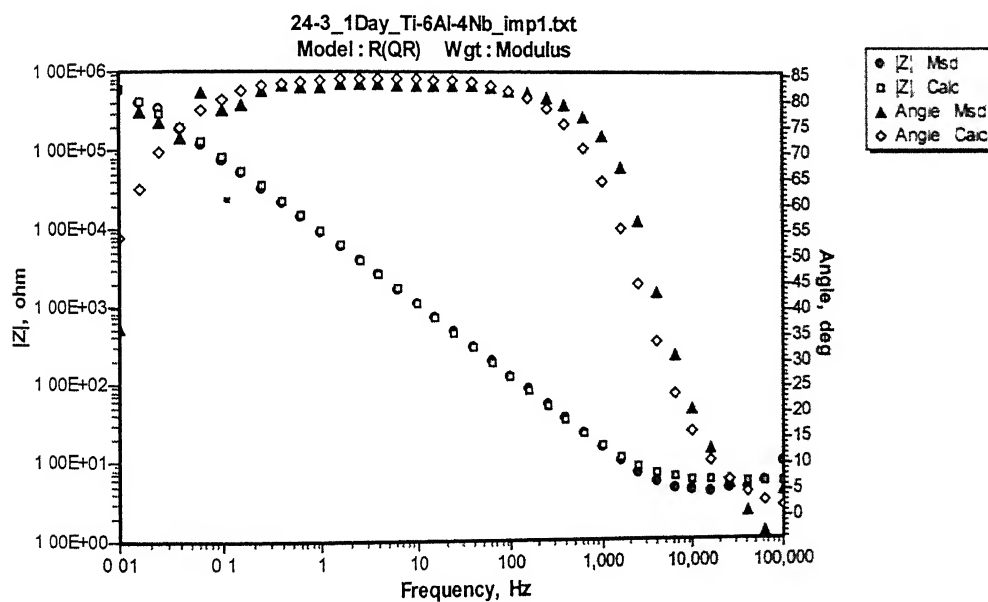


Figure C-44 Experimental (Msd.) and simulated (Calc.) Bode phase and magnitude plots for Ti-6Al-4Nb after 24 hrs of immersion in Hank's solution.

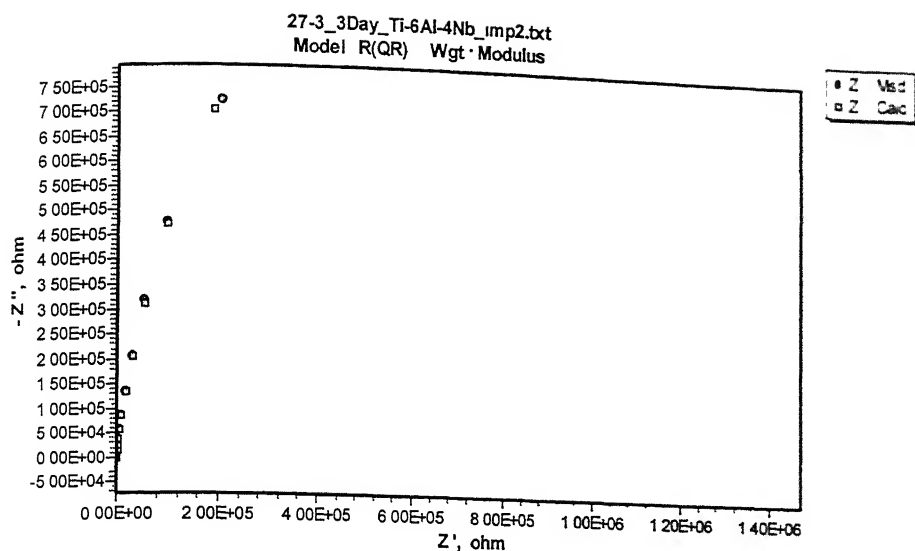


Figure C-45 Experimental (Msd.) and simulated (Calc.) Nyquist plots for Ti-6Al-4Nb after 72 hrs of immersion in Hank's solution.

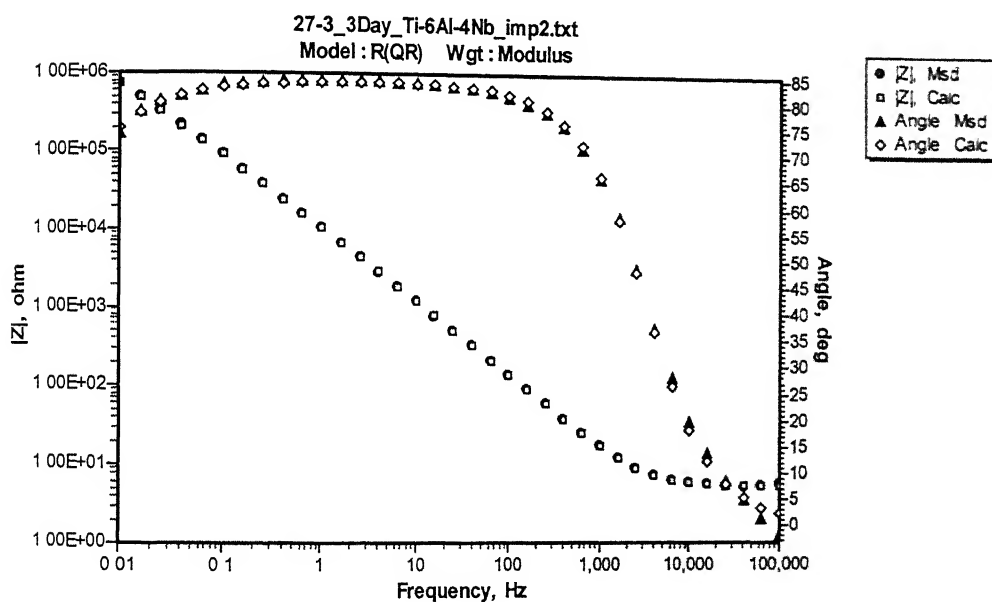


Figure C-46 Experimental (Msd.) and simulated (Calc.) Bode phase and magnitude plots for Ti-6Al-4Nb after 72 hrs of immersion in Hank's solution.



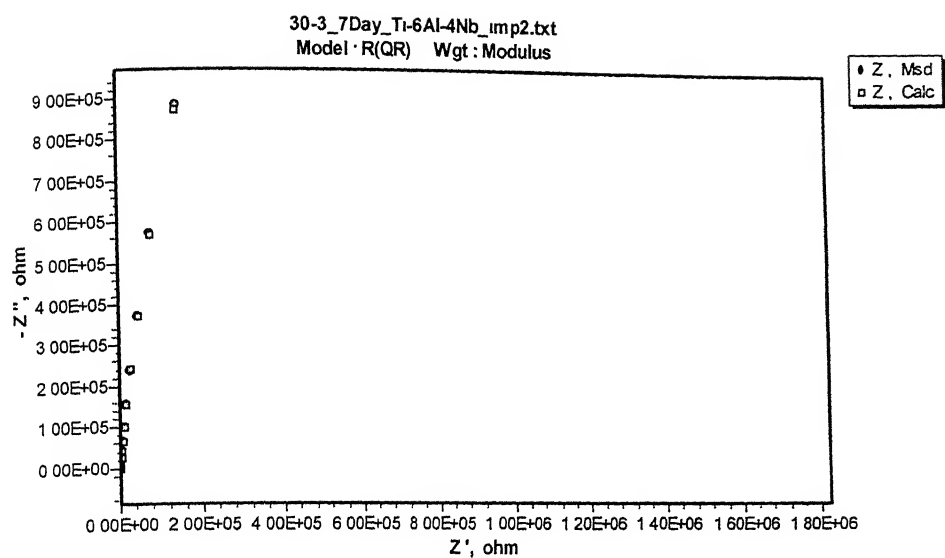


Figure C-47 Experimental (Msd.) and simulated (Calc.) Nyquist plots for Ti-6Al-4Nb after 168 hrs of immersion in Hank's solution.

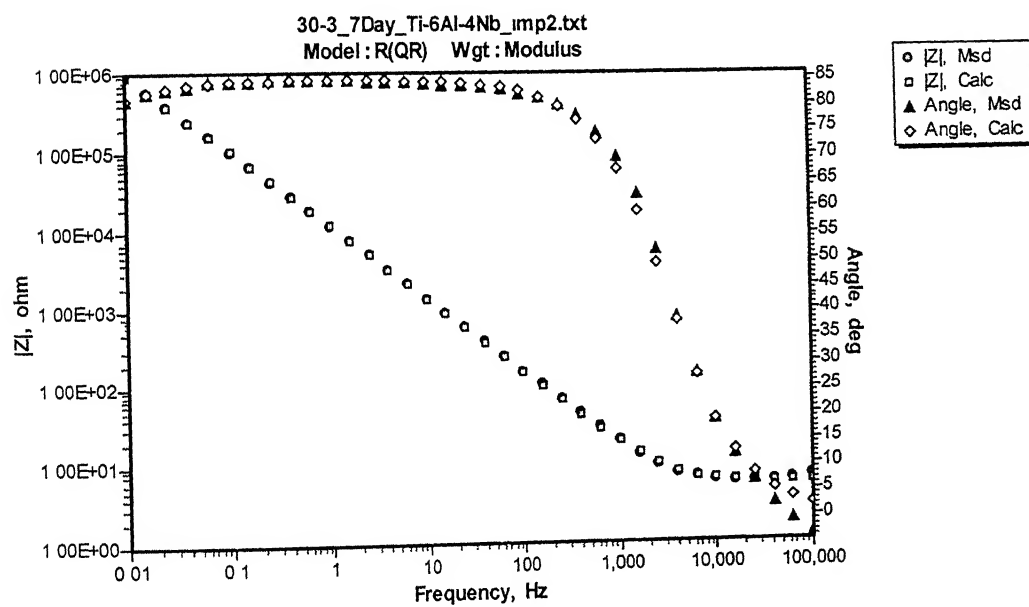


Figure C-48 Experimental (Msd.) and simulated (Calc.) Bode phase and magnitude plots for Ti-6Al-4Nb after 168 hrs of immersion in Hank's solution.

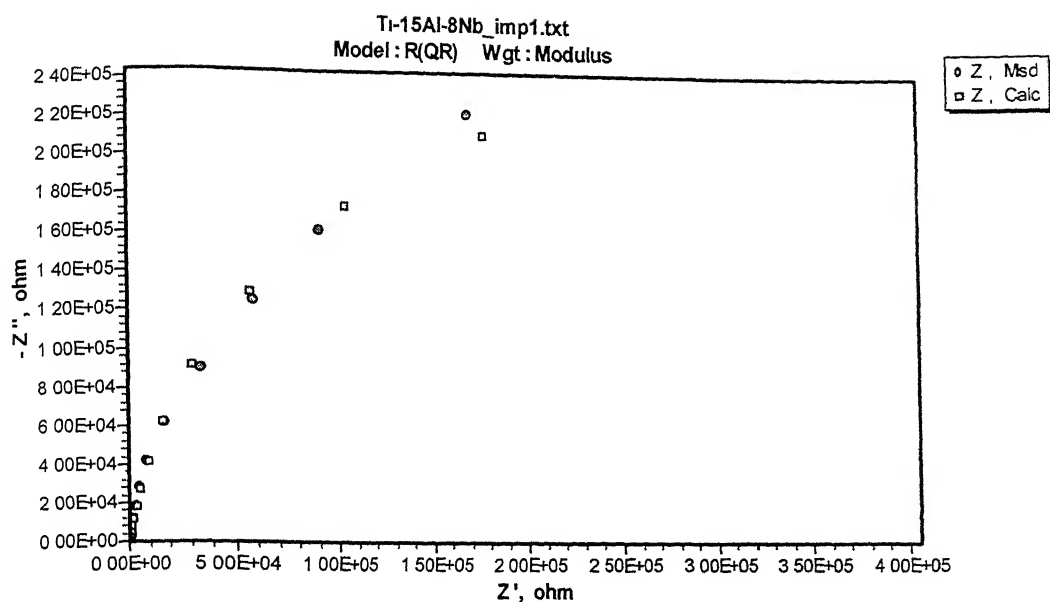


Figure C-49 Experimental (Msd.) and simulated (Calc.) Nyquist plots for Ti-8.4Al-15.4Nb after 1 hr of immersion in Hank's solution.

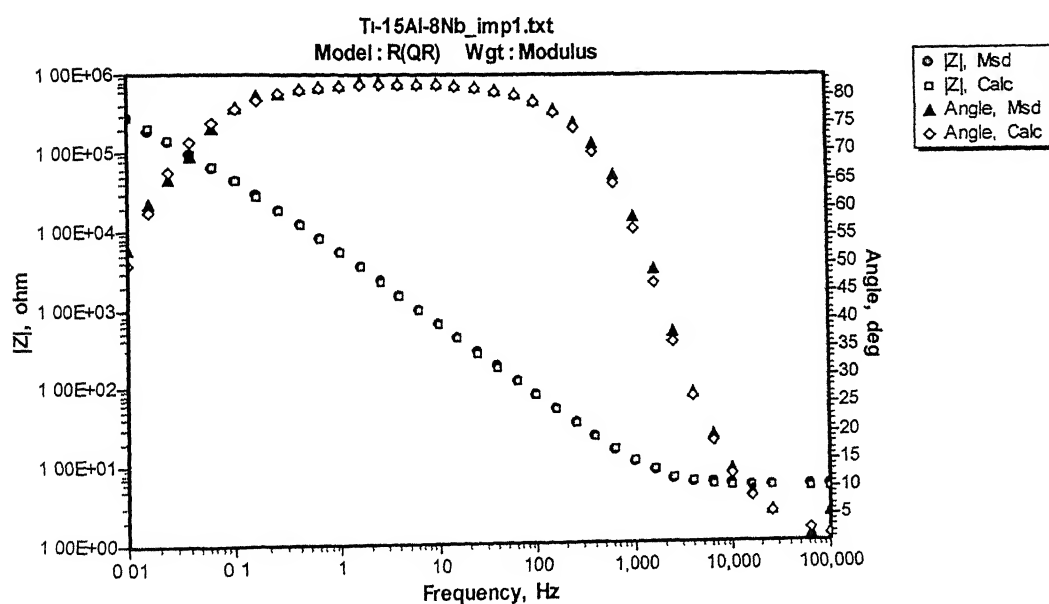


Figure C-50 Experimental (Msd.) and simulated (Calc.) Bode phase and magnitude plots for Ti-8.4Al-15.4Nb after 1 hr of immersion in Hank's solution.

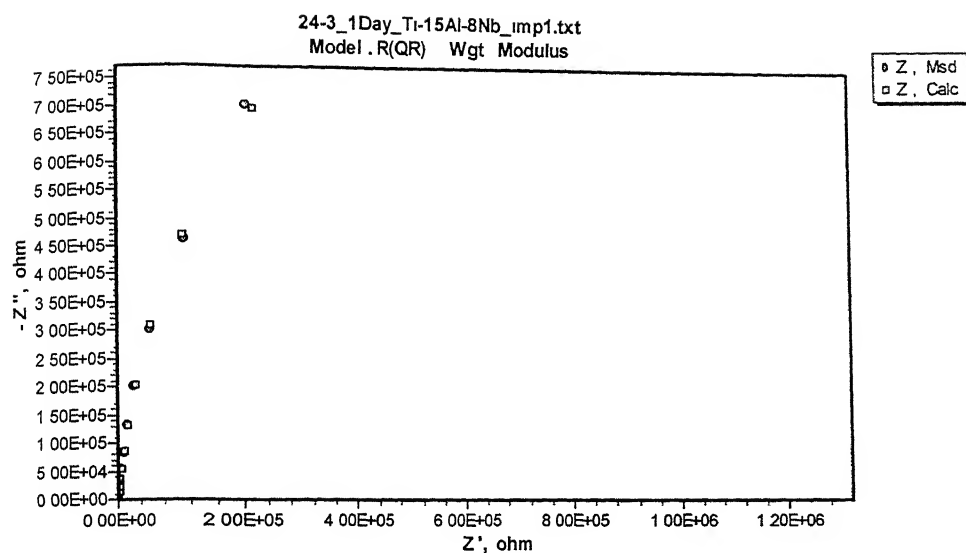


Figure C-51 Experimental (Msd.) and simulated (Calc.) Nyquist plots for Ti-8.4Al-15.4Nb after 24 hrs of immersion in Hank's solution.

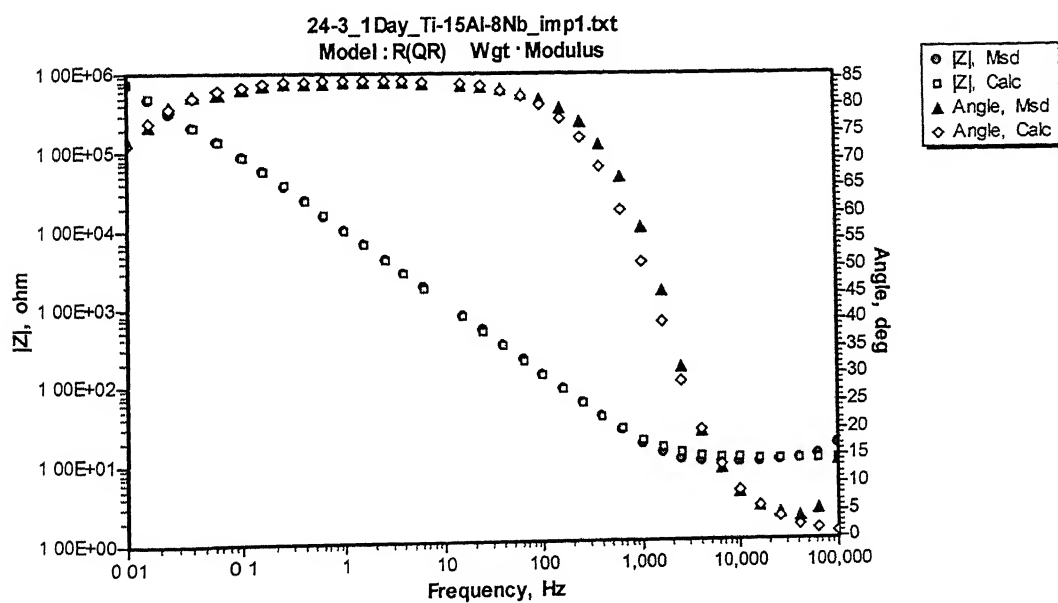


Figure C-52 Experimental (Msd.) and simulated (Calc.) Bode phase and magnitude plots for Ti-8.4Al-15.4Nb after 24 hrs of immersion in Hank's solution.

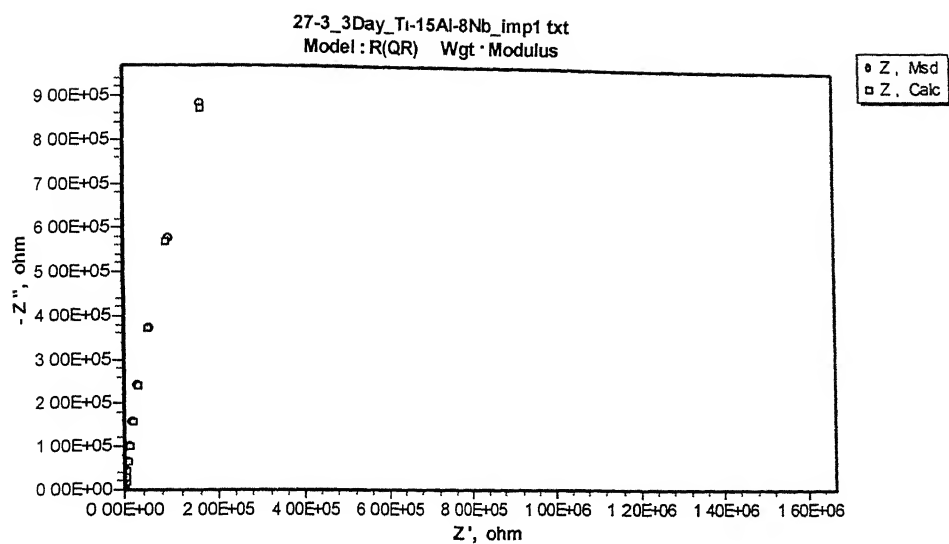


Figure C-53 Experimental (Msd.) and simulated (Calc.) Nyquist plots for Ti-8.4Al-15.4Nb after 72 hrs of immersion in Hank's solution.

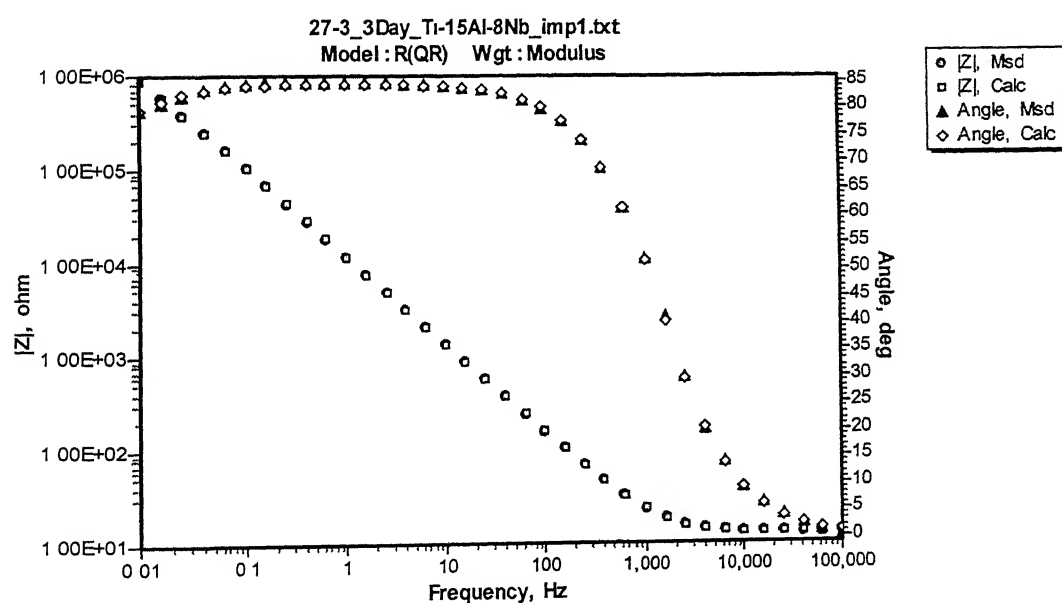


Figure C-54 Experimental (Msd.) and simulated (Calc.) Bode phase and magnitude plots for Ti-8.4Al-15.4Nb after 72 hrs of immersion in Hank's solution.

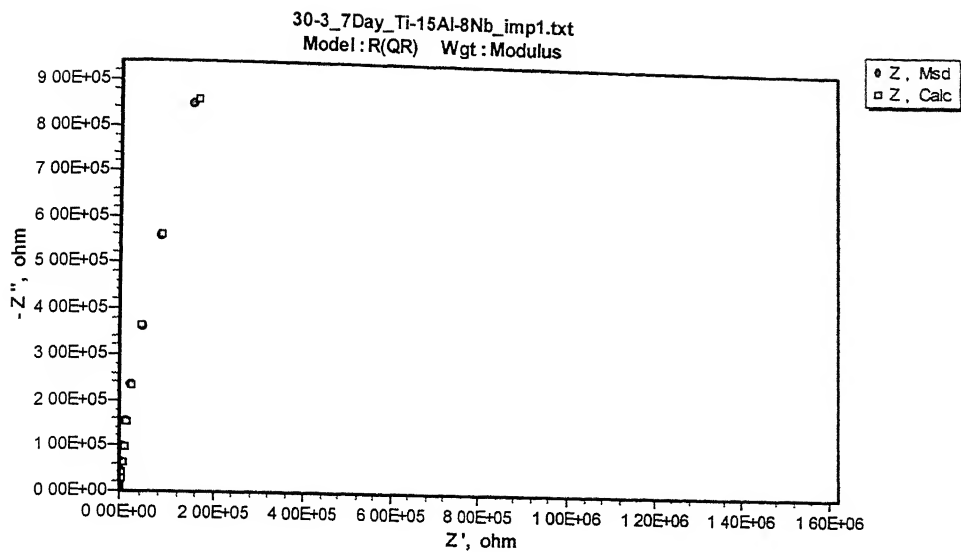


Figure C-55 Experimental (Msd.) and simulated (Calc.) Nyquist plots for Ti-8.4Al-15.4Nb after 168 hrs of immersion in Hank's solution.

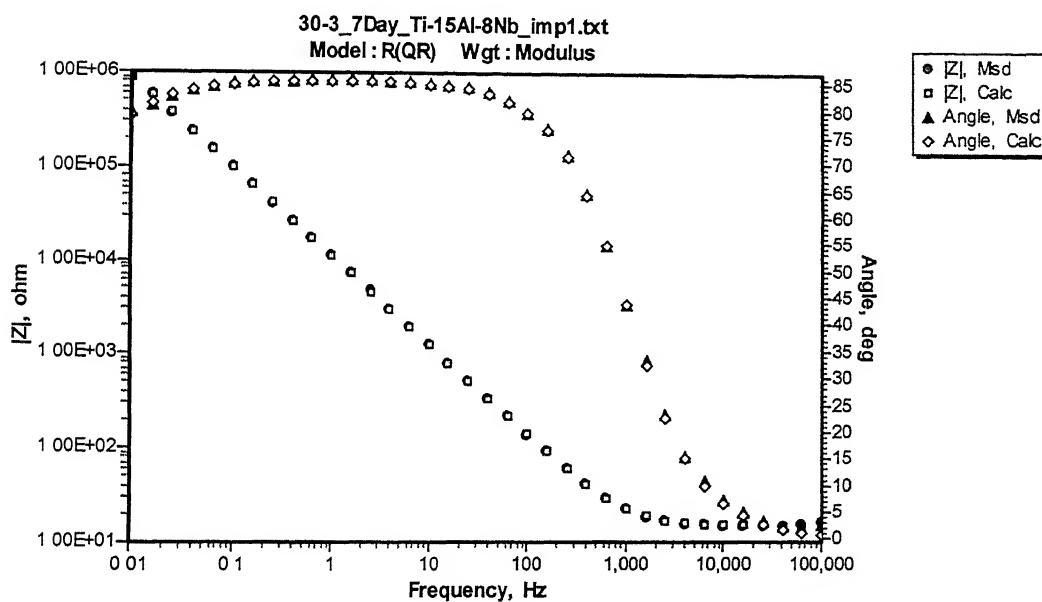


Figure C-56 Experimental (Msd.) and simulated (Calc.) Bode phase and magnitude plots for Ti-8.4Al-15.4Nb after 168 hrs of immersion in Hank's solution.

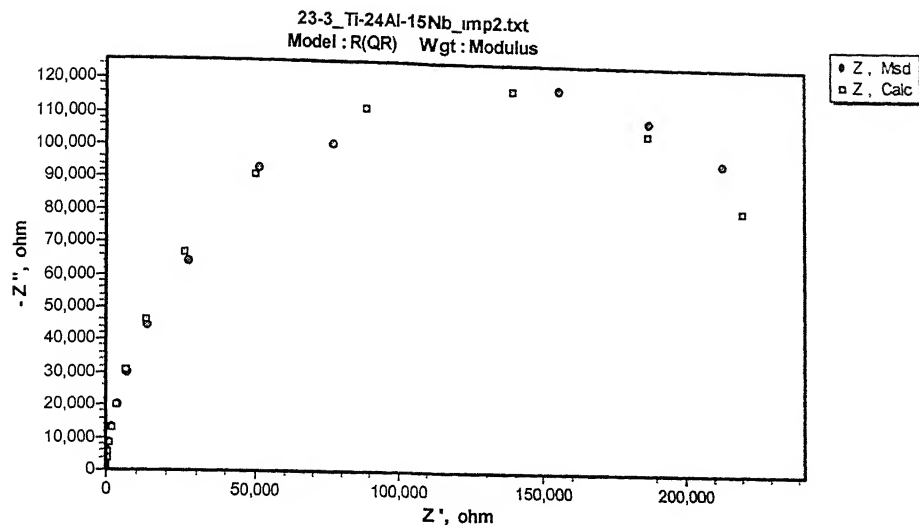


Figure C-57 Experimental (Msd.) and simulated (Calc.) Nyquist plots for Ti-13.4Al-29Nb after 1 hr of immersion in Hank's solution.

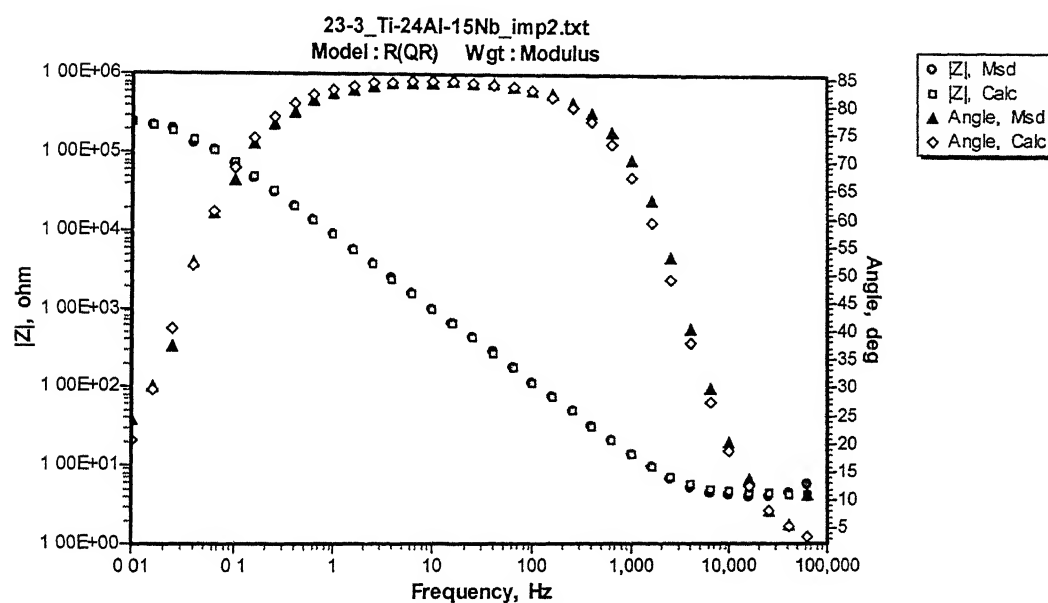


Figure C-58 Experimental (Msd.) and simulated (Calc.) Bode phase and magnitude plots for Ti-13.4Al-29Nb after 1 hr of immersion in Hank's solution.

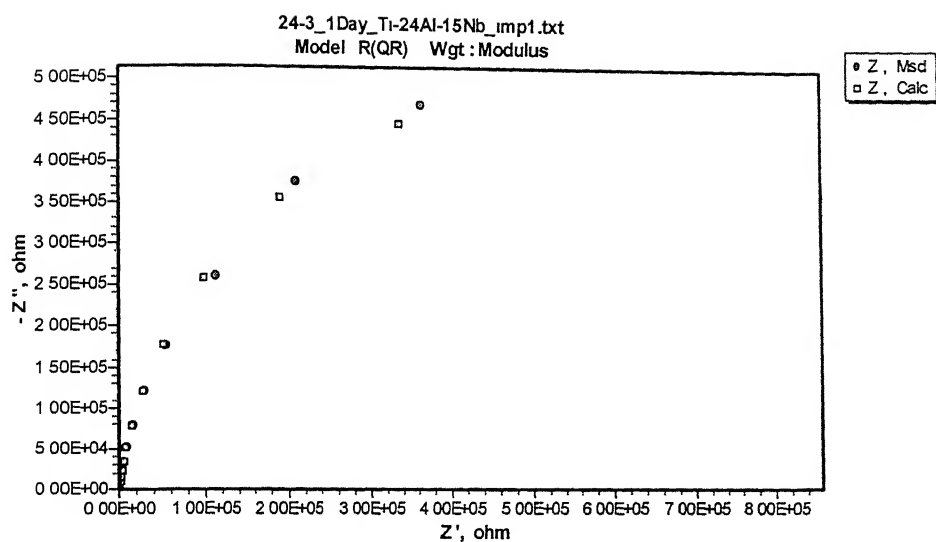


Figure C-59 Experimental (Msd.) and simulated (Calc.) Nyquist plots for Ti-13.4Al-29Nb after 24 hrs of immersion in Hank's solution.

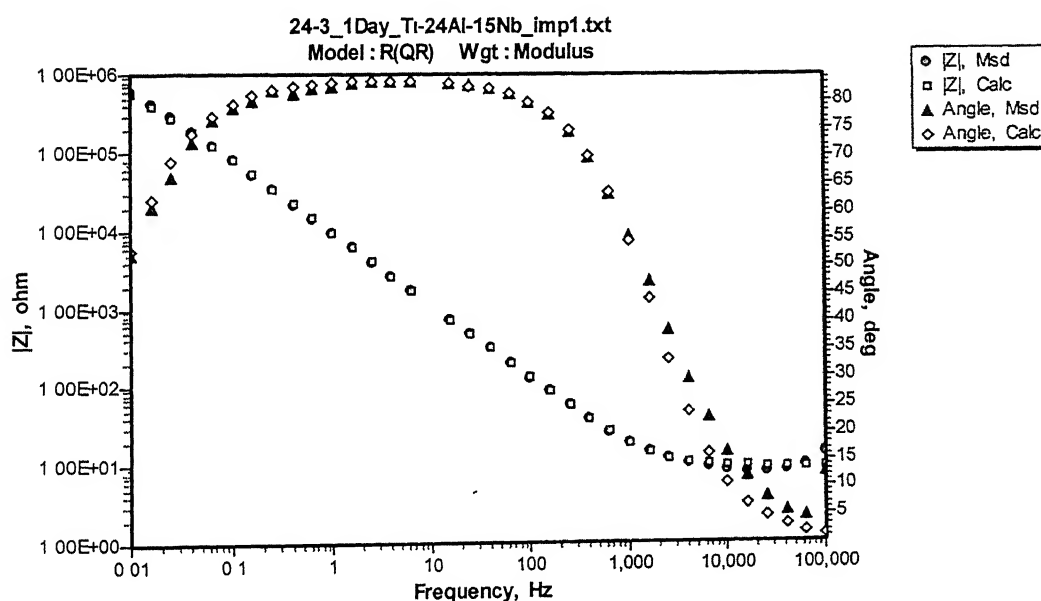


Figure C-60 Experimental (Msd.) and simulated (Calc.) Bode phase and magnitude plots for Ti-13.4Al-29Nb after 24 hrs of immersion in Hank's solution.

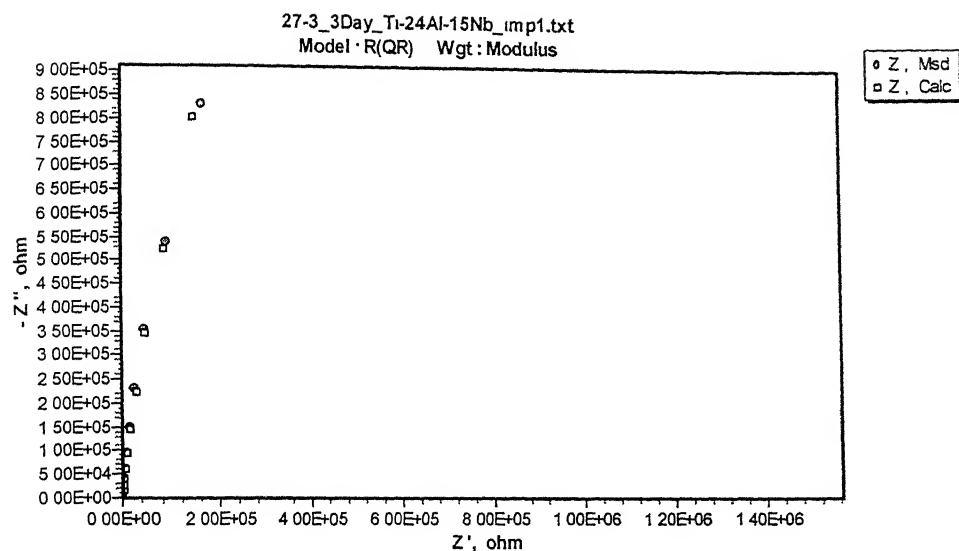


Figure C-61 Experimental (Msd.) and simulated (Calc.) Nyquist plots for Ti-13.4Al-29Nb after 72 hrs of immersion in Hank's solution.

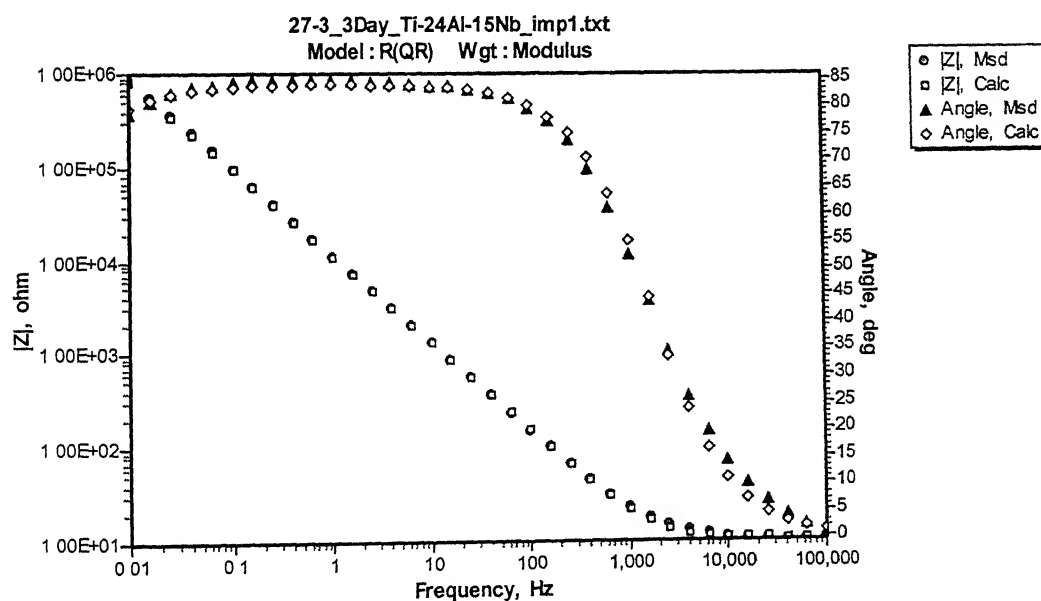


Figure C-62 Experimental (Msd.) and simulated (Calc.) Bode phase and magnitude plots for Ti-13.4Al-29Nb after 72 hrs of immersion in Hank's solution.



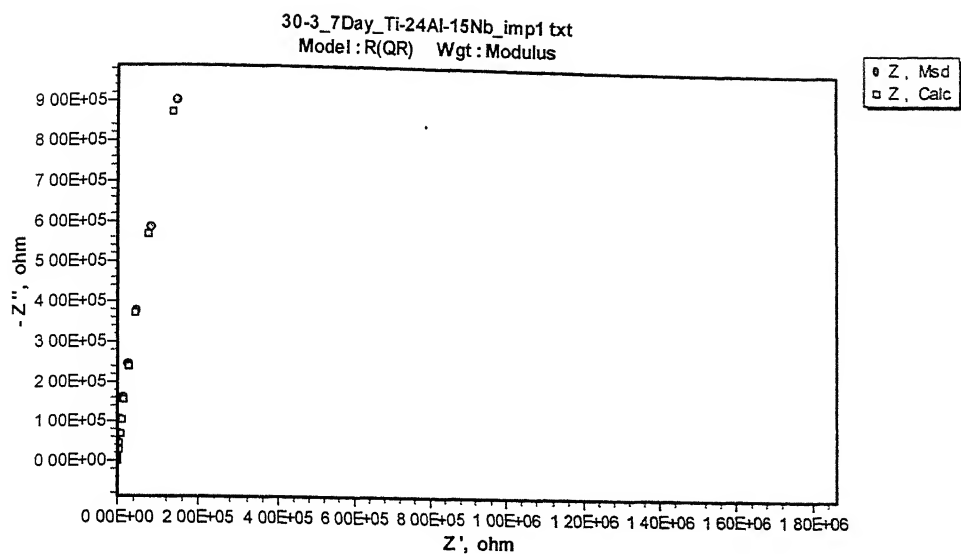


Figure C-63 Experimental (Msd.) and simulated (Calc.) Nyquist plots for Ti-13.4Al-29Nb after 168 hrs of immersion in Hank's solution.

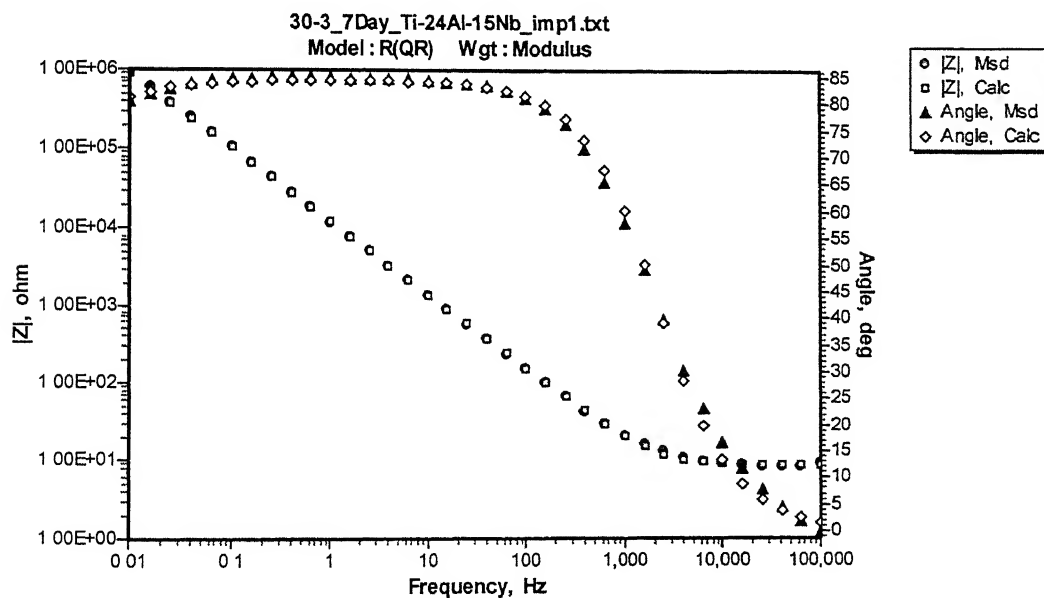


Figure C-64 Experimental (Msd.) and simulated (Calc.) Bode phase and magnitude plots for Ti-13.4Al-29Nb after 168 hrs of immersion in Hank's solution.

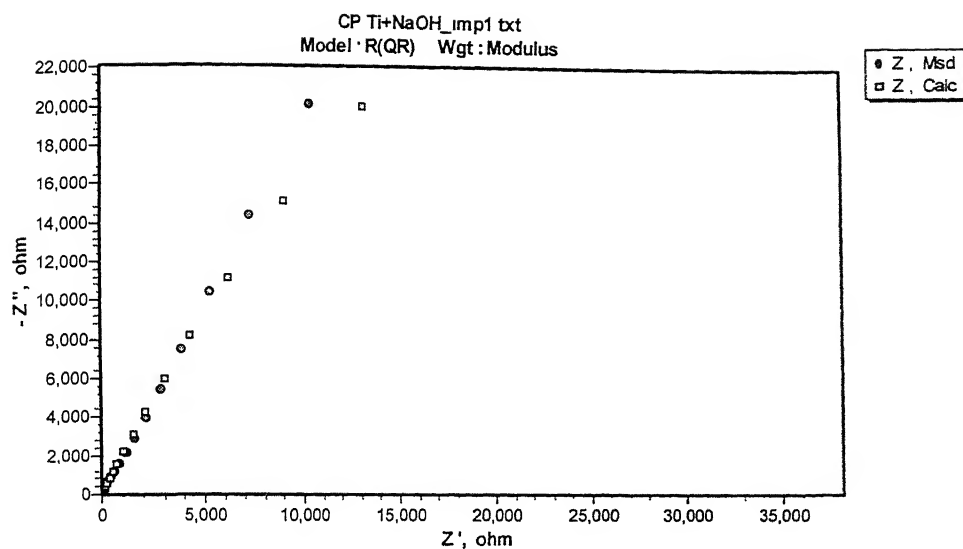


Figure C-65 Experimental (Msd.) and simulated (Calc.) Nyquist plots for NaOH-treated CP Titanium after 1 hr of immersion in Hank's solution.

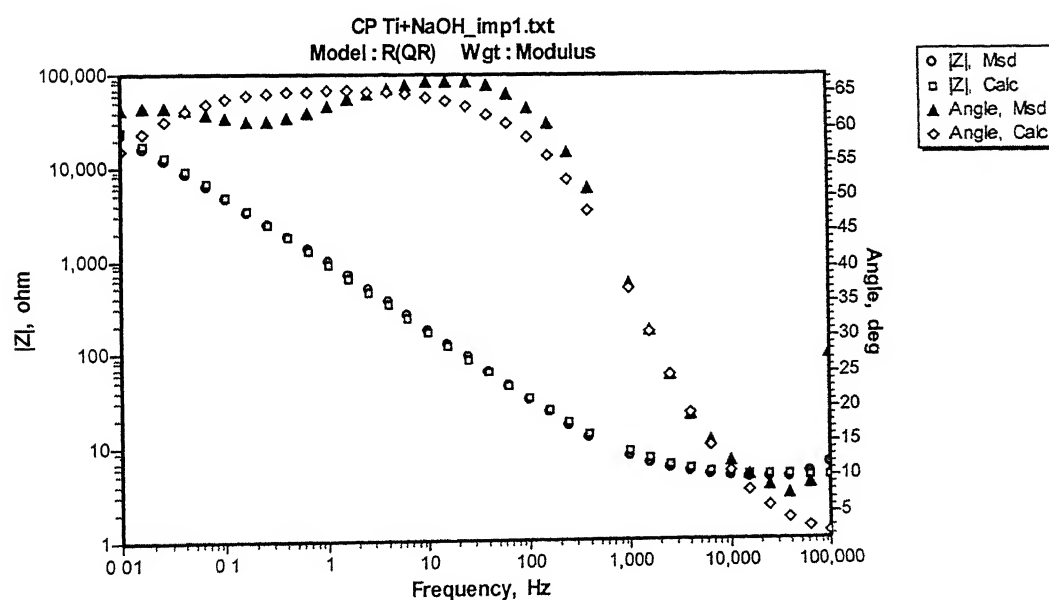


Figure C-66 Experimental (Msd.) and simulated (Calc.) Bode phase and magnitude plots for NaOH-treated CP Titanium after 1 hr of immersion in Hank's solution.

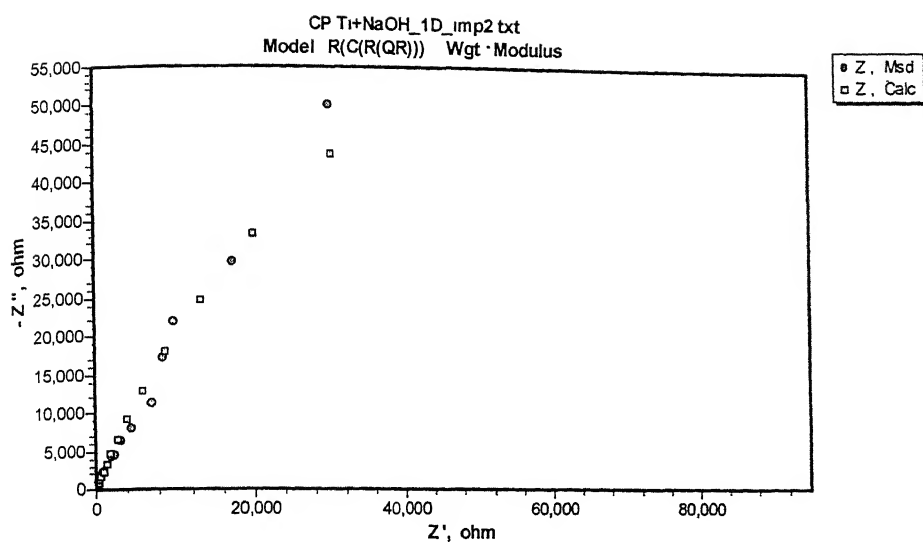


Figure C-67 Experimental (Msd.) and simulated (Calc.) Nyquist plots for NaOH-treated CP Titanium after 24 hrs of immersion in Hank's solution.

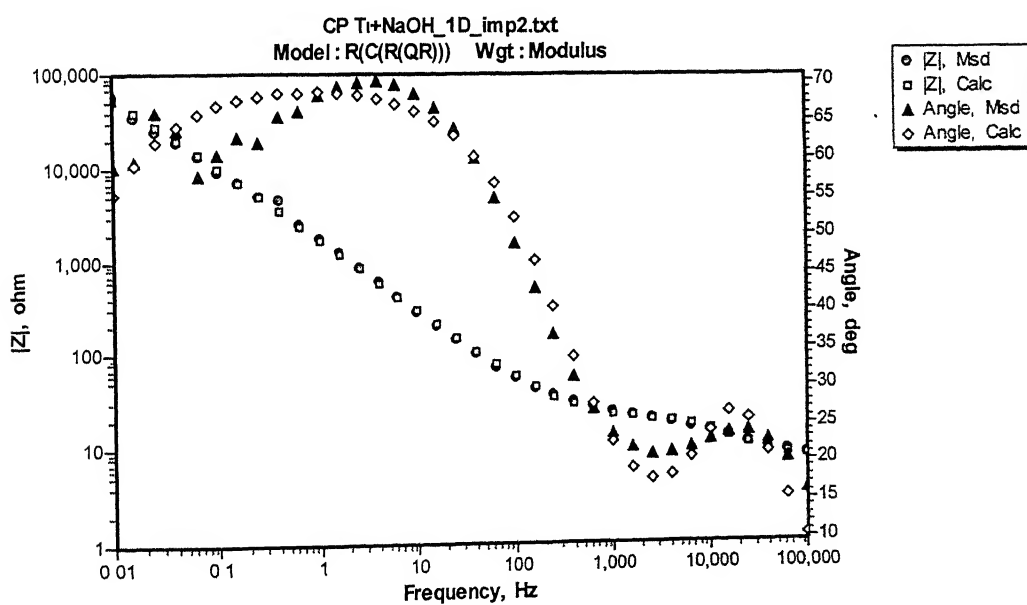


Figure C-68 Experimental (Msd.) and simulated (Calc.) Bode phase and magnitude plots for NaOH-treated CP Titanium after 24 hrs of immersion in Hank's solution.

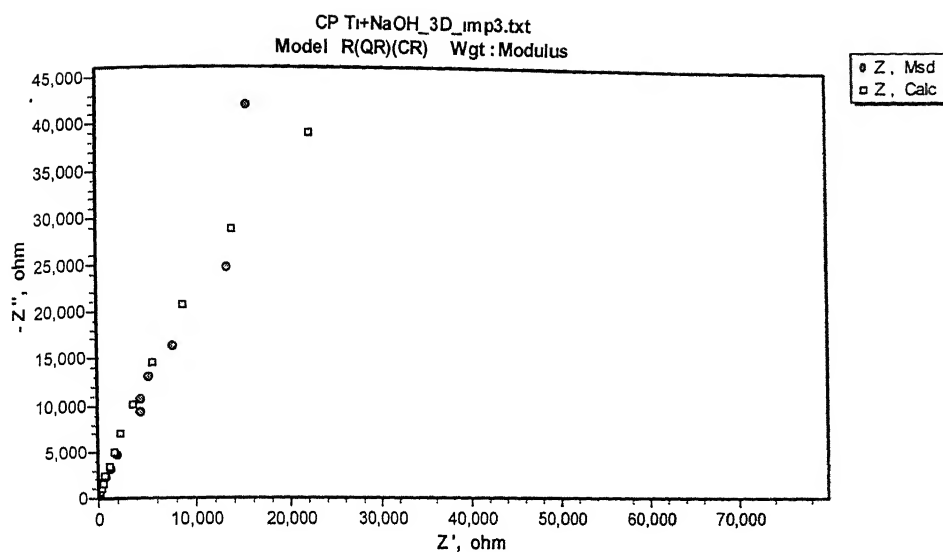


Figure C-69 Experimental (Msd.) and simulated (Calc.) Nyquist plots for NaOH-treated CP Titanium after 72 hrs of immersion in Hank's solution.

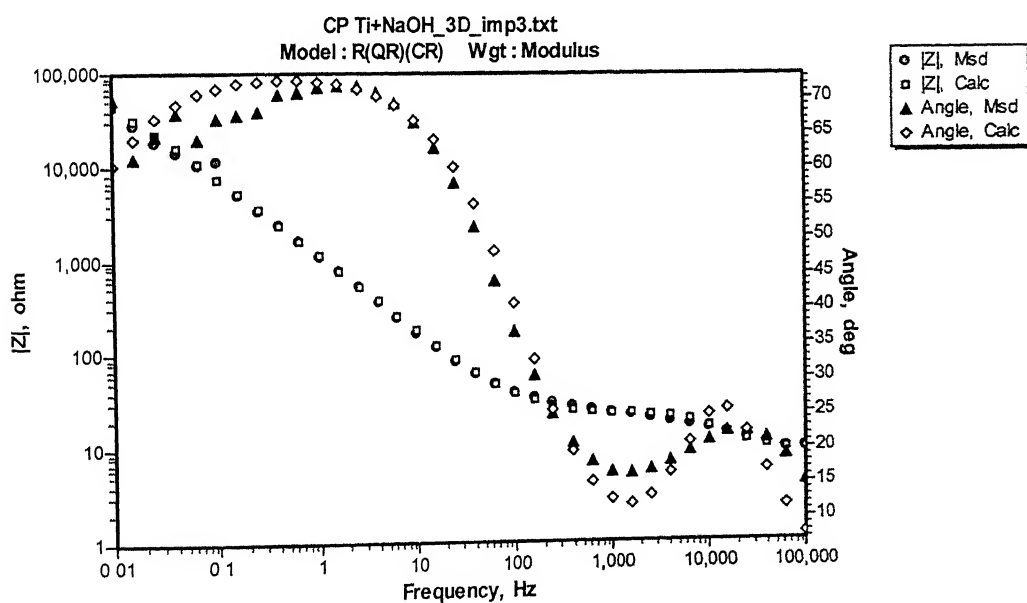


Figure C-70 Experimental (Msd.) and simulated (Calc.) Bode phase and magnitude plots for NaOH-treated CP Titanium after 72 hrs of immersion in Hank's solution.

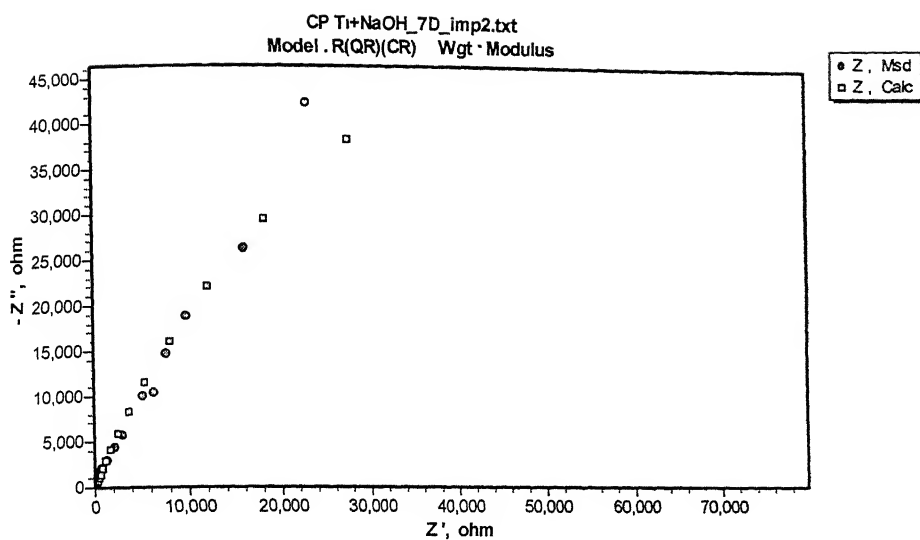


Figure C-71 Experimental (Msd.) and simulated (Calc.) Nyquist plots for NaOH-treated CP Titanium after 168 hrs of immersion in Hank's solution.

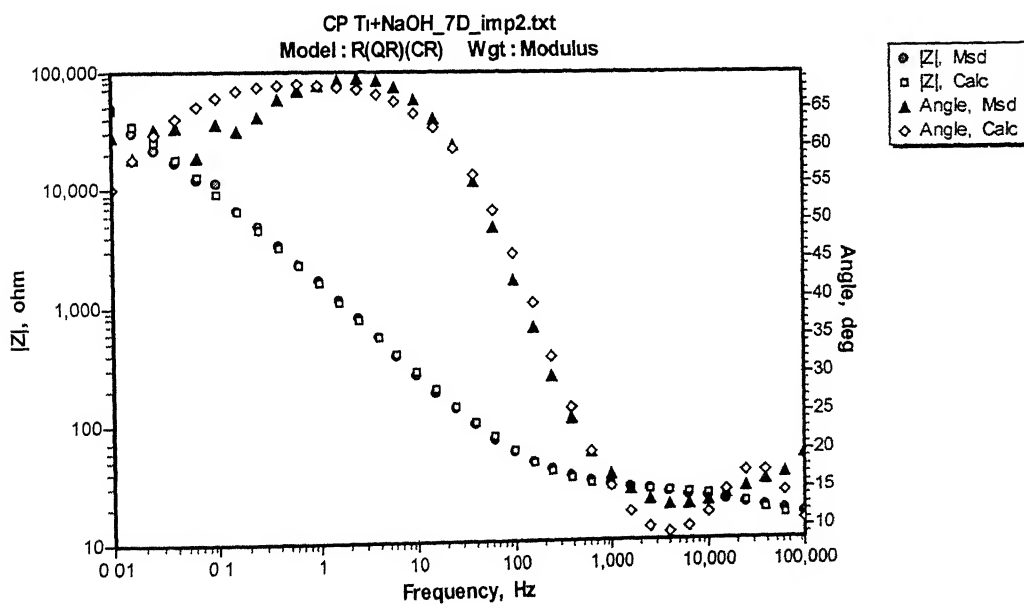


Figure C-72 Experimental (Msd.) and simulated (Calc.) Bode phase and magnitude plots for NaOH-treated CP Titanium after 168 hrs of immersion in Hank's solution.

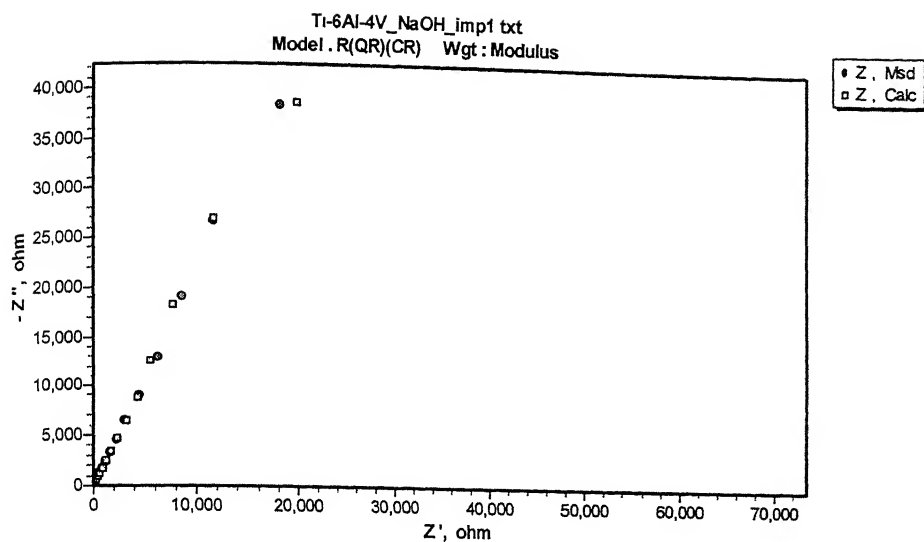


Figure C-73 Experimental (Msd.) and simulated (Calc.) Nyquist plots for NaOH-treated Ti-6Al-4V after 1 hr of immersion in Hank's solution.

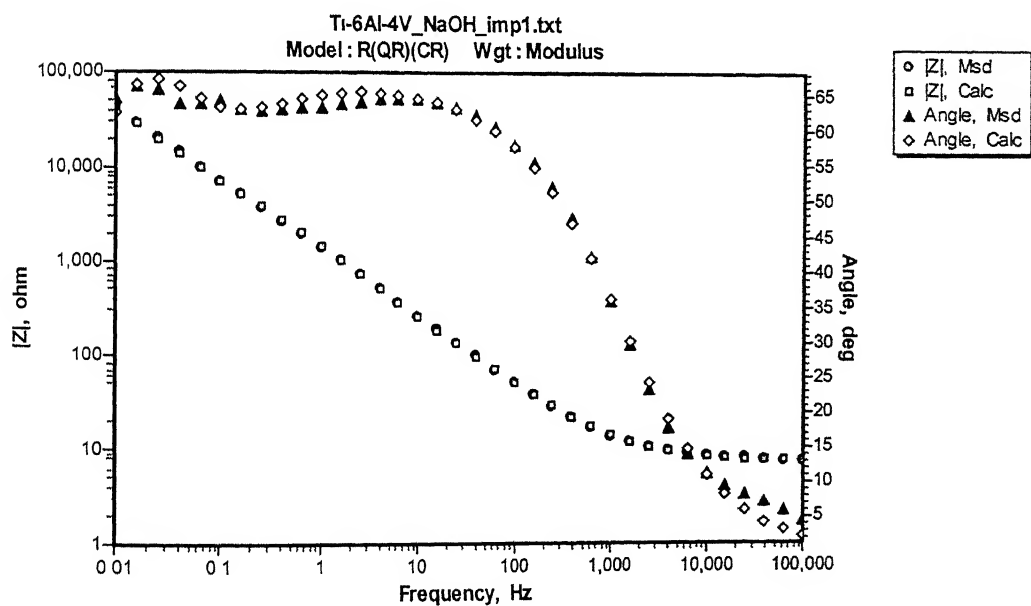


Figure C-74 Experimental (Msd.) and simulated (Calc.) Bode phase and magnitude plots for NaOH-treated Ti-6Al-4V after 1 hr of immersion in Hank's solution.

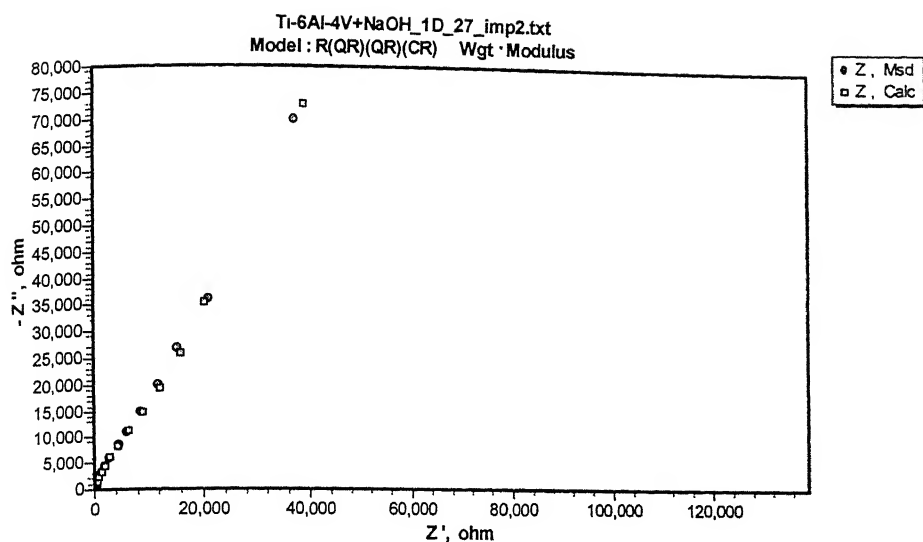


Figure C-75 Experimental (Msd.) and simulated (Calc.) Nyquist plots for NaOH-treated Ti-6Al-4V after 24 hrs of immersion in Hank's solution.

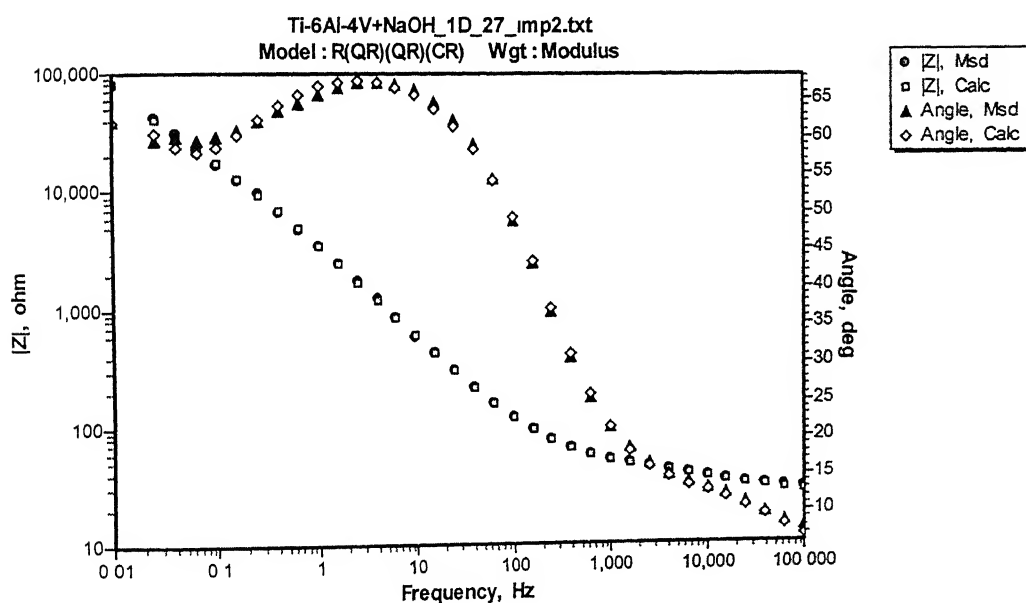


Figure C-76 Experimental (Msd.) and simulated (Calc.) Bode phase and magnitude plots for NaOH-treated Ti-6Al-4V after 24 hrs of immersion in Hank's solution.

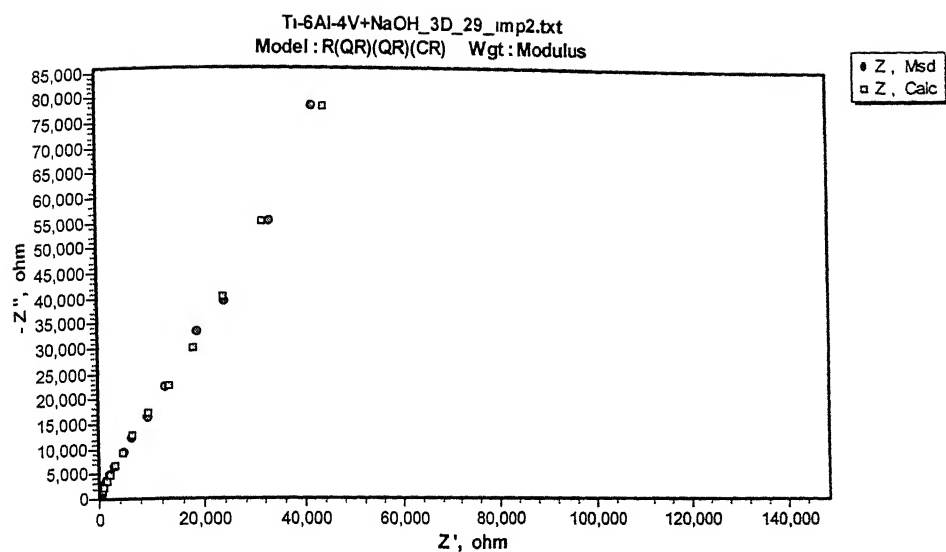


Figure C-77 Experimental (Msd.) and simulated (Calc.) Nyquist plots for NaOH-treated Ti-6Al-4V after 72 hrs of immersion in Hank's solution.

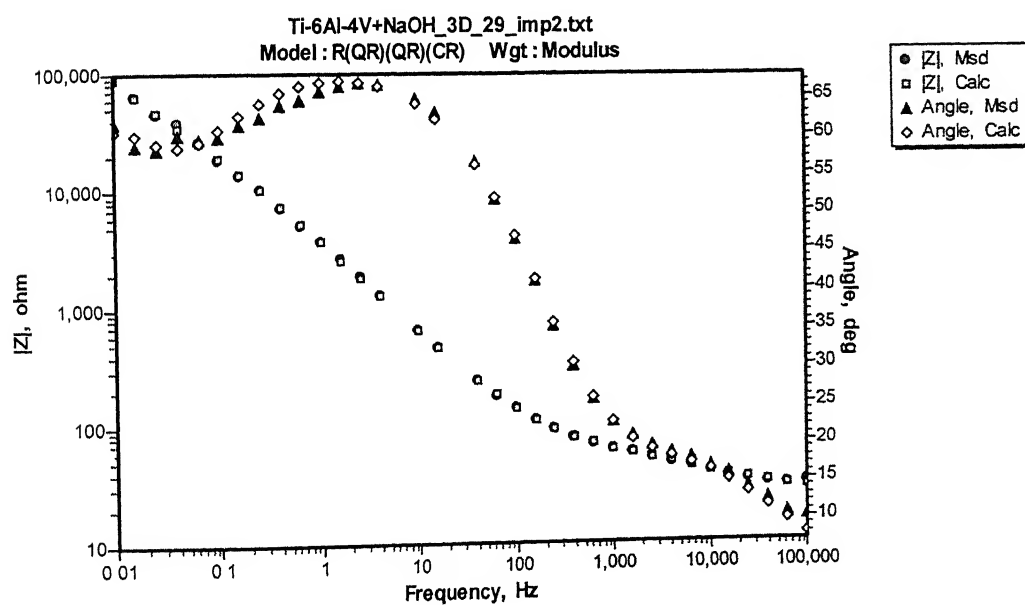


Figure C-78 Experimental (Msd.) and simulated (Calc.) Bode phase and magnitude plots for NaOH-treated Ti-6Al-4V after 72 hrs of immersion in Hank's solution.



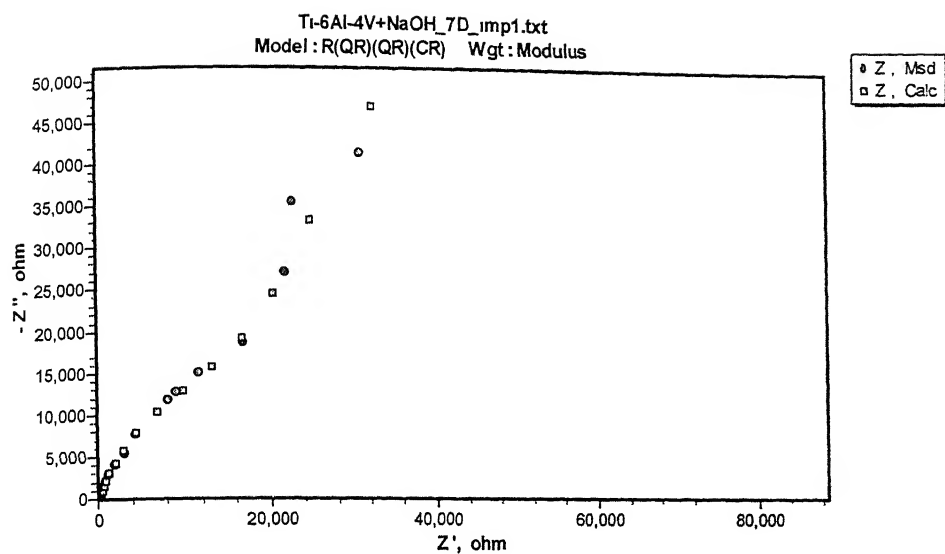


Figure C-79 Experimental (Msd.) and simulated (Calc.) Nyquist plots for NaOH-treated Ti-6Al-4V after 168 hrs of immersion in Hank's solution.

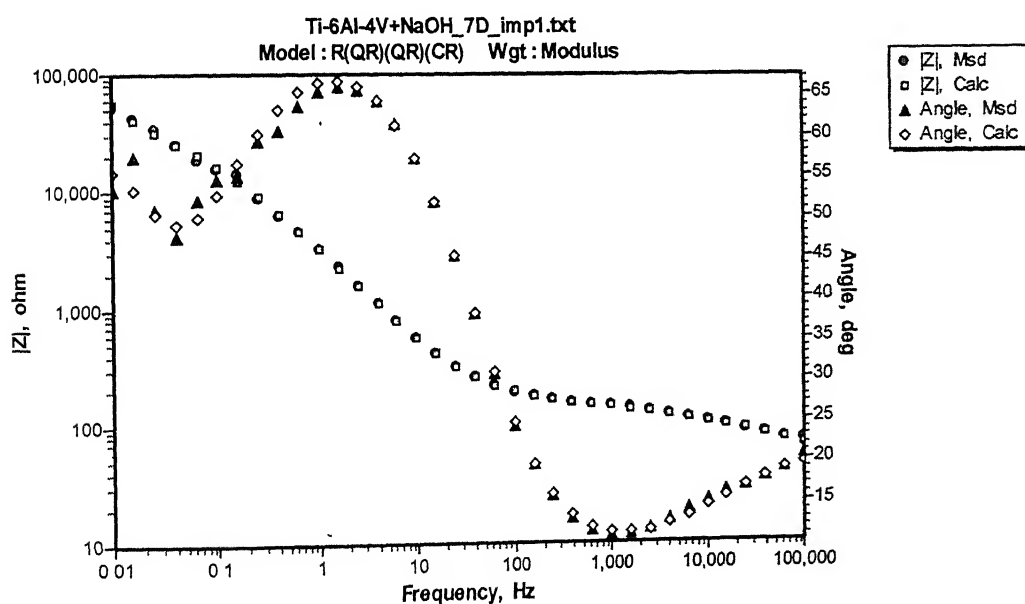


Figure C-80 Experimental (Msd.) and simulated (Calc.) Bode phase and magnitude plots for NaOH-treated Ti-6Al-4V after 168 hrs of immersion in Hank's solution.

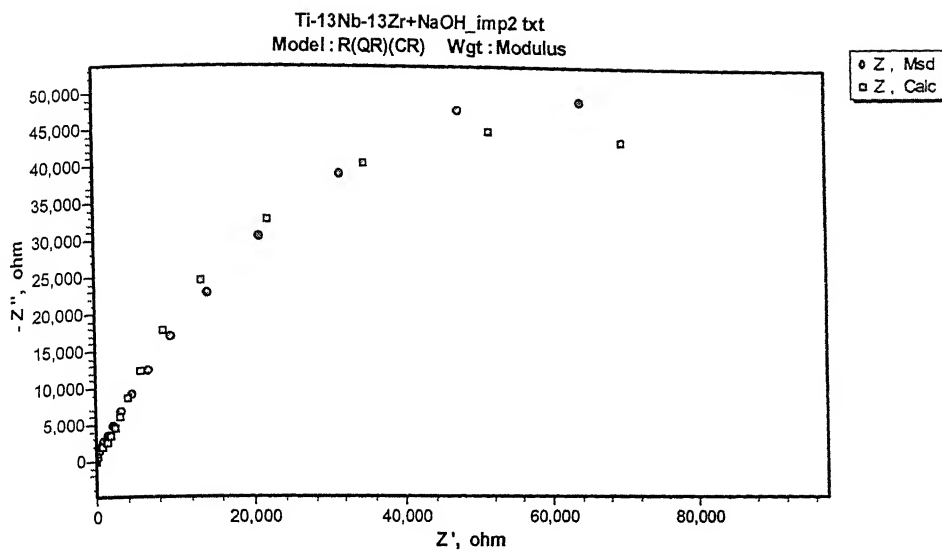


Figure C-81 Experimental (Msd.) and simulated (Calc.) Nyquist plots for NaOH-treated Ti-13Nb-13Zr after 1 hr of immersion in Hank's solution.

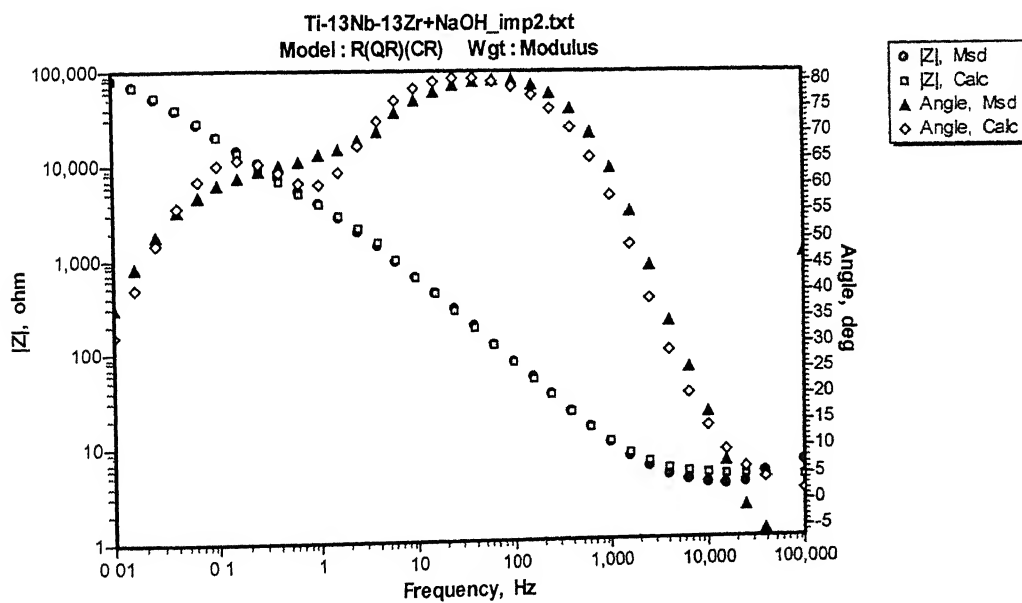


Figure C-82 Experimental (Msd.) and simulated (Calc.) Bode phase and magnitude plots for NaOH-treated Ti-13Nb-13Zr after 1 hr of immersion in Hank's solution.

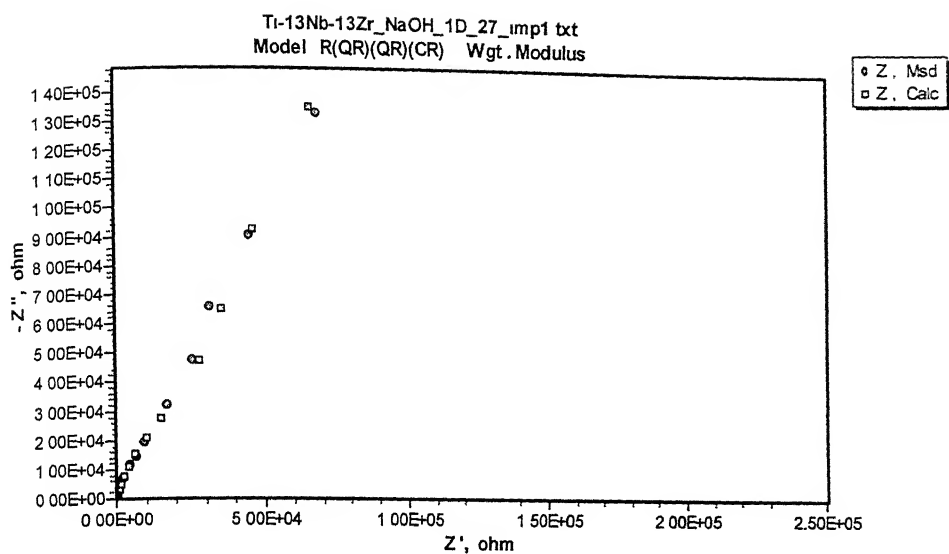


Figure C-83 Experimental (Msd.) and simulated (Calc.) Nyquist plots for NaOH-treated Ti-13Nb-13Zr after 24 hrs of immersion in Hank's solution.

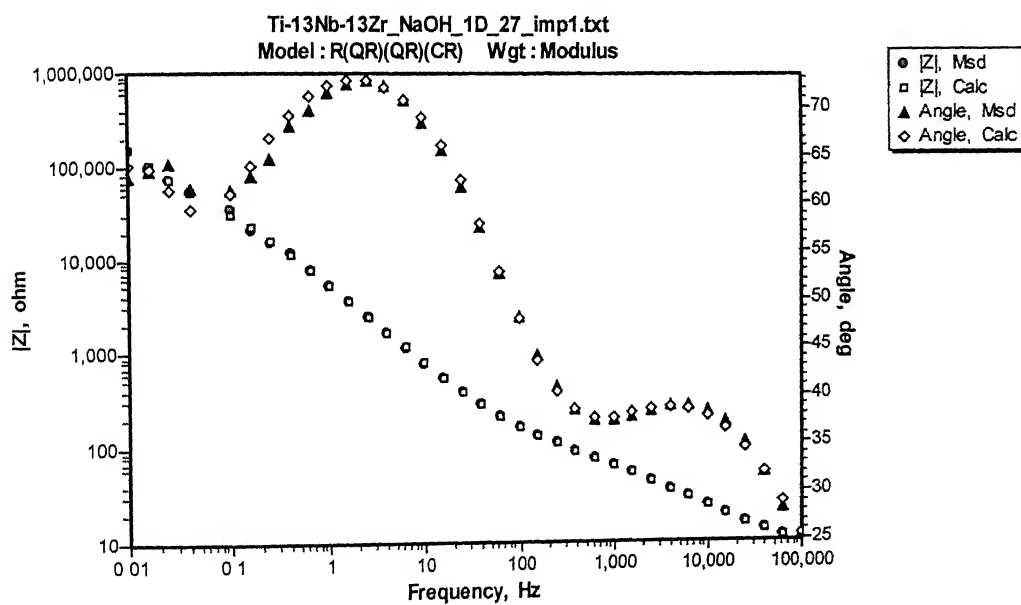


Figure C-84 Experimental (Msd.) and simulated (Calc.) Bode phase and magnitude plots for NaOH-treated Ti-13Nb-13Zr after 24 hrs of immersion in Hank's solution.

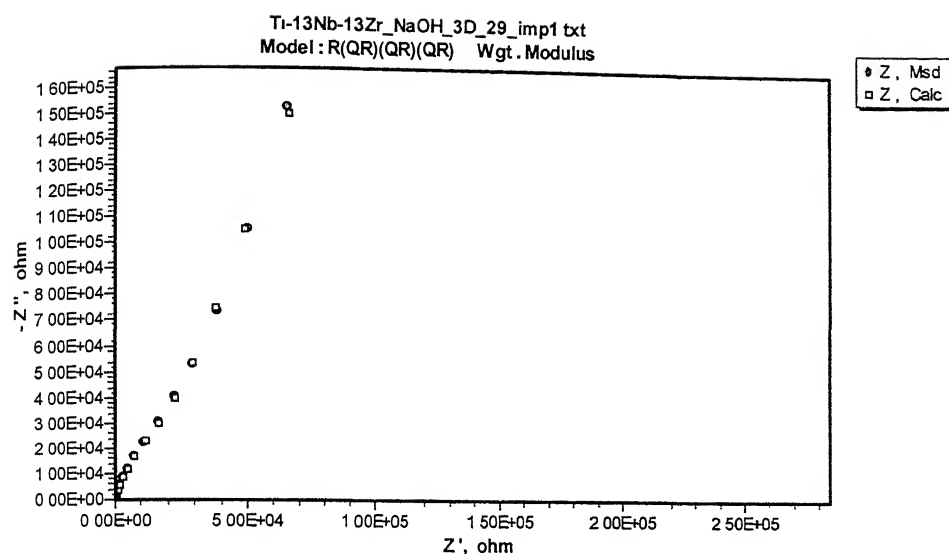


Figure C-85 Experimental (Msd.) and simulated (Calc.) Nyquist plots for NaOH-treated Ti-13Nb-13Zr after 72 hrs of immersion in Hank's solution.

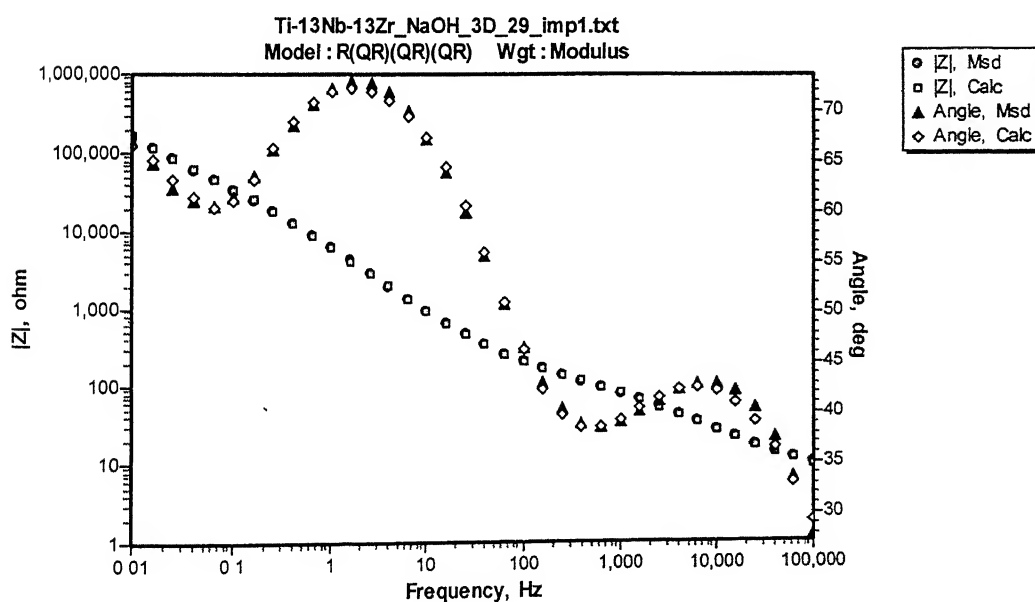


Figure C-86 Experimental (Msd.) and simulated (Calc.) Bode phase and magnitude plots for NaOH-treated Ti-13Nb-13Zr after 72 hrs of immersion in Hank's solution.

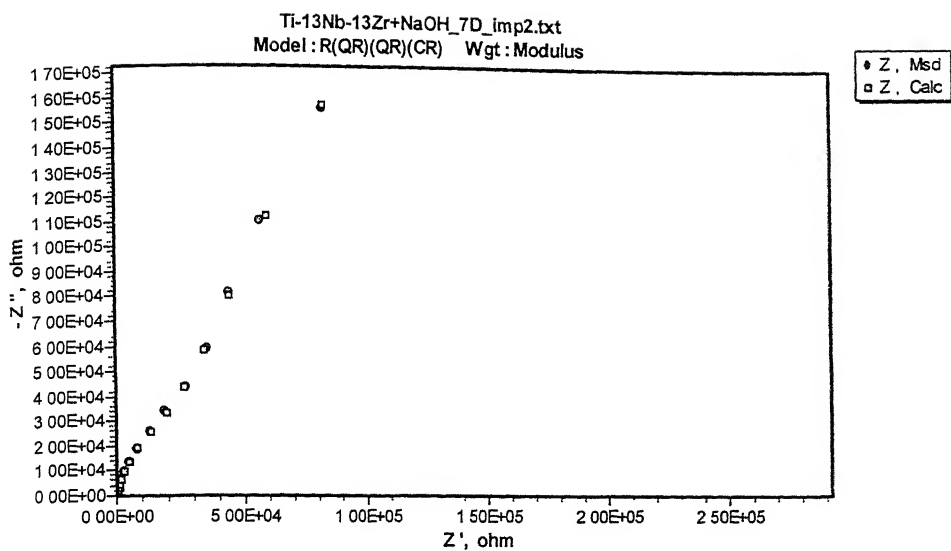


Figure C-87 Experimental (Msd.) and simulated (Calc.) Nyquist plots for NaOH-treated Ti-13Nb-13Zr after 168 hrs of immersion in Hank's solution.

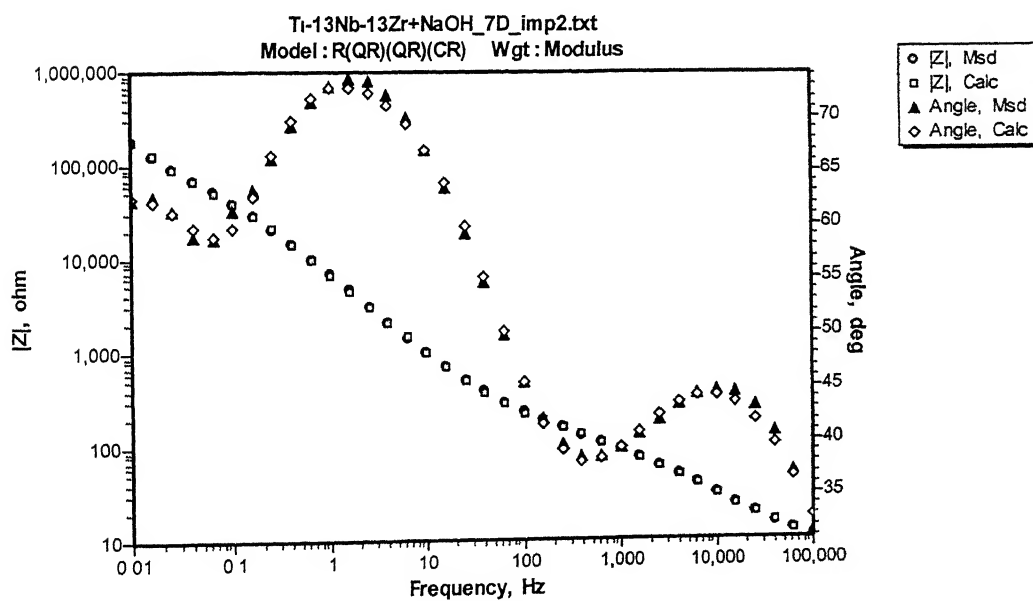
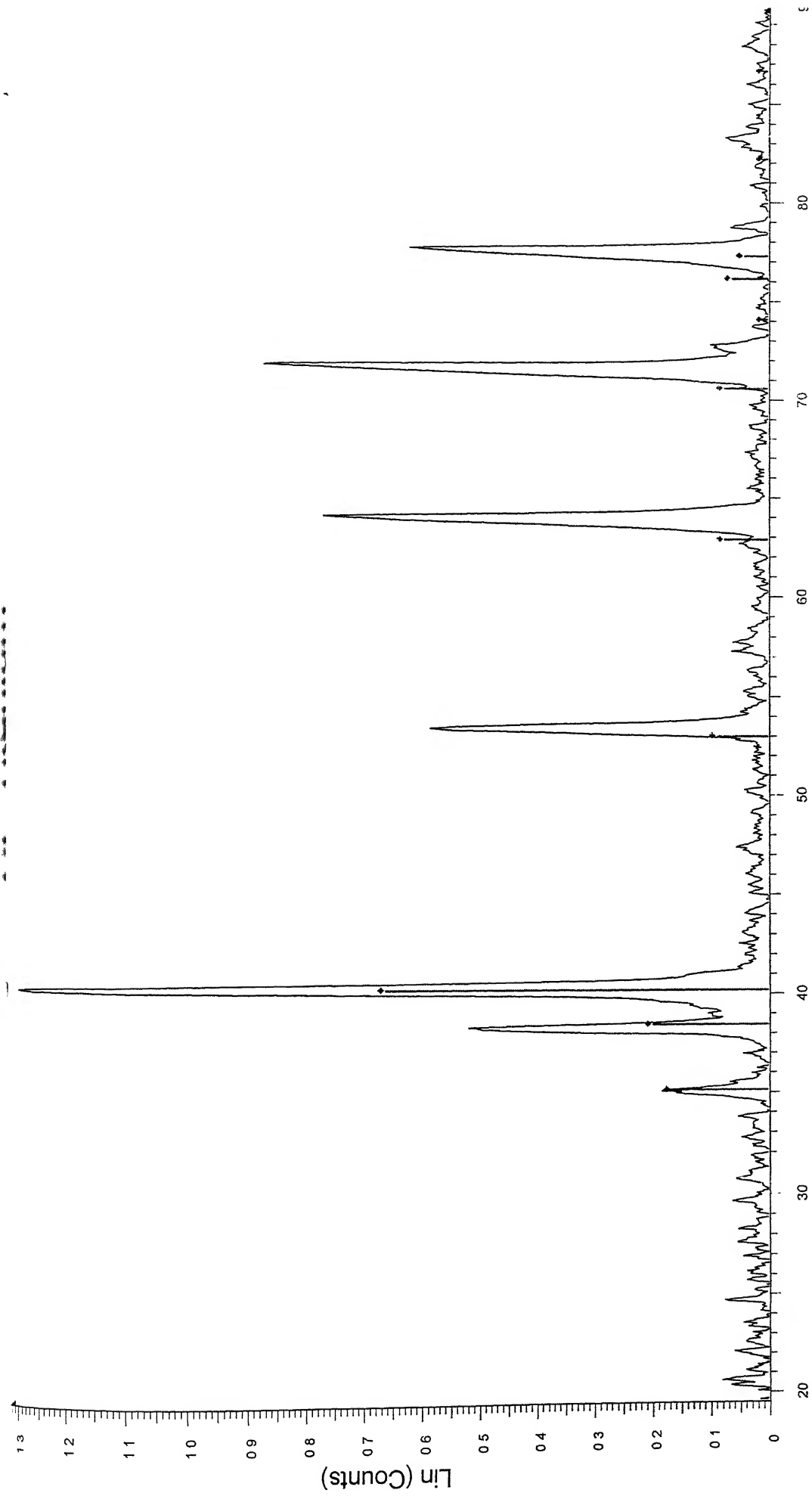


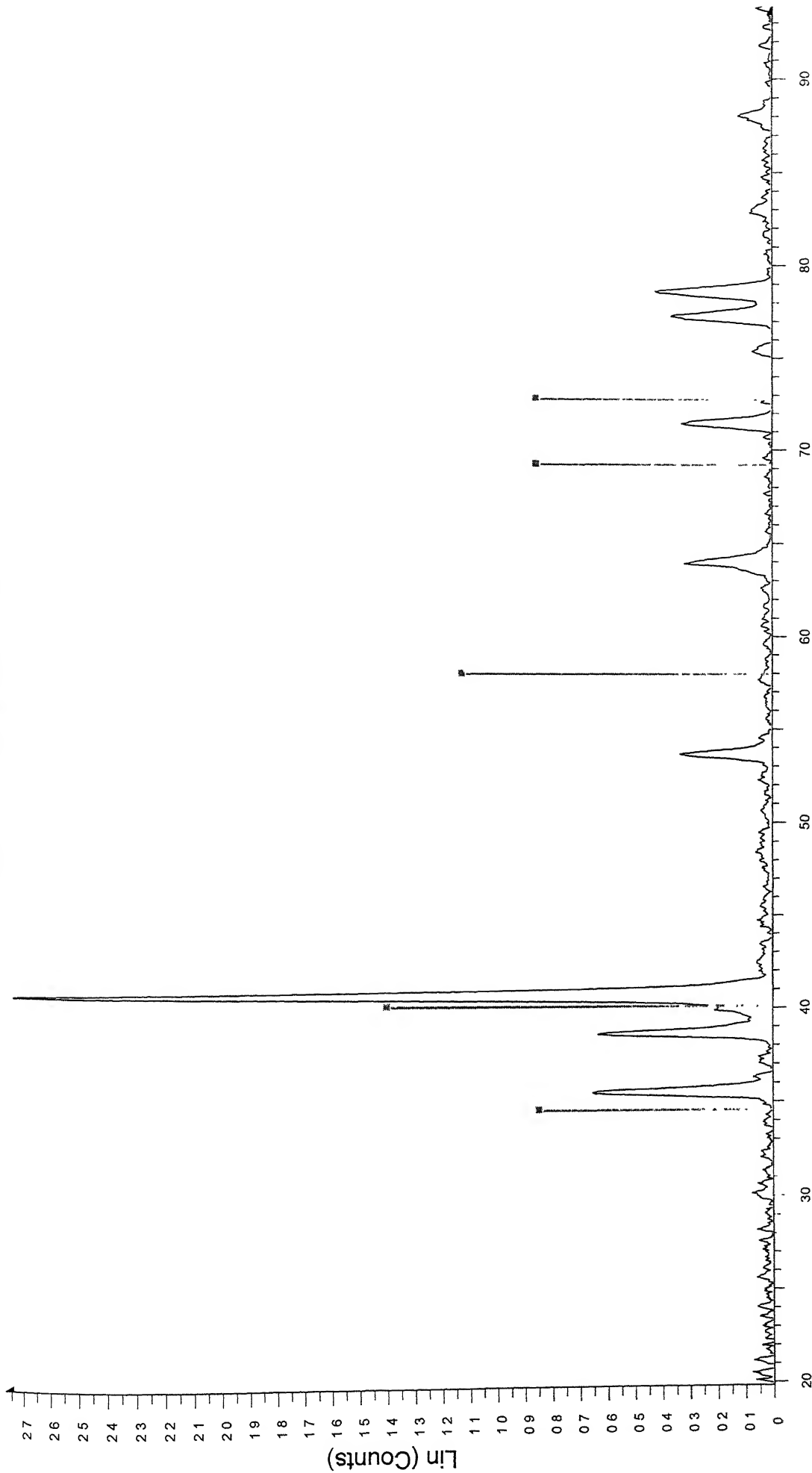
Figure C-88 Experimental (Msd.) and simulated (Calc.) Bode phase and magnitude plots for NaOH-treated Ti-13Nb-13Zr after 168 hrs of immersion in Hank's solution.



### 2-Theta - Scale

CP Titanium - File CP Titanium raw - Type 2Th/Th locked - Start 19 490 ° - End 90 040 ° - Step 0 050 ° - Step time 1 s - Temp 25 °C (Room) - Time Started 0 s - 2-Theta 19 490 - Theta 9 745  
Operations Background 1 000 1 000 | Import  
◆ 44-1294 (\*) - Titanium - Ti - Y 50 00 % - d x by 1 - WL 1 5406 - Hexagonal - I/Ic PDF 0 9 -

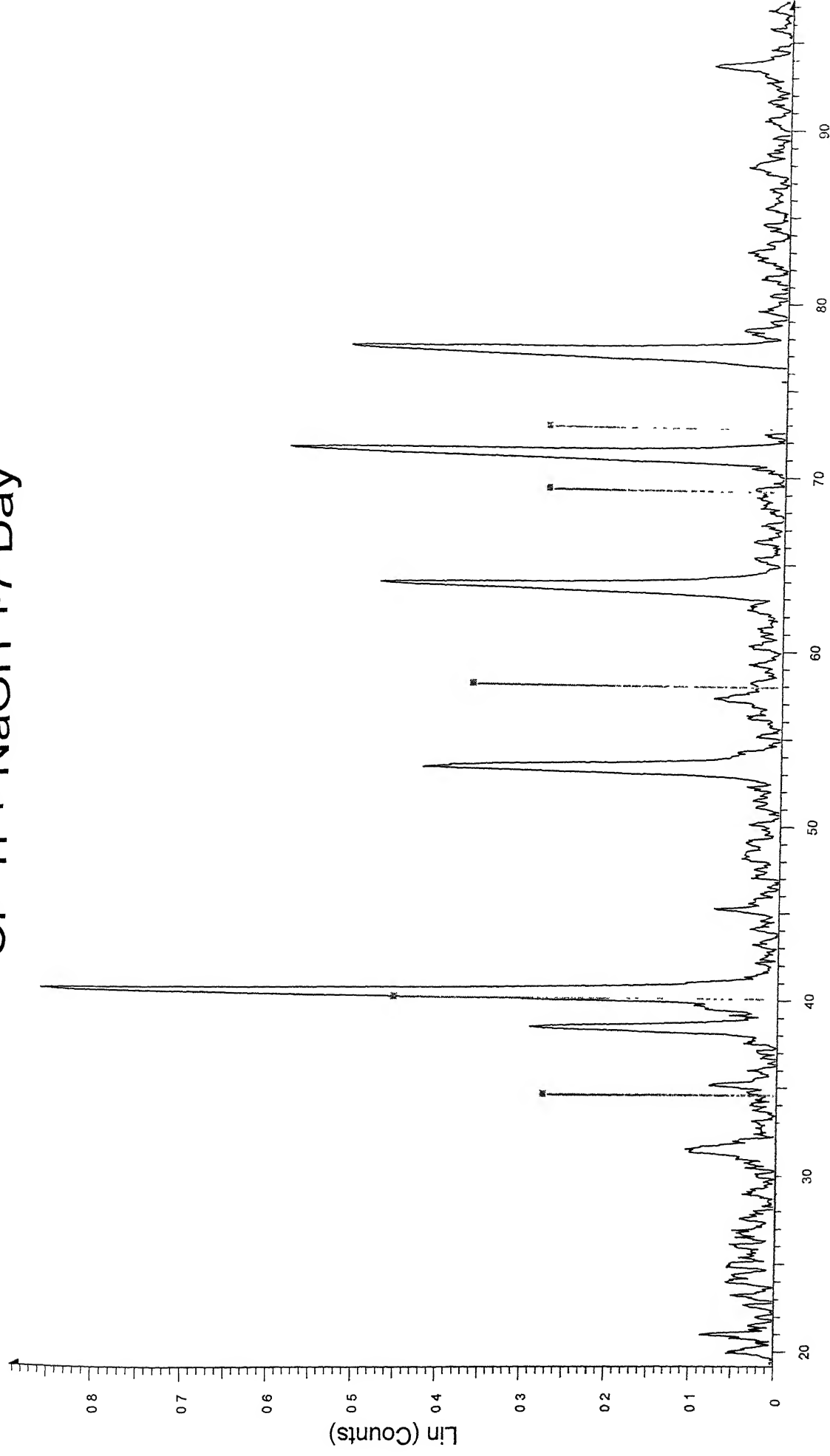
# CP Ti + NaOH



## 2-Theta - Scale

CP Ti + NaOH - File CP Ti + NaOH raw - Type 2Th/Th locked - Start 19.810 - End 93.960 - Step 0.050 - Step time 1 s - Temp 25 °C (Room) - Time Started 0 s - 2-Theta 19.810 - Theta 9.9  
Operations Background 1.000 1.000 | Import  
28-1152 (I) - Sodium Titanium Oxide - Na<sub>2</sub>TiO<sub>3</sub>/Na<sub>2</sub>O TiO<sub>2</sub> - Y 50.00 % - d x by 1 - WL 1.5406 - Cubic -

# CP Ti + NaOH +7 Day

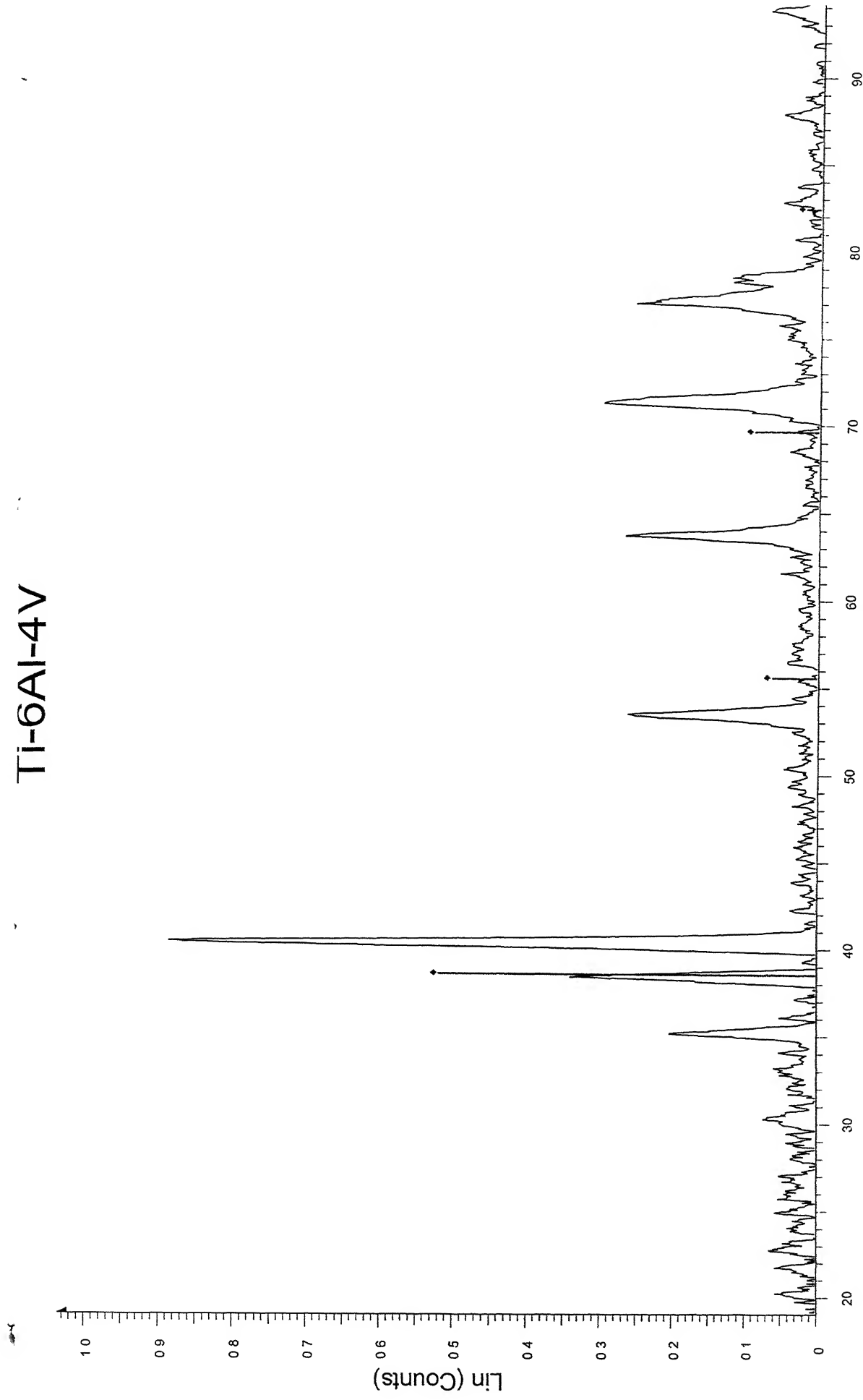


2-Theta - Scale

CP Ti + NaOH +7 Day - File CP Ti + NaOH +7 Day raw - Type 2Th/Th locked - Start 19 140 - End 97 390 - Step 0 050 - Step time 1 s - Temp 25 C (Room) - Time Started 0 s - 2-Theta 19 14  
Operations Background 1 000 1 000 | Import  
28-1152 (I) - Sodium Titanium Oxide - Na<sub>2</sub>TiO<sub>3</sub>/Na<sub>2</sub>O TiO<sub>2</sub> - Y 50 00 % - d x by 1 - WL 1 5406 - Cubic -



# Ti-6Al-4V

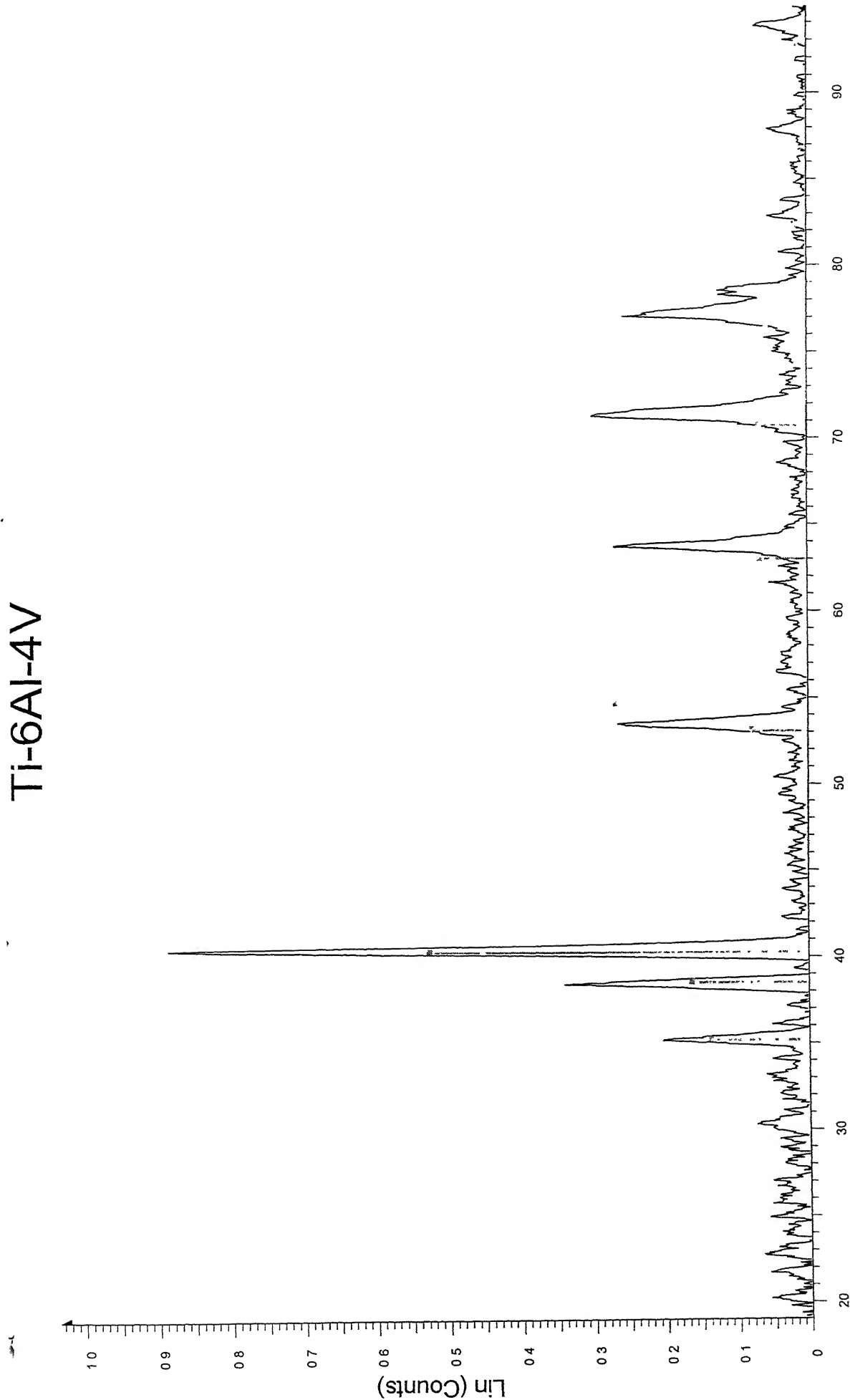


## 2-Theta - Scale

TI-6Al-4V - File: Ti-6Al-4V raw - Type: 2Th/Th locked - Start: 19.030 ° - End: 95.180 ° - Step: 0.050 ° - Step time: 1 s - Temp: 25 °C (Room) - Time Started: 0 s - 2-Theta: 19.030 ° - Theta: 9.515 ° - Chi: 0.000 ° - Background: 1.000 - 1.000 | Import

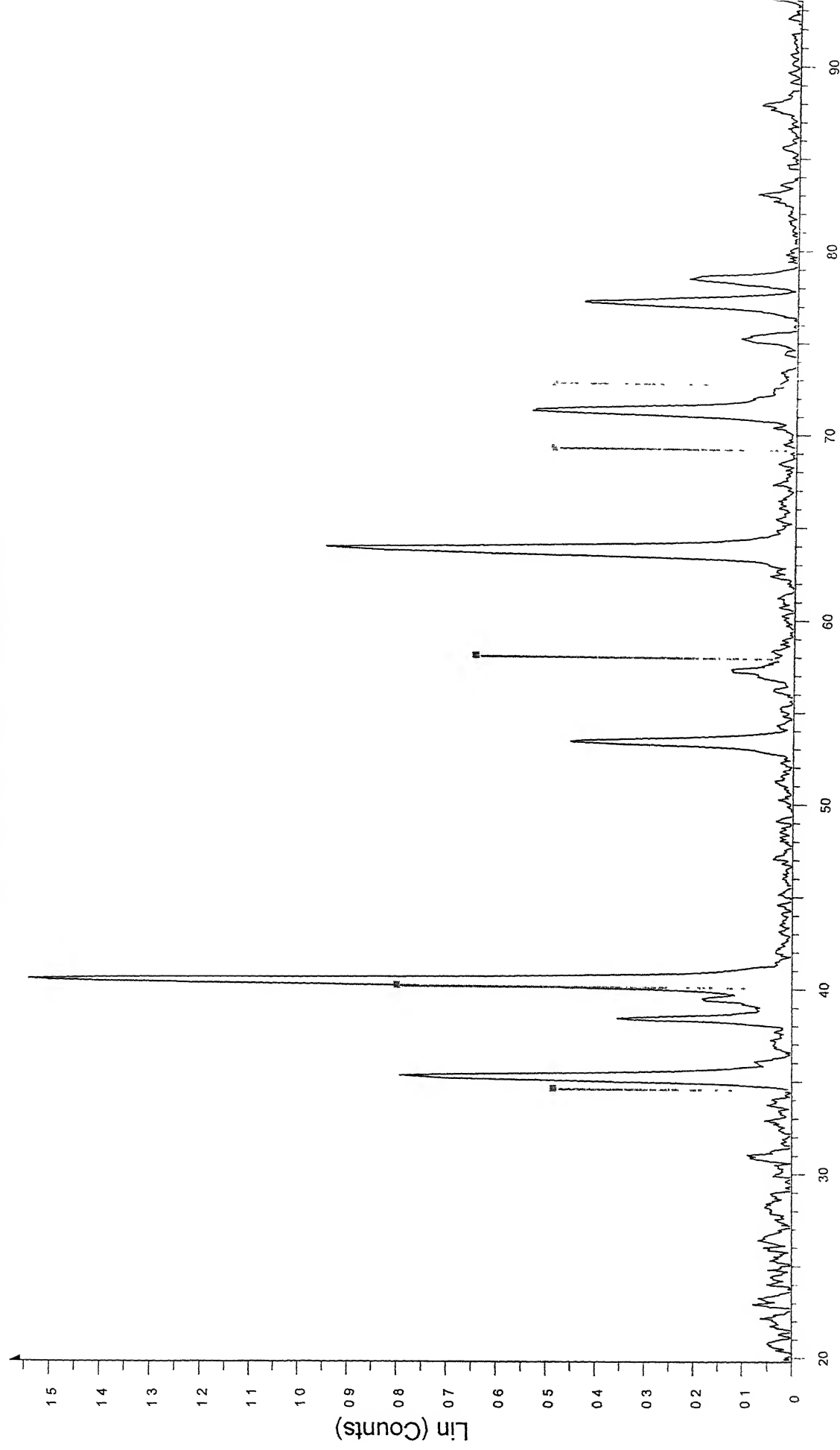
◆ 44.1288 (C) - Titanium - Ti - Y: 50.00 % d x by 1 - Wt: 1.5406 - Cubic - l/c PDF 8.7 -

# Ti-6Al-4V



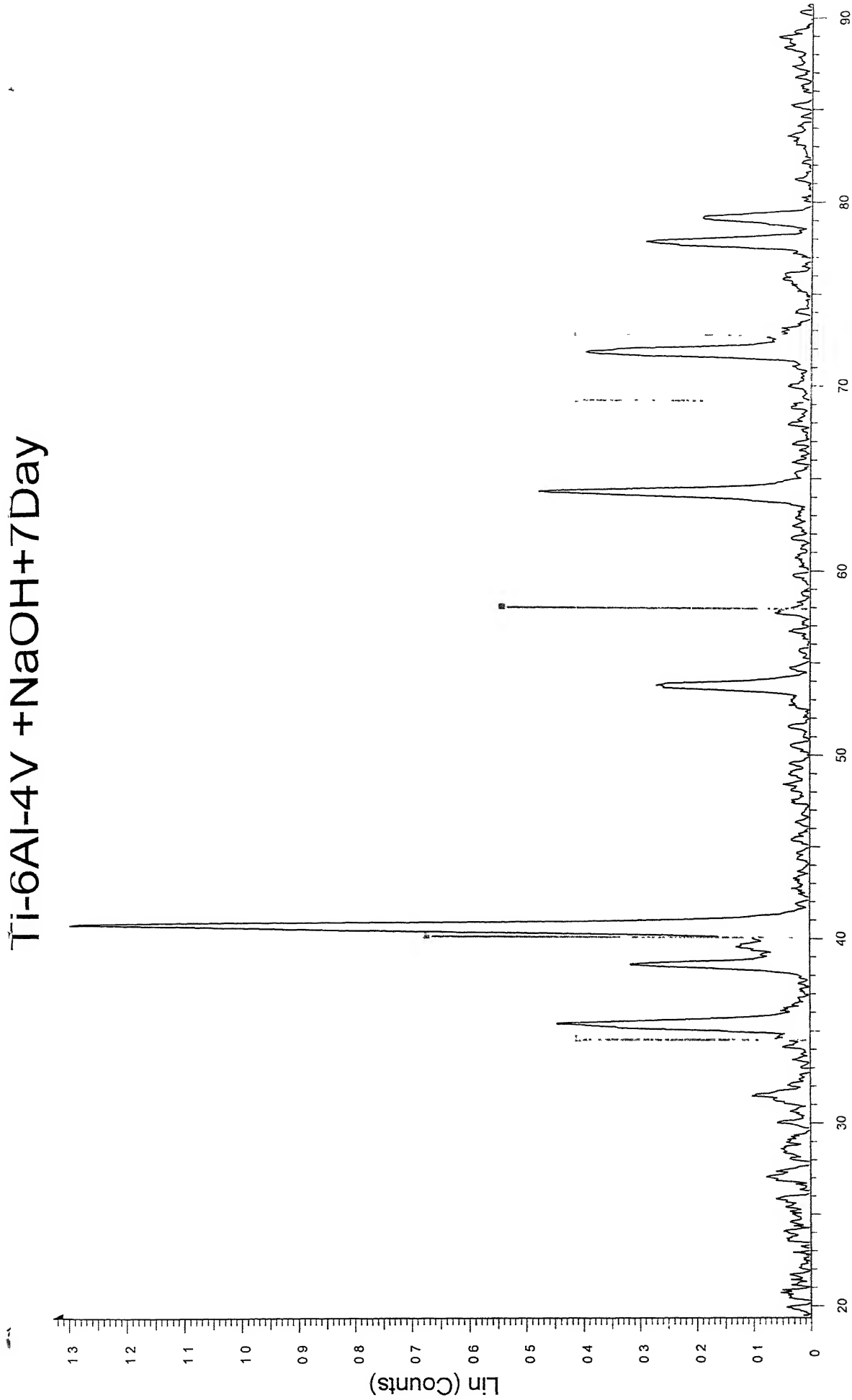
TI-6Al-4V - File TI-6Al-4V raw - Type 2 Th/Th locked - Start 19 030 ' - End 95 180 ' - Step 0 050 ' - Step time 1 s - Temp 25 ' C (Room) - Time Started 0 s - 2-Theta 19 030 ' - Theta 9 515 ' - Chi Operations Background 1 000.1 000 | Import  
44-1294 (\*) - Titanium - Ti - Y 50 00 % - d x by 1 - WL 1 5406 - Hexagonal - I/Ic PDF 0 9 -

# Ti-6Al-4V +NaOH



TI-6Al-4V +NaOH - File Ti-6Al-4V +NaOH raw - Type 2Th/Th locked - Start 19 780 ° - End 93 980 ° - Step time 1 s - Temp 25 °C (Room) - Time Started 0 s - 2-Theta 19 780 ° - Thet  
Operations Background 1 000 1 000 | Import  
28-1152 (I) - Sodium Titanium Oxide - Na<sub>2</sub>TiO<sub>3</sub>/Na<sub>2</sub>O TiO<sub>2</sub> - Y 50.00 % - d x by 1 - WL 1 5406 - Cubic -

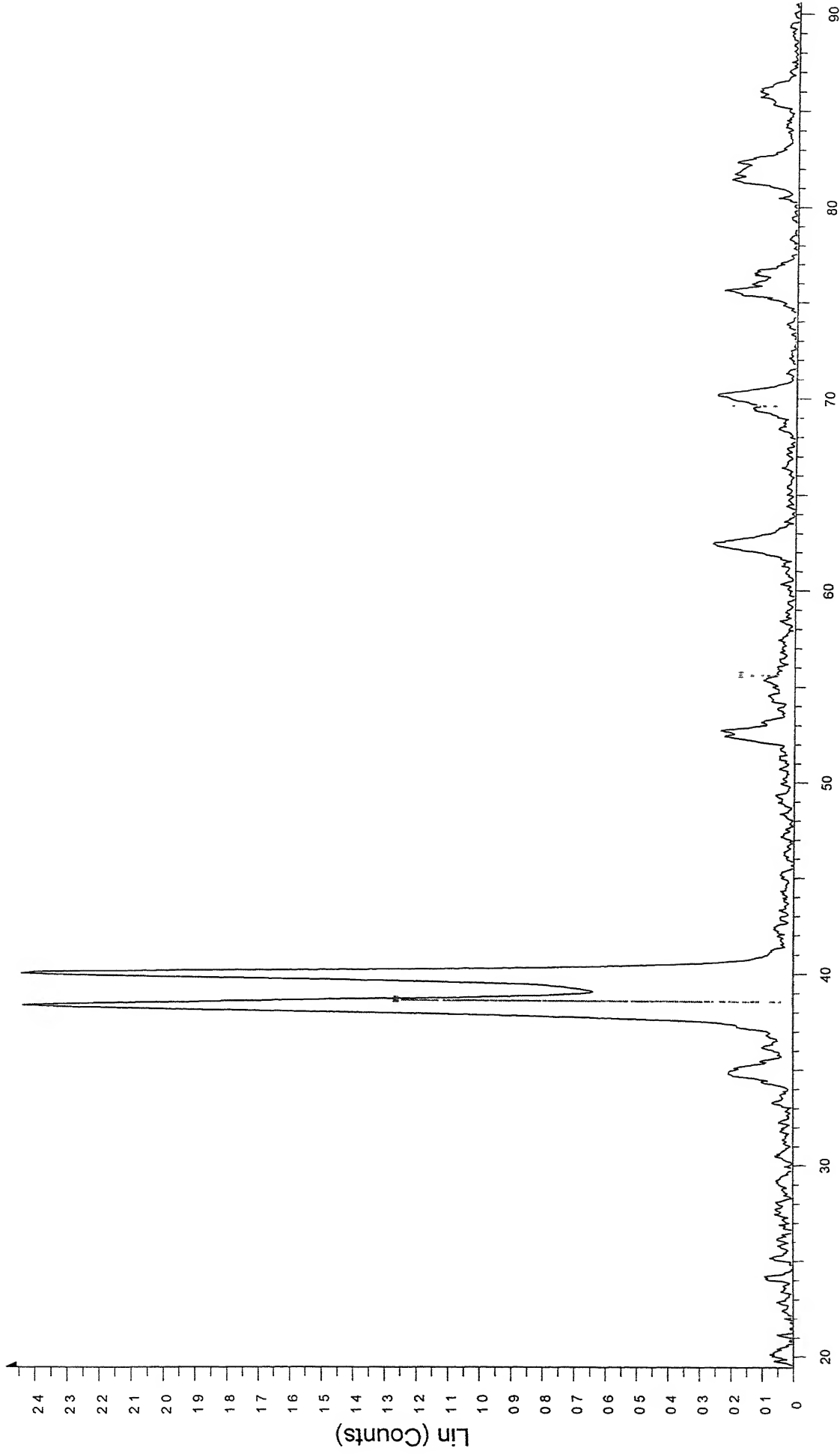
# Ti-6Al-4V +NaOH+7Day



2-Theta - Scale

File Ti-6Al-4V +NaOH+7Day - Type 2Th/Th locked - Start 19 350 ° - End 91 200 ° - Step 0 050 ° - Step time 1 s Temp 25 C (Room) - Time Started 0 s - 2-Theta 1  
Operations Background 1 000 | Import  
28-1152 (I) - Sodium Titanium Oxide - Na<sub>2</sub>TiO<sub>3</sub>/Na<sub>2</sub>O TiO<sub>2</sub> - Y 50 00 % - d x by 1 - WL 1 5406 - Cubic -

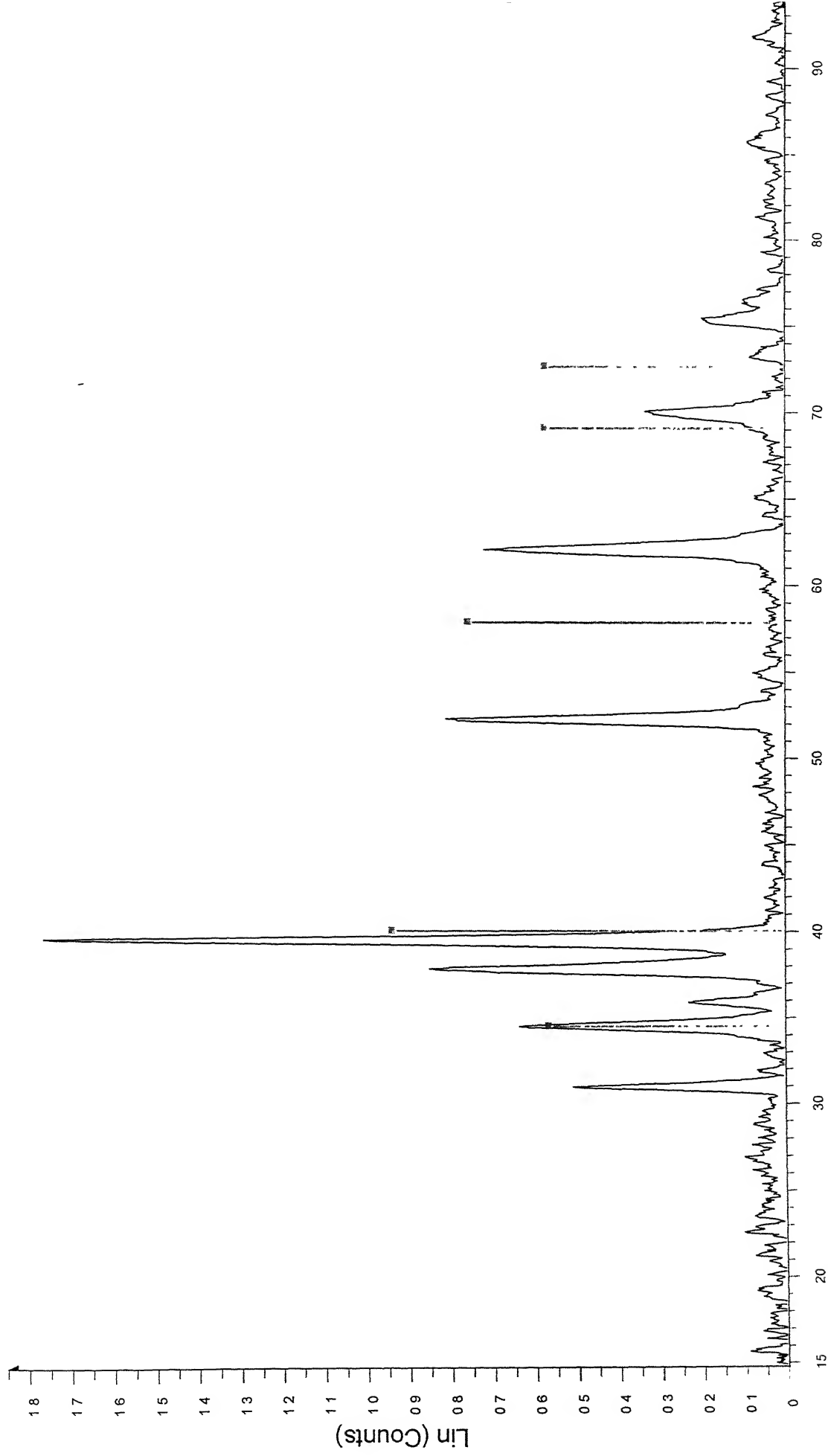
# Ti-13Nb-13Zr



2-Theta - Scale

☒ Ti-13Nb-13Zr - File Ti-13Nb-13Zr raw - Type 2Th/Th locked - Start 19 420 ° - End 91 220 ° - Step 0 050 ° - Time Started 0 s - 2-Theta 19 420 ° - Theta 9 710  
Operations Background 1 000,1 000 | Import  
44-1288 (C) - Titanium - Ti Y 50 00 % - d x by 1 - WL 1 5406 - Cubic - I/c PDF 8 7 -

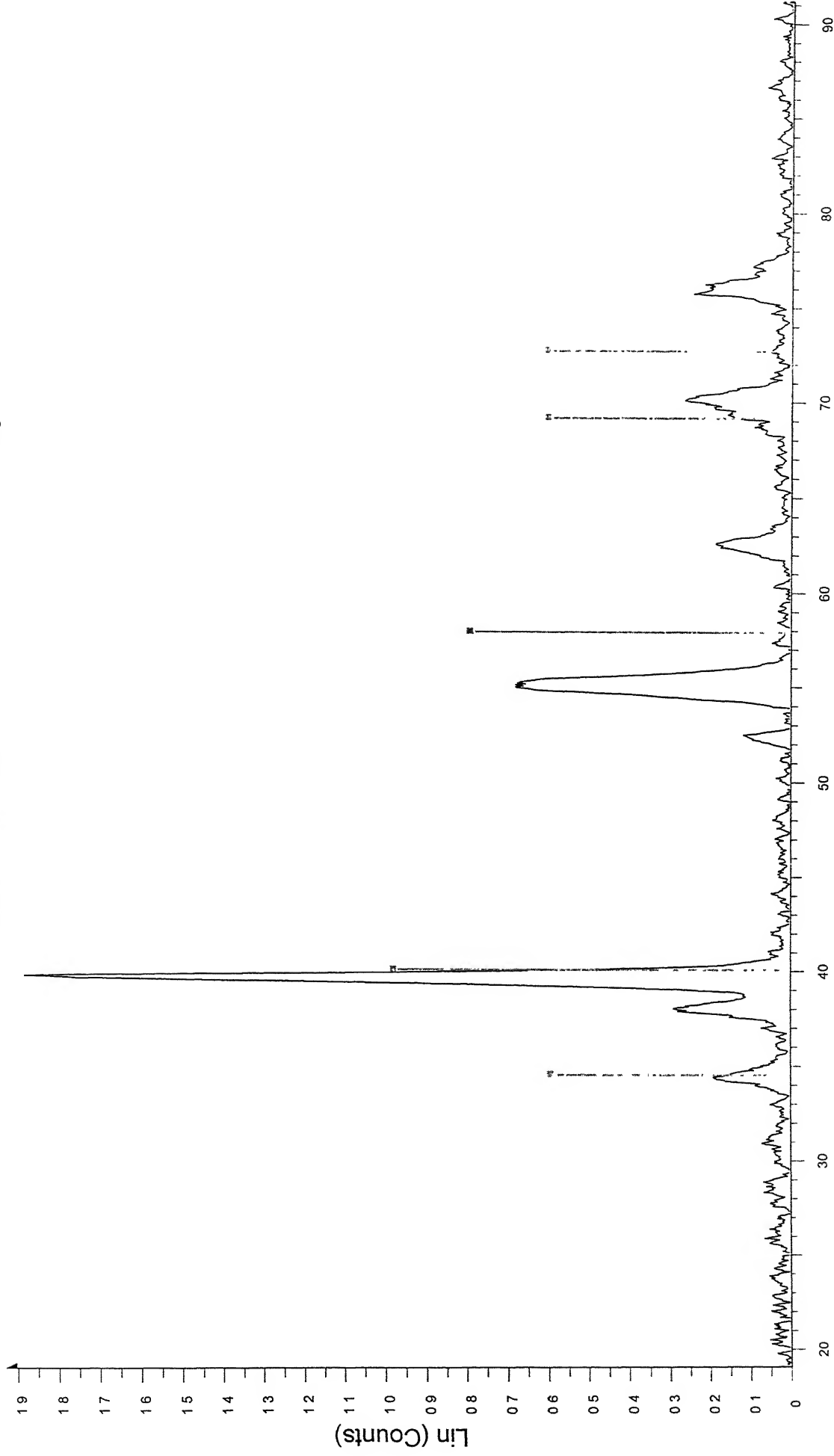
# Ti-13Nb-13Zr +NaOH



2-Theta - Scale

TI-13Nb-13Zr +NaOH - File TI-13Nb-13Zr +NaOH raw - Type 2Th/Th locked - Start 14 760 ° - End 94 010 ° - Step 0 050 ° - Step time 1 s - Temp 25 °C (Room) - Time Started 0 s - 2-Theta 14 760 Operations Background 1 000.1 000 | Import  
28-1152 (I) - Sodium Titanium Oxide - Na<sub>2</sub>TiO<sub>3</sub>/Na<sub>2</sub>O TiO<sub>2</sub> - Y 50 00 % - d x by 1 - WL 1 5406 - Cubic -

# Ti-13Nb-13Zr +NaOH+7Day



## 2-Theta - Scale

File: Ti-13Nb-13Zr +NaOH+7Day - File: Ti-13Nb-13Zr +NaOH+7Day raw - Type: 2Th/Th locked - Start: 19.070 - End: 91.620 - Step: 0.050 - Slit: 1 s - Temp: 25 C (Room) - Time Started: 0 s - 2-T  
Operations: Background: 1.000 1.000 | Import  
28-1152 (I) - Sodium Titanium Oxide Na2TiO3 Na2O TiO2 - Y: 50.00 % - d x by: 1 - WL: 1.5406 - Cubic -